Unravelling the Role of DJ-1 in Extracellular-Vesicle-Mediated Intercellular Communication.

By Thomas Page

Doctor of Philosophy

Aston University

Submitted September 2024

Abstract

Mutations in DJ-1 cause familial Parkinson's disease. DJ-1 plays a role in protection from oxidative stress, but the relation to PD is unclear. Recently, DJ-1 has been identified at higher concentration in extracellular vesicles (EV) from biological fluids of PD patients, providing a link between EV and a protein associated with PD. EV from neuronal and glial cells have demonstrated roles in synaptic activity, morphological plasticity, neurovascular integrity, contributing to the spread of neurodegeneration.

The effects of DJ-1 KO on the EV populations of neuronally-differentiated SH-SY5Y were studied under healthy and rotenone-treated conditions to understand the role of DJ-1 in EV-mediated intercellular communication in PD. EV number was studied via flow cytometry, protein content via mass spectrometry, and function via macrophage migration assays.

Results showed that the EV response to increasing rotenone concentration was altered in DJ-1 KO cells. While an EV increased was observed upon rotenone treatment in both genotypes compared to their control, treatment caused a 43 % increase of small EV in DJ-1 KO vs WT. However small EV count did not increase due to DJ-1 KO at 5 nM rotenone. EV protein content was altered at 10 nM rotenone; mass spectrometry identified 117 proteins with different concentrations between the two genotypes, suggesting that DJ-1 is functionally linked to EV production or uptake. While at 10 nM rotenone no increase in cell death was detected, a decrease in mitochondria health in DJ-1 KO vs WT was observed, suggesting EV changes are part of a stress response, not due to dying cells. Furthermore, DJ-1 KO alters the function of EV: at 10 nM rotenone EV from DJ-1 KO stimulated high macrophage migration, with no migration promoted by WT EV.

The results provide insights into mechanisms underpinning early stages of DJ-1-linked PD, revealing unknown links between EV and DJ-1.

Acknowledgements

Principally I would like to extend my heartfelt gratitude to my primary supervisor, Dr Mariaelena Repici. The guidance and support provided to me throughout this PhD project has been nothing short of exemplary, allowing this project to be substantially more successful than I could have anticipated, and my development as scientist to flourish. It is through her enthusiasm for her field that I have been successfully converted into one with an interest in imaging and microscopy, a field that I now wish to specialise in for my future career. Providing me with a specific path for future endeavors that I was previously lacking. P.s Thank you for putting up with my quirks through these years!

I would also like to provide my sincere gratitude to Prof. Andrew Devitt who in his role as secondary supervisor for this project has provided exemplary support and advice into the research of his fields of expertise: extracellular vesicles and immunology. His support was imperative to the correct interpretation of much of the data from this project and directions of follow up experiments.

Several pieces of work described in this thesis were performed in collaboration with other researchers. I would like to explicitly state their contributions thank those who contributed those these works. Dr Ivana Milic, Aston University, for the performance of mass spectrometry analysis of the EV proteome, and for providing support and training into many of the extracellular vesicle related protocols in the lab. Dr Saskia bakker, Advanced bioimaging facility at the University of Warwick, for carrying out CryoTEM imaging of extracellular vesicles. Last but not least, Dr Clara Alice Musi, Aston University, for providing me with neuronally differentiated iPSCs with which to study their extracellular vesicles.

On a personal level I would not have been able to deal with the stresses of PhD life without the support and friendship provided my brilliant PhD colleagues. Our comradery in the face of frequent set-backs, issues and stresses throughout the project have provided immeasurable comfort. Where would we be without the ability to vent our frustrations and have each-others understanding. Weekly Badminton and frequent visits to the various cafes, restaurants and food stalls in Birmingham has provided a consistent and important improvement in my emotional health. Thank you greatly for helping me maintain my sanity throughout this PhD. I would not be here today in such a great and successful position without you.

A very heartfelt thank you to Mom and Dad for your support during this stressful time and throughout my life. I have not always been receptive to your efforts but without your support I would likely never have been I the position to perform a PhD, I cannot thank you enough for all of your love and support throughout my life that has led to this moment.

Furthermore, I Would like to thank my home tutor during my high school years, Mr Barnett, who provided me with exemplary teaching in spite of my mental issues and truly is the reason I developed a true love and interest in science to begin with. I do not wish to imagine where I would have been without his support and enthusiasm for science during such a troubling time in my life. Though I am afraid I have let down his expectations as he always maintained that biology was not a real science 😉. Sorry!

Saving the best for last I would like to thank my dog Ollie for always greeting me with the utmost enthusiasm upon my return from work each day no matter the weather. Many stressful days have been provided warmth and comfort upon return by his unshaking love.

Table of Contents

Chapter 1: Introduction

Optimal and correct functioning of the central nervous system (CNS) is facilitated by rapid and efficient transmission of mechanistically diverse intercellular signals. The CNS hosts a variety of cell types with distinct roles, with glial cells (astrocytes, microglia and oligodendrocytes) representing approximately 33–66% of total brain cell mass and supporting neurons in many different ways (Jäkel, 2017).

Both glial cells and neurons release extracellular vesicles (EV), lipid bound vesicles containing proteins, nucleic acids and lipid signalling molecules (Fitzner, 2011; Venturini, 2019; Guo, 2020). While in the past EV were thought to be unwanted material released by cells (Rashed, 2017), we now know that their role is key in regulating both physiological and pathological intercellular communication processes in the CNS (Lorena, 2021). In this context, we are interested in understanding the role of EV in Parkinson's disease

Neurodegenerative diseases are a group of diseases of the central or peripheral nervous system that are principally characterised by but not limited to the progressive degradation of neurons, to which Parkinson's disease belongs (Dugger, 2017). The underlying mechanisms of their pathologies are presently still highly elusive, though large revelations have occurred in recent years such as the involvement of the gastro-intestinal tract microbiome (Sampson, 2016). This is despite intense efforts of study due to the rising public health cost of these diseases as our country's populations age and incidence rises, and the attraction of developing effective treatment for pharmaceutical companies created by these circumstances (Reitz, 2011).

The importance of intercellular communication in PD is multifaceted, as it is involved both in the spread of disease state, and immune responses towards the disease. Indeed, EV are major players both in the transfer of misfolded alpha-synuclein between cells and in the aberrant inflammatory response (Luk, 2012; Sampson, 2016).

Thus, PD provides a perfect avenue to explore the intricacies of intercellular communication in the brain. In this work, we focussed on a specific form of PD, induced by genetic mutations in the *Park7* gene, encoding for DJ-1 protein (Nuytemans, 2010).

1.1 DJ-1

Encoded by the gene *park7*, human DJ-1 is a small ~ 20 kDa protein of 189 amino acids in the large functionally heterogenous DJ-1/PfpI superfamily which forms a homodimer in physiological conditions (Bandyopadhyay, 2004; Lucas, 2010). Proteins of the superfamily are highly conserved and exist in most organisms, with human DJ-1 homologs existing throughout the biological kingdoms (Bandyopadhyay, 2004; Lucas, 2010). In humans DJ-1 is expressed ubiquitously, however expression is higher in cells with high-energy demand in tissues such as testes which show high glycolytic flux (Chuna, 2017).

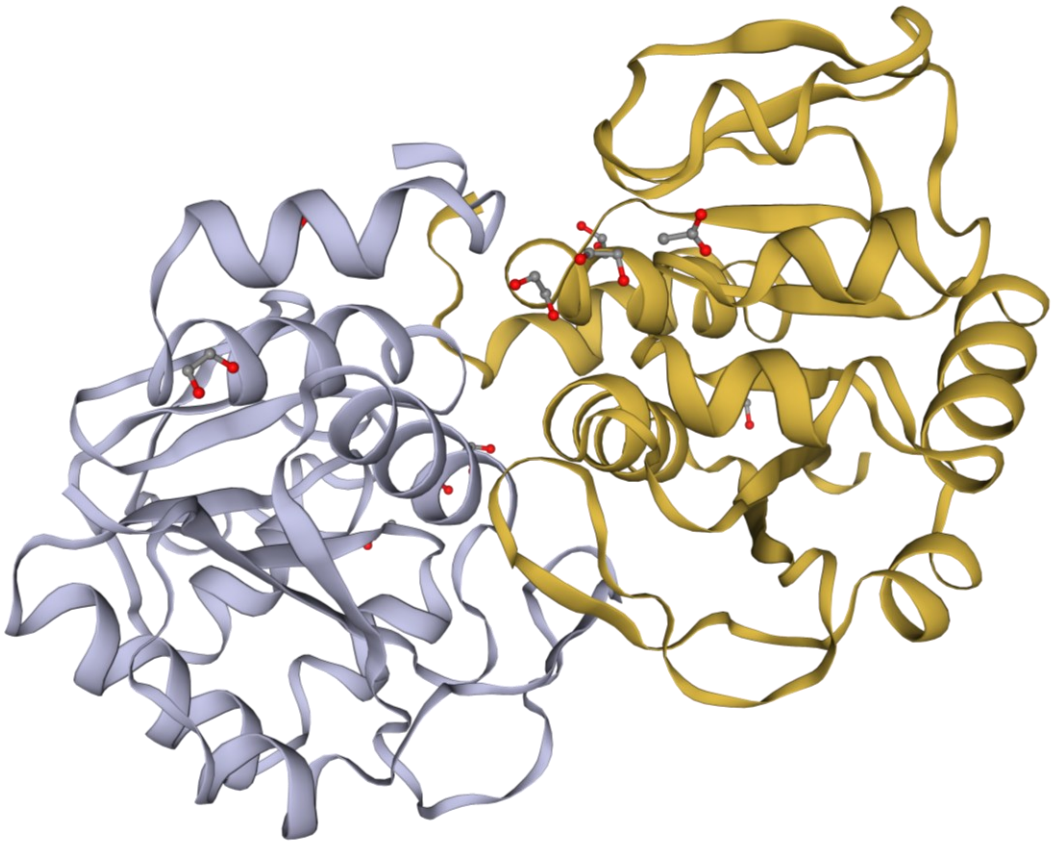

Figure 1:1. A graphical representation of the dimeric structure of DJ-1. Dimeric DJ-1 represented as a ribbon diagram. Component monomers are shown as distinct colours with monomer 1 as silver and 2 as gold. Alpha-helices are shown as coils and beta-sheets as arrows. (Milkovic, 2015) (PDB ID 4s0z).

DJ-1 has attracted substantial research interest due to its link to several diseases. It has been characterised as an oncogene in multiple cancers (Nagakubo, 1997; Hod, 1999; Sekito, 2005; Pardo, 2006; Davidson, 2008; Tian, 2008; Yuen, 2008; Kim, 2009; Miyajima 2010; Zhu, 2010; Fan, 2018), in addition to potential

roles in ischemic injury (Aleyasin, 2007; Yanagisawa, 2008), amyotrophic lateral sclerosis (Annesi, 2005; Lev, 2009) and multiple other inflammatory disorders (Zhang, 2020). In 2003, Bonifati identified the causative role of DJ-1 mutations in autosomal recessive Parkinson's disease (Bonifati, 2003).

1.1.2 DJ-1 and Parkinson's

Parkinson's Disease is an age-related progressive neurological disorder of the central nervous system, characterised by a combination of motor and non-motor symptoms. The cardinal features of Parkinson's disease are often described as tremor at rest, bradykinesia, muscle rigidity and postural abnormality, along with other motor and non-motor symptoms (Jankovic, 2008). At the cellular level Parkinson's disease also presents with consistent pathophysiological mechanisms. These are selective degradation of specific neuronal cell populations (particularly dopaminergic of the substantia nigra), α-synuclein aggregation and misfolding, dysfunction of the mitochondria, protein clearance deficiency, neuroinflammation and oxidative stress (Savitt, 2019).

The causative factors of Parkinson's disease are still poorly understood. They appear to be highly heterogenous involving intricate links between environmental, genetic, and epigenetic factors. Despite this, many familial inherited forms of Parkinson's disease exist due to mutations in a variety of genes. *Park7* mutations causes autosomal-recessive familial forms of Parkinson's disease through multiple distinct mutations with varying clarity of linkage to pathogenesis. At present in 2021, 19 distinct mutations with pathogenic linkage to Parkinson's disease have been discovered at both the genetic and protein level (Repici, 2019). (Table 1.)

DJ-1 linked parkinsonism manifests with distinct similarities to idiopathic PD. 2 brains of patients DJ-1 linked parkinsonism have been investigated post-mortem, with both presenting with Lewy body pathology. Furthermore, of 3 genetic causes of parkinsonism (DJ-1, PINK1 and Parkin) studied in a MDSGene systemic review DJ-1 linked cases showed the highest percentage of non-motor symptoms. Thus, showing that DJ-1 linked Parkinsonism as model does not limit study to motor symptoms (Kasten 2018). Finally, the experienced clinician and expert on Parkinson's disease Vincenzo Bonifatti stated in personal correspondence that DJ-1 clinically speaking is the closest genetic Parkinsonism to idiopathic Parkinson's.

Table 1:1. Current known pathogenic mutations of *Park7* / DJ-1 with links to Parkinson's disease. Table modified from Repici, 2019.

Mutation	Type	Location	Reference
g.159C > G ; IVS4+3insA	Compound heterozygous" nucleic acid substitution and insertion	5' UTR; intron 4	(Tarantino, 2009)
Ex1-5del (g.4443-18524del)	Homozygous: exon deletion	Exon 1-5	(Bonifati, 2003)
p.Leu10Pro	Homozygous: amino acid substitution	Exon 2	(Guo, 2008)
p.Thr19Lysfs*5 ; IVS6-1G > C	Compound heterozygous: frameshift; nucleic acid substitution	Exon 2; Intron6	(Hague, 2003)
p. Asp24Metfs*3	Homozygous: frameshift	Exon 2	(Taghavi, 2018)
p.Met26Ile	Homozygous: amino acid substitution	Exon 2	(Abou-Sleiman, 2003)
p.Ile31Aspfs*2	Homozygous: frameshift	Exon 2	(Stephenson, 2019)
g.11032A > G	Homozygous: nucleic acid substitution	Intron 2	(Ghazavi, 2011)
p.Gln45*	Homozygous: amino acid substitution (to stop codon)	Exon 3	(Hanagasi, 2016)
p.Glu64Asp	Homozygous: amino acid substitution	Exon 3	(Hering, 2004)
Ex5del (non-reported break points)	Homozygous: exon deletion	Exon 5	(Darvish, 2013)
p.Ile105Phe	Homozygous: amino acid substitution	Exon 5	(Abbas, 2016)
p.Ala107Pro	Homozygous: amino acid substitution	Exon 5	(Ghazavi, 2011)
g.16677A > C	Homozygous: nucleic acid substitution	Intron 5	(Erer, 2016)
p.Thr154Lys	Homozygous: amino acid substitution	Exon 7	(Di Nottia, 2017)
p.Pro158del	Homozygous: amino acid deletion	Exon 7	(Macedo, 2009)
p.Glu163Lys	Homozygous: amino acid substitution	Exon 7	(Annesi, 2005)
p.Leu166Pro	Homozygous: amino acid substitution	Exon 7	(Bonifati, 2003)
p.Leu172Gln	Homozygous: amino acid substitution	Exon 7	(Taipa, 2016)

Despite the number of recorded Parkinson's disease pathogenic mutations in the *Park7* gene, the underlying mechanisms through which these mutations act is still not understood. Study of pathogenic mutants has revealed multiple structural phenotypes, such as non-dimeric DJ-1 caused by change in 3D conformation (Ramsey, 2010). However, the variety in sequence location, and structural and functional outcomes of pathogenic *Park7* mutations have substantially hampered efforts to isolate the cause of pathogenicity (Wilson, 2003; Gorner, 2007; Malgieri, 2008; Ramsey, 2010). The lack of consistent structural characteristics in pathogenic mutants implies the potential existence of a consistent outcome of structural change such as a reduced or removed functionality. To date, we are still trying to identify the underlying functional mechanisms and roles of DJ-1, as well as the neuropathology of *Park7* mutations linked Parkinson's disease (Taipa, 2016; Repici, 2019).

1.1.3 The functions and roles of DJ-1

The importance of pathogenic mutations has prompted extensive study of its role and functions in both healthy and diseased states. Despite this, the functions and roles of *Park7/* DJ-1, particularly the mechanisms through which it is regulated and acts, have remained elusive. Over the years many variant independent functions have been attributed to *Park7/*DJ-1 both in healthy and diseased conditions, as shown in several extensive reviews (Mihoub, 2017; Raninga, 2017; Takahashi-Niki, 2017). The primary role of *Park7*/DJ-1 is related to Redox state signalling/sensitivity and protection against oxidative stress. Indeed, DJ-1 and it's homologues has been proven to be protective against oxidative stress in multiple organisms such as *mus musculus* (Kim, 2005) and *Drospholia melanogaster* (Canet-Avilés, 2004), as well as several cell model systems such as SH-SY5Y (Junn, 2005; Björkblom, 2013). However, the substantial variety of DJ-1 activities is becoming clearer as studies continue to reveal alternative functions, some with potential links to Parkinson's.

DJ-1 is a protector against oxidative stress

Specific neuron populations in the brain show heightened sensitivity to oxidative-stress-induced cellular damage and apoptosis. This is particularly true for the hippocampus and particularly the dopaminergic populations of the substantia nigra. In the hippocampus, the neurons of the CA1 subregion, when exposed to various oxidative agents, show substantially increased cell death compared to those of the

adjacent and morphologically similar CA3 (Wilde, 1997; Vornov, 1998; Sarnowska, 2002; Wang, 2009). Furthermore, the dopaminergic neurons of the substantia nigra (A9, according to the nomenclature of Dahlstrom and Fuxeare) (Dahlstrom, 1964) are sensitive to oxidative stress whereas the dopaminergic neurons of the ventral tegmental area (A10) are relatively resistant (Olney, 1990; Jenner, 1992). Thus, selective sensitivity to oxidative stress is believed to play a role in the pathology of a variety of neural pathologies, including Parkinson's where the loss of A9 dopaminergic neurons is a hallmark (Moore, 2001).

While DJ-1 mechanisms of action remain elusive, evidence of the oxidative-stress protection function of DJ-1 is conclusive. DJ-1 is a protein expressed primarily in tissues showing high ROS species concentration due to energy demands, such as testes, islets-of-Langerhans's beta cells, and cancer cells (Chunna, 2017; Eberhard, 2017; Kawate, 2017). In conjunction, overexpression of DJ-1 was shown to confer protection from oxidative stress, while knock-out increased sensitivity to oxidative stress in a variety of animal and cell culture experiments (Batelli, 2015; Kim 2005; Meulener, 2005; Ottolini, 2013; Taira, 2004; Thomas, 2011).

The localisation and activity of DJ-1 is modulated by a redox state sensitive cysteine residue.

DJ-1 also shows an ability to sense ROS concentration through the Cys106 residue, which is required for DJ-1 to exert protection against oxidative stress induced damage (Wilson, 2011). Cys106 is interesting because the oxidation state of its sulphur containing thiol side chain appears to be involved in protein activity/structure regulation. The Cys106 sidechain exists predominantly as a reactive thiolate anion ($R\text{-}S^-$) at physiological pH due to a low thiol pKa value of ~5 (Witt, 2008). Sequential oxidation of Cys106 results in sulfenate ($R\text{-}SO^-$), sulfinate ($R\text{-}SO_2^-$), and sulfonate ($R\text{-}SO_3^-$) anionic forms stabilised by hydrogen bonding to surrounding residues such as Ala107, Gly75, and Glu18. However, the sulfenate form is unstable and is believed to act as a transient intermediate between the thiolate and sulfinate forms in WT DJ-1 (Blackinton, 2009; Kinumi 2004).

Various reports state altered activity profiles of DJ-1 dependant on cys106 oxidation. For example, in the S^- and SO^- forms of Cys106, DJ-1 was reported to bind directly to and modulate tyrosine-hydroxylase (TH) and Dopa-decarboxylase (DDC) (Ishikawa, 2009), enzymes responsible for dopamine production and therefore highly relevant to Parkinson's pathology (Masato, 2019). Further oxidation of the cys106

to SO_2^- results in a change in localisation from the cytoplasm to the mitochondria drastically altering its activity and interactions, such as removing its interactions with TH and DDC (Masato, 2009). Finally, the highest stage of oxidation of Cys106, SO_3^-, is associated with unstable DJ-1 structure, loss of function and aggregation, potentially providing a link to Parkinson's pathology where oxidative stress is known feature. (Wilson 2011; Zhou, 2006}.

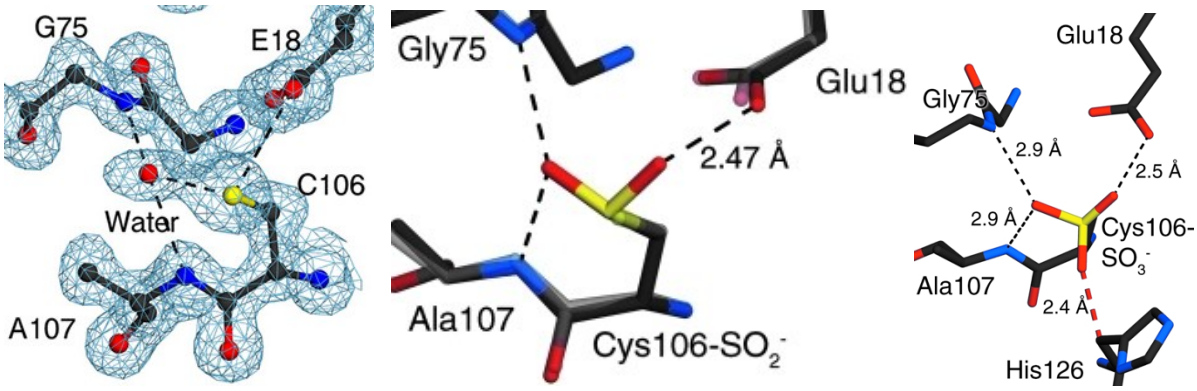

Figure 1.2 Cys106 oxidation states and resulting altered hydrogen bonding states in DJ-1. From left to right the stick and ball diagrams represent sequentially the 3 stable oxidation states of Cys106 in DJ-1. Amino acids named by code and residue number: A + Ala = alanine, G + Gly = glycine, E + Glu = glutamate, C + Cys = cysteine, His = histidine. Elements represented by colour: black = carbon; blue = nitrogen; yellow = sulphur; red = oxygen. Hydrogen bonding represented by dashed lines between atoms. (Wilson, 2011.) (PDB 1SOA, 1P5F)

DJ-1 regulates of the endocytic pathways through association with lipid rafts.

Similarly to other Parkinson's pathogenic proteins such as Parkin, α-synuclein, LRRK2, and PINK1, regulation of endocytosis has been attributed to DJ-1 (Kim, 2013). This was first reported in 2013 when DJ-1 palmitoylated at the cys46, 53, and 106 residues was shown to be associated with lipid rafts in astrocytes (Kim, 2013). In this work, knock-out of *Park7*/DJ-1 was shown to impair TLR4 endocytosis via down-regulation of lipid-raft dependent endocytosis (Kim, 2013). Interestingly, clathrin dependent endocytosis was reported as unaffected in this study, suggesting that DJ-1 may only affect specific endocytic pathways (Kim, 2013). Further information on DJ-1 lipid-raft association in astrocytes was reported in 2016, where DJ-1 deficiency caused down-regulation of major lipid-raft-components flotillin-

1 and caveolin-1, providing evidence towards a potential role of DJ-1 in lipid-raft based endocytosis (Kim, 2016). Interestingly, DJ-1 KO was also shown to impair endocytosis and recycling of synaptic vesicles at the synaptic terminals. (Kyung, 2018). Thus, highlighting another possible link between DJ-1 dysfunction and Parkinson's (Zou, 2021).

DJ-1 is involved in regulation of the immune system through a variety of distinct mechanisms.

Through research into the role of DJ-1 in a variety of diseases, particularly inflammatory disorders, a multitude of novel functions of DJ-1 relating to the immune system have been revealed, suggesting roles for DJ-1 both within immune cells and in the signalling between such cells (Zhang, 2020).

DJ-1 was shown to have multiple distinct effects on T cell populations (Zeng, 2022). In this context, research largely suggests that DJ-1 drives T cells towards non-inflammatory phenotypes with reduced migration (Zeng, 2022). In a study of CD8 positive T cells of human and murine organisms, DJ-1 KO was reported to reduce multiple markers of immunoaging (Zeng, 2022). DJ-1 KO was found to reduce oxidative phosphorylation and TCR sensitivity in hematopoietic and naïve T cells of young mice, resulting in an accumulative reduction in cell aging (Zeng, 2022). Furthermore, c.192G>C mutation and KO of *Park7* resulted in lower circulatory naïve and higher senescent CD8/4 T cell concentrations (Zeng, 2022). Similarly, DJ-1 deficient CD3 positive T cells show increased proliferation and migration towards chemokine receptor 4 stimuli via receptor overexpression (Min, 2022). In addition, it was reported that increased differentiation into pro-inflammatory phenotypes was observed in DJ-1 deficient CD4 positive T cells (Jung, 2014). This is in agreement with a recent study on rheumatoid arthritis (Min, 2022). Therein, DJ-1 was reported to induce regulatory T cell differentiation, inhibit pro-inflammatory phenotypes, and modulate activity of Th17, RANKL positive, and CD4 positive T cells (Min, 2022). T cell regulation involves redox signalling, and expression of the T cell activation related signalling proteins CD3 and TCR-β is diminished in DJ-1 deficient cells. Thus, DJ-1 has been postulated to be involved in regulation of T cell activity through several mechanisms. These mechanisms may also contribute towards its effects on differentiation (Zhou, 2017).

In addition to T cells, DJ-1 has been reported to play multiple roles within macrophages (Zhang, 2017). There are multiple varieties of macrophages distinguished by their residence in a particular tissue, and the most relevant to the work contained herein are the microglia, the CNS resident macrophages (Davies,

2013; Ginhoux, 2013). DJ-1 has been reported to be involved in multiple pathways in microglia, primarily controlling macrophage polarisation, as shown by the review of Zhang *et al* (2017). Indeed, multiple studies have shown that DJ-1 specifically regulates polarisation towards the anti-inflammatory M2 phenotype (Zhang, 2017). DJ-1 modulates the interaction between STAT1 and its phosphatase; potentially modulates the Atg5-Atg12-Atg16L1 complex through sirt1; reduces expression of P62, inhibits NLRX1 interaction with TRAF6, and blocks nuclear localisation of IRF5; regulates expression of TREM2; and finally regulates the Nrf2/Trx1/NLRP3 axis (Kim, 2013; Zhao, 2022; Wang, 2020; Peng, 2020; Trudler, 2014; Ji, 2020). These roles commonly lead to a heightened inflammatory M1 phenotype when DJ-1 expression is inhibited (Kim, 2013; Zhao, 2022; Wang, 2020; Peng, 2020; Trudler, 2014; Ji, 2020). However, a lack of information regarding the oxidation/activity state of DJ-1 in these studies complicates results interpretation (Kim, 2013; Zhao, 2022; Wang, 2020; Peng, 2020; Trudler, 2014; Ji, 2020). Furthermore, DJ-1 deficiency also appears to increase the sensitivity of microglia to dopamine, resulting in increased pro-inflammatory polarisation (Trudler, 2014). This effect possibly occurs through the reported increase in monoamine oxidase dependant dopamine catabolism.

Resident macrophages, the microglia, are important in the immune responses of the CNS. However, infiltration of circulatory monocyte derived macrophages also plays a role (Choi, 2020). In fact, DJ-1 expression is required for astrocyte-dependant CCl2-mediated infiltration of monocytes into the damaged brain (Choi, 2020). The astrocytic functions of DJ-1 are not however limited to the regulation of chemotaxis. In zebrafish astrocytes, DJ-1 was shown to regulate proteins associated with redox regulation, inflammation, and mitochondrial respiration in response to oxidative-stress-inducing toxin MPP+ (Frøyset, 2018). The majority of these proteins were shown to be nrf2 regulated, which is congruent with DJ-1 regulation of nrf2 in microglia (Frøyset, 2018). Similarly to its role in microglia, DJ-1 shows anti-inflammatory effects in astrocytes via the regulation of STAT1 and its phosphatase (Kim, 2013). Furthermore, in reactive astrocytes after cerebral ischaemia/reperfusion injury, DJ-1 negatively regulates the inflammatory response via regulation of SHP-1–TRAF6 interaction (Peng, 2020). This is consistent with other findings which showed that DJ-1 KO damaged astrocytes, via prostaglandin D_2 synthase, show an upregulation of pro-inflammatory mediator tumour-necrosis factor alpha and a downregulation of anti-inflammatory heme-oxygenase-1 (Choi, 2019).

Overall, the data suggests that DJ-1 in an immune context is consistently involved in driving anti-inflammatory and pro-regenerative aspects of immune cells, with particular evidence supporting this role in T cells, microglia and other macrophages, and astrocytes.

1.1.4 DJ-1 is linked with extracellular vesicles in Parkinson's patients.

While DJ-1 itself is an interesting avenue of research, this thesis is specifically interested in the link between DJ-1 and extracellular vesicles in Parkinson's disease. Very little information on this aspect of DJ-1 biology has been reported to date. A study of Korean males in 2014 (Ho, 2014) first reported a significant increase of DJ-1 in EV from urine of Parkinson's patients compared to a healthy cohort. This was followed by a second study from the same group showing a significantly higher, 2-fold, Oxidized DJ-1 level in the urine of Korean PD patients than in non-PD controls (Jang et al, 2018}. Furthermore, in 2019, Zhao et al showed a positive correlation between DJ-1 and alpha-syn present in plasma neural-derived exosomes in PD patients (Zhao, 2019). These results opened an exciting novel path of research into the mechanisms of DJ-1 action, its roles and how it may contribute to Parkinson's pathology. But what exactly are EVs and why are they of interest?

1.2 Extracellular Vesicles

1.2.1 What are extracellular vesicles?

Extracellular vesicles are heterologous phospholipid-bilayer enclosed vesicular structures produced by a wide variety of cells and secreted into the extracellular environment. (Figure 4.) They present with a large range of sizes, from diameters of 50 nm to 5000 nm. EVs are believed to be ubiquitous, however specific cell types with strong supporting evidence of EV production include neurons, platelets, epithelial cells, and immune cells such as B lymphocytes and dendritic cells (Maas 2017; Doyle, 2019; Bazzan, 2021).

EVs can be divided by several known types, with the exosomes, micro vesicles and apoptotic bodies being the best described and accepted distinctions. These three types of EV can be distinguished easily by distinct biosynthetic pathways (Maas 2017; Doyle, 2019; Bazzan, 2021). Exosomes are formed from the endocytic pathway, whereas micro vesicles are formed by budding of the plasma membrane, and

apoptotic bodies are only formed during apoptosis through apoptotic cell disassembly (Kerr, 1972; Tram, 1981; Harding, 1983; Pan, 1985). However, overlaps in size range, particularly between exosomes and micro vesicles, in conjunction with a heterogeneity of cargo and lack of readily detectable type-specific markers, makes differentiating between type at isolation a current difficulty. Thus, these type distinctions are not employed in favour of simple designation of size and or density-based distinction of entire EV isolates in many cases (Maas, 2017).

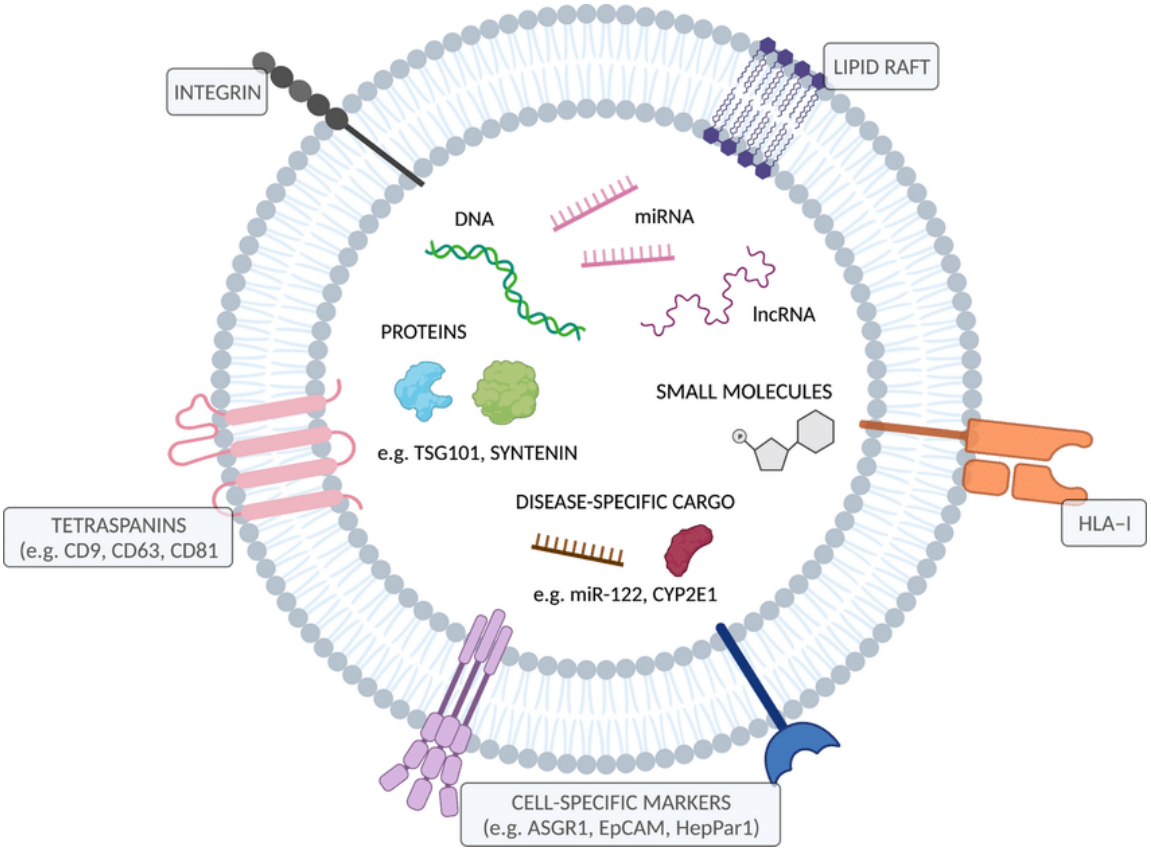

Figure 1.3 The structure and contents of extracellular vesicles. A diagram describing the structure and molecular components of extracellular vesicles. Taken from Newman, 2022.

EV types show distinct pathways of biogenesis.

The biosynthetic pathways of EV creation are varied and complex. Exosomes are derived from the endosomal compartment, where inward budding of the late endosome/multivesicular body membrane

forms intraluminal vesicles. Highly regulated selective packaging of cargo into intraluminal vesicles occurs at this stage (Pan, 1985; Akers, 2017). Multivesicular bodies are subsequently transported via cytoskeletal networks to the plasma membrane where fusion results in exocytic releasee of intraluminal vesicles as exosomes (Pan, 1985; Akers, 2017). As part of the endosomal pathway, exosome biogenesis would be assumed to be ESCRT (endosomal-sorting complex that is required for transport) dependant due to ESCRT involvement in intraluminal vesicle formation of multivesicular bodies (Babst, 2002; Wollert, 2010; Hurley, 2010). However, ESCRT-independent biogenesis of exosomes has been reported involving ceramide, syndecan/ALIX, and tetraspanins (Fang, 2007; Trajkovic, 2008). (Figure 4.)

In contrast to exosome biogenesis, microvesicles are directly formed from the plasma membrane (Zwaal, 1997; Muralidharan-Chari, 2009; Akers, 2013}. The process of sequential budding and pinching of the plasma membrane is believed to be dependent on a variety of factors and results from an interplay between membrane lipid redistribution and cytoskeletal proteins (Zwaal, 1997; Muralidharan-Chari, 2009; Akers, 2013}. It requires flippases and other flopases, actin and microtubules in conjunction with molecular motors such as dynasin and vesicular fusion proteins such as SNAREs (Zwaal, 1997; Muralidharan-Chari, 2009; Akers, 2013). (Figure 1:4.)

Regarding apoptotic bodies, their biogenesis occurs as part of the standard apoptosis pathway and shows similarities to that of microvesicles such as being plasma membrane derived (Kerr, 1972). Cells undergoing apoptosis progress through condensation of the chromatin, membrane blebbing and disintegration into distinct vesicular compartments. These distinct vesicular compartments are the apoptotic bodies. (Figure 1:4.) (Kerr, 1972).

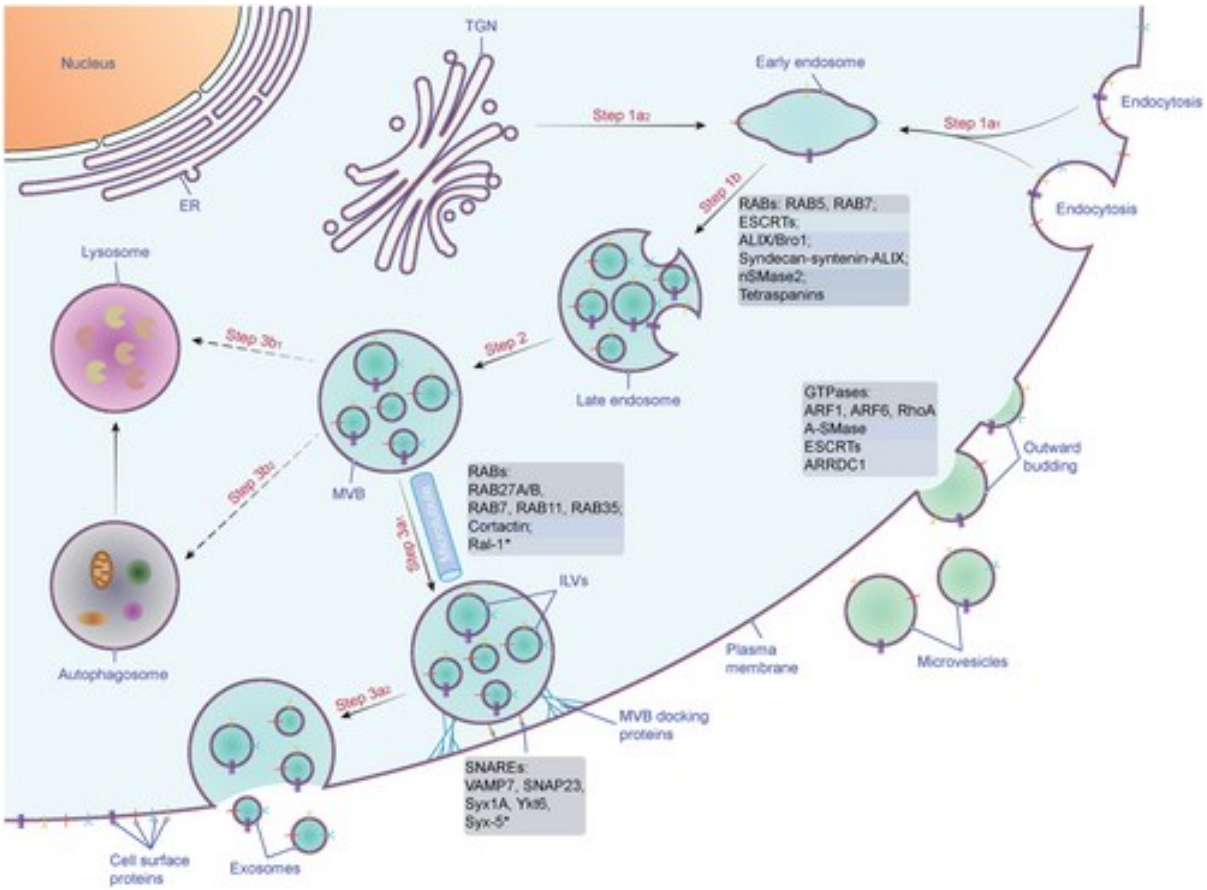

Figure 1:4. Biogenesis pathways of EVs. A diagram explaining the distinct biogenesis pathways through which extracellular vesicles can be created, with specific focus on exosomes and microglia. (Fussenegger, 2020)

EVs can transfer signals to recipient cells through several distinct pathways.

All EVs have been described to carry a wide range of molecules both as luminal and membrane associated cargo (Zaborowski, 2015; Harazsti, 2016). Examples of cellular contents carried as EV cargo includes proteins, DNA, RNA, and lipids. Originally EVs were believed to carry this cargo as a means of disposal, however, they are now known to act as an important signalling pathway players via their cargo, which they protect from degradation. The signalling role of EVs has been particularly well studied in angiogenesis, the immune system and CNS (Doyle, 2019).

Several distinct pathways exist through which an EV can signal to a recipient cell: direct interaction, fusion, and internalisation (Kwok, 2021). Direct interaction, as the name suggests, involves a direct

interaction between a membrane associated signalling molecule and or receptor on the surface of the EV and its partner on the surface of a recipient cell, subsequently initiating an intracellular signalling cascade (Kwok, 2021). An example of direct interaction signalling was shown by small EVs of dendritic cell origin activating T lymphocytes via interaction with MHC (Hsu, 2003). In the same work, blood-derived small exosomes of umbilical cord origin expressing MHC-I/II and CD34/80 also have been shown to stimulate T cell proliferation (Figure 6.) (Hsu, 2003).

Membrane fusion on the other hand while likely involving direct interactions with integrins/adhesion molecules to facilitate the event, involves the fusion of the vesicular membrane with that of the target cell (Jahn, 2003). As a result, the luminal cargo is delivered into the cytosol of the recipient cell (Jahn, 2003). Evidence of small EV fusion at present is specific to dendritic and tumour cells (Parolini, 2009; Montecalvo, 2010). Lower membrane pH in conjunction with higher sphingomyelin has been hypothesised as the reason for said specificity (Parolini, 2009; Montecalvo, 2010). Fusion as a method of cargo delivery to date has the lowest supporting evidence compared with direct interaction and internalisation. (Figure 6.)

Internalisation is the third and final proposed method of EV signal delivery. Internalisation, in contrast to fusion, refers to the uptake of the entire structurally-sound EV into a recipient cell by the endocytic pathways (Feng, 2010; Escrevente, 2011; Fitzner, 2011 Nanbo, 2013; Svensson, 2013). There have been reports of EVs been internalised by clathrin, caveolin, and lipid-raft dependant endocytosis, as well as phagocytosis and pinocytosis (Feng, 2010; Escrevente, 2011; Fitzner, 2011 Nanbo, 2013; Svensson, 2013). Evidence of uptake through these pathways likely is dependent on a variety of factors such as EV lipid and surface composition, and recipient cell type. This is particularly obvious in the case of phagocytosis and micropinocytosis which appear to be specific to immune cells and carcinoma cells, respectively (Feng, 2010; Escrevente, 2011; Fitzner, 2011 Nanbo, 2013; Svensson, 2013). Caveolin, clathrin, and lipid-raft dependant pathways on the other hand are less cell-type specific, with lipid-raft pathways showing the most supporting evidence (Figure 6.) (Mulcahy, 2014).

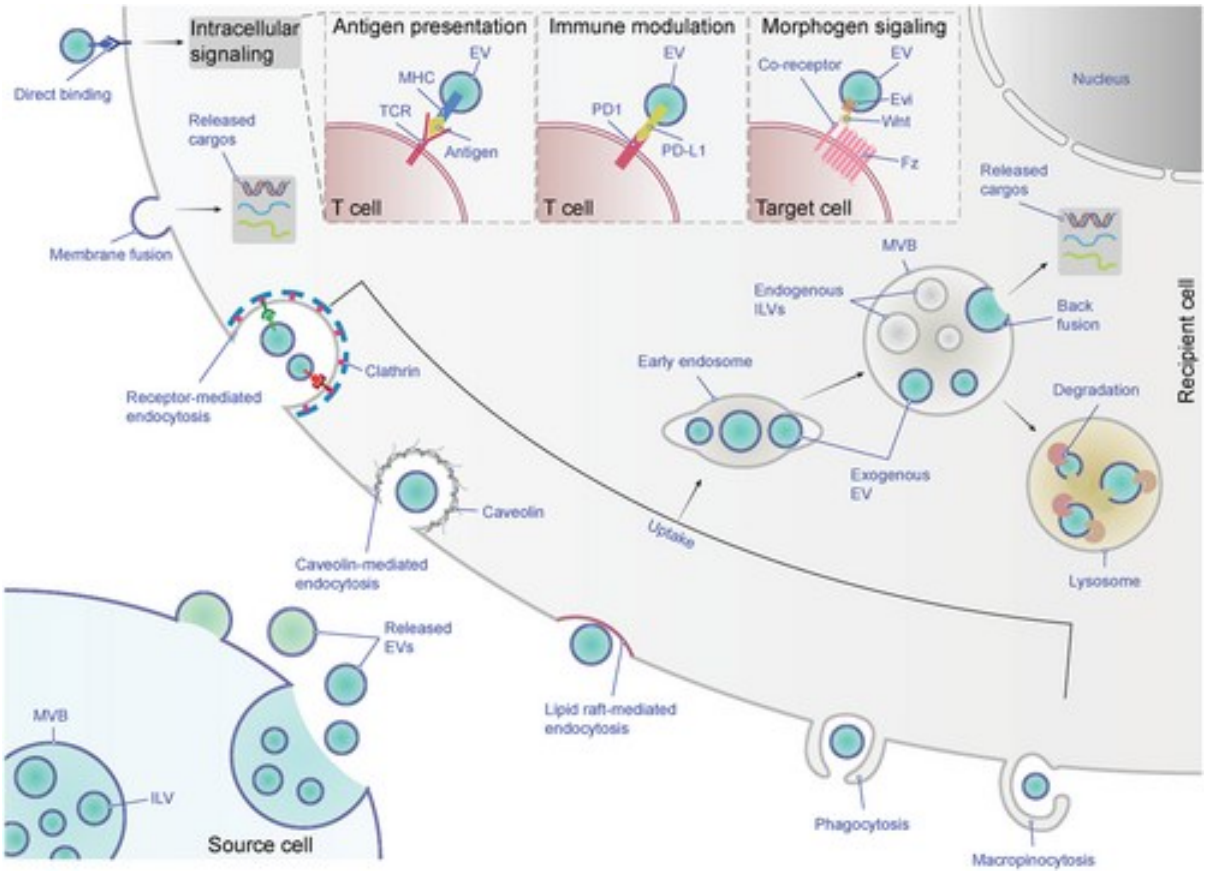

Figure 1:5. Routes and mechanisms of EV uptake and effects. A diagram describing in detail the routes and mechanisms of EV uptake and generation of functional effects. (Fussenegger, 2020)

EVs have been shown as capable of exerting varied functional effects on the activities of cells largely reflecting the role of the source cell, when applied as treatments of EV isolates. For example, EVs derived from breast cancer cells induced CD8 positive T cell exhaustion via activation of Smad (Xie, 2022}. Whereas mesenchymal-stem-cell-derived EVs promote tissue regeneration such as human cartilage (Vonk, 2018}. EV are believed to be capable of eliciting these effects in a local environment or in distinct areas of the body far from the producing cell in vivo. The existence of long-range signalling is supported by the discovery of EVs in most human bodily fluids such as blood, CSF and urine as well as their cargo-protective nature (Caby, 2005; Li, 2021; Ho, 2014; Boukouris, 2015). However, the tissue of most interest for the works herein is the brain where EVs have been reported to show a variety of roles in both the healthy and diseased state (Gassama, 2021).

1.2.2 Extracellular vesicles in the CNS

Our ability to study and the understand the physiological role of EVs in the CNS is highly limited by the lack of in vivo potential. Furthermore, the shared pathways of synaptic vesicles with EVs in neurons complicates study further, as functional studies which interfere in EV pathways could present significant off-target effects due to the intrinsic role of synaptic vesicles in neuron physiology (Gassama, 2021). Despite this, in vitro studies have revealed a variety of CNS cells that produce EVs and their potential roles. Neurons, microglia, oligodendrocytes and astrocytes all produce EVs, highlighting a substantial variation in EV potential functions due to the distinct roles of each cell type within the CNS (Gassama, 2021).

Neurons

The role of EVs in neurons was originally believed to be intrinsically linked to synaptic vesicles (Lachenal, 2010). However, more recent studies showed that while EVs are indeed heavily involved in synaptic activity, they are not limited to such (Goldie, 2014).

Through EV exchange neurons engage in both neuron-neuron and neuron-glia interactions. Interestingly, EV release from neurons appears to be linked to neurotransmitter release and strong depolarisation. Both neurons and oligodendrocytes produce increased amounts of EV upon stimulation by glutamate, an excitatory neurotransmitter (Lachenal, 2011; Barres, 2013). Similarly, neurons strongly depolarised by KCl have also shown increased EV release (Chivet, 2014). Furthermore, heterogenic stimulation of EV release from astrocytes and microglia stimulated by ATP released as a co-transmitter from neurons at synaptic junctions has been reported (Bianco, 2009; Antonucci, 2012). Thus, there is a litany of evidence supporting an increased role of EV release in high neuronal activity regions, suggesting an increased EV demand for neuronal activity.

EV release has also been reported as a potential regulator of synaptic plasticity. In 2018, Lee *et al* reported that the Wnt-secretion inhibitor, PRR7 was present on small EV (< 200 nm diameter) released in an activity-dependant manner wherein PRR7 was responsible for synaptic pruning of the excitatory synapses of surrounding neurons (Lee, 2018). Furthermore, the protein Arc-1, involved in almost all

known aspects of synaptic plasticity, and critical for long term synaptic regulation, has been shown to self-assemble with its mRNA into retroviral-like capsid structures. Subsequently, it can be encapsulated into EVs and transferred across synapses and undergo activity dependant translation in the post-synaptic cell (Pastuzyn, 2018).

In addition to neuron-neuron interactions at the synapse, neuron-astrocyte interactions are also involved in synaptic plasticity (Morel, 2013). Transfer of neuron-derived EVs containing miRNA124-3p to astrocytes was reported to result in an increase in glutamate transporter 1 expression, allowing increased uptake of glutamate from the synaptic cleft by astrocytes, thus contributing to neurotransmitter homeostasis in the synaptic cleft (Morel, 2013).

While a variety of research has highlighted the potential role of EVs in synaptic plasticity and maintenance, EVs are not only secreted at the synapse. EV release from the neurites of neurons has similarly been reported (Goldie, 2014). However, much less is known about non-synaptic EVs and how they may differ from those of the synapse.

EVs play a crucial role in the regulation of immune responses, and this is no different in the CNS. Neuron-derived EVs have been reported to regulate the activity of microglia, the brain-resident macrophages (Peng, 2021). For example, cortical-neuron EVs derived from healthy rats, when applied to rat primary microglia culture resulted in suppression of LPS-induced activation towards an inflammatory phenotype through inhibition of apoptosis and pro-inflammatory cytokines TNF-α, IL-6, and MCP-1 expression, and up-regulation of anti-inflammatory cytokine IL-10 (Peng, 2021). These data suggest that neuron-derived EVs can play a crucial role in microglia regulation and are capable of neuroinflammation suppression.

Astrocytes

As previously stated, astrocytes play a supportive role to neurons in the CNS. They are involved in the regulation of synaptogenesis, synaptic plasticity and function, metabolic support, and homeostasis. There have been multiple reports of the involvement of astrocyte-derived EVs in these standard astrocyte functions (Li, 2021).

Astrocytes surround synapses and play a crucial role in the regulation of multiple synaptic facets. Astrocytes were reported to react to neuronal EV, However, this is a bidirectional process with astrocyte EVs also affecting neurons (Li, 2021). Astrocyte-derived EVs via miRNA-26a-5p showed an ability to regulate multiple proteins responsible involved in morphological changes in hippocampal neurons, with EVs causing a reduction in dendritic complexity responsible for post-synaptic signal reception (Luarte, 2020). Small EVs derived from primary astrocytes have also been reported to promote synapse formation in primary cortical neurons, via fibulin-2 mediated activation of TGF-β (Chun, 2021).

Astrocyte-derived EVs also appear to be involved in their immunomodulatory functions. Wang *et al* (Wang, 2017) reported increased extracellular EV concentration in primary mouse astrocyte cultures upon stimulation with TNF-α. Similarly, the results of Dickens *et al* showed increased concentration of EVs in response to IL-β stimulation of mouse primary cortical astrocytes (Dickens, 2017). They also reported that said EVs rapidly localised to the periphery and upregulated transmigration of peripheral leukocytes, suggesting they function as chemo attractants rather than eliciting local effects. Furthermore, astrocyte-derived EVs appear to have the potential to elicit neuroprotective effects via neuroglobin transfer. Neuroglobin itself is antioxidant, anti-inflammatory, and anti-apoptotic in nature (Venturini, 2019).

Microglia

Microglia are primarily involved in immunomodulatory functions in the brain by reacting to various stimuli shifting between proinflammatory and pro-regenerative phenotypes (Muzio, 2021). The EVs of microglia reflect the pro inflammation/regeneration phenotype of the parent cell. Thus, depending on cargo they can promote inflammation or regenerative responses in other cells. For example, Lombardi *et al* reported the effects of EV derived from proinflammatory and pro-regenerative primary rat microglia on oligodendrocytes remyelination (Lombardi, 2017). Therein, EVs derived from proinflammatory microglia inhibited remyelination by oligodendrocytes, whereas EVs derived from pro-regenerative microglia promoted remyelination and oligodendrocyte recruitment (Lombardi, 2017). These results highlighted the dual aspects of microglia and their dependence of correct signals from surrounding cells. Additionally, microglia are phagocytic cells and have been shown to clear EVs from the parenchyma of the brain (Yuyama, 2014).

When microglial cells are the EV recipient cell type, the diversity of the reactive response of microglia would suggest that the cargo and uptake route of EVs affects the response of the receiver microglia cells. Indeed, EVs derived from cells in different biological states result in different effects on microglia. Healthy-oligodendrocyte derived EVs for example have been shown not to induce microglia activation when internalised by micropinocytosis, suggesting a homeostatic role of EV clearance (Fitzner, 2011). However, neuron-derived EVs containing high miR-21-5p induce proinflammatory M1 microglia polarisation (Yin, 2020), while an M2 polarisation has been achieved can also be induced by astrocyte derived EVs carrying miR-873a-5p (Long, 2020).

Oligodendrocytes

Neurons of the CNS are electrically isolated by the oligodendrocyte-created myelin sheath to facilitate fast and accurate electrical signal transduction. The process of myelin sheath generation and degeneration is a tightly controlled plasticity process involved in memory formation and learning (Krmerr-Albers,2020).

Oligodendrocyte-derived EVs are potentially involved in a negative feedback mechanism of myelination regulation, as they have been reported to downregulate myelination in an autocrine manner (Bakhti, 2011). Oligodendrocyte derived EVs may also be involved in the regenerative processes in response to neuronal pathologies. Oligodendrocytes have been reported to invade brain lesions, where they upregulate neurite growth and regeneration of neurons via transfer of retinoic acid loaded EVs (Goncalves, 2019). Furthermore, mature myelinating oligodendrocytes appear to produce EVs which promote stress resistance in local neurons, including high metabolic activity and axonal transport, and oxidative stress (Frühbeis, 2020). While supporting evidence is lower, it has been suggested that oligodendrocyte EVs are also involved in microenvironment clearance and immunosurveillance via signalling to microglia and astrocytes (Krämer-Albers, 2020). Additionally, oligodendrocytes release EVs in response to excitatory neurotransmitter glutamate, suggesting that their role is required at locations of high neuronal activity (Frühbeis, 2013).

1.2.3 Extracellular vesicles in Parkinson's

With the numerous reports of EV function in vital aspects of healthy brain function such as myelination, synaptic plasticity and homeostasis, neurotransmitter recycling, and immunomodulation; it is unsurprising that EVs are believed to be involved in pathological states of the brain as well (Balaj, 2021). Dysfunctional intercellular signalling via EVs has been linked to a variety of pathologically distinct conditions (Xiao, 2021). They have been shown to be involved in transfer of disease-associated misfolded protein aggregates such as Tau fibrils between neurons in Alzheimer's (Ruan, 2020). In Addition, dysfunction of EV signalling is also reported as contributing to neuroinflammation in multiple disorders, which is believed to be causative of neuron degeneration (Marostica, 2021). Thus, there has been substantial interest in EVs as agents of pathology and as novel sources of biomarkers in diseases ranging from cerebral ischaemia to neurodegenerative conditions such as Parkinson's and Alzheimer's. For the purposes of this thesis, the focus will be on the role of EVs in Parkinson's. However, several in depth reviews have covered EVs in neurodegenerative disorders as a whole (Xia, 2021; Croese, 2018).

EVs as modulators of alpha-synuclein pathology

In Parkinson's the hallmark misfolded and aggregated protein so common among neurodegenerative disorders is α-synuclein which is found as the major constituent of Lewy body aggregates. α-synuclein itself is a small protein, abundant in the brain and particularly in neurons of the substantia nigra, olfactory bulb and dorsal motor nucleus of the vagus, that regulates synaptic vesicle trafficking and neurotransmitter release (Henderson, 2019; Taguchi, 2019). The transmission or prion hypothesis states that intercellular transmission of misfolded α-synuclein is responsible for the spread of neurodegeneration in Parkinson's. This is supported by evidence of structural colocalisation of synuclein misfolding and neurodegeneration in the brain, and multiple reports of intercellular transmission of misfolded synuclein (Visanji, 2013, Jan, 2021). If this is true, then how might EVs be involved in transmission? Do they transfer the protein at all and if they do are the effects on recipient cells different than those of healthy origin?

The first point to link alpha-syn pathology and EV would be checking whether EVs even contain α-synuclein, in the native or a misfolded state. Kurzawa-Akanbi *et al,* interested in an altered sphingolipid

profile in glucocerebrosidase-mutation-linked Lewy body disorders, investigated post-mortem cerebrospinal fluid and brain-tissue EVs of glucocerebrosidase-mutation carriers and non-carriers (Kurzawa-Akanbi, 2021}. They discovered that purified EV from Lewy body disorder CSF and brain tissue were indeed loaded with α-synuclein, along with other neurodegeneration associated proteins such as Tau (Kurzawa-Akanbi, 2021}. Furthermore, in an in-vitro solution-NMR experiment, they found that these EVs facilitated aggregation of α-synuclein, though the causative mechanism was not understood (Kurzawa-Akanbi, 2021}. While this suggests a possibility of EV-induced aggregation, determining whether this interaction and effect could persist in the complex environment of the CNS where diverse homeostatic mechanisms are at play (De Luca, 2018), rather than the isolated system employed, would require more advanced study.

Stuendl *et al* also investigated the effects of EVs derived from Parkinson's patients CSF on α-synuclein in H4 human neuroglia cells transfected with human α-synuclein without identifying isolated EV contents (Stuendl, 2016}. They discovered a similar effect, where aggregation of α-synuclein was induced by treatment with EV. Thus, there is reproducibility of effect in distinct environments. However, in both studies the causative mechanism is not understood. Furthermore, both studies employ CSF EV isolates and as such do not know the cellular origin of their EVs. This raises the question: how does the effect that EVs have on α-synuclein change depending on cellular origin?

There have been several studies into EVs derived from specific CNS related cells in Parkinson's disease and their relation to alpha-synuclein pathology. One such study, again primarily regarding GBA-mutation-linked Parkinson's Disease, found that EVs of cultured fibroblasts from Parkinson's patients with severe GBA mutation increased the levels of internal phosphorylated α-synuclein in neuron-like differentiated SH-SY5Y cells (Cerri, 2021). However, the SH-SY5Y cells in this study were genetically engineered to overexpress α-synuclein. It is unclear what effect overexpression may have on aggregation mechanisms. Furthermore, the fibroblasts were originally obtained from skin biopsies, thus they are not CNS fibroblast cultures. While this does support the idea of a potential global stress response which is simply conductive to α-synuclein defects, it would be interesting to understand whether CNS fibroblasts show a different effect.

Grey *et al* studied the aggregation of soluble α-synuclein in a cell free environment but with undifferentiated mouse neuroblastoma N2a cells as the EV source (Grey, 2015}. Similarly to other

studies, they observed a promotion of aggregation upon EV exposure, and they reported on this effect in more detail. The promotion of aggregation appeared to be a catalytic effect as the lag phase of aggregation was decreased upon EV exposure. Furthermore, while the aggregation promotion was interestingly not dependant on whether the N2a cell source over-expressed α-synuclein or showed native expression, it was dependant on vesicle lipid content. N2a EVs were found to contain several distinct lipid classes. When exposed to vesicles created using the observed lipids, α-synuclein aggregation was only promoted by Ganglioside vesicles. The observed catalytic effect and lipid dependence suggests that EVs of particular lipid compositions could act as seeds for nucleation of aggregation by binding or interacting with α-synuclein.

While the results of the previously described experiments are interesting, understanding how EVs of a specific cellular origin affect α-synuclein mis-folding and aggregation in a cellular environment is necessary to achieve improved understanding. It has been shown that SH-SY5Y EVs contain α-synuclein (Zhou, 2021), and that exogenous α-synuclein induces Lewy body formation in differentiated SH-SY5Y cells (Taylor-Whiteley). However, there appears to be a distinct lack of study into the effects of EVs of known cell origin on α-synuclein pathology in cellular models to corroborate these results.

Other than increasing aggregation of α-synuclein, EVs are also postulated to cause intercellular transmission of α-synuclein (Danzer, 2012). Indeed, Danzer, *et al* reported that EV associated α-synuclein from H4 neuroblastoma cells showed a higher propensity to be internalised into H4 cells than free α-synuclein (Danzer, 2012). However, a distinct lack of corroborating evidence of this effect and the use of neuroblastoma introduces concerns about relevance in better model systems.

Additionally, lipid-peroxidation product 4-hydroxynonenal has been shown to induce increased α-synuclein aggregation and secretion within EVs of rat primary neuron cultures (Zhang, 2018). Multiple forms of Parkinson's disease present with and appear to be linked to increased ROS production and/or other lipid defects including GBA and DJ-1 linked Parkinson's disease (Puspita, 2017; Alecu, 2019; Xiao, 2022). This not only provides further confidence in the hypothesis of intercellular transmission of α-synuclein, but evidence that said transmission may be altered in diseased states.

Interestingly, it is not only the neurons that appear to be involved in propagating α-synuclein aggregation. Substantial evidence implicates both microglia and astrocytes as modulators of the pathology such as in multiple systems atrophy where α-synuclein aggregates in oligodendrocytes. Glial cells, and microglia in-particular, endocytose aggregated α-synuclein (Stefanova, 2011; Tremblay, 2019). However, excessive endocytosis of aggregated α-synuclein induces aggregation within the glial cells, resulting in packaging of fibrils into EVs. (Guo, 2020) Multiple studies have shown that microglial EVs containing such aggregated α-synuclein can effectively transfer the protein to neurons propagating aggregation (Guo, 2020). Interestingly, another facet of endocytosis of aggregated α-synuclein by glial cells is an induction of a harmful inflammatory phenotype
(Guo, 2020) suggesting an important link between neuroinflammation, EVs and α-synuclein aggregation.

EVs as immunomodulatory agents in Parkinson's disease

α-synuclein, Lewy-body pathology, and the prion hypothesis, are major facets of our traditional understanding of Parkinson's disease (Amor, 2010; Visanji, 2013). However, as with many neurodegenerative disorders, as our understanding increases, the role of inflammation and other aberrant immune responses has attracted significant attention (Amor, 2010). Perhaps one of the most interesting and attractive aspects of study into EVs, is their roles in the immune system (Buzas, 2022). So, how do we link our understanding of EV in immune cells and the pathology of Parkinson's disease?

Small EV (< 200 nm) secretion from mouse microglia cultures of BV-2 cells is increased upon treatment with aggregative α-synuclein (Chang, 2013). These EVs were found to contain high levels of MHC class 2 and TNF-α, and to induce apoptosis in rat cortical neuron cultures. Considering that the EVs contained TNF-α, an inflammatory cytokine, it stands to reason that the EVs induce or are part of an inflammatory response by the microglia (Chang, 2013). However, whether alpha-synuclein treatment entailed treatment with oligomers or fibrils was not reported, resulting in difficulty in interpreting this studies reliability. Interestingly, this is congruent with an increase in EV production and TNF-α presence seen in EV from bacterial-lipopolysaccharide activated BV-2 microglia (La Torre, 2022). Additionally, injured neurons have been reported to induce inflammatory response through release of α-synuclein (Codolo, 2013) suggesting that a microglial response to α-synuclein released either by secretion or cell death

could induce further death of surrounding neurons. Thus, causing a feedback loop mechanism similar to that described by Ando *et al* in virus-associated myelopathy contributing to disease spread to previously healthy regions (Ando, 2013).

While the EVs of inflammatory / M1 activated microglia appear to possess inflammation stimulating and negative effects on the surrounding cells, the EVs of M2 / anti-inflammatory activated microglia potentially play a beneficial role. If cultured in the presence of mice traumatic-brain-injury brain extracts, microglia adopt an M2 phenotype and EVs from these cells reflect this. Such EVs contain higher levels of anti-inflammatory mediators such as miR-124-3p, promoting differentiation into M2 of other microglia and conferring protection to neurons from inflammatory damage (Huang, 2017).

Are changes in EV production and phenotype a result of dysfunctional endocytic pathways?

Despite the heterogeneity of Parkinson's disease, advancements in genetics and model studies have revealed a dysfunction of the endosomal pathways across a variety of distinct Parkinson's forms, including *Park7*, *LRRK2*, *VPS35*, *GBA*, *ATP13A2, ATP6AP*2, *DNAJC13/RME-8, RAB7L1,* and *GAK* linked (Perrett, 2015). Disruption of protein trafficking and or degradation has also been described as a consequence of this dysfunction (Perrett, 2015). If, endosomal pathway disruption is a common feature of Parkinson's, could observed changes in EV phenotype and production/uptake be a consequence of these effects?

As previously mentioned, there is a clear link between EV production/ packaging and the endosomal pathway. Certain forms of EV, namely the exosomes, are produced via said pathway and their contents and secretion are thus dependant on its correct functioning (Gurung, 2021). EVs derived from Parkinson's patients CSF and α-synuclein fibril/aggregate treated cells both show distinctly different effects on other cells compared to healthy counterparts. Generally, they induce pathogenic features such as further α-synuclein misfolding/aggregation (Stuendl, 2016, Guo, 2020), suggesting that the content of the EV differ, potentially because of dysfunctional packaging pathways.
Dysfunctional endosomal pathways can in fact also be linked back to α-synuclein pathology. Aggregate deposition of α-synuclein is reduced if secretion is increased; and dysfunction or knock-out of the protein degrading enzyme cathepsin D in the lysosome increases aggregation (Sevlever, 2008, Follett, 2014, Miura, 2014). Thus, suggesting that aggregation occurs primarily within the endo-lysosomal

pathway due to dysfunctional degradation. α-synuclein itself is also directly involved in the regulation of membrane fusion events throughout the standard endosomal and lysosomal pathways as well as specialised synaptic vesicle pathways. This is known to occur via regulation of SNARE complexes and potentially RAB-GTPase cycling, both of which are necessary for endocytic and exocytic function (Khounlo, 2021; Teiceira, 2021). Additionally, treatment of primary neurons with α-synuclein fibrils has been shown to cause development of endogenous α-synuclein accumulation within axons, impaired RAB7 dependant endosome transport and fusion to the lysosome (Desplats, 2009). These data suggest a feed-back loop of α-synuclein aggregate release via EVs inducing further aggregation in adjacent cells, repeating the cycle and spreading pathology throughput the brain.

1.3 Aims

The overarching aim of this thesis was to determine how DJ-1 is linked to EVs with relevance to Parkinson's disease. How does DJ-1 presence and absence impact EVs and their effects on other cells? This aim was split into several distinct smaller goals corresponding to specific sections of the project timeline, described as follows:

1. Determine how the EV population changes in absence of DJ-1 compared to WT, in a cell line model (differentiated SH-SY5Y cells). Are there more or less EV?
2. Determine a suitable PD-like model system of SH-SY5Y via testing of varying conditions of parkinsonian toxins such as rotenone and MPP+.
3. Determine how the EV population changes (concentration, size, and cargo) in PD-like model conditions in WT and DJ-1 knock-out SH-SY5Y cells.
4. Assess differences in how EV isolated from SH-SY5Y (WT, DJ-1 KO) cells under healthy and PD-like conditions affect cell line models of the immune system such as THP-1 cells, or primary astrocytes.
5. To verify data in a more advanced model system, differentiate neuronal cells from iPSC cells (WT, DJ-1 KO), and generate PD-like model of iPSC derived neurons via parkinsonian toxins
6. In iPSC derived neuronal cells, assess the differences in EV population between genotypes (WT, DJ-1 KO), in PD-like conditions.

Chapter 2: Characterisation of SH-SY5Y Cells differentiation into Neuron-Like Cells.

2.1 Introduction.

For many of the experiments described herein this thesis, the SH-SY5Y cell line was employed as the cellular model system. But what is the SH-SY5Y cell line, and why was it suitable for the research?

The SH-SY5Y cell line is a human-origin neuroblastoma cell line, historically derived as a subline of the SK-N-SH cell line, itself established as a culture from a metastatic neuroblastoma bone-marrow biopsy of a 4-year-old girl in 1970 with 3 rounds of clonal selection (Biedler, 1978). The original classifications showed a catecholaminergic if not specifically dopaminergic phenotype. This classification was justified due to a lack of cholinergic metabolism markers choline acetyltransferase, acetylcholinesterase and butyryl-cholinesterase, coupled with moderate catecholaminergic / dopaminergic metabolism markers dopamine-β-hydroxylase and tyrosine hydroxylase activity. (Biedler, 1978). Furthermore, despite the genetic mutations associated with its nature as a cancer derived cell line, many of the important pathways relevant to Parkinson's disease are intact (Krishna, 2013). Specifically relevant to the study of DJ-1, the protein's gene *Park7* is present in a native state within SH-SY5Y cells and associated ROS metabolism pathways are particularly intact (Krishna, 2013).

While the base characteristics of SH-SY5Y cells provide some useful features for use in the study of Parkinson's disease, a major facet is their ability to be differentiated. In fact, SH-SY5Y cells can be converted from their neuroblastoma form into a mature-neuron-like state (Xicoy, 2017). There are multiple methods through which SH-SY5Y cells can be differentiated and the resulting neuron phenotype differs depending on the method but lacks systemic reporting (Xicoy, 2017). Indeed, retinoic-acid induced cholinergic (Lopes, 2010; Hashemi, 2003), TPA induced adrenergic (Påhlman, 1984) B-27 induced glutamatergic (Martin, 2022), and sequential retinoic-acid TPA induced dopaminergic

(Pennypacker, 1989) neuronal differentiation. Thus, while SH-SY5Y cells are of particular interest to Parkinson's disease research, they have a rich history of being employed to study many different disorders of the brain that require specific neuron phenotypes.

Of specific interest for the study of Parkinson's disease pathological mechanisms are SH-SY5Y cells differentiated into dopaminergic-neuron-like phenotypes, as progressive loss of the dopaminergic neurons of the substantia nigra is the primary feature of PD (Braak, 2003). While originally a subject of controversy in the literature, methods of SH-SY5Y neuronal differentiation and their end phenotypes have become better described over time. Specifically, differentiation methods employing retinoic acid treatment followed by TPA or BDNF have both been shown to induce dopaminergic phenotypes in differentiated cells (Pennypacker, 1989; Encinas, 2002). In particular, in 2016 a highly optimised Retinoic-acid and BDNF differentiation methodology was developed, taking only 6 days to differentiate into mature-dopaminergic-like phenotypes (Forster, 2016).

SH-SY5Y cells are suitable as an experimental model for the study of Parkinson's disease due to the features described above. In conjunction with their suitability for Parkinson's disease research, the known production of EV (Alvarez-Erviti, 2011) suggests that they are a good experimental model for the preliminary research described herein. Thus, they were chosen as the cellular model. In our work, we employed the RA + BDNF differentiation methodology described by Forster (2016.). Thus, the first goal of this project was to understand the cellular model and verify that expected features are present.

2.2 Methodology.

2.2.1 Cell Source and Genotypes.

Wild-type SH-SY5Y were bought from ATCC, product code ATCC-CRL-2266. Subsequently a *Park7* (DJ-1) knock-out cell line was genetically engineered via Crispr by Synthego (Redwood City, California) with a guide sequence of CAGGACAAAUGACCACAUCA or maintained as WT using an empty guide sequence. Clonal selection for the KO did not occur as the KO showed a higher expansion rate than the WT and a KO efficiency of 98 %.

2.2.2 General culture and passaging practice.

Unless specifically stated otherwise the following culture and passaging practices were identical throughout all work described herein this thesis.

All processes described herein are identical for both WT and DJ-1 KO cell lines. SH-SY5Y cells were grown in Dulbecco's Modified Eagle's Medium (DMEM) F-12 Glutamax^{tm} (GIBCO31331093) medium supplemented with 10 % (v/v) foetal bovine serum (FBS) (GIBCO10500064) and 100 U/ml penicillin/streptomycin (GIBCO15140122), at 37 °C and 5 % CO_2.

The passage number of cells did not exceed 10 and confluence did not exceed 70 % at any point during the work described. Passaging of cells was carried out as follows: removal of growth media; wash with DPBS (Calcium and Magnesium negative, GIBCO12559069); detachment of cells with 0.025 % trypsin for 2 min at 37 °C and 5 % CO_2; neutralisation with FBS + P/S supplemented DMEM F-12 Glutamax^{tm} at 3.3 times the volume of trypsin. The required number of cells was next seeded in T-75 flasks at the desired concentration.

2.2.3 Differentiation Method.

Unless specifically stated otherwise the following SH-SY5Y differentiation method was identical throughout all work described herein this thesis.

The growth surface for differentiation of cells was coated with 11.4 ug / 9.6 cm^2 Laminin (Corning, 354232) in DPBS (Calcium and Magnesium negative, GIBCO, cat 12559069) for 2 hr at 37 °C and 5 % CO_2. SH-SY5Y cells were seeded in standard culture conditions and 48 h later they were treated with 10 μM Retinoic acid (Sigma-Aldrich, R2625) in FBS and P/S supplemented DMEM F-12 Glutamax^{tm} for 5 days, with a refresh of medium and retinoic acid on day 2. Subsequently, growth medium was replaced with FBS negative, but otherwise identical medium and cells were treated with 50 ng/ml recombinant human brain-derived neurotrophic factor (BDNF) (Peprotech 450-02) for 5 days at 37 °C and 5 % CO_2. Half of the medium and the BDNF treatment was refreshed at day 2.

2.2.4 Characterisation of differentiation.

Characterisation was achieved through analysis of morphological changes, and immunostaining and western blotting of markers of neuronal differentiation.

Cell morphology and immunostaining

For the assessment of changes in morphology, namely neurite cell and cell body polarity, the following method was applied. 6-well tissue culture plates (Corning, 3516) were coated with 11.4 μg / 9.6 cm^2 laminin (Corning, 354232) per 1 ml in PBS by incubation at 37 °C and 5 % CO_2 for 2 hr. WT and DJ-1 KO cells were seeded at a density of 100,000 cells per well in 2 ml of FBS and P/S supplemented DMEM F-12 Glutamax^{TM}. Half of the cell cultures were left undifferentiated while half were differentiated as

described above via RA and BDNF treatment. For the undifferentiated cultures the growth media was simply replaced on the same days as mandated by the differentiation process.

Cells were then fixed with 4 % paraformaldehyde for 20 min, followed by 1 quick wash and 3 5-minute washes with PBS (Calcium and magnesium negative; Gibco, 20012019). Fixed cells were blocked for 30 min in blocking buffer (1 % w/w BSA (Sigma-Aldrich, A3059), 0.2 % v/v Triton™ (Sigma-Aldrich, X-100) in 1 X PBS). Cells were then incubated with anti-dopamine antibody (rabbit monoclonal; Abcam, ab6427) and anti-NFH antibody (mouse monoclonal; Cell Signalling, mAb #2836), or anti-β-tubulin antibody (rabbit monoclonal; Cell Signalling, #2128) in blocking buffer overnight at 4 °C. The following day, cells were washed with PBS (3x 5min) and nuclei were then stained with Hoechst 33342 (Life Technologies, H3570) at a dilution of 1:2000 in PBS for 5 min. Incubation with the secondary antibodies (Alexa-647-conjugated goat anti-rabbit, Thermo Fisher, A21244; Alexa-488-conjugated goat anti-mouse Thermo Fisher, A11001; or Alexa-488-conjugated goat anti-rabbit (Thermo Fisher, A11034), for dopamine, NFH and β-tubulin respectively, wasin blocking buffer for 1 hr at room temp. Stained cells were washed with PBS for 5 min 3 time before observation..

Brightfield and fluorescence images were then taken of 7 different fields in each well on an Cytation 5 Microscope (BioTek)at 20 X magnification. Subsequently, the neurite length of cells was measured in β-tubulin-stained field using the simple neurite tracer plugin (Arshadi, 2021) in ImageJ (FIJI) When measuring neurite length, the longest neurite visibly originating from a cell body was taken as the length and mean average length was calculated for about xxx cells per condition. Changes in cell body polarity and dopamine/NFH expression were observed as a qualitative measure in the same images.

For this experiment N=3, with 3 wells of cell culture per condition. XXX cells were analysed per well.

Confocal Microscopy analysis of neuronal markers

For the assessment of changes in the NFH and DOPA-decarboxylase neuronal markers by immunostaining, the following method was applied. Ibidi μ-Slide 2 well ibiTreat chamber slides (Ibidi, cat 81156) were coated with 11.4 μg / 9.6 cm^2 laminin (Corning, 354232) per 1 ml PBS by incubation at 37 °C and 5 % CO_2 for 2 hr. WT and DJ-1 KO cells were seeded at a density of 50,000 cells per well?? in 1 ml of FBS and P/S supplemented DMEM F-12 Glutamax™. Half of the cell cultures were left undifferentiated

while half were differentiated. Cells were then fixed and stained as described above then incubated with either 1:400 anti-NFH (mouse mono; Cell Signalling, right code here), 1:1000 anti-DOPA-decarboxylase (mouse monoclonal; Abcam, ab211535) or anti-α-tubulin (mouse monoclonal; Santa Cruz, sc-8035) primary antibodies in blocking buffer overnight at 4 °C. Secondary antibody staining was with Alexa-488-conjugated goat anti-mouse (Goat monoclonal; Thermo fisher, A11001). The final wash was replaced with Ibidi immersion liquid (Ibidi, 50101), and cells were then imaged on a Leica SP8 confocal microscope using the dye assistant settigns for DAPI, and Alexa 488.

Western Blotting

For the assessment of markers via western blotting cells were seeded in Corning 6-well culture plates coated with laminin. Culture medium was aspirated and cells were washed with PBS, followed by incubation for 10 min in Lysis buffer (20 mM Trizma® Acetate; 0.27 M sucrose; 1 mM EDTA; 1 mM EGTA; 50 mM NaF; 5 mM Sodium pyrophosphate decahydrate; 1 mM Sodium orthovanadate; 10 mM beta-sodium glycerophosphate; 1 mM DTT; 1 % Triton x-100; 1X Cocktail Roche) and detachment of cells via cell scraper. Lysate samples were then centrifuged at 2000 x g for 20 min at 4 degrees C and the supernatant (cell lysate) was stored at -80 °C.

β-mercaptoethanol was added to 4X loading buffer (62.5 mM Tris-HCL pH 6.8, 2% w/w Sodium-dodecyl-sulphate, 0.1 % w/w Bromophenol blue, 10 % w/w Glycerol) at a final concentration of 9 % v/v. Protein samples were diluted in lysis buffer to equal volumes containing 10 μg protein and placed on ice. 4X loading buffer was added to each sample in such volume to be diluted to 1X in the final sample volume. Samples were then heated in a heating block at 95 °C for 6 min, and loaded at a volume of 12 μl (containing 10 μg protein) into Biorad mini TGX 4:20 gradient gels with Tris-Glycine-SDS running buffer (pH 8.3). Precision plus protein™ standards (Biorad, 161-0374) were employed as molecular weight markers. Any Empty wells were filled with 75 % lysis buffer and 25 % complete 4X loading buffer with β-mercaptoethanol. SDS-PAGE was carried out in a mini-Protean vertical chamber at constant 100 V for 90 min. Proteins were then transferred to nitrocellulose membranes by using a Trans-blot Turbo Transfer System (Biorad, #1604150) using the default settings for Biorad mini TGX gels. Membranes were then treated with Biorad EveryBlot blocking buffer™ for 5 minand incubated in primary antibody on a rocking table overnight in Biorad EveryBlot™ blocking Buffer (Biorad, 12010020) at 4 °C.

Primary antibodies and dilutions were as follows: NFH (mouse mono; Cell Signalling, RMdO20; 1:1000 dilution); DOPA-decarboxylase (mouse mono; Abcam, ab211535; 1:1000 dilution); PSD-95 (rabbit mono; Cell Signalling, D27E11; 1:1000 dilution); DJ-1 (rabbit poly; Novus Biologicals; 1:2000). For loading controls antibodies and dilutions were as follows: GAPDH (mouse mono; Santa Cruz sc-265062; 1:500 dilution); β-tubulin (rabbit mono; Cell Signalling, 9F3. 1:1000 dilution). Membranes were then washed 3 times for 5 min with TBS-T, before treatment for 1 hr at room temp with a 1:10000 dilution of horseradish-peroxidase-conjugated secondary goat anti-mouse igG (Vector Laboratories, P-2000-1) or goat anti-rabbit igG (Vector laboratories, P-1000-1) antibodies.

Protein bands were resolved using SuperSignal™ West Dura Extended Duration Substrate (ThermoFisher, ref 34075) according to the manufacturer's instructions and imaged on a Syngene G-box. Protein bands were then quantified in ImageJ (FIJI) and marker of interest quantifications were normalised to loading controls quantifications.

2.3 Results.

2.3.1 Differentiation of SH-SY5Y results in morphological features consistent with neuronal morphology.

To discern the effects of the differentiation protocol, we first looked at any visible morphological changes in the cells. The first parameter analysed was the length of the neurites possessed by undifferentiated and differentiated SH-SY5Y cells. To achieve this, neurites were traced, and their lengths quantified in FIJI Through this method, mean neurite lengths ~ 120 times higher than that of undifferentiated cells were observed in differentiated cells of both WT and *Park7* KO genotypes (Welch's T test, $p < 0.001$, $N = 3$) (Figure 2:1).

2.3.2 Immunofluorescent staining reveals increases in neuronal and dopaminergic markers upon differentiation.

The second goal within the aim of assessing the differentiation of SH-SY5Y cells was to verify the presence of two different markers, NFH (neuronal marker) and dopamine (dopaminergic marker), and to determine whether differentiation affects their expression. We first confirmed the presence of NFH and dopamine by epifluorescence microscopy, and we observed an increase upon differentiation with retinoic acid and BDNF (Figure 2:2). In addition, further investigations into NFH and DOPA-decarboxylase were carried out via confocal microscopy, confirming their presence and their increase in differentiated cells compared to undifferentiated. (Figure 2:3). Furthermore, at higher magnifications the punctate nature of DOPA-decarboxylase staining is revealed in the cell body and neurites of differentiated cells (Figure 2:4).

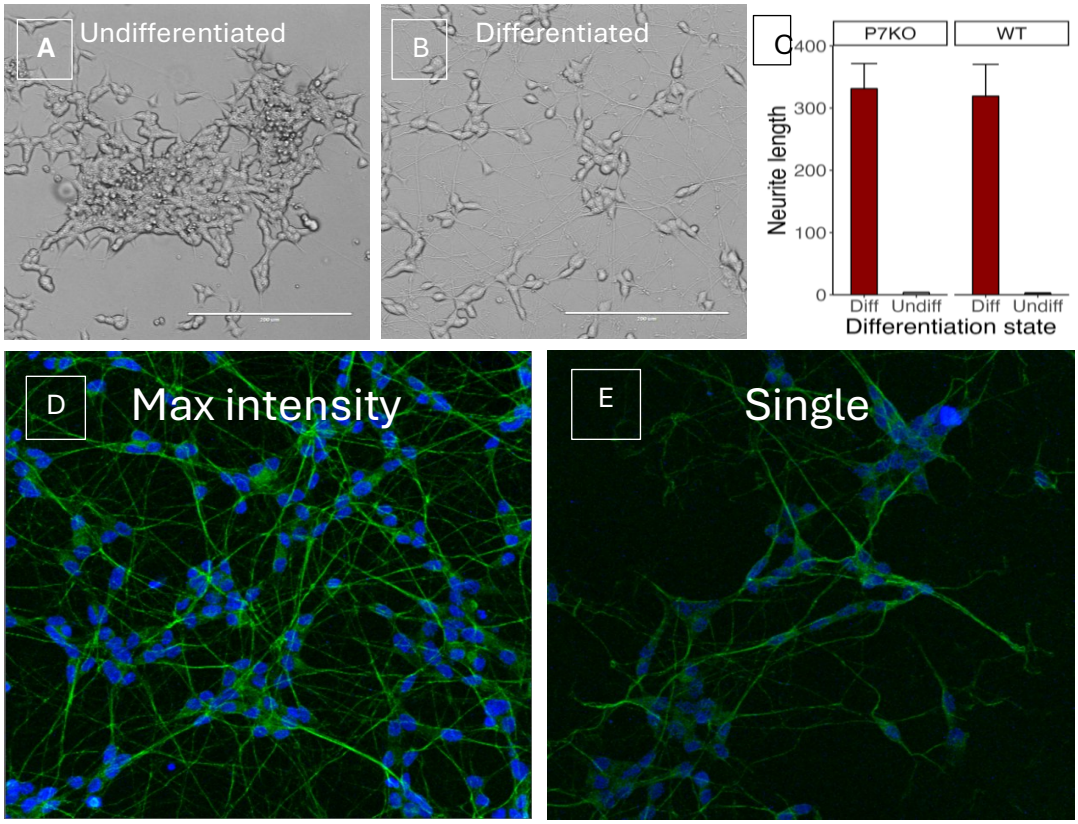

Figure 2.1 Differentiation of SH-SY5Y results in enhanced neurite length, neurite-based interconnectivity, and cell body polarisation. Representative images and graph describing morphological changes upon differentiation of SH-SY5Y cells. A and B: Bright-field images of undifferentiated and differentiated SH-SY5Y cells respectively; taken at 10 X magnification on a Cytation 5 wide-field microscope; Scale bar = 200 nm. C: Column chart showing neurite lengths of undifferentiated and differentiated cells; Columns = mean + standard deviation, N = 3. D and E: Representative images of differentiated SH-SY5Y with nuclei (blue) and α-tubulin labelled by immunofluorescence. Additionally, while only analysed in a qualitative manner, cells bodies appeared to be more polarised in differentiated cells. 3D representations of cells obtained via z-slice imaging on the confocal microscope revealed a heavily interconnected web of cells joined by their neurites, reminiscent of primary neuronal culture (Figure 2:1).

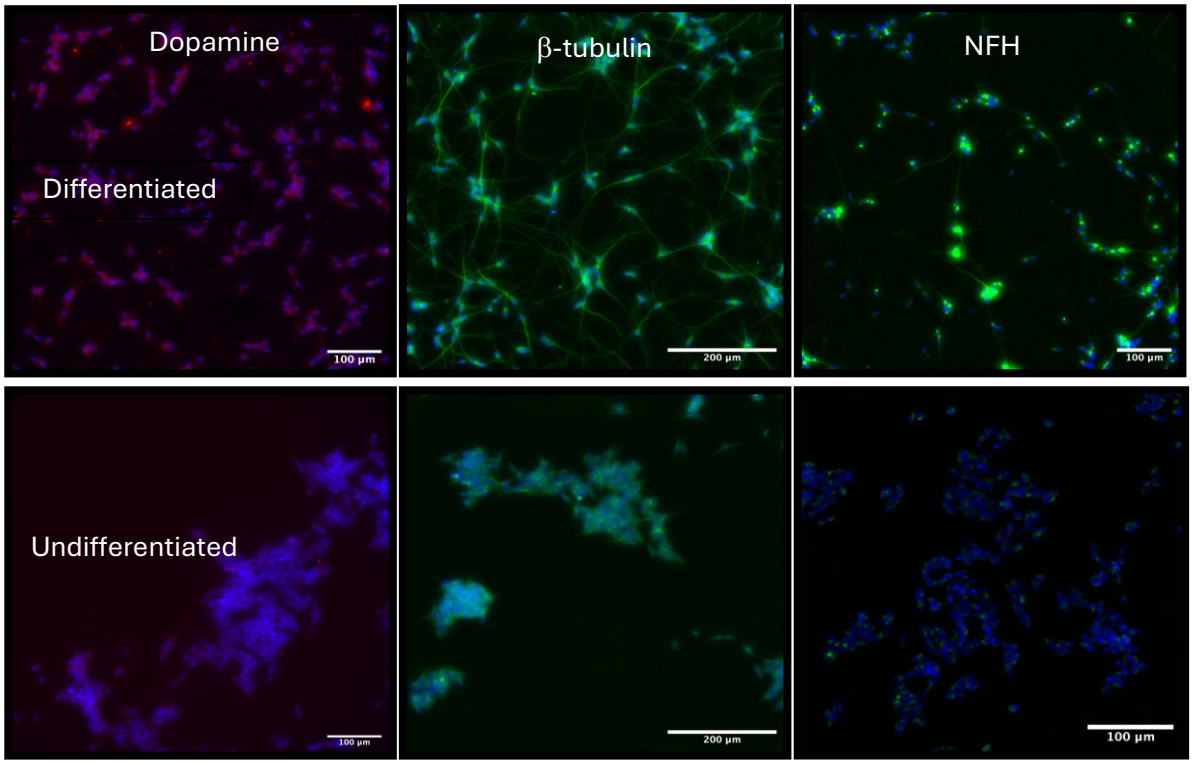

Figure 2.2 Wide-field microscopy reveals changes in expression of markers of SH-SY5Y differentiation, NFH and dopamine. Representative images of immune-stained undifferentiated and RA + BDNF differentiated SH-SY5Y cells captured on a Cytation 5 microscope. Row 1: Dopamine. Row 2: β-tubulin. Row 3: neurofilament-H. Column 1: undifferentiated cells. Column 2 Differentiated cells.

2.2.3 Western blotting provides interesting insights into changes in marker expression.

We next confirmed the changes upon differentiation of SH-SY5Y cells in a quantitative manner by western blot analysis. The results obtained successfully confirmed the presence of NFH, DOPA-decarboxylase, and PSD-95. Singular strong bands were present for NFH and PSD-95 at 150 and 95 kDa respectively. As a loading control, singular strong bands were also detected for GAPDH around 37 kDa. NFH expression showed significantly increased in differentiated cells with a fold change of 2.12 (Welch's T test, $p < 0.05$) (Figure 2:5), whereas PSD-95 and DOPA-decarboxylase showed no change, contradicting the results of immune fluorescence in the case of DOPA-decarboxylase.

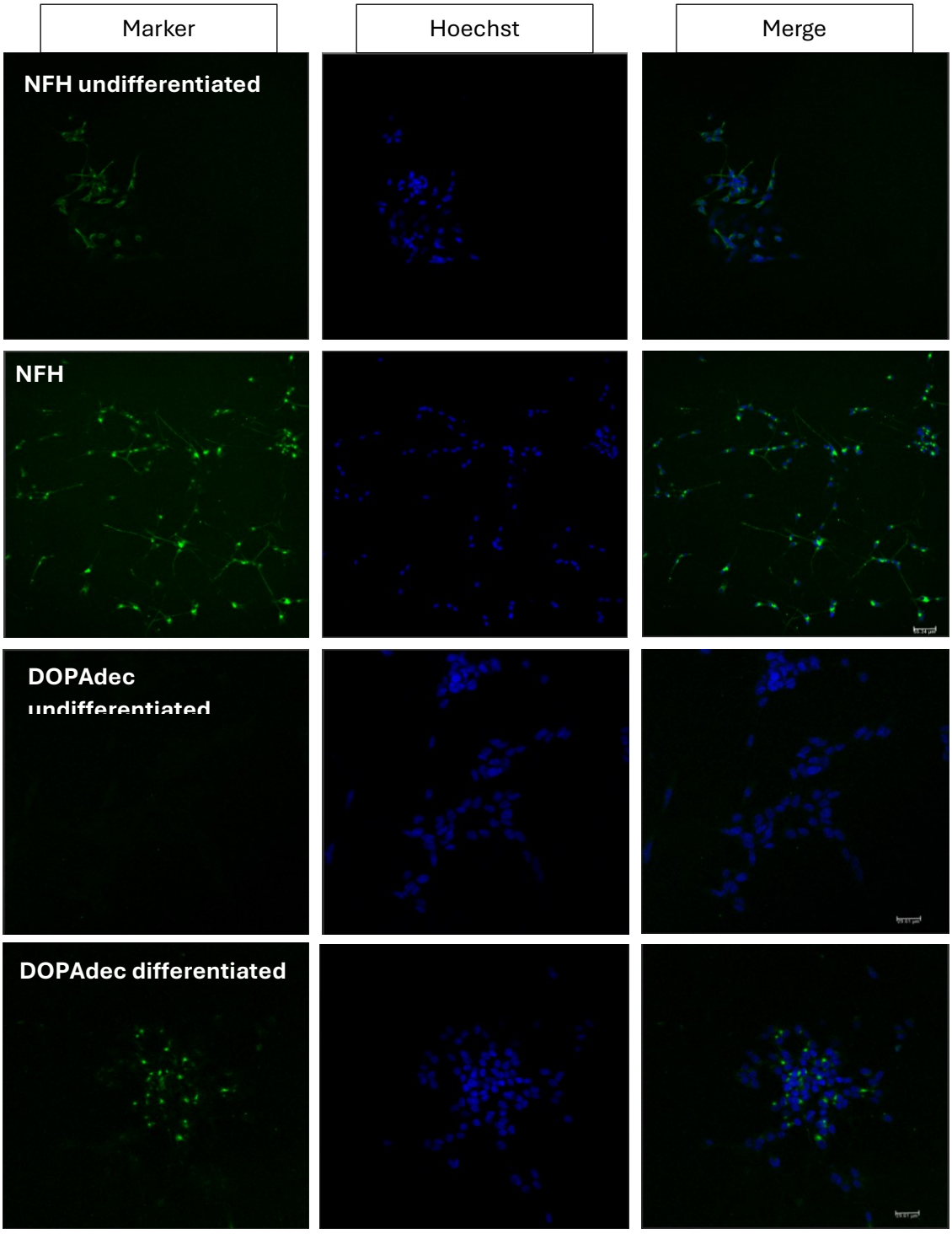

Figure 2:3. Confocal microscopy reveals changes in expression of markers of SH-SY5Y differentiation; NFH and DOPA-decarboxylase. Representative images of undifferentiated and differentiated SH-SY5Y with markers of differentiation (green) and nuclei (blue) stained by immunofluorescence. Row 1–4: Neurofilament-H, undifferentiated cells, 20 X objective; Neurofilament-H, differentiated cells, 20 X objective; DOPA-decarboxylase, undifferentiated cells, 40 X objective; DOPA-decarboxylase, differentiated cells, 40 X objective.

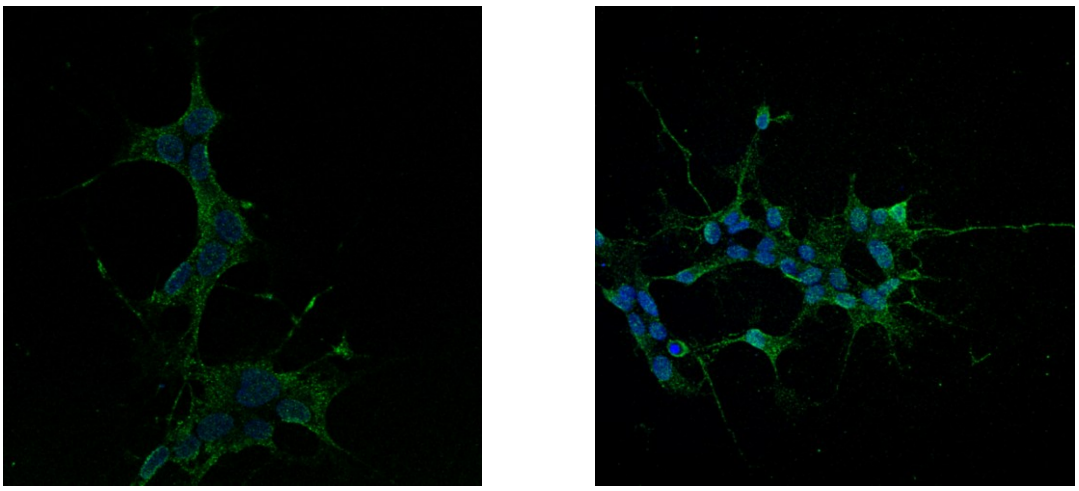

Figure 2:4 Confocal imagining reveals punctate nature of DOPA-decarboxylase expression in differentiated SH-SY5Y. Representative images of DOPA-decarboxylase (green) and nuclei (blue) staining in differentiated SH-SY5Y. Taken at 63 X magnification on a SP8 Leica confocal microscope.

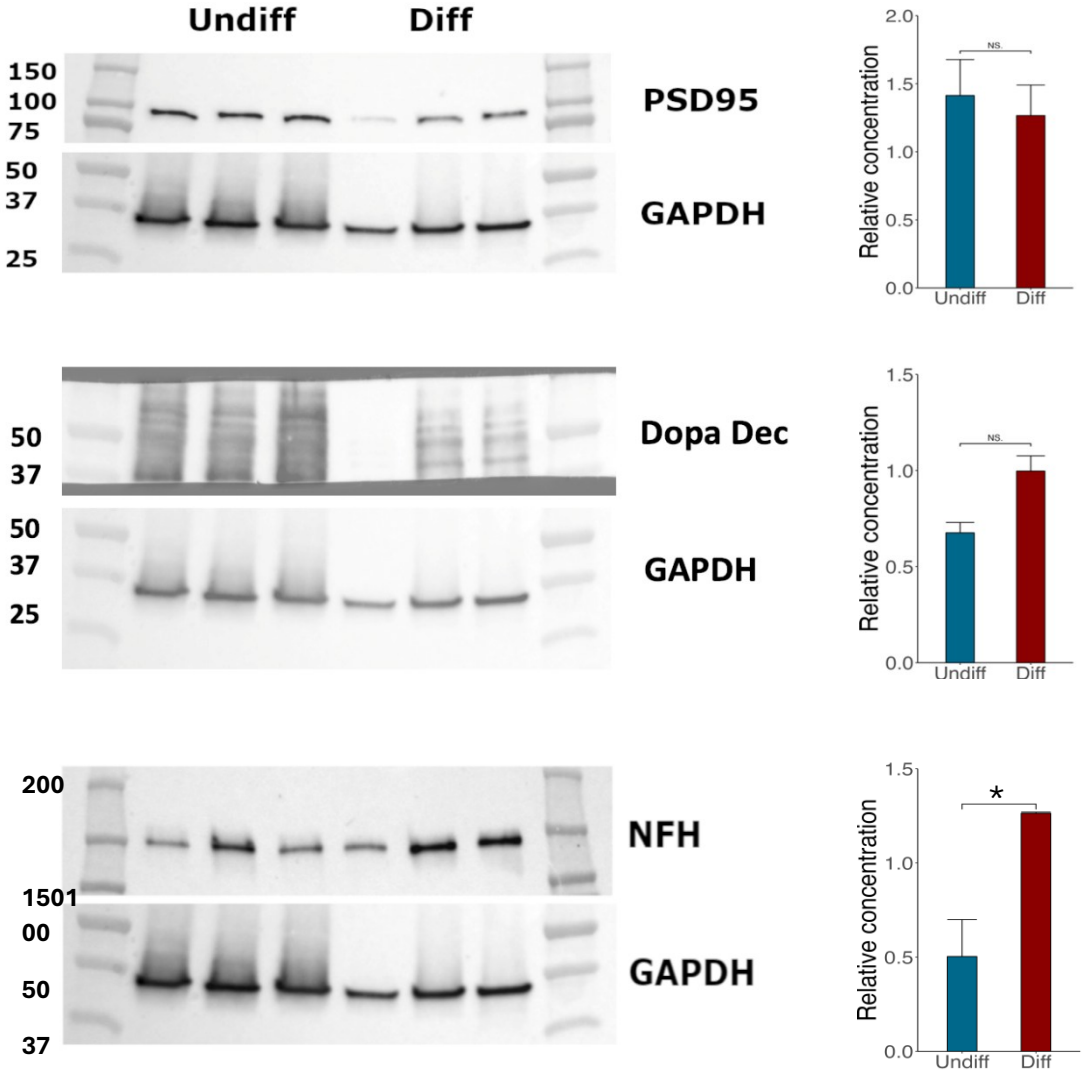

Figure 2:5. Differentiation of SH-SY5Y significantly increases NFH expression. Western blots targeting neuronal markers of cell lysates from undifferentiated and differentiated SH-SY5Y. Western blots are split into 2 sections displaying marker of interest and the loading control GAPDH. From left to right the lanes of each western blot correspond to: labelled protein marker; 3 undifferentiated samples; 3 differentiated samples; labelled protein marker. Column charts correspond to their adjacent western blot image and show the mean relative concentration of marker to loading control + standard deviation. * indicates a significance value of p <= 0.05.

Discussion.

Understanding the phenotypic state of the cell model employed for research allows one to make informed interpretations of experimental results. Previous work showed retinoic acid and BDNF differentiation resulting in a dopaminergic neuron-like phenotype (Forster, 2016). However, neuronal differentiation of SH-SY5Y cells has also been reported to be variable even within the same methods, not necessarily resulting in the expected neurotransmitter phenotype (Xicoy, 2017). Thus, it was imperative to first verify the differentiation method (Braak, 2003}.

To this end, neurite length, cell body morphology and culture interconnectivity were investigated in conjunction with immunofluorescence staining for specific markers of neuronal (NFH) and dopaminergic (dopamine and DOPA-decarboxylase) phenotype. Clear changes were observed in the morphology of the cells: undifferentiated cells preferred to grow in large clumps whereas differentiated spread out more evenly in small clusters. Differentiated cell bodies showed the characteristic polarised triangular shapes of cultured primary neurons, paired with the expected neurite outgrowths 120 times longer than undifferentiated on average (van Niekerk, 2022). Morphology wise, these differentiated cells clearly matched the features expected in primary neuron cultures (van Niekerk, 2022). As for the markers of differentiation, immunofluorescence showed again the expected changes upon differentiation towards a dopaminergic phenotype (Meiser, 2013). Neuronal marker protein NFH, and dopaminergic-metabolism markers dopamine and DOPA-decarboxylase all showed increased presence within differentiated cells (Meiser, 2013). Thus, retinoic acid and BDNF based differentiation appeared to successfully differentiate SH-SY5Y cells into a dopaminergic neuron-like phenotype.

To lend credence to the previous conclusion based on microscopy, western blotting was employed to generate more precise semi-quantitative measure of marker presence. Bands for PSD-95 and DOPA-decarboxylase were detected at the correct weight of 95 kDa (Stathakis, 1997) and 50 kDa (Meiser, 2013) respectively, whereas the singular strong band for NFH was detected at 150 kDa, contradictory to its weight of 115 kDa in humans. However, NFH is known for substantial post translational modification and large number of negatively charged residues, which can cause anomalous migration in SDS-PAGE (Yuan, 2017). Paired with the presence of only 1 singular strong band there is no reason to believe that

anything other than NFH was detected. Congruent with immunofluorescence, western blotting of NFH showed a significant 2.12 times increase in expression in differentiated cells. However, interestingly western blotting of DOPA-decarboxylase and post-synaptic density protein 95 (PSD95) showed no significant changes in expression. As SH-SY5Y have been reported to have active dopaminergic metabolism in the undifferenced state (Xicoy, 2017), the differentiation protocol could simply maintain said dopaminergic metabolism. In our experiments a strong band was detected at the correct weight for the DOPA-decarboxylase monomer (50 kDa), however the signal was not clean and presented a laddering of protein bands, which could have impaired correct quantification.

The lack of a significant increase of PSD95 in the western blots was confusing as being a marker of the post-synaptic density region of neurons, it would be assumed to only be present in the differentiated SH-SY5Y (Arnold, 1998). However, SH-SY5Y cells appear to natively express PSD-95 by default (Leuba, 2008). However, considering the results obtained upon differentiation of SH-SY5Y via retinoic acid and BDNF, we were confident to have a suitable model for further research into DJ-1, EVs, and intercellular communication in PD.

Chapter 3: How does DJ-1 knock-out affect the EVs of healthy SH-SY5Y cells?

3.1 Introduction

While the SH-SY5Y cell line was proven to be a valid cell model for the analysis of Parkinson's disease, this project requires the ability to study EV produced by these cells. Several previous studies have reported the existence of EV produced by SH-SY5Y cells, which provided confidence that the SH-SY5Y cell line would be a valid model for the research described within this thesis (Zhou, 2019; Yuyama, 2020; Tortolici, 2021; Aliakbari, 2024}. However, while the production of EV by SH-SY5Y has been verified, there is a dearth of information on the morphological characteristics of their entire EV population.

As explained in the introduction the morphological features of EV such as size and surface markers are predictors of the biosynthetic origin and are relevant to EV classification. Thus, it was important to have thorough understanding of the entire EV population produced by SH-SY5Y cells. To date, studies on SH-SY5Y EV have been narrowly focussed on specific populations, mainly exosomes, which present the standard exosome markers described in MISEV 2014 (Théry, 2014}. While providing strong evidence that exosomes are indeed being studied, it has ignored all other marker-negative exosomes. Instead, in this study, EV were classified based on size, considering those EV below 200 nm diameter as small EV and those above as large, making no assumptions of biosynthetic origin as is now recommended in MISEV 2024 (Welsh, 2024}.

In conjunction with a thorough understanding of the SH-SY5Y EV population, understanding how the knock-out of DJ-1 affects this population was of utmost importance, due to the lack of information on the links between DJ-1 and EV. However, DJ-1 has been proved to be present in EV and its concentration has been reported to increase in urine-isolated EVs of Parkinson's disease patients (Ho, 2014; Jang et al, 2018; Zhao, 2019), suggesting a disease related role for DJ-1 packaging into EV. While further information is lacking regarding EV-enclosed DJ-1, DJ-1 has also been reported to affect the endosomal pathways which are involved in EV biogenesis and uptake (Akers, 2013; Kim, 2013; Kyung 2018;}. Specifically, DJ-1 KO impaired synaptic vesicle endocytosis in primary mouse neurons, and TLR4 endocytosis in rat primary astrocytes (Kim, 2013; Kyung, 2018}. These previous data seem to suggest a DJ-1 involvement in EV biogenesis and uptake if these effects extend to a wholistic effect on the endosomal pathway rather than just these specific circumstances.

Understanding the effects of DJ-1 KO on EV production and the endosomal pathway in healthy conditions is thus an important first step towards understanding its possible effects in Parkinson's disease. Thus, this chapter describes such investigations into the EV and endosome population of healthy SH-SY5Y cells with and without DJ-1.

3.2 Methodology

3.2.1 Cell source and growth conditions

The cells employed and their culture conditions throughout the works described in this chapter are identical to those described in detail in sections 2:2:1 and 2:2:2.

3.2.2 SH-SY5Y differentiation

The differentiation method employed throughout the works described herein this chapter is identical to that described in detail in section 2:2:3.

3.2.3 Verification of EV isolation methods

CryoTEM

T-75 flasks (Corning) were coated with 8 ml of 8 ml Laminin/ml PBS for 2 hr at 37 °C and 5 % CO_2. 3 flasks per genotype were seeded with 800,000 WT or DJ-1 KO SH-SY5Y cells in 16 ml DMEM F-12 glutamax^{tm} media supplemented with FBS and P/S.

Cells were then differentiated as described above. Growth media was harvested and cells were spun down at 300 x g for 5 min at 4 °C. Supernatant was collected and debris spun down at 2000 x g for 20 min at 4 °C. Supernatant was harvested and concentrated to 500 ml via centrifugation in Amicon 30 K centrifugal filter units at 3260 x g at 4 °C. EV were then purified via IZON qEV size exclusion chromatography columns according to the manufacturer's instructions. Pure EV samples were then

concentrated again via centrifugation in Amicon 30 K centrifugal filter units at 3260 x g at 4 °C from 3 ml to 200 ml and placed on ice.

Samples were subsequently processed and imaged via a cryoTEM system by Dr Saskia Bakker, at the Advanced Imaging Facility at the University of Warwick.

Flow cytometry

6-well plate wells were coated with 2 ml of 8 ml Laminin/ml PBS for 2 hr at 37 °C and 5 % CO_2. 3 wells per genotype were seeded with 100,000 cells in 2 ml of DMEM F-12 glutamax^{tm} media supplemented with FBS and P/S each. Cells were grown for 5 days at 37 °C and 5 % CO_2. Growth media was subsequently collected, and debris spun down at 2000 x g for 20 min at 4 °C, followed by collection of supernatant. EV in collected supernatant were stained overnight by 5 mM Bodipy^{TM} FL-maleimide.

Verification of EV staining was analysed by flow cytometry using a Beckman Coulter Cytoflex S. The detectors employed were FITC and violet light side scatter (SSC_1). Megamix 7032 + 7303 standardisation beads ranging from 100 nm to 900 nm diameter were employed to generate EV gates. The acquisition settings were as follows: SSC_1 threshold of 18,000 and gain of 400; FITC gain of 250. The flow rate was set to 30 ml/min and sample analysis stopped at 10,000 total events recorded.

Confocal microscopy

The generation of pure EV samples for this experiment was identical to that described above in section 3:2:3 CryoTEM. Pure EV samples were concentrated in the same manner as described above but to a lesser extent, from 3 ml to 500 ml. Furthermore, concentrated pure EV samples were then stained with 2.5 mM Memglow^{TM} Green for 1 hr at RT. 10 ml of EV sample was spotted onto glass slides and covered with a glass coverslip. Samples were then imaged on a Leica SP8 Falcon confocal microscope using the Alexa 488 dye assistant settings.

3.2.4 EV population analysis

2 experiment types were performed differing in level of optimisation (2nd more optimised) and notably the method of cell quantification. Each experiment was carried out in batches of cell cultures, the seeding of which occurred with equal and balanced culture conditions each week for 3 weeks.

6-well culture plate wells were coated with 1 ml of 8 ml laminin/ml PBS for 2 hr at 37 °C and 5 % CO_2. Equal cultures of WT and DJ-1 KO SH-SY5Y cells were seeded at a density of 100,000 cells in 2 ml of DMEM F-12 glutamax^{tm} media supplemented with FBS and P/S.
per well of a 6-well culture plate. Half of the cultures were left undifferentiated, and half differentiated as described above. After differentiation, the growth medium of a cell culture was harvested and placed on ice, followed by centrifugation at 2000 x g for 20 min at 4 °C. Supernatant containing EV was harvested and placed on ice or stored at 4 °C until further use. Prior to analysis EV were stained overnight with 5 mM Bodipy^{TM} FL-Maleimide. EV concentration and sizes were analysed by flow cytometry using a Beckman Coulter Cytoflex S. The detectors employed were FITC and violet light side scatter (SSC_1). Megamix 7032 + 7303 standardisation beads ranging from 100 nm to 900 nm diameter were employed to generate EV gates. The acquisition settings were as follows: SSC_1 threshold of 18,000 and gain of 400; FITC gain of 250. The flow rate was set to 30 ml/min and 10 ml/min in experiment 1 and 2 respectively. Sample analysis stopped at 10,000 total events and 30,000 EV events detected in experiment 1 and 2 respectively.

In experiment 1 cells were detached via a 5 min treatment of 5 mM EDTA followed by quantification of live and dead cell concentration via flowcytometry using a Beckman Coulter Cytoflex S. The detectors employed were forward scatter (FSC) and side scatter (SSC), the outputs of which were used to separate live/dead cell populations. Acquisition settings were as follows: FSC threshold of 400,000 and gain of 97; SSC gain of 70. Flow rate was set to 60 ml/min and analysis was halted after 10,000 events were detected. In experiment 2 cells were lysed in Lysis buffer (20 mM Trizma® Acetate; 0.27 M sucrose; 1 mM EDTA; 1 mM EGTA; 50 mM NaF; 5 mM Sodium pyrophosphate decahydrate; 1 mM Sodium orthovanadate; 10 mM beta-sodium glycerophosphate; 1 mM DTT; 1 % Triton x-100; 1X Cocktail Roche). Lysates were then used to quantify protein concentration as a proxy for cell number via Bradford assay.

3.2.5 Endosome analysis

Nile red staining was employed to detect endosomes. Firstly, a suitable timepoint and Nile Red concentration for endocytosis to occur and thus endosome detection was required. WT SH-SY5Y were seeded at a density of 100,000 cells in 2 ml DMEM f-12 glutamax^{TM} supplemented with FBS and P/S. Cells were incubated for 4 days at 37°C and 5 % CO_2. Cells were then stained with 300 nM Nile red and imaged at 0, 5, 10, 15 and 20 min on a Leica SP8 Falcon Confocal microscope in an environment control box set to 37 °C and 5 % CO_2. Nile red was imaged using the Alexa 555 dye assistant settings.

Ibidi culture dishes were coated with 2 ml of 8 ml laminin/ml PBS for 2 hr at 37 °C and 5 % CO_2. Dishes were seeded with 100,000 WT or DJ-1 KO SH-SY5Y cells in 2 ml of DMEM f-12 glutamax^{TM} supplemented with FBS and P/S. Cells were then differentiated as previously described and then stained with 300 nM Nile red for 15 min at 37 °C and 5 % CO_2 before being imaged on a Leica SP8 Falcon Confocal microscope in an environment control box set to 37 °C and 5 % CO_2. Nile red was imaged at using the Alexa 555 dye assistant settings. For this experiment N = 6 spread evenly across 3 weeks of cultures, and for each N at least 200 cells were imaged. Endosome size and number per cell were analysed in FIJI (ImageJ). A semi-automatic analysis pipeline was created in the ImageJ macro language wherein endosomes in the Nile red fluorescence channel were identified by the Find Maxima FIJI command (Strict = True; Exclude edges = True; Output type = Maxima within tolerance; Prominence = set dependant on individual image); followed by analysis of endosome size and number by the FIJI analyse particles command (Exclude edges = True; Size = 0-5 mm^2; Circularity = 0.2-1). Endosome counts per image were normalised to cell number per image counted by eye in the brightfield channel. Full code written by me is available at my GitHub page. (https://github.com/Bioinformatics-Lover/My-PhD-Project/blob/main/Nile_red_endosome_counter.ijm) and a list of variable parameter values per image is available in the supplementary section.

For colocalization analysis to verify staining of endosomes, WT cultures identical to those above were fixed with 4 % para-formaldehyde for 20 min after Nile red staining. Fixative was washed once quickly with PBS, followed by 3 x 5-min washes with PBS. Fixed cells were then blocked with blocking buffer (1 % w/w BSA (Sigma-Aldrich, A3059), 0.2 % v/v Triton^{TM} (Sigma-Aldrich, X-100), in 1 X PBS) for 30 min at RT. Fixed cells were then treated with either 1:100 anti-Rab7 antibody (Rabbit monoclonal antibody; Cell Signalling # 9367) or 1:200 anti-EEA1 antibody (Mouse monoclonal antibody ; BD transduction, #

610457) overnight at 4 °C. After primary antibody incubation cells were washed 3 times for 5 min with PBS, followed by 1 hr incubation at RT with Alexa-488-conjugated goat anti-rabbit (Goat mono; Thermo fisher, A11034) for anti-Rab7 stained, or Alexa-488-conjugated goat anti-mouse (Goat mono; Thermo fisher, A11001) for anti-EEA1 stained, followed by 3 5-min PBS washes, with PBS as final media. Stained cells were then imaged on a Leica SP8 Falcon confocal microscope. EEA1 and Rab7 antibodies were imaged with Alexa 488 dye assistant settings. Colocalisation of Rab7/EEA1 with Nile red was analysed in FIJI (ImageJ) via the JACoP plugin employing Pearson and Mander's coefficients outputs (https://github.com/fabricecordelieres/IJ-Plugin_JACoP).

3.3 Results

3.3.1 EV can be successfully isolated from SH-SY5Y cells and visualised by flow cytometry, CryoTEM and confocal microscopy

The verification of the isolation of EV was first performed by fluorescent staining with Bodipy™ FL-maleimide and flow cytometry. This step also served as a verification of the flow cytometry analysis for future experiments. An "EV" gate was created by comparing the plots of calibration beads with size and fluorescence similar to that of stained EV against bufferonly samples and gating only those events that are clearly present in the bead samples. The effectiveness of the stain with Bodipy™ FL-maleimide, Bodipy™ FL-SE and Memglow™ 488 was verified by splitting several EV samples into stained and non-stained sub samples and comparing the presentation of their flow cytometry outputs. Non-stained samples showed no identifiable EV population, whereas stained samples showed a clearly fluorescent population of events in the "EV" gate generated from fluorescent calibration beads ranging from 100 to 700 nm diameter. Thus, staining of EV with Bodipy™-FL-(maleimide / SE) and Memglow™ 488 was determined to successfully render EV detectable via flow cytometry (Figure 3.1). Specifically, staining with 5 μM Bodipy™-FL-maleimide resulted in an increase of 1662.22 times, from 0.027 % in unstained samples to 44.88 % in stained samples, while staining with 5 μM Bodipy™ FL-SE resulted in 98.2 % events localising to the EV gate. Finally staining with 2 μM Memglow™ 488 resulted in 75.5 % events localised to EV gate. The positive flow cytometry signal resulted in the presence of 2 populations: noise, those events that did not shift; and EV, those that possess sufficient fluorescence to shift into the bead-generated EV gate and be declared EV (Figure 3.1).

To confirm the results of the flow cytometry, 2 microscopy techniques were employed to directly visualise EV, namely cryoTEM and confocal microscopy. Identical isolation methods where EV of neuronally differentiated SH-SY5Y cells were purified via size exclusion chromatography after several steps of centrifugation to remove floating cells and debris were employed. CryoTEM allowed for direct visualisation of entire EV and their complete structure at the nanoscale. EV samples from both WT and DJ-1 KO yielded largely structurally intact EV of a wide variety of forms, ranging from standard circular EV to ovoid, to pear shaped. Furthermore, multilamellar EV with 2-3 double membranes were also observed alongside structures that were believed to be nanotubules rather than EV (Figure 3.2). Manual

categorisation of EV shape into largely arbitrary classifications (Figure 3.3) revealed that the majority of EV from SH-SY5Y were spherical. Additionally, there were no clear differences in the occurrence of morphologies between WT and DJ-1 KO. However, the experiment only employed 1 replicate each hurting comparisons and not allowing for statistical tests. (Figure 3.3.)

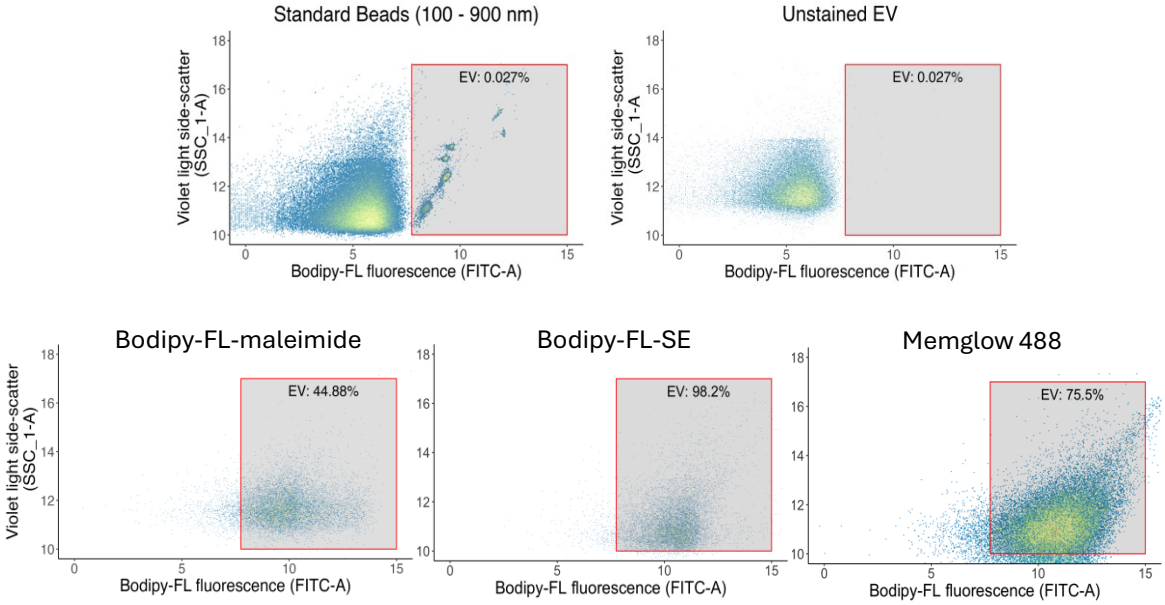

Figure 3.1 Flow cytometry validates staining of EV with Bodipy-FL maleimide, Bodipy FL-SE and Memglow 488. A comparison of the flow cytometry data of Standard sized FITC-like fluorescent beads, unstained EV and stained EV, showing how correct gating of EV was achieved. Y axis = violet light side scatter. X axis = Bodipy or memglow fluorescence. EV gate is indicated by red bordered and grey shaded rectangle. Local density of points represented by colour with blue = lowest and red = highest density. All data displayed generated on Beckman colter cytoflex S flow cytometer.

While not allowing for the detail provided by the resolution of CryoTEM, confocal microscopy also served to prove isolation of EV. Via confocal microscopy the visualisation of Memglow™ 488 stained EV was achieved. Images showed clear independent fluorescent objects of the size range expected of EV (< 1 μm) with little to no background noise (Figure 3.4). Similarly to Bodipy staining of EV, staining with Memglow™ was verified via flow cytometry analysis of stained vs unstained isolates (Figure3.4).

Taken as a whole, the 3 methods of verifying the correct isolation of EV corroborate each other. Each process though distinct in its preparation and methodology provided strong evidence of EV isolation.

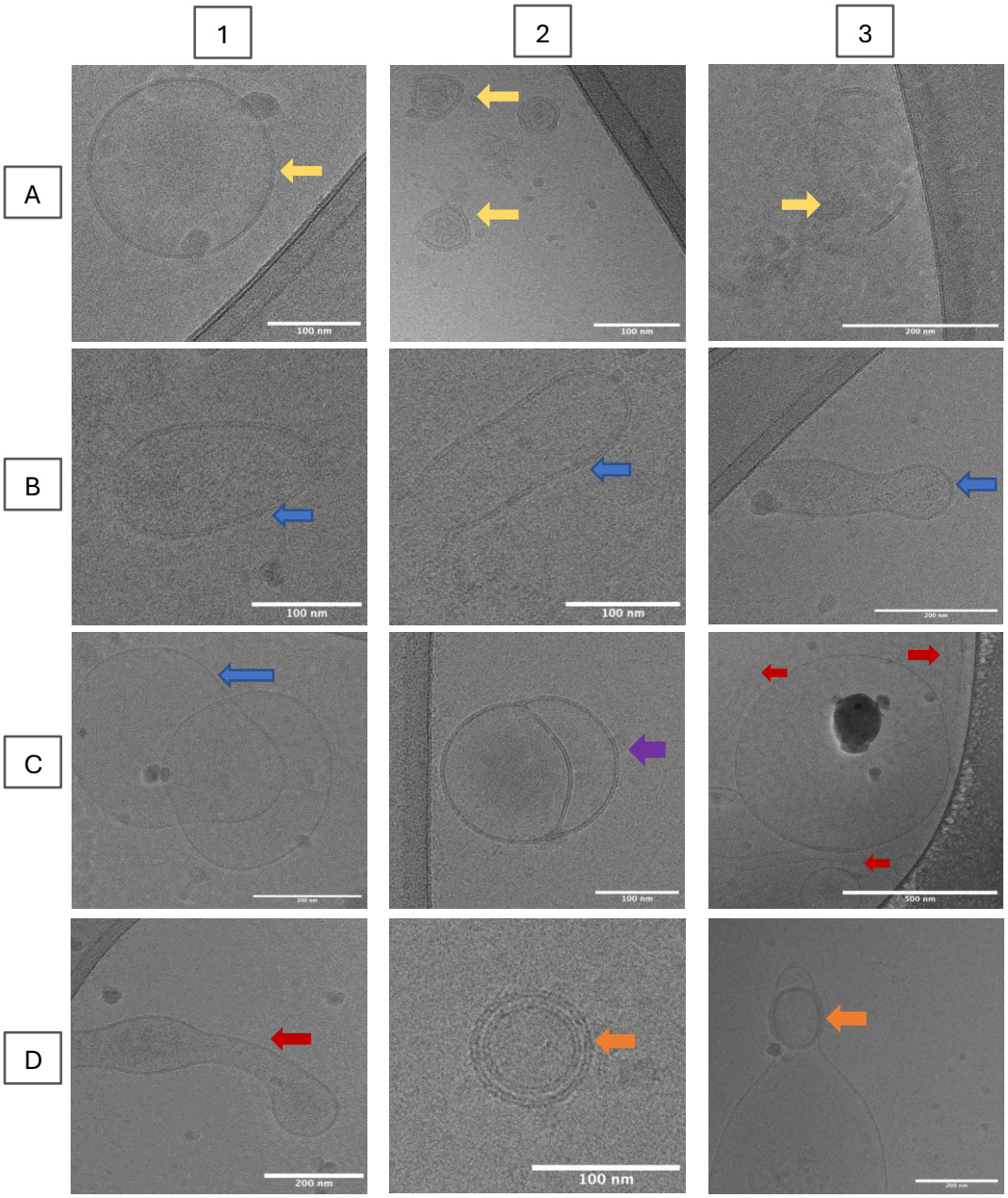

Figure 3.2 CryoTEM of EV isolated from neuronally differentiated SH-SY5Y reveals a variety of possible shapes and forms. CryoTEM images of the variety of forms neuronally differentiated SH-SY5Y EVs can take and their structural integrity. Images A1/2/3 show a structurally intact classical-spherical EV, 3 moderately damaged EV, and a broken EV respectively. B1/2/3 and C1 show EVs of non-classical shapes, i.e elliptical, elongated, bowling pin, and pear respectively. C2 shows an apparent EV fusion or splitting event. C3 and D1 show what are likely to not be EV but in fact tunnelling nanotubes due to substantially elongated tube like structure.

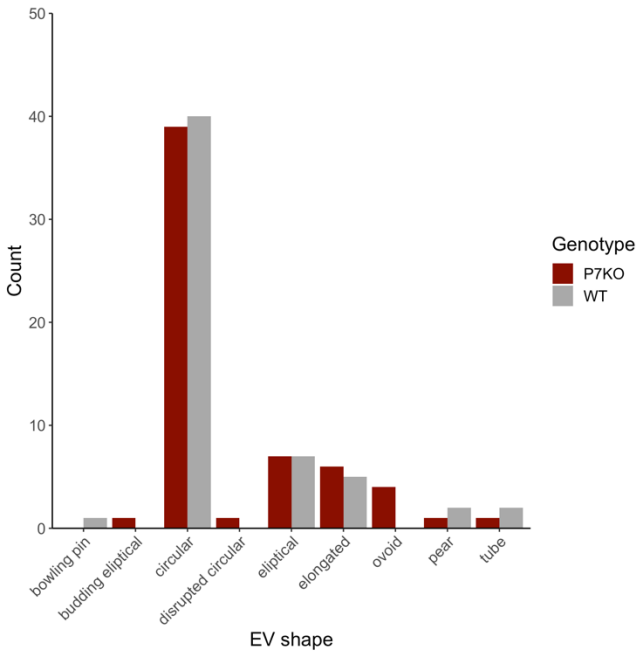

Figure 3.3 SH-SY5Y EV imaged by cryoTEM can be categorised as a variety of shapes and morphologies but are primarily spherical/circular. Classification was carried out manually and individual categories created as EVs that did not fit previous categories were observed.

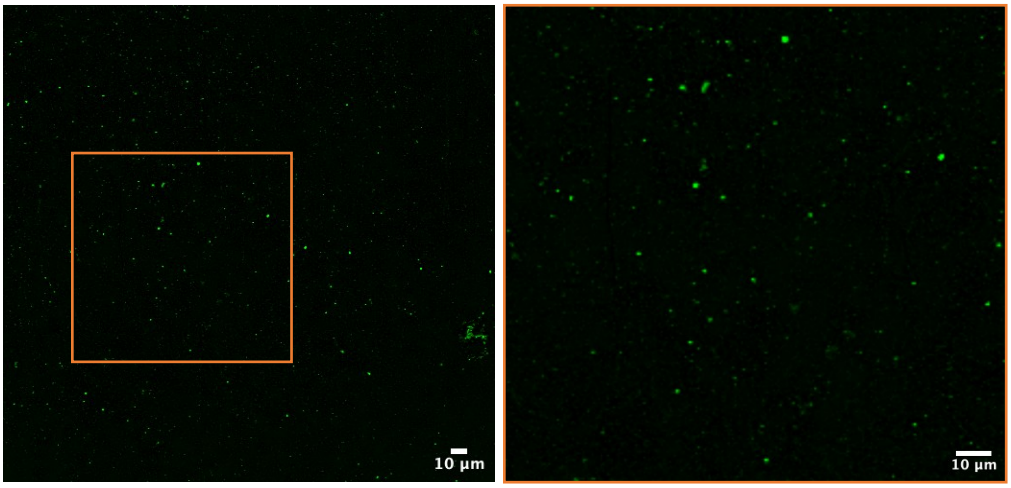

Figure 3.4 Confocal Microscopy proves the presence of EV in purified samples. Confocal microscopy images of EV isolated from differentiated SH-SY5Y cells stained with Memglow^{TM} 488 membrane dye. Left image shows full image at native resolution. Right image shows zoomed representation of a selection of the left image.

3.3.2 Differentiation and DJ-1 KO alter EV concentration in SH-SY5Y cells.

To analyse the effect of DJ-1 KO on EV concentration and size in SH-SY5Y cells, 2 experiments were performed. These 2 experiments were identical in principle, but were performed sequentially with the second being an optimised version of the first, employing changes based on lessons learned from the first experiment.

In experiment 1, the EVs of undifferentiated and dopaminergic-like neuronally differentiated WT and DJ-1 KO SH-SY5Y cells were analysed via flow cytometry. The goal of this experiment was to provide a preliminary understanding of the effects of differentiation and DJ-1 KO on EV concentration and inform on the further optimisation of the protocol. Importantly, unlike further experiments, this experiment employed flow cytometric measurements of cell number as a normalisation factor for EV concentration. Flow cytometric detection and analysis of the cells of WT and DJ-1 KO SH-SY5Y in undifferentiated and differentiated states detached with 5mM EDTA was possible. EV counts were then normalised to the number of cells in parent cultures that were determined to be "live" via the forward and side scatter parameters employing the change towards higher side-scatter and lower forward scatter presented by dead cells (Figure 3.5).

Experiment 1 data was analysed by passing it into a mixed effect model of the form $Response\ variable \sim Genotype * Differentiation\ state + (1|Batch)$ followed by post hoc pairwise comparisons via Tukey's HSD. This resulted in 2 major observations: in SH-SY5Y cells both differentiation with retinoic acid and BDNF, as well as DJ-1 KO induce an increase in the number of EV isolated per cell. When looking at the total EV population (large and small), differentiation only significantly affected EV per cell in DJ-1 KO cells, resulting in an increase of 5.32 from 8.74 to 14.06 in the total EV of undifferentiated and differentiated cells respectively (Tukey HSD: p = 0.0012; N = 18). Additionally, DJ-1 KO significantly increased total EV per cell compared to WT in differentiated cells only by 3.67 from 10.39 to 14.06 (Tukey HSD: p = 0.0378; N = 18). (Figure 3.5.)

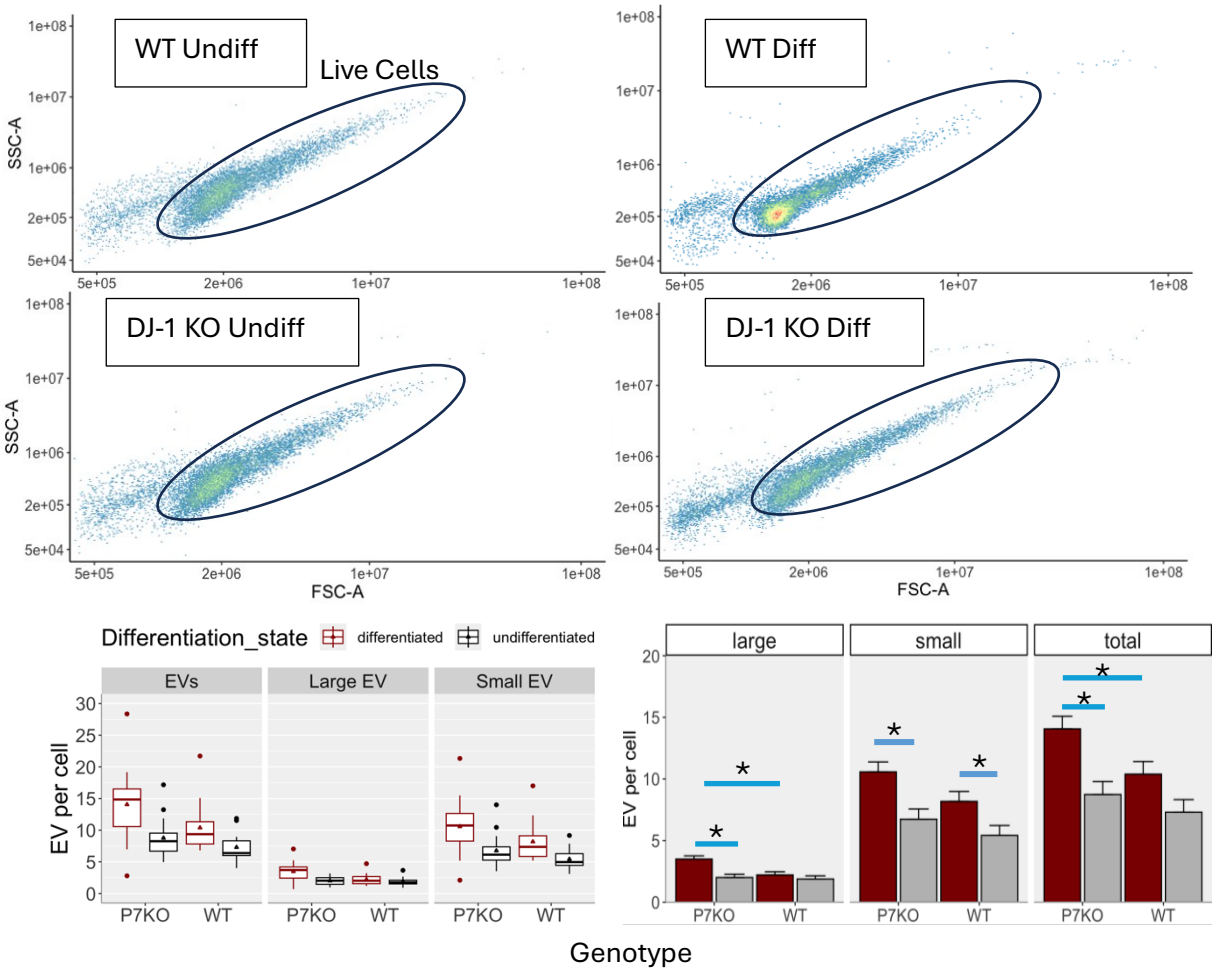

Figure 3.5 Differentiation and DJ-1 KO increase the number of EV per SH-SY5Y cell.

Top panels: hex plots of flow cytometry analysis of parent cell cultures representative of each condition; WT undiff, WT diff, P7KO (DJ-1 KO) undiff, P7KO diff. y axis = side scatter area, x axis = forward scatter area. Colour scale indicates point density within each hex bin, blue least dense and red most dense. **Bottom graphs:** The number of EV per SH-SY5Y cell as detected by flow cytometry on a Cytoflex S platform. EV counts are shown as a total (right panel), and broken down into 2 sized based categories; small (< 200 nm diameter, middle panel), large (> 200 nm diameter, left panel). Top Graph = Box and whisker plot showing range and summary of raw data points. Bottom graph = Column chart of modelled data. Columns represent least squares means calculated using emmeans R package from data modelled using mixed linear modelling via lme4 package. Blue bars represent significant differences between 2 conditions with p values indicated by "*…" (* = p<0.05, ** = p < 0.005, *** = p < 0.001, Tukey HSD). WT = wild-type and P7KO = DJ-1 KO. Colours indicate differentiation state: red = differentiated, grey = undifferentiated.

EV can be categorised based on their diameter as large or small, those above or below 200 nm diameter respectively (MISEV, 2024). Looking at these divisions rather than the whole EV population revealed intricacies in the effects of differentiation and DJ-1 KO. Regarding large EV, the significant effects were same as the in comparisons total EV. Differentiation increased the large EV per cell only in DJ-1 KO cells by 1.49 from 2.01 to 3.50 (Tukey HSD: p = 0.0002; N = 18), whereas DJ-1 KO increased large EV per cell compared to WT by 1.285 from 2.21 to 3.50 (Tukey HSD: p = 0.0011; N = 18) only in differentiated cells. Unlike the previous 2 groupings, differentiation significantly increased small EV per cell in both WT and DJ-1 KO cells, showing an increase of 2.76 from 5.42 to 8.18 (Tukey HSD: p = 0.0484; N = 18) and by 3.84 from 6.73 to 10.57 (Tukey HSD: p = 0.0032; N = 18) in WT and DJ-1 KO cells respectively. Also, unlike previous groupings, DJ-1 KO did not significantly increase small EV per cell compared to WT in differentiated cells (Tukey HSD: p = 0.11; N = 18). (Figure 3.5.)

The experiment described above was used as a baseline for the optimisations in the analysis. Based on this first experiment, changes which optimised flow cytometer settings were made (changes described in methods). However, cell number was also replaced with cell lysate protein concentration as a normalising factor for EV, due to the difficulty of detaching neuron-like cells while maintaining health and passing these cells through a flow cytometer.
Thus, a second experiment was carried out with these optimised parameters with the same goal of assessing differences in EV concentration between undifferentiated and differentiated WT and DJ-1 KO SH-SY5Y cells.

This experiment notably showed different results compared to the first experiment. When considering the amount of EV detected normalised to cell protein concentration, the following observations were made: the total EV of every condition was different than every other, the only difference in large EV amount was DJ-1 KO differentiated vs undifferentiated; finally, the small EV amount was different in every comparison identically to total EV. (Table 3.1; Figure 3.6) Thus, the changes in total EV detected are primarily driven by changes in small EV. Similar to the previous experiment, these result were achieved via passing the data through a general mixed linear model of the form $Response\ variable \sim Genotype * Differentiation\ State + (1|Batch)$, followed by post hoc analysis via Tukey HSD.

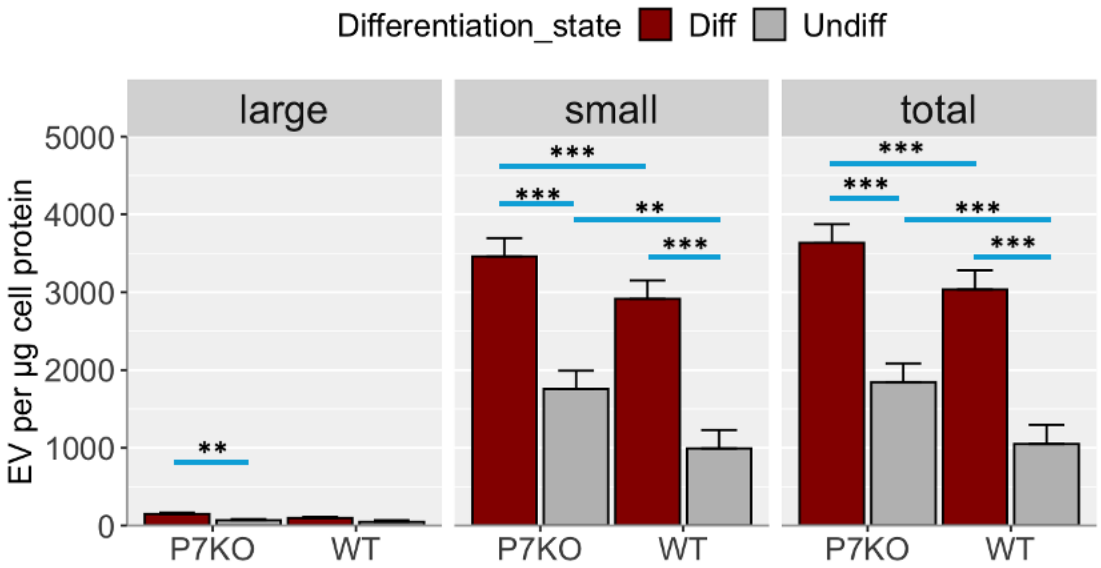

Figure 3.6 Validation that differentiation and DJ-1 KO increase the amount of EV in SH-SY5Y cells. The number of EV per SH-SY5Y cell as detected by flow cytometry on a Cytoflex S platform. EV counts are shown as a total (right panel), and broken down into 2 sized based categories; small (< 200 nm diameter, middle panel), large (> 200 nm diameter, left panel). Columns represent least squares means calculated using emmeans R package, from data modelled as a linear mixed effects model of the form: $Response\ variable \sim Genotype * Differentiation\ state + (1|Batch)$ using lme R package. Error bars represent the standard error of the emmeans least square mean calculation. Blue bars represent significant differences between 2 conditions with p values indicated by "*…" (* = p<0.05, ** = p < 0.005, *** = p < 0.001, Tukey HSD, N = 9). WT = wild-type and P7KO = DJ-1 KO.

More specifically, when looking at total and small EV groupings DJ-1 KO cells showed higher EV counts than their WT counterpart. Furthermore, in the small and total EV groupings an increase is detected in differentiated cells of both genotypes. However, while the increase in large EV between undifferentiated and differentiated DJ-KO was again detected, unlike the previous experiment there is no detectable difference between differentiated DJ-1 KO and WT cells.

Table 3.1 Post hoc comparisons between conditions on EV number from undifferentiated and differentiated WT and DJ-1 KO SHh-SY5Y cells. A table showing all statistical comparisons made between conditions on the EV of SH-SY5Y cells in experiment 2. Contrast = the comparisons made; contrast result = the difference between the contrasted groups; SE = standard error of the difference; P value = adjusted p values from Tukey HSD for multiple comparisons.

EV size grouping	Contrast (Right hand conditions act as reference for fold change)	Contrast result.	Contrast fold change	SE	t ratio	P value
Total	P7KO Diff - WT Diff	599	1.19	185	3.235	0.0052
Total	P7KO Diff - P7KO Undiff	1790	1.97	176	10.187	<0.0001
Total	WT Diff – WT Undiff	1985	2.89	192	10.313	<0.0001
Total	P7KO Undiff - WT Undiff	794	1.75	185	4.288	0.0011
Large	P7KO Diff - WT Diff	53.5	1.5	25.3	2.114	0.2022
Large	P7KO Diff - P7KO Undiff	81.9	2.2	24.1	3.395	0.0185
Large	WT Diff – WT Undiff	46.8	1.9	26.4	1.769	0.2877
Large	P7KO Undiff - WT Undiff	18.3	1.3	25.3	0.725	0.5562
Small	P7KO Diff - WT Diff	547	1.18	182	3.011	0.0083
Small	P7KO Diff - P7KO Undiff	1703	1.96	172	9.876	<0.0001
Small	WT Diff – WT Undiff	1922	2.9	189	10.180	<0.0001
Small	P7KO Undiff - WT Undiff	767	1.77	182	4.221	0.0013

Interestingly, while in both experiments the small EV population was the vast majority of the total EV population, in experiment 2 the small population was a larger percentage of the whole, validating the optimisation of the process in experiment 2 which would be expected to reduce “swarming”, the effect in which multiple smaller objects pass the detector too close together, thus acting like one of larger size.

3.3.3 DJ-1 KO in differentiated SH-SY5Y cells results in a reduction in the number of endosomes per cell

To increase understanding on the processes involved in the changes in EV count previously observed, an investigation into the endosomes of differentiated WT and DJ-1 KO SH-SY5Y was performed. To this aim, we first optimized the protocol, particularly the time needed after Nile red staining to perform the imaging and analysis. Indeed, Nile red staining visualised immediately and after 5 min showed no distinguishable endosomes in living cells, as the staining was still primarily localised to the plasma membrane. After 10 min endosomes started to become distinguishable but with a large degree of plasma membrane still existing. After 15 min endosomes were largely distinguishable as individual objects with little to no plasma membrane staining obscuring the cells. Thus, 15 min was chosen as the time point for analysis (Figure 3.7).

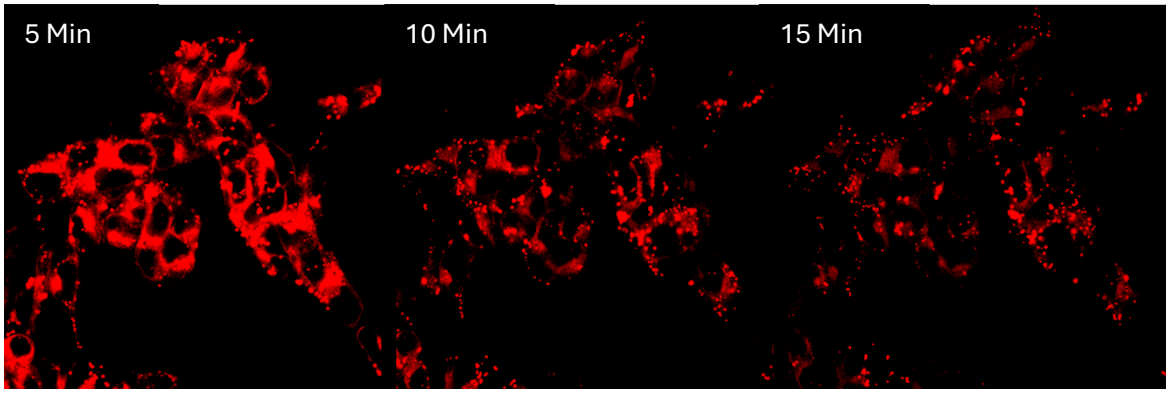

Figure 3.7 Individual endosomes become easily distinguishable 15 minutes after staining with Nile red. Confocal Microscopy images of living SHSY5Y cells taken on a Leica SP8 system showing the reduction in plasma membrane staining by Nile red as the dye becomes internalised into endosomal structures.

While confidence was high that Nile red was truly staining endosomes, proof was needed. To achieve this, the colocalization of Nile red with early and late endosome markers, EEA1 and Rab7 respectively, was investigated. This was achieved via immunofluorescent staining of EEA1 and Rab7 in fixed Nile-red stained cells, and colocalization measures of Pearson's correlation and Mander's coefficients. Regarding the early endosome marker EEA1, the Pearson coefficient of colocalization with Nile red was 0.459, whereas regarding Rab7 it was 0.329. Mander's coefficients are directional, testing the colocalization with image 1 on 2, and 2 on 1 separately as the M1 and M2 coefficients respectively. In this case M1 is the result of testing what proportion of the marker colocalises with Nile red, and M2 is the opposite. Colocalisation of Nile red and EEA1 showed an M1 and M2 of 0.336 and 0.635 respectively, whereas

colocalisation of Nile red and Rab7 showed an M1 and M2 of 0.129 and 0.415 respectively (Figure 3.8). These results showed that Nile red colocalises better with EEA1, i.e early endosomes, rather than the late endosomes marked by Rab7. Interestingly in both cases Nile red clearly colocalises better to the marker than the reverse (Figure 3.8).

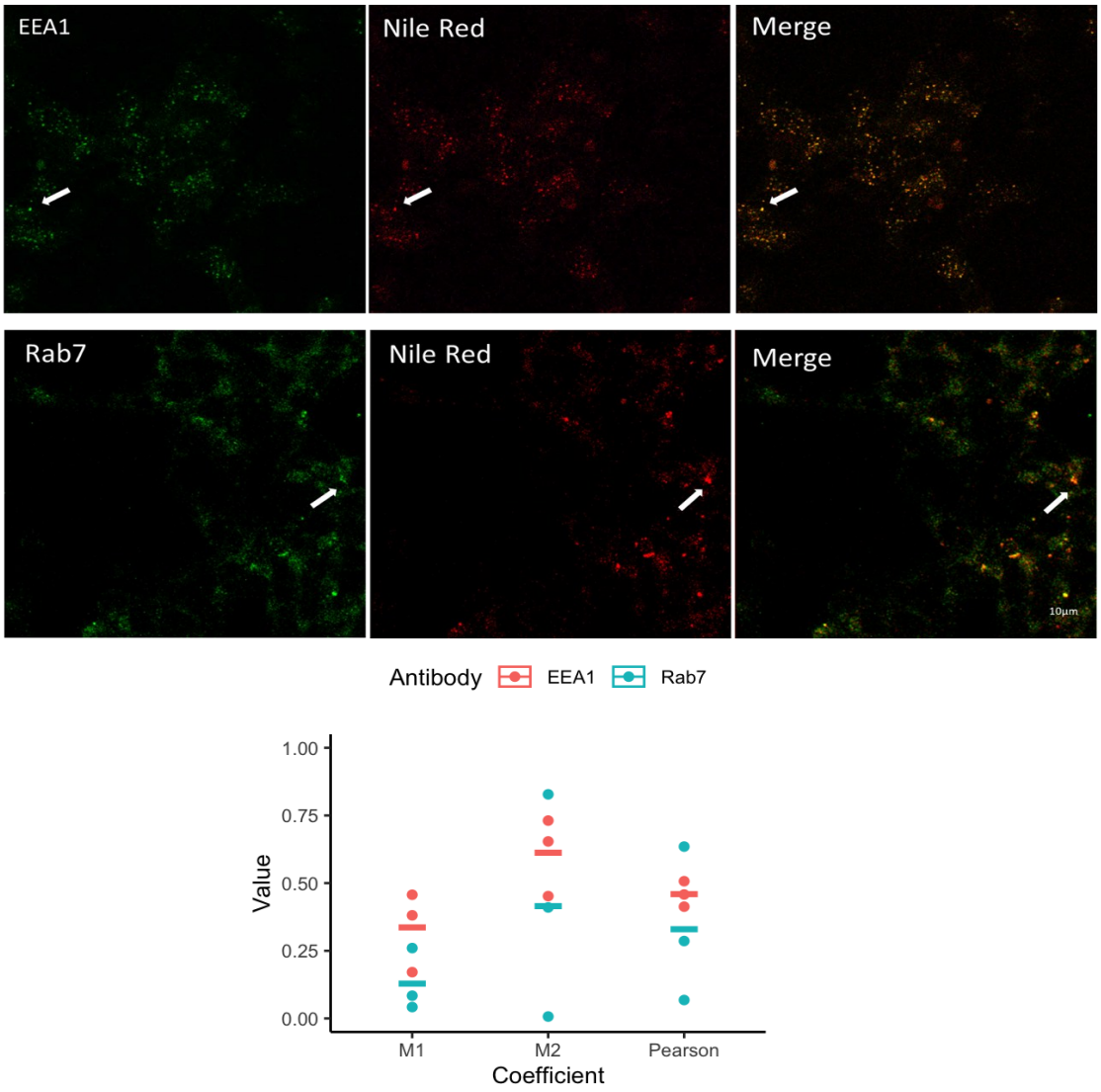

Figure 3.8 Nile red colocalises with early endosome marker EEA1 better than late endosome marker Rab7. Top: Images of EEA1, Rab7 and Nile red taken on a Leica Sp8 confocal microscope. Bottom graph: Graph showing measures of colocalization between Nile red and EEA1 (red) and Rab7 (blue). Each point refers to one field of view from one culture. Crossbars refer to mean. M1 and M2 are Mander's coefficients of the forms; M1 = marker on Nile red, M2 = Nile red on marker.

With confidence that Nile red was staining endosomes achieved, analysis of the number of size of endosomes that could be detected per cell was performed. Endosomes analysis was performed by applying the find Maxima within tolerance ImageJ (FIJI) command, followed by analyse particles with restrictions on size and circularity congruent with endosome morphology (Figure 3.8). After this process was applied the number and size of objects classified as endosomes was measured, as these parameters potentially reveal insights into the synthesis and uptake of EV (particularly small EV) via the endosomal pathway. This analysis revealed that in differentiated SH-SY5Y cells, DJ-1 KO resulted in a reduction in the number of endosomes per cell by from 7.2 to 5.6 (Tukey HSD: p = 0.019, N = 6). (Figure 9.)

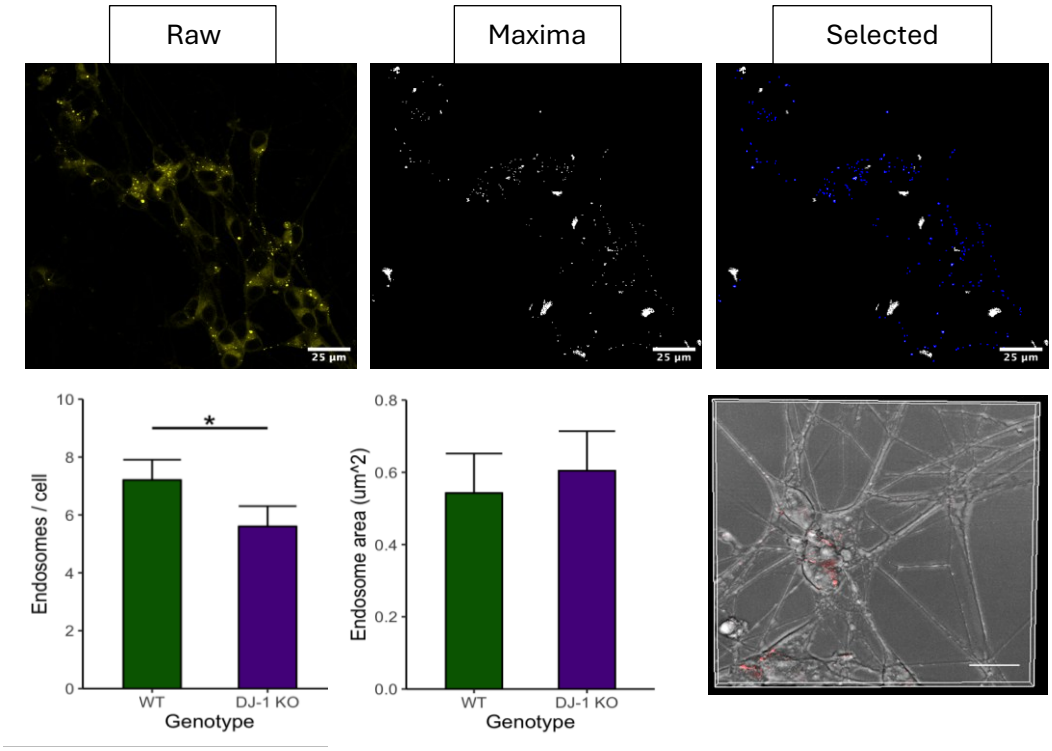

Figure 3.9 DJ-1 KO results in a lower number of endosomes per cell with no change in size. Top 3 images show major milestones of the image processing and analysis pipeline: raw image on the left, particles detected by find maxima within tolerance FIJI command in the middle, and finally the particles determined to be endosomes by morphology on the right. Bottom left graph shows the number of endosomes detected per cell. Bottom middle graph shows the mean area of endosomes. Green columns = Wild type, Purple = DJ-1 KO. Significance represented by horizontal bar between columns and *s. (* = $p < 0.05$). Bottom right image shows a 3D representation of z stack of cells and overlayed stained endosomes in red.

3.4 Discussion

The first milestone that needed to be achieved for all research within this chapter and further throughout this thesis was “can EV be isolated from SH-SY5Y cells and can they be visualised studied to a sufficient degree”. EV isolation was verified by a combination of methods to provide confidence in the isolation and increased understanding of EV structure. Each of the methods employed: flow cytometry, cryoTEM and confocal microscopy proved the isolation of EV following the recommendations of the MISEV 2024 guidelines (Welsh, 2024}, thus confirming the validity of the protocols of isolation and study for future use.

Interestingly, via cryoTEM it was discovered that the EV of SH-SY5Y cells are not uniform in shape (Figure 3.2). The majority of EV in this study were observed to be spherical. However, a variety of other interesting shapes and structures were clearly identified. These results are congruent with a cryoTEM study of CSF EV (Emelyanov, 2020}. Interestingly, despite non spherical shapes being present in said study as well, the distinct shapes visualised are not consistent between this study and those reported herein this thesis (Emelynov, 2020}. Unfortunately, no other studies of the EV of differentiated SH-SY5Y via cryoEM are available to compare results to, but this may represent function specific changes in shape that are associated with certain cells of origin. Other possibilities behind the distinct morphologies may be preparation methods, and potentially structural disruptions. Interestingly, the long tubular structures detected in the EV isolates are likely not EV at all. Instead, they appear to be a separate type of double-membrane-bound extracellular structure known as tunnelling nanotubes. The structures match the morphology of those described in Satori-Rupp’s cryoTEM study of SH-SY5Y tunnelling nanotubes (Satori-Rupp, 2019}, where they showed evidence of cargo transport in the form of a small bulging region of higher electron density (Satori-Rupp, 2019}, suggesting that while the isolate is majority EV, there is the possibility of contamination with other membranous extracellular structures.

Due to the lack of SH-SY5Y neuronal-differentiation methods standardisation and the variety and lack of differentiation employed in many studies, it was difficult to make meaningful comparisons between the results of EV population study herein and previous research by others. Further complications arose due to the variety of methods employed to isolate EV and inconsistency of reporting on information required to truly understand the reported results

Regarding the EV of undifferentiated and RA + BDNF differentiated WT and DJ-1 KO SH-SY5Y, the results of the optimised flow cytometric analysis showed that a vast majority were small EV (~ 99 %) in all samples. It was not possible to assign type classifications such as “exosomes” to the EV detected due to no information on biosynthetic origin being investigated (Welsh, 2024}. However, it can be inferred that the EV detected are primarily exosomes and ectosomes, as the small EV classification as defined by MISEV 2024 guidelines is composed of those EV types (Welsh, 2024}. This reading of our results is in line with the understanding that the largest of EV produced by SH-SY5Y are the apoptotic bodies which are produced during apoptosis, thus not produced in substantial amounts in healthy cell cultures as employed herein (Welsh, 2024}.

Interestingly, the first major visible difference between conditions is that in differentiated SH-SY5Y cells the protein-normalised total of EV is 2.97 and 1.87 times higher in WT and DJ-1 KO respectively. This increase upon differentiation appears to be primarily mediated by an increase in small EV, which is present in both genotypes. However, unlike WT, the DJ-1 KO cells also showed increased large EV in differentiated cells compared to undifferentiated. This represented an interesting discovery as no papers published have looked at the effect of neuronal differentiation on SH-SY5Y EV number or size, but raised several questions. 1) Why does the amount of EV increase upon differentiation; 2) why did DJ-1 KO cells show increased large EV while WT cells did not; and 3) why did DJ-1 KO cells show a smaller increase in small and total EV upon differentiation?

The difference seen in EV number between undifferentiated and differentiated cells has not previously been studied either in SH-SY5Y or in systems such as iPSC derived or animal neural precursor and neural cell cultures. A possible explanation is that the increased number of EV in differentiated cells represents the complex interconnected network of neuronal cells (Stogsdill, 2017}., which requires a substantial degree of intercellular communication that can be mediated by EV (Brenna, 2021}. Indeed, EV have been shown to have a complex variety of roles in interactions between neurons and glia in the CNS and appear linked to regions of high neuronal activity (Bianco, 2009; Antonucci, 2012; Chivet, 2014}. Thus, our results support the idea of EV functions being in demand in differentiated neuronal cells

As to why DJ-1 KO cell cultures show an increase in large (>200 nm) upon differentiation while WT doesn’t, it could be explained by higher levels of apoptosis in the KO cells during the process. Apoptosis during cellular differentiation is common in developmental processes and is known to occur during SH-

SY5Y neuronal differentiation methods (Kristiansen, 2014}. Apoptosis itself results in the formation of large EV known as apoptotic bodies (Welsh, 2024}. Thus, an increase in apoptosis would assumedly increase the amount of large EV. DJ-1 is also a known inhibitor of oxidative stress triggered apoptosis providing a mechanism for this action in DJ-1 KO cells (Fu, 2011; Oh, 2018}, potentially representing a largely unrecognised role of DJ-1 in developmental processes of neural differentiation.

Despite the interesting effects of differentiation on EV count, further investigation into the effect of differentiation was not in the remit of this thesis, as the interest falls upon those differences present between genotypes. Comparisons between WT and DJ-1 KO revealed increased EV number in both the total and small EV of DJ-1 KO cells, and this was consistently present in both undifferentiated and differentiated states. However, the nature of the experiment (wherein EV in the growth media was simply counted) could not determine whether the increase was due to effects on EV production or uptake.

An inherent problem with the method of EV analysis is that it is not possible to distinguish between increased production of EV vs reduced uptake, as both would result in higher EV number in the growth medium. To try and rectify this lack of knowledge, the size and number of endosomes in differentiated WT and DJ-1 KO SH-SY5Y cells was investigated. This resulted in the discovery of a decrease in endosome presence in DJ-1 KO cells with no change in size. Interestingly, DJ-1 role in the endo-lysosomal pathways is not unknown, but is poorly understood (Kim, 2013; Kyung, 2018}. Endosomal dysfunction is in fact a common feature of many forms of familial Parkinson's disease such as *Park7*, *LRRK2*, *VPS35*, *GBA1*, *ATP13A2, ATP6AP*2, *DNAJC13/RME-8, RAB29,* and *GAK* linked, as well as other neurodegenerative conditions (Perrett, 2015}.

EV are involved in many aspects of neuronal homeostasis ranging from synaptic and myelination regulation to immune system regulation as discussed in depth in Chapter 1. Therefore, the changes discovered may represent an underlying dysfunction of neuronal homeostasis that causes vulnerability in neuronal populations, and or results in a build-up of issues that eventually progress to neuron degeneration.

Changes in EV number whether by secretion or uptake differences have been reported in neurons and glia in a calcium flux and glutamatergic synaptic transmission regulated manner, suggesting an

important role for EV in high activity regions (Bianco, 2009; Antonucci, 2012; Chivet, 2014}. The activity of the dopaminergic neurons of the substantia nigra is particularly energy intensive, thus present with lower capacity to react to stress (Pissadaki, 2013; Muddapu, 2021; Ni, 2022}. Even small changes could result in substantial negative effects over long periods of time such as those expected in familial Parkinson's disease pathology. However, while knowing that DJ-1 KO in control condition results in increased EV was interesting, a more thorough understanding of EV content and functionality was required to shed light on DJ-1's role in EV dynamics in Parkinson's disease. Knowing that DJ-1 KO increase EV present in the medium, do these EV cause damage via potentially altered content, either via direct effects on cells or via incorrect immune system regulation; or does it decrease uptake, thus reducing the efficiency of vital signalling.

The changes discovered in EV and endosome number present and interesting discovery of dysfunction induced by DJ-1 KO in otherwise healthy cells, potentially providing insights into early disease development that have been missing from our understanding of Parkinson's. However, to truly understand the role of DJ-1 in EV, an investigation into how these effects change upon oxidative stress and how EV content and function changes was required.

Chapter 4: Optimising the Parkinsonian-toxin conditions with which to mimic the effects of Parkinson's disease on SH-SY5Y cells

4.1: Introduction

In the previous chapter, the effects of DJ-1 KO on the EV population of SH-SY5Y cells was investigated in healthy conditions. These studies revealed substantial insights into possible deficiencies in intercellular communication that could underpin the development of DJ-1 linked Parkinson's, even without an independent stressor. Indeed, DJ-1 loss of function mutations cause autosomal-recessive early-onset Parkinson's disease regardless of the presence of any known independent stressor (Bonifati, 2003). Thus, understanding how DJ-1 KO affects cells in healthy conditions is important for understanding disease development. However, DJ-1 protects cells against oxidative stress induced damage (Oh, 2018). Therefore, an increased susceptibility to common environmental oxidative stressors resulting in an accumulation of damage which eventually results in disease is likely.

In vitro experiments in healthy conditions of course lack an ability to represent the effects of potential environmental stressors without a specific targeted design. While protein KO alone can reveal important aspects of a protein's activity, designing an experiment in which a treatment should increase a protein's activity in conjunction with KO is substantially more revealing of its actions and downstream effects. This is especially important in proteins which are involved in protection against specific stresses as Knock-outs are logically present without obvious effects without stressor presence. With the goal of further understanding DJ-1's role in EV mediated intercellular communication, the use of oxidative-stress-based Parkinsonian toxins to mimic the stresses that may underpin Parkinson's development was desired (Salama, 2011). By oxidatively stressing the WT and DJ-1 KO cells, a greater divergence between genotypes should arise due to the lack of protective DJ-1 action in the knock-out line (Oh, 2018), allowing for easier identification of DJ-1 roles associated with EV. To achieve this however, the toxins to employ and the specific conditions of their use such as time scale and concentration needed to be determined.

Parkinsonian neurotoxins rotenone and MPP+ were decided on for investigations of suitability (Burns, 1983; Butcher, 2000). Rotenone, originally used as a pesticide (Nature, 1933), was found to increase the risk of Parkinsonism occurrence in humans via its ability to cross the blood-brain barrier and inhibit mitochondria complex 1. Specifically, rotenone inhibits the electron transport chain by blocking electron

transport from iron-sulphur clusters to ubiquinone. This causes a blockade of electrons at complex 1 resulting in reduction of cellular oxygen to the free radical form, causing oxidative damage (Heinz, 2017). Interestingly, rotenone also disrupts microtubule formation (Heinz, 2017). MPP+ on the other hand is a derivative of the Parkinsonian toxin MPTP, a lipophilic chemical that can cross the blood brain barrier (Burns, 1983). MPP+ is used rather than MPTP because MPTP requires conversion to toxic MPP+ by astrocyte monoamine oxidase B once in the brain which is not present in the astrocyte-lacking cell cultures employed in the work described herein this thesis (SchildKnecht, 2015). MPP+ unlike rotenone is specific to dopaminergic neurons as its uptake by cells is reliant on expression of dopamine transporter transmembrane proteins (Pifl, 1993). However, it is similar to rotenone as it's mode of action is a creation of oxygen free radicals by inhibition of mitochondria complex 1, though MPP+ acts by scavenging electrons itself via a reduction reaction (Cleeter, 2006). MPP+ also has the effect of inhibiting catecholamine synthesis and thus dopamine metabolism (Naoi, 1988).

The aim was to investigate several timepoints and concentrations of both toxins, to find a condition that minimally affects the health of differentiated SH-SY5Y cells. The idea being that this would provide insights into the most elusive stage of Parkinson's development wherein neuronal degeneration has not occurred yet and thus known symptoms not presented. Parkinson's disease still lacks effective biomarkers for this stage of the disease, and detection at this early stage is imperative as once degeneration has begun it cannot be rescued (Hällqvist, 2024). To achieve this, apoptosis and necrosis levels were studied in differentiated SH-SY5Y cultures via microscopy analysis of neuronal morphology for apoptosis and vital dyes for necrosis. Following identification of suitable conditions, further analysis to verify the presence of oxidative stress was performed to allow for final selection for future studies.

Apoptosis is the quintessential form of programmed cell death and has been studied to incredible detail. It is particularly known for its consistent characteristic changes in nucleus morphology, namely nucleus shrinkage, DNA condensation and nucleus fragmentation which can be measured via detection of single nuclei like objects as ROIs and subsequent shape analysis (Doonan, 2008; Rose, 2022). Necrosis on the other hand is a generally uncontrolled death in response to traumatic stress/injury of the cell by external stimuli. It lacks the distinct nucleus morphology changes present in apoptosis, but does present with a characteristic breakdown of plasma membrane integrity (Fink, 2005). Thus, necrosis allowsfor passage of DNA binding agents into the cell and nucleus that in healthy conditions are

excluded by the structurally intact membrane. This can be analysed via the use of membrane impermeable fluorescent DNA binding dyes.

4.2 Methodology

4.2.1 Cell source and growth conditions

The cells employed and their culture conditions throughout the works described in this chapter are identical to those described in detail in sections 2:2:1 and 2:2:2.

4.2.2 SH-SY5Y differentiation

The differentiation method employed throughout the works described herein this chapter is identical to that described in detail in section 2:2:3.

4.2.3 Toxin prep and treatments

To ensure that cell health was not affected by a lack of BDNF, half of the growth medium was refreshed (Dulbecco's Modified Eagle's Medium (DMEM) F-12 Glutamax^{tm} (GIBCO31331093) media supplemented with 10 % (v/v) foetal bovine serum (FBS) (GIBCO10500064) and 100 U/ml penicillin/streptomycin (GIBCO15140122)), followed by addition of 25 ng/ml BDNF before toxin treatment?

Rotenone stocks were prepared to a concentration of 10 nM in DMSO. MPP+ stocks were prepared to a concentration of 1 mM in ddH_2O. Treatments of cells with rotenone and MPP+ were carried out from stocks diluted in DMSO or ddH_2O respectively at a concentration 1000 X higher than the desired treatment such that no more than 1 % DMSO was ever present in cell growth media. Controls were always 1 % DMSO or ddH_2O respectively.

4.2.4 Verification of expected apoptotic and necrotic nuclei characteristics upon oxidative stress

Ibidi μ-Slide 2 well ibiTreat chamber slides (Ibidi, cat 81156) were coated with 11.4 μg / 9.6 cm^2 mouse laminin (Corning, 354232) per 1 ml PBS by incubation at 37 °C and 5 % CO_2 for 2 hr. WT and DJ-1 KO cells

were seeded at a density of 50,000 cells in 1 ml of FBS and P/S supplemented DMEM F-12 Glutamax™. Cells were differentiated as described above and treated with 10 nM rotenone

Following differentiation cells were treated with 5 μl of ReadyProbes™ Cell viability kit (Invitrogen: R37609) blue (total) and green (necrotic) for 5 min at 37 °C and 5 % CO_2 . Nuclei were visualised on a Leica SP8 confocal microscope at 40 X magnification in an environmental control chamber at 37 °C and 5 % CO_2. The Images were Taken employing the DAPI and Alexa 488 dye assistant settings respectively. The presence of apoptotic and necrotic nuclei and their characteristic morphologies were verified by eye across at least 100 cells per genotype.

4.2.5 Preliminary investigations into the effect of toxins on necrosis incidence

12-well culture plate wells were coated with 500 μl of 11.4 μg / 9.6 cm^2 in PBS for 2 hr at 37 °C and 5 % CO_2. Equal cultures of WT and DJ-1 KO SH-SY5Y cells were seeded at a density of 50,000 cells in 1 ml of DMEM F-12 glutamax™ media supplemented with FBS and P/S.
per well of a 12-well culture plate. Cells were differentiated as described above, and treated with toxin concentrations ranging from 0-1000 nM MPP+ or 0-100 nM rotenone for 24 hrs.

Cells were then treated with 5 μl of ReadyProbes™ Cell viability kit (Invitrogen: R37609) blue (total) and green (necrotic) for 5 min at 37 °C and 5 % CO_2. After staining cells were imaged on a Cytation 5 microscope (BioTek) via an automated protocol in using the fluorescent channel settings DAPI and GFP. Each well was imaged 9 times in an evenly spaced 3 by 3 grid centred on the well centre. Autofocus with scan occurred at each new image location and autoexposure for every image in all channels.

The number of nuclei stained with ReadyProbe™ blue (Total nuclei) and ReadyProbe™ green (necrotic nuclei) was counted in FIJI (ImageJ) using the find maxima (strict, exclude edge, and count output) command via a batch processing script written by me. Full code available at https://github.com/Bioinformatics-enthusiast/PHD-FIJI/blame/db271e556af1756c01a43f89c2409ffdd738eeb9/Toxin%20Prelim%20fluor%20nuclei%20counter.ijm, and in supplementary section .

4.2.6 Comprehensive investigations into the effect of toxins on cell death

12-well culture plate wells were coated with 500 µl of 8 ml laminin/ml PBS for 2 hr at 37 °C and 5 % CO_2. Equal cultures of WT and DJ-1 KO SH-SY5Y cells were seeded at a density of 50,000 cells in 1 ml of DMEM F-12 glutamax^{tm} media supplemented with FBS and P/S.
per well of a 12-well culture plate. Cells were differentiated as described above, and treated with toxin concentrations ranging from 0-3 µM MPP+ or 0-250 nM rotenone for 24 hrs.

Cells were then treated with 5 µl of ReadyProbes^{TM} Cell viability kit (Invitrogen: R37609) blue (total) and green (necrotic) for 5 min at 37 °C and 5 % CO_2. After staining cells were imaged on a Cytation 5 microscope (BioTek) via an automated protocol in using the fluorescent channel settings DAPI and GFP. Each well was imaged 9 times in an evenly spaced 3 by 3 grid centred on the well centre. Autofocus with scan occurred at each new image location and autoexposure for every image in all channels.

Counts of nuclei stained with ReadyProbe^{TM} blue (total) and ReadyProbe^{TM} green (necrotic), and analysis of nuclei morphology (size and shape) were performed in FIJI (ImageJ). Necrotic nuclei were counted via the same method as Total nuclei counting and morphology analysis was accomplished by using the Stardist (https://github.com/stardist/stardist-imagej) deep learning plugin for nuclei ROI creation followed by characteristic analysis and counting by using the measure command. Automation of the process was preformed via script written by me, and full code can be found at https://github.com/Bioinformatics-enthusiast/PHD-FIJI/blob/9271f0cff8231c15a64c182aac405274f2af2bd2/Diff%20SHSY%20Nuclear%20morphology%20analysis.ijm, and in supplementary section .

4.3 Results

Prior to investigating how the chosen parkinsonian toxins rotenone and MPP+ affect cell health it was imperative to derive a verification that apoptotic and necrotic nuclei behave as expected. This was achieved via confocal microscopy of rotenone-treated differentiated WT SH-SY5Y nuclei stained with ReadyProbes™ blue (total) and green (necrotic) dyes. The presence of apoptotic cells presenting with condensed nuclei (reduced size) and an increased intensity of fluorescence was verified, in conjunction with the presence of necrotic nuclei. All visible necrotic nuclei presented with the characteristic physical features of apoptotic nuclei and overlapped perfectly with apoptotic nuclei detected in the total nuclei stain images (Figure 4.1). Thus, suggesting that necrosis occurs post apoptosis.

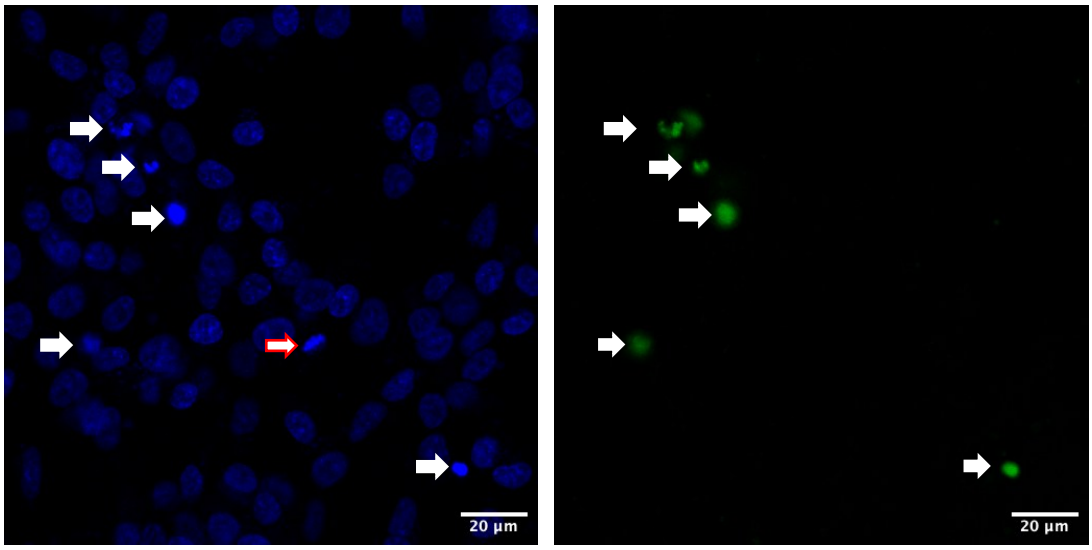

Figure 4.1 Confocal microscopy verifies the characteristic features of apoptotic and necrotic nuclei in differentiated WT SH-SY5Y. Images are representative of nuclei in differentiated WT SH-SY5Y. Both images are the same field of view. Left = ReadyProbes™ blue stained nuclei (All nuclei). Right = ReadyProbes™ green stained nuclei (necrotic nuclei). Apoptotic nuclei present with characteristic condensation (reduced size), white and red arrows on left image. White arrows show those which have undergone secondary necrosis as represented on the right image. The red arrow represents an apoptotic but not necrotic nuclei. Captured on a Leica SP8 confocal microscope.

4.3.1 Preliminary investigations into the effect of rotenone and MPP± on necrosis incidence

The first foray into understanding rotenone and MPP+ toxicity looked at their effects on necrosis incidence in WT and DJ-1 KO SH-SY5Y cells after 24 hrs of treatment. Unpublished work in the lab had previously looked at the effects of rotenone and MPP+ in the μM range on SH-SY5Y differentiated only with retinoic acid. As it was assumed that cells differentiated with retinoic acid and BDNF would be more susceptible due to their dopaminergic nature, concentrations in the nM range were employed as the starting point of investigations.

Unfortunately, the data for rotenone in this first preliminary experiment was of extremely low quality, and thus not suitable for any statistical analysis. The data for MPP+ was however suitable for further analysis outside of 1 control data point that required removal due to extreme nature (> 60 % necrosis). The percentage of nuclei that were necrotic was significantly increased 3.3-fold at 1 μM MPP+ vs 100 nM in DJ-1 KO cells (Figure 4.2). However, no significant differences between genotypes were observed. Interestingly, via ANOVA, cell number as calculated by total number of nuclei showed a significant main effect ($p = 2.44*10^{-5}$) and interaction with toxin concentration ($p = 0.003$) towards necrotic nuclei percentage. However, the slope of the relationship between cell number and necrotic nuclei percentage was not significantly different from 0. Furthermore, when graphed, a meaningful relationship as described by these significant effects is not present. Significance primarily appears to be derived from the effects of 1 μM, the data points of which are generally substantial outliers in both necrotic nuclei percentage and cell number (Figure 4.3).

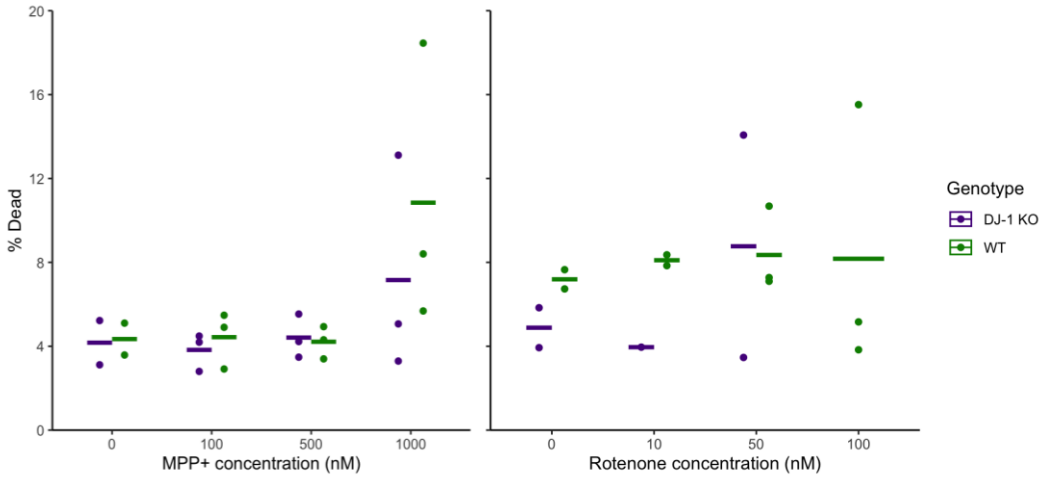

Figure 4.2 First preliminary investigation into the toxicity of rotenone and MPP+ on differentiated WT and DJ-1 KO SH-SY5Y cells. A preliminary investigation of the effects of 24 hr MPP+ (top left) and rotenone (top right) treatment on necrosis incidence in WT and DJ-1 KO differentiated SH-SY5Y. Y axis = necrotic nuclei as a percentage of total. X axis = toxin concentration. Each data point represents the results of one culture in one well o f a tissue culture plate. Crossbars represent the mean of the results at each condition.

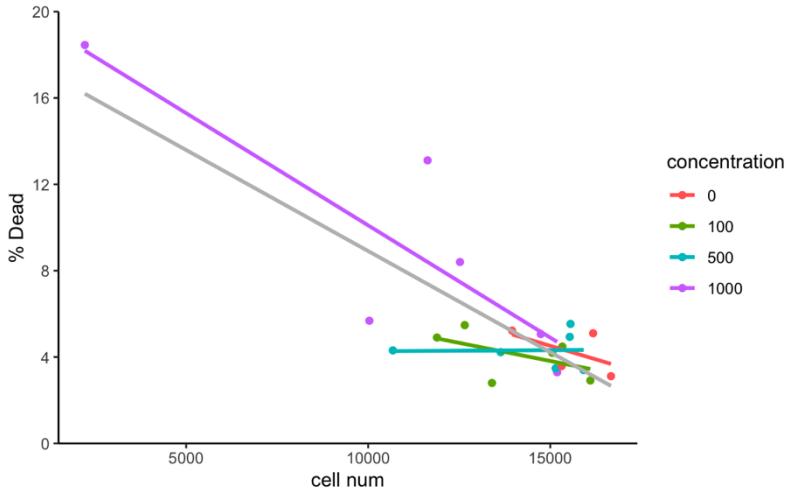

Figure 4.3 First preliminary investigation into the toxicity of MPP+: relationship between cell number, necrotic percentage and toxin concentration. Trendlines represent relationships between the variables cell number (x axis) and % of dead cells (y xais) at each toxin concentration (colours), and the average across all concentrations (grey). Each data point represents the results from one culture in one well of a tissue culture plate. Trendlines generated by ggplot2 smooth function with method “lm” and graph created in R via ggplot2.

Due to the results of the first preliminary experiment wherein the rotenone treatment data quality was too low to carry out any analysis, the 24hr rotenone treatment experiment was repeated. While regarding MPP+ treatment, the results at 48 hrs of treatment were investigated. In these experiments, 2 new parameters were of interest and analysed in conjunction with total nuclei and necrotic nuclei percentage: nuclei area and circularity, both of which change upon apoptosis.

Regarding the effects of 48 hr MPP+ treatment on cell health data quality at several conditions was poor with extreme outliers in necrotic nuclei percentage being present (Figure 4.4). These outliers were dealt with by removing any data points above 40 % necrotic nuclei percentage before statistical analysis. Upon analysis, several significant main effects and interactions were detected by ANOVA. A significant interaction was present between Genotype and MPP+ concentration when predicting necrotic nuclei percentage ($p = 0.015$), without significant main effects. Genotype when predicting cell number showed a significant main effect ($p = 0.005$). Regarding nuclei Area, Genotype and MPP+ concentration both had significant main effects ($p = 0.003$ and 0.05 respectively) and had a significant interaction ($p = 0.007$). Finally, regarding nuclei circularity only MPP+ concentration had a significant main effect. (Figure 4.5)

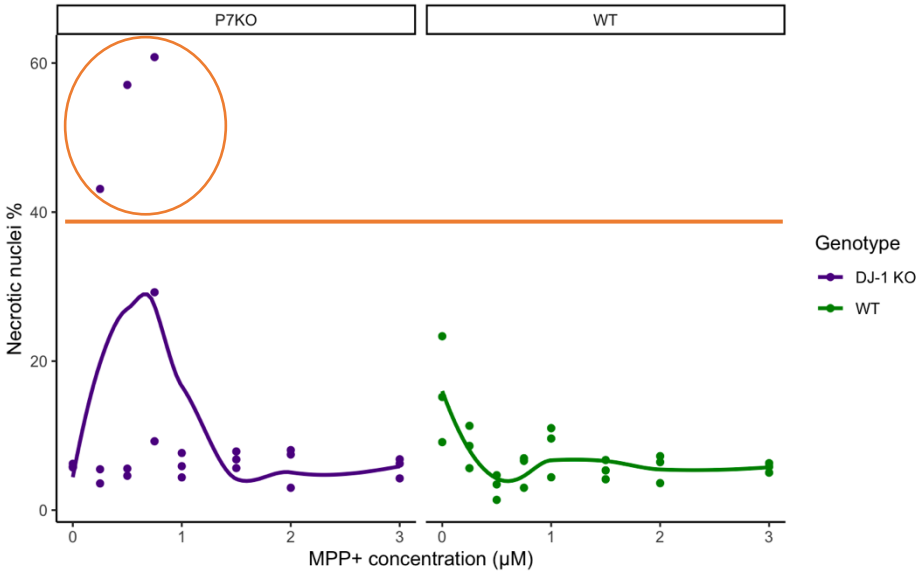

Figure 4.4 Data regarding 48 hr MPP+ treatment of WT and DJ-1 KO differentiated SH-SY5Y presents with low quality data at several conditions. Necrotic nuclei percentage as a function of 48 hr MPP+ treatment concentration in differentiated SH-SY5Y cells. Extreme outlier data points in DJ-1 KO data outlined by orange circle, and cut-off point for data exclusion indicated by orange horizontal line. Trendlines are LOESS regression carried out by ggplot2 smooth function in R. Graph created in with ggplot2 in R.

Pairwise comparisons via TukeyHSD of necrotic nuclei percentage data showed that only DJ-1 KO at 750 nM MPP+ was significantly different to its relevant control and to its WT counterpart (p = 0.012 and 0.008 respectively). Despite the presence of a significant main effect of Genotype on total nuclei, TukeyHSD post-hoc test did not detect any significantly different conditions. Regarding nuclei area, only 1 mM MPP+ in WT cells showed any relevant significant differences via TukeyHSD:nuclei area at 1 mM MPP+ in WT cell was significantly different both from its control and DJ-1 KO counterpart (p = 0.018 and 0.001 respectively). Finally, regarding nuclei circularity, despite the significant main effect of concentration, no relevant comparisons were significantly different from each other.

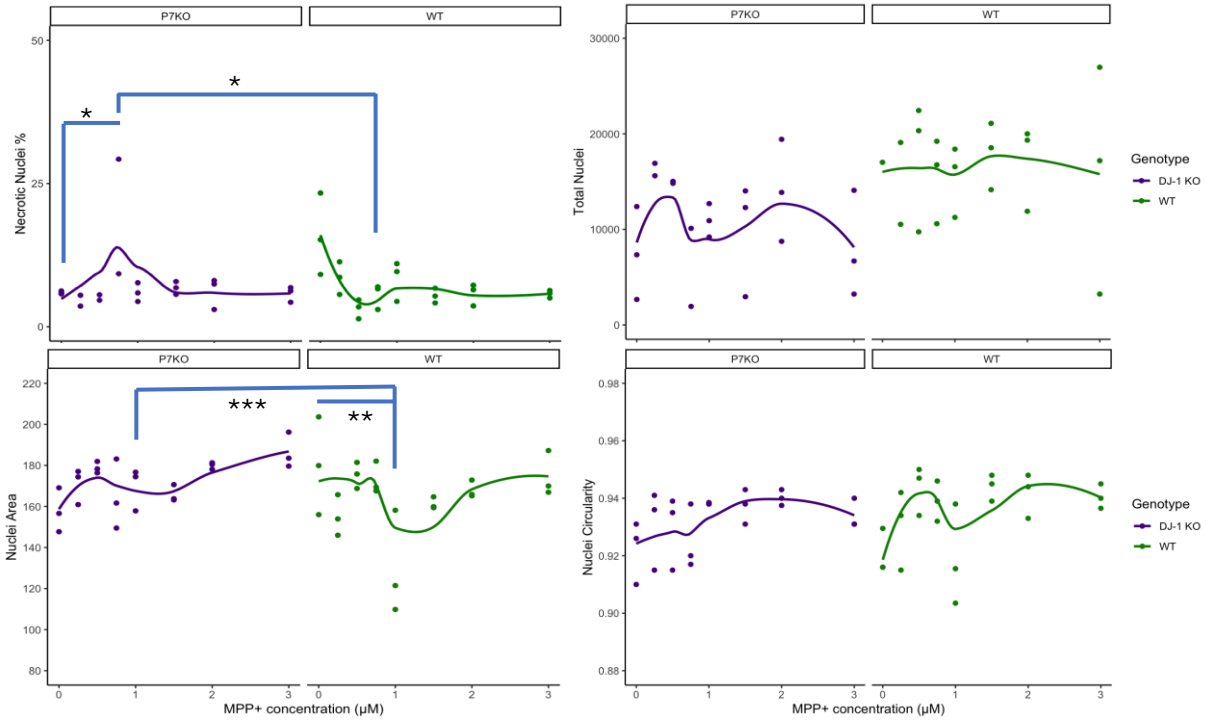

Figure 4.5 2nd preliminary investigation into the effects of parkinsonian toxins on differentiated SH-SY5Y health: 48 hr MPP+ treatment. Measurements of cell health upon treatment of WT and DJ-1 KO differentiated SH-SY5Y cells with 48 hrs of MPP+. From top left to bottom right graphs represent on the y axis the following: the percentage of nuclei that are necrotic, the total number of nuclei, the median area of the nuclei, the median nuclei circularity. Each data point represents the results in one culture well of a tissue culture plate. Trendlines were generated in R via the ggplot2 smooth function with method LOESS. Graphs generated in R via ggplot2.

Regarding the repeated 24 hr rotenone treatment experiment, the only significant main effects or interactions detected by ANOVA were main effects for genotype and concentration on total nuclei (p = 0.0003 and 0.026 respectively). Post hoc analysis was performed via TukeyHSD. On average WT cultures presented with 7596.54 more nuclei than DJ-1 KO. However, the only relevant pairwise comparisons to show significance were 1, 5, and 10 nM rotenone treatments vs control in WT cells, with treatments resulting in increases of 18293, 18347 and 19814 detected nuclei compared to control (p = 0.048, 0.047, 0.022 respectively) (Figure 4.6)

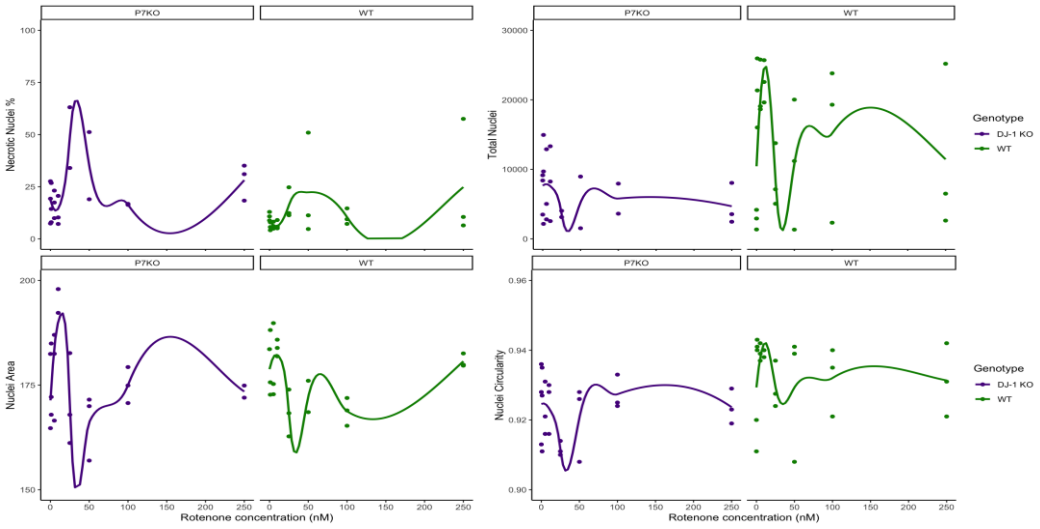

Figure 4.6 2nd preliminary investigation into the effects of parkinsonian toxins on differentiated SH-SY5Y health: 24 hr rotenone treatment. Measurements of cell health upon treatment of WT and DJ-1 KO differentiated SH-SY5Y cells with 24 hrs of rotenone. From top left to bottom right graphs represent on the y axis the following: the percentage of nuclei that are necrotic, the total number of nuclei, the median area of the nuclei, the median nuclei circularity. Each data point represents the results in one culture well of a tissue culture plate. Trendlines were generated in R via the ggplot2 smooth function with method LOESS. Graphs generated in R via ggplot2.

4.3.2 Full investigation into the effects of rotenone on cell death in WT and DJ-1 KO differentiated SH-SY5Y

Rotenone experiments previously presented with low data quality. Thus, before making a decision on the best toxin and conditions to employ the decision was made to attempt to obtain results for rotenone treatment with better data quality. An experiment was derived wherein 3 batches of cell cultures with 2 wells per condition would be individually performed with each batch consisting of 0,1,5,10,25, and 50 nM treatments of rotenone for 24 hrs on both WT and DJ-1 KO genotypes. The analysed parameters relating to different aspects of cell death were as follows: total nuclei (apoptosis and necrosis), necrotic nuclei percentage (necrosis), nuclei area, circularity and integrated density (apoptosis).

Upon consolidation of data from the 3 batches, visualisation of the nuclei morphology data (area, circularity, and integrated density) at image level revealed that severe outliers with impossible mean area values for nuclei existed. To improve data quality, images with area values higher than 300 (arbitrary unit, matches approximately the size expected from doublets) were excluded from the data for any further processing and analysis (figure 4.7). Furthermore, any images with a mean value of 0 in any measurement of nuclei morphology were excluded as this represents a technical error in the detection and analysis function (figure 4.7). Removal of the outlier area data points effectively cleaned up the area data, in addition to the side effect of cleaning up the circularity and integrated density data, suggesting that outliers across all measures were the same aberrant images. Unlike the nuclei morphology data, there were no such extreme outliers in the total nuclei, total necrotic nuclei or percentage necrotic nuclei variables. Thus, there was no pruning of data points in these sets (Figure 4.8).

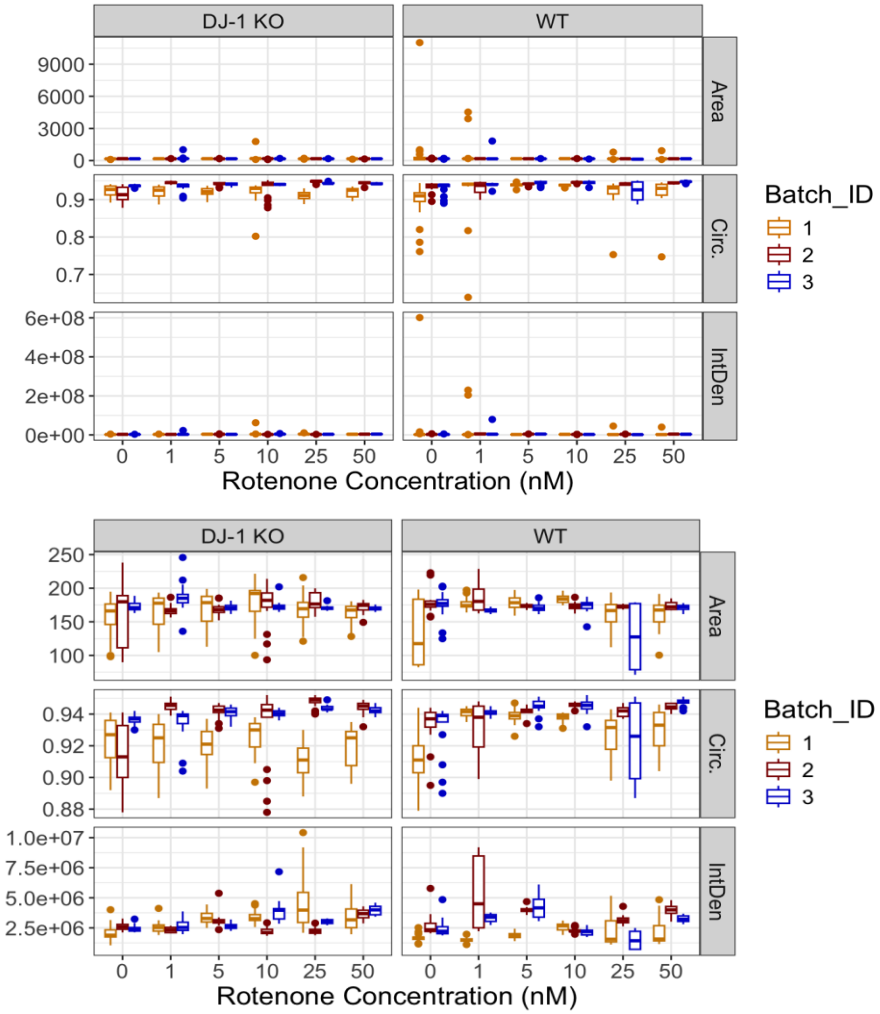

Figure 4.7 Removal of aberrant data points identified by nuclei area measurement improves data set across all measures. Boxplots showing the distribution of nuclei morphology variables for each culture batch. Top = plots including extreme outliers, bottom = plots excluding outliers via area threshold of < 300. Left vs right columns of plots = DJ-1 KO vs WT cell data. Rows of plots = nuclei area, circularity (Circ.) and integrated density (IntDen). Each data point contributing to the boxplot = 1 image (nuclei). Graphs created via ggplot2 in R.

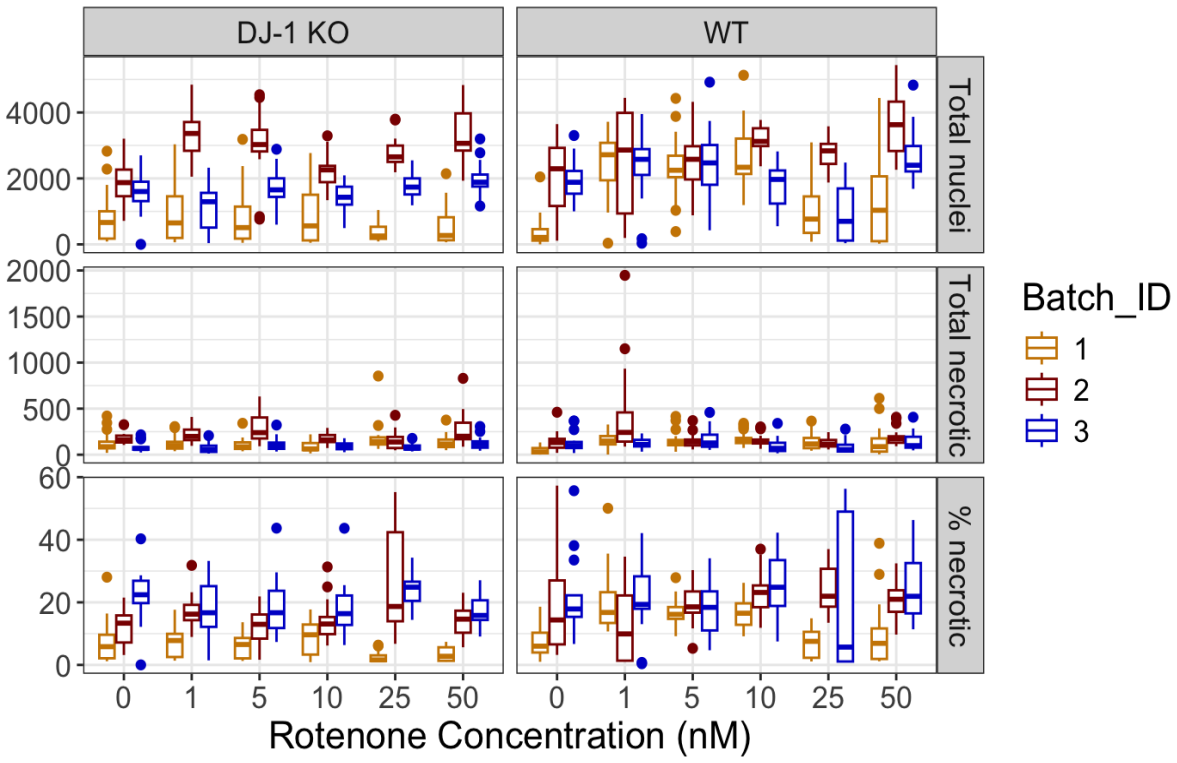

Figure 4.8. Distribution of non-nuclear morphology variables between batches at each concentration of Rotenone. Boxplots showing the distribution of the total nuclei (1st row of plots), total necrotic nuclei (2nd row of plots) and the necrotic nuclei percentage (3rd row of plots) variables for each culture batch. Left vs right columns of plots = DJ-1 KO vs WT cell data. Each data point = 1 image. Graphs created in R via ggplot2.

Further analysis into data quality by looking into the variation in data within batches revealed that WT culture well C2 of batch 2 differed substantially from all other data points (Figure 4.9). This culture was treated with 1 nM rotenone, and the decision was made to thus remove the 1 nM concentration data from further analysis to maintain N number equality between conditions. After removal of all aberrant data, the data was summarised to the individual culture level by taking the mean values of all parameters other than necrotic nuclei percentage which was calculated post summarisation of total nuclei and total necrotic nuclei counts.

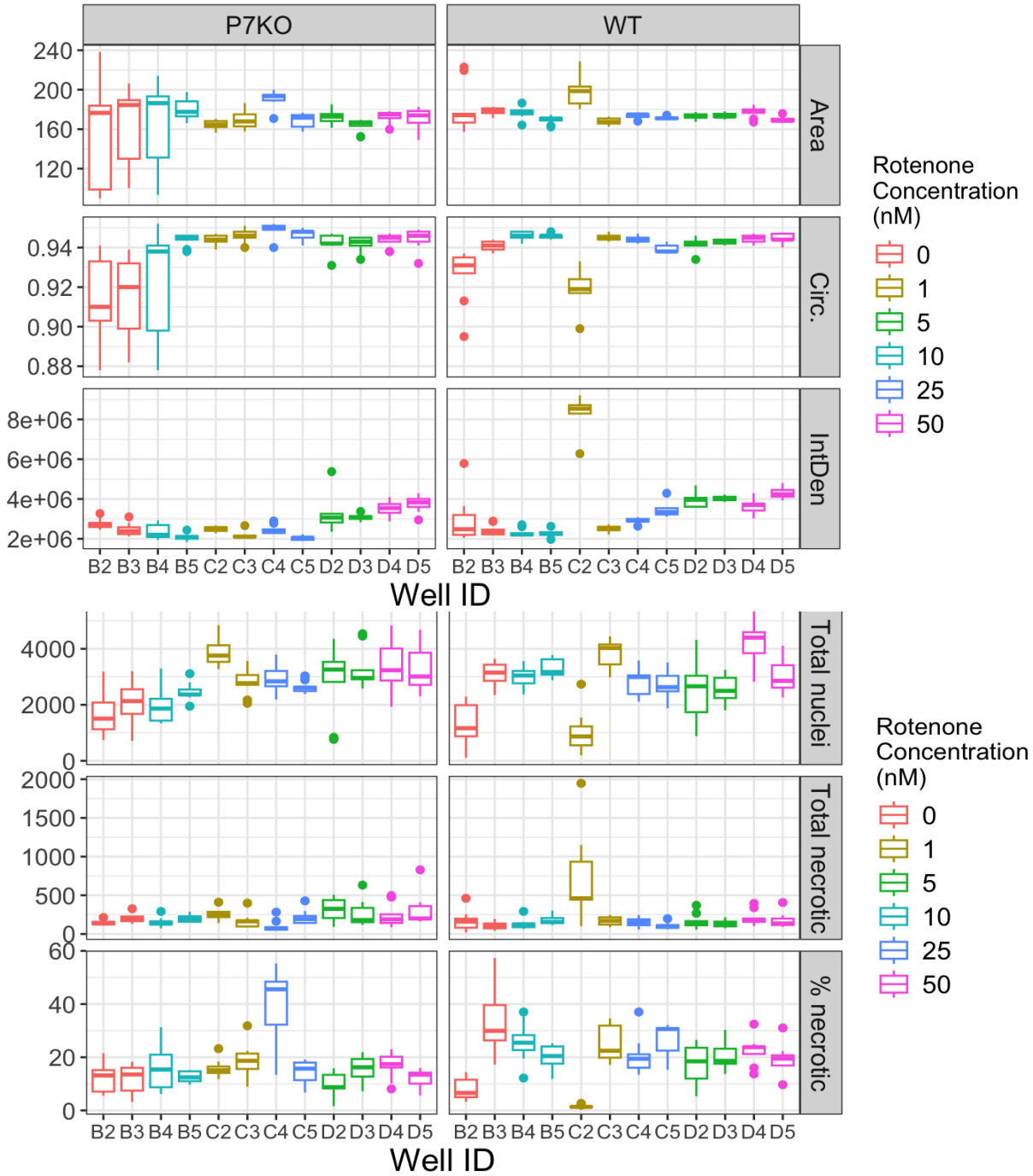

Figure 4.9 Batch 2 WT culture well C2 is an aberrant data point. Boxplots showing the distribution of collected variables relating to cell death for cultures in batch 2 to visualise the aberrant nature of well C2 in experimental batch 2. Top = plots of nuclei morphology data, bottom = plots showing nuclei counting information. Left vs right columns of plots = DJ-1 KO vs WT cell data. Rows of plots = nuclei area, circularity (Circ.) and integrated density (IntDen) in top plots and total nuclei count, total necrotic nuclei count, and the percentage of nuclei that were necrotic. Each data point = 1 image in all plots. Graphs generated in R via ggplot2.

Once quality control processes and subsequent summarisation of data occurred, statistical analysis of the data commenced. To account for the variations in effects between batches a linear mixed effect mode approach was employed. The variables that were investigated for significant differences were nuclei area, circularity, integrated density, and necrotic nuclei percentage. The predictive model employed for necrotic nuclei percentage and total nuclei was as follows: $dependant\ variable \sim Rotenone\ Concentration * Genotype + (1|Batch) + (Concentration|Batch)$. For nuclei circularity, area and integrated density instead the model $dependant\ varaible \sim Concentration + Genotype + (1|Batch)$. For the purposes of statistical analysis toxin concentration was considered discrete. All mixed effects models were fitted via the REMLmethod.

Statistical comparisons were performed for all dependant variables between all concentration values and control for both genotypes, as well as between genotypes at each concentration. Significant differences were detected by the emmeans R package contrast function in total nuclei, and nuclei circularity, area and integrated density. Regarding comparisons at different concentrations of rotenone compared to control the significant differences were as follows: 10 nM rotenone – control, nuclei area = 17.95 (p = 0.045), nuclei circularity = 0.014 (p = 0.002); 5 nM rotenone – control, nuclei circularity = 0.013 (p = 0.002); and 50 nM rotenone, nuclei circularity = 0.012 (p = 0.003). The differences between WT and DJ-1 KO at identical concentrations were as follows: DJ-1 KO – WT at 10 nM rotenone, total nuclei = -1083.8 (p = 0.002); DJ-1 KO – WT at 5 nM, total nuclei = -740 (p = 0.031); all concentrations, integrated density = 538069 (p = 0.004). (Figure 4.11)

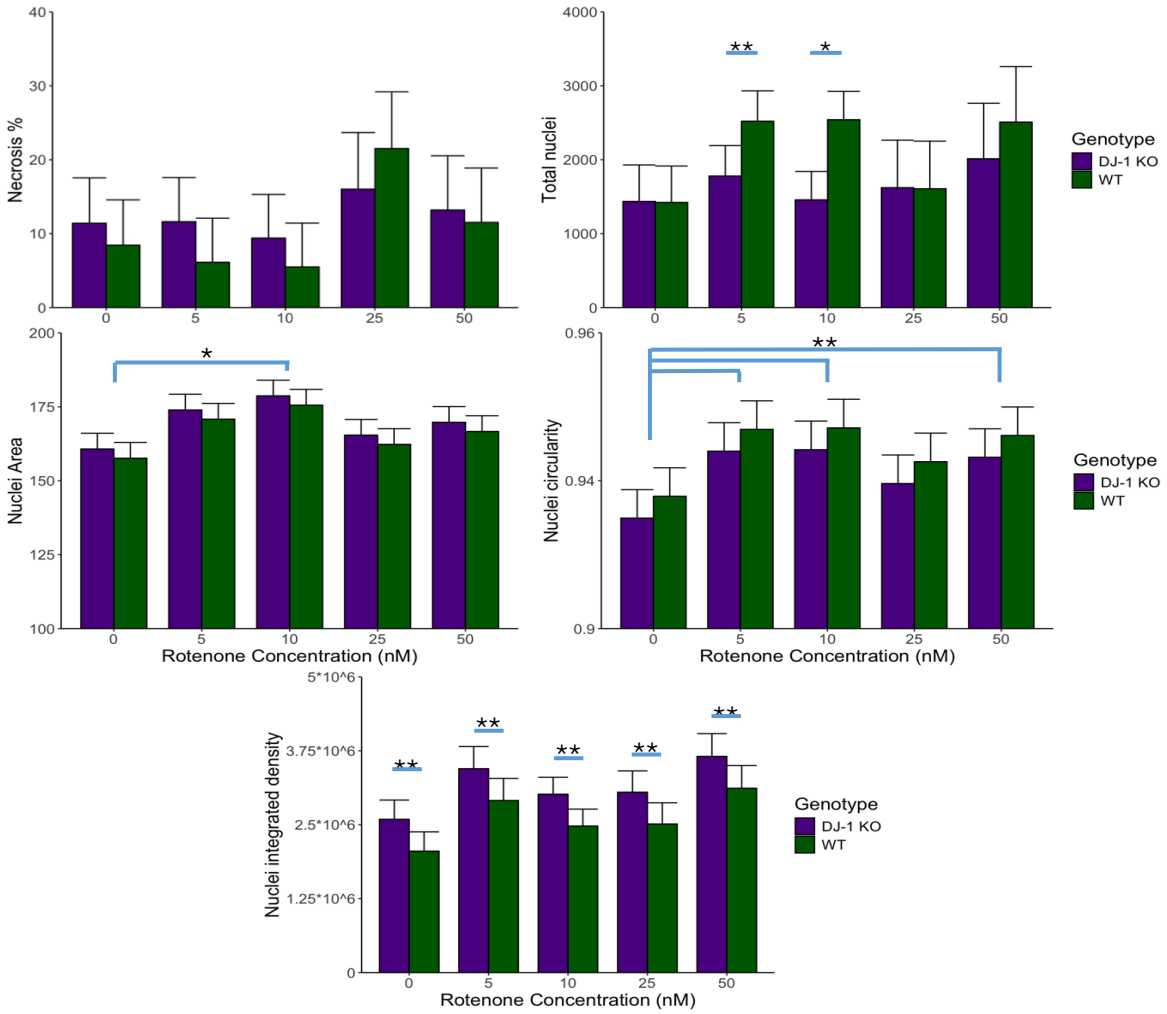

Figure 4.10 Rotenone treatment (24h) results in changes across several variables describing cell death. Each graph shows the values for a cell-death describing variable in control and rotenone treated conditions in differenitated WT and DJ-1 KO SH-SY5Y. Top left = percentage of total nuclei that are necrotic. Top Right = Total nuclei count. Mid left = Nuclei area. Mid right = Nuclei circularity. Bottom = nucei integrated density. Purple bars = DJ-1 KO, green = WT. Bar height = least squares mean. Error bars = standard error. N = 6.

By visualisation of the data and calculation of correlations several interesting factors were discerned. The Expected changes in nuclei morphology upon apoptosis were increased circularity and integrated density, and reduced area. However, while circularity on average did increase upon rotenone treatment (Fig 4.10), nuclei area and circularity had a strong positive correlation of 0.647 ($p < 0.001$) in total and 0.489 ($p < 0.01$) and 0.803 ($p < 0.001$) in DJ-1 KO and WT respectively (Fig 4.10). A point of contention was whether differences in total nuclei represented changes in cell distribution within or between wells, or the level of cell death. Due to the variety of possible explanations for changes in this variable its

relationships with other variables were investigated. Total nuclei showed a strong proportional correlation with total necrotic nuclei that was consistent between genotypes (Figure 4.11). However, only the images with the lowest of total nuclei (< 1000) showed an increased necrotic nuclei percentage. Similarly, but not to the same degree, with nuclei circularity only images with total nuclei below ~2000 showed decreased circularity.

Figure 4.11 Correlation between variables describing apoptosis and necrosis upon rotenone treatment in differentiated WT and DJ-1 KO SH-SY5Y. Relationships between variables described as whole and split by genotype as Pearson correlations (above diagonal), and plotted data points with each point representing the average of one well of culture (below diagonal). Density graphs along the diagonal show the distributions of each variable. Abbreviations: Circ. = nuclei circularity; IntDen = nuclei integrated density. Graph generated by ggplot2 extension GGally in R.

4.4 Discussion.

4.4.1 Analysing cell death.

Cell death is not a simple process. Death can occur through controlled pathways described as programmed cell death but can also occur via uncontrolled physical processes acting on the cell. To understand the effects of the parkinsonian toxins rotenone and MPP+ on WT and DJ-1 KO differentiated SH-SY5Y, cell death was investigated with a focus on the programmed cell death pathway of apoptosis and the "uncontrolled" method known as necrosis (Fink, 2005). Thus, allowing for the selection of the most optimal conditions for future experimentation.

Apoptosis is incredibly tightly regulated due to its roles in many highly specific developmental pathways and immune responses (Ekert, 1997; Voss, 2020). Apoptosis can be triggered through one of 2 broad pathways: the extrinsic, primarily initiated via interactions with other cells or extracellular signals and cell surface death receptors; and the intrinsic, activated by internal cell pathways generally in response to internal stress (Fulda, 2006). The activation of both pathways results in specific morphological changes at the nucleus. So, while it was the intrinsic pathway that was of interest in this case there is no meaningful distinction in the parameters analysed between the two. Specifically, during apoptosis the nucleus shrinks as heterochromatin condenses (Doonan, 2008). This shrinkage and condensation of the nucleus pushes the nucleus towards a more circular shape with increased intensity of DNA stains seen in 2D via confocal microscopy (Figure 4.1). Thus, it is these parameters that were chosen to analyse the level of apoptosis occurring.

Necrosis on the other hand is an uncontrolled form of cell death induced by traumatic damage to the cell from an external agent. It is characterised by a physical process in which the plasma membrane loses integrity and cellular contents are released into the extracellular space in an uncontrolled manner (Fink, 2005; Nirmala, 2019). Due to the loss of membrane integrity, necrosis can be assessed via DNA binding dyes that are not able to cross the hydrophobic interior of the membrane such as propidium iodide (PI) (Lekshmi, 2017), as they become able to access DNA only where integrity is lost. Interestingly, in recent years, a form of programmed cell death with a semi-necrotic phenotype has been discovered termed necroptosis (Laster, 1988; Fink, 2005; Nirmala, 2019}. Furthermore, it has been reported that the ultimate outcome of apoptosis in absence of scavenger phagocytic immune cells is a necrotic phenotype known as secondary apoptosis (Silva, 2010). Secondary necrosis was of particular relevance

in this work as the in-vitro assays did not contain scavenging immune cells. However, all forms of necrosis are detectable by the aforementioned dyes and cannot be distinguished except in the case of secondary necrosis which should present lost membrane integrity with changes in nucleus morphology s consistent with apoptotic processes.

Ultimately after verifying their applicability via confocal microscopy (Figure 4.1), cell death was analysed by a group of variables that are associated with the distinct morphological and phenotypic physical changes associated with the distinct forms of cell death. Specifically, these were: nucleus size, circularity and integrated density, measuring apoptotic-like death; and necrotic nuclei percentage via vital dye staining measuring necrotic like death (Doonan, 2008; Lekshmi, 2017).

Additionally, to the above-described variables, the total number of nuclei was measured. Total nuclei is a particularly interesting variable: indeed, it is incredibly difficult to ascertain its correct interpretation as there are several likely possibilities that would appear as changes in this variable. Each culture of cells was seeded with an identical number of cells. However, nuclei number for each culture was calculated within distinct fields of view and averaged across them. Thus, differences in total nuclei could represent true differences in seeding number or in propagation after seeding, or may also show non-equal spatial distribution of cells, or toxin effect. Furthermore, while differentiated cells are incapable of division (Anda, 2016), apoptotic death results in nuclear fragmentation which could be picked up as an increase in total nuclei in conditions where increased apoptosis is occurring.

Looking on a per image basis of the final rotenone experiment, it was observed that in images with below 1000 nuclei the proportional relationship between total nuclei and total necrotic nuclei was broken. This effect is replicated with necrotic nuclei percentage where the otherwise flat relationship breaks in images with below 1000 nuclei. Furthermore, looking at the distribution of all variables across all conditions and batches, images with necrotic percentages above 25 appear to be distributed across samples outside of outliers which are not consistent with other images of their condition (Figure 4.8). Thus suggesting that when looking at individual images, low numbers of nuclei are representative of insufficient spatial distribution of cells and or toxin, and not a true increase in toxin effect.

When looking at fully summarised data at the sample level the relationships between cell number and other variables appear different. Even in the earliest experiments of MPP+ effect, it was observed that

lower cell number resulted in higher necrotic percentage. However, this only occurred in the highest concentration tested, 1 μM. inverse relationship at a sample level appeared relatively consistent across experiments. Suggesting that total nuclei at a sample level was truly describing differences in pre-treatment cell number between samples, as toxin would be distributed at higher concentrations per cell in the case of lower cell number.

4.4.2 Issues with MPP+ and why rotenone was preferred as the toxin of choice

Originally both MPP+ and rotenone were considered as potential parkinsonian toxins to be employed in further research. However, ultimately rotenone was the only toxin used in further experiments. One main reason contributed to this decision: it was found out that an interaction between DJ-1 and dopamine transporter had been reported by Luk et al, (Luk, 2015), who showed that DJ-1 physically interacted with dopamine transporter increasing its localisation to the membrane (Luk, 2015). Dopamine transporter localisation to the membrane is regulated by the endocytic pathways (Bu, 2021). Interestingly, DJ-1 was reported to affect the endocytic pathways (Kim, 2013; Kim, 2016; Kyung, 2018), thus suggesting this DJ-1 dopamine transporter interaction has credence despite been the only of its kind. MPP+ is transported into cells via dopamine transporter (Pifl, 1993), thus changes in dopamine transporter membrane localisation can alter the MPP+ dose per cell resulting in difficulty of interpreting results and unentangling effects of changed uptake vs direct action. Rotenone then became the preferred choice, having transporter independent entry to the cell as a lipophilic molecule (La Forge, 1933; Higgins, 1996, and assumedly resulting in higher consistency of dose and thus higher consistency of effect and easier data interpretation.

4.4.3 Rotenone affects the health of differentiated WT and DJ-1 KO SH-SY5Y cells

It was decided that a thorough experiment looking into the effects of rotenone on differentiated SH-SY5Y rather than MPP+ would be performed due to the aforementioned reasoning. This experiment was comprised of 3 batches split by 1 week, each containing N = 2 cell cultures per condition for a total of N = 6, thus, providing a highly robust analysis of the effects of rotenone and DJ-1 KO.

When analysing cell death after rotenone treatment, several variables of interest showed significant difference. The only variable to have no significant differences between any conditions was necrotic nuclei percentage, suggesting that all tested treatments of rotenone are not inducing traumatic stress

and primary necrosis, and that apoptotic events are primarily non-necroptotic and largely early-stage due to the lack of significant secondary necrosis (Silva, 2010).

On the other hand, nuclei circularity significantly increased upon rotenone treatment in both WT and DJ-1 KO genotypes at 5, 10, 50 nM compared to their respective control. An increase in circularity was the expected outcome of increased apoptosis due to the characteristic nuclei shrinking and condensation results in a more uniform circular shape (Doonan, 2008) (Figure 4.1). Interestingly, nuclei area while showing a significant difference to control in both genotypes at 10 nM rotenone, increased instead of the expected decrease (Doonan, 2008). There is a likely explanation for this oddity: a particular issue with the analysis of apoptosis is that at 10 X magnification on the citation 5 system employed, it is impossible to detect both healthy and apoptotic nuclei in the same channel without overexposing apoptotic nuclei. Condensation and shrinking of nuclei during apoptosis results in a highly concentrated and thus high signal, as the same amount of DNA and fluorescent dye is present in a smaller space. The citation 5 employs a CCD sensor system, which are susceptible to the effect of “blooming” artifacts due to saturation in overexposed regions (Balaji, 2024). Blooming artefacts result in objects appearing larger than their true size (Balaji, 2024). Thus, the likely explanation is that apoptotic nuclei are in fact appearing larger than healthy nuclei in images despite their true shrinkage.

It would be interesting to investigate the performance of this experiment at higher magnifications as previous preliminary tests did not result in the same issues at 40 X. 40 X is too high magnification for high-throughput live imaging due to the substantially increased time taken to image a sufficient number of cells, thus mandating the use of fixed cells. However, 20 X magnification would be particularly interesting to test as it potentially would provide a good middle ground where the small changes can be detected, and live imagining is viable.

Finally, integrated density as a measure of apoptosis showed significant differences between the two genotypes at all concentrations of rotenone and control. The differences remained static at each rotenone condition and comparable to the difference between the two genotypes in control condition. This could be representative of a baseline increase in apoptosis in DJ-1 KO cells. This would match with visual assessments of cell cultures throughout the culturing process. DJ-1 is in fact known to interact with apoptosis pathways, primarily showing an inhibitory effect through mechanisms such as p53 regulation via binding and promotion of miRNA-22 function, downregulating pro-apoptotic proteins

such as bcl-2-like protein (Bim) (Junn, 2005; Fu, 2012; Oh, 2018). However, it would logically be expected that under oxidatively stressed conditions, such as those induced by rotenone, DJ-1 KO would result in larger difference to WT than that seen in healthy control. This expected effect was surprisingly not observed in the research described herein. This gives further support to the hypothesis that only minimal early-stage apoptosis was observed in this study. A longer treatment period and or increased concentration of treatment may potentially exacerbate the differences between the 2 genotypes. However, the similar level of minimal apoptosis observed served the goal of these experiments well, as model of the pre-neurodegenerative phase of Parkinson's disease was desired.

Overall, rotenone appears to increase cell death via apoptosis in both WT and DJ-1 KO to a similar albeit small degree, as demonstrated by the expected changes in nuclei morphology expected during apoptosis. This provided a strong baseline wherein cell death is minimal and or early-stage for further analysis into the effects rotenone on EV.

Chapter 5: DJ-1 KO and rotenone induces mitochondrial stress in differentiated SH-SY5Y and alters the EV population

5.1 Introduction

The work described in previous chapters provided a suitable cellular Parkinson's mimicking model system upon which to truly study the role of DJ-1 and EV in intercellular communication. With the discovery of rotenone treatment conditions resulting in minimal changes in cell health/death, work was thus to be carried out to study the effects of such treatment on EV populations.

Oxidative stress has a strong link to Parkinson's disease, particularly those autosomal recessive forms caused by DJ-1 mutations (Bonfiati, 2003; Abou-Sleiman, 2003; Repici, 2018). DJ-1 is a protein with the assumed primary role of sensing ROS and protecting the cell against damage induced by such oxidative stress (Di Nottia, 2017; Repici, 2018). Furthermore, the dopaminergic neurons of the substantia nigra, those most vulnerable to Parkinson's, are inherently susceptible to ROS induced stress and damage. The distinctive morphology of long, heavily-branched (Matsuda, 2009), unmyelinated axons (Orimo, 2011) coupled with the characteristic intense energy demand of dopaminergic neurons (Pissadaki, 2013) is a perfect recipe to render a cell weak to oxidative stress (Surmeier, 2018). Even the identifying dark colouration of the neurons is caused by the presence of the pigment neuromelanin, a compound produced during catecholamine metabolism which exists as a protective mechanism against the ROS generated by the high levels of dopamine metabolism (Usunoff, 2010).

However, ROS production and oxidative stress are not always ultimately detrimental. ROS molecules are heavily involved in signalling roles during normal cell activity (Helmut, 2022). Furthermore, under normal functioning conditions, ROS induced responses from astrocytes and microglia maintain homeostatic balance ultimately removing or severely dampening any negative effects (Chen, 2020; Zhu, 2022).

Outside of the traditional understandings of oxidative stress and ROS signalling, it has also been reported that oxidative stress induces changes in EV population (Chiaradia, 2021). Specifically oxidative stress is well reported to increase the number of recovered EV across a spectrum of distinct cell types and inducing chemicals, but appears to be dependent on the combination of cell type and inducer (Chiaradia,

2021). For example, 4-HNE has been reported to result in increased EV in endothelial cells and fibroblasts, but not monocytes (Vatsyayan, 2013). However, this study only investigated tissue-factor (TF) positive EV and could be missing changes of “tissue-factor negative” EV. Furthermore, these responses can be dampened by incubation of cells with antioxidants, supporting that it is an ROS-mediated response (Benedikter, 2017). It is this aspect which was of interest to the research within this thesis, as comparing how the EV population changes upon rotenone treatment compared to in healthy conditions with and without DJ-1 is imperative to understand the link between DJ-1 and EV. The work described in this chapter thus describes experiments undertaken to verify and the understand these changes.

5.2 Methodology

5.2.1 Cell source and growth conditions

SH-SY5Y

The SH-SY5Y cells employed and their culture conditions throughout the works described in this chapter are identical to those described in detail in sections 2:2:1 and 2:2:2.

iPSC

iPSC with a 1bp deletion in the *PARK7* gene and its isogenic control (A18945, DJ1 WT and A18945, DJ1 KO, 2B10 clone) were kindly provided by Dr Mark Cookson, NIH. iPSCs were maintained under a feeder-free condition with Essential 8 medium (Gibco) on 10 µg/mL vitronectin (Gibco)-coated plates. Cells were fed daily with full media changes and passaged using EDTA 0.5 mM (Lonza) at 80% confluence.

5.2.2 SH-SY5Y and iPSC differentiation

SY-SY5Y

The differentiation method employed throughout the works described herein this chapter is identical to that described in detail in section 2:2:3.

iPSC

Neuronal Induction: After 24 hours from the plating, the medium was changed into neural induction media (NIM) composed of E6 (ThermoFisher), 2µM XAV-939 (HelloBio), 10µM SB431542 (HelloBio), 0.1µM LDN193189 (HelloBio). For cell seeding medium was supplemented with 10 µM RHO/ROCK pathway inhibitor Y-27632, and after 24 hours, this was removed. Cells were fed daily for 12 days. At around day 5, neural rosettes began to form.

Neural Precursor Cells (NPCs) Differentiation: Cells were detached using Accutase (Sigma Aldrich) at 37°C for 4 minutes. The cell suspension was then centrifuged at 200g for 5 minutes and the pellet resuspended in Neural Maintenance Media (NMM) composed of Advanced DMEM: F12 (ThermoFisher), Neurobasal Media (ThermoFisher), 1% Glutamax (ThermoFisher), 0.5X N2 (ThermoFisher), 0.5X B27 (ThermoFisher) and βMercaptoethanol (1:1000, ThermoFisher). Cells were seeded at a density of 100,000 cells/cm^2 on 6-well plates or coverslips to perform immunostaining, coated with 20 µg/mL of Poly-L-Ornithine (ThermoFisher) and 10 µg/mL of laminin (Biolamina, LN511-0502). For cell seeding medium was supplemented with 10 µM Rock-Inhibitor, and after 24 hours, this was removed. Cells were then fed every 3-4 days and passaged at around 90% confluence. On day 7, FGF2 (1:10000, Qkine) was added to the medium.

Neural Differentiation: At passage 2 or 3, NPCs were transferred to the final plating format. They were seeded at 285,000 cells/well on coverslips in 24-well plates coated with 20 µg/mL of Poly-L-Ornithine (ThermoFisher) and 10 µg/mL of laminin (Biolamina, LN511-0502). Cells were seeded into NMM with 10µM Rock inhibitor. The day after, the media was changed into BrainPhys, SM1 (Stem Cell Technologies), 20ng/mL BDNF (Qkine), 20ng/mL GDNF (Qkine), 2µM Compound E (Stem Cell Technologies). Every 3 days, half media change was performed. After 6 days in the presence of Compound E, this was removed, and cells were fed every 3 days with BrainPhys, SM1, 20ng/mL BDNF and 20ng/mL GDNF. At DIV12, cells were used for the experimental procedures.

5.2.3 Toxin prep for treatments

Toxin preparation and treatments were performed identically to those methods described in chapter 4 section 4.2.3.

5.2.4 EV isolation and analysis from SH-SY5Y and iPSC-derived cells

Isolation

For the experiments employing SH-SY5Y and iPSC-derived neuronal cells described in this chapter where EV were isolated from cell cultures, they were isolated identically via the following method. Culture medium was aspirated, and floating cells and large debris were removed from the media via sequential centrifugation at speeds of 300 and 2000 xg for 5 and 20 min, respectively. Centrifugation occurred at a temperature of 4 °C. Supernatant containing EV was harvested and placed on ice or stored at 4 °C until further use. Prior to analysis EV were stained overnight with 5 mM Bodipy™ FL-Maleimide.

Analysis: SH-SY5Y and iPSC-derived neural precursors

EV concentration and sizes were analysed by flow cytometry using a Beckman Coulter Cytoflex S. The detectors employed were FITC and violet light side scatter (SSC_1). Megamix 7032 + 7303 standardisation beads ranging from 100 nm to 900 nm diameter were employed to generate EV gates. The acquisition settings were as follows: SSC_1 threshold of 18,000 and gain of 400; FITC gain of 250. The flow rate was set to 10 ml/min and sample analysis stopped at 30,000 EV events detected.

Analysis: iPSC-derived neurons

EV concentration and size were analysed by nano flow cytometry using a NanoFCM Nanoanalyser system. The detectors employed were green fluorescence and violet light side scatter. EV count was normalised to true nuclei count as a assessed by total culture growth area Tilescan, capturing images in using the DAPI dye assistant settings of a Leica SP8 confocal microscope of the entire culture area and quantification of nuclei in FIJI (ImageJ).

5.2.5 Endosome quantity and size analysis

Ibidi culture dishes were coated with 2 ml of 8 ml laminin/ml PBS for 2 hr at 37 °C and 5 % CO_2. Dishes were seeded with 100,000 WT or DJ-1 KO SH-SY5Y cells in 2 ml of DMEM f-12 glutamax™ supplemented with FBS and P/S. Cells were then differentiated as previously described. Cells were stained with 300 nM Nile red for 15 min at 37 °C at 5 % CO_2 before being imaged on a Leica SP8 Falcon Confocal microscope in an environment control box set to 37 °C and 5 % CO_2. Nile red was imaged using the Alexa 555 dye

assistant settings. For this experiment N = 6 spread evenly across 3 weeks of cultures and for each N at least 200 cells were imaged. Endosome size and number per cell were analysed in FIJI (ImageJ).

An automatic pipeline was built in FIJI (ImageJ) by me to analyse endosome count and size. Full code is available at https://github.com/Bioinformatics-enthusiast/PHD-FIJI/blob/bbf470326836f8e5a6a4e8db3ac7bd456b2d713f/Endosome%20analyser.ijm and in the supplementary section. Briefly, a top hat filter of radius 1.5 was applied to images of Nile red staining, followed by binarisation via the Find Maxima command (parameters = exclude, strict, maxima within tolerance output) with prominence set as the minimum pixel intensity determined by the default auto-threshold command. Particles of area 0-10 μm^2 and circularity > 0.5 were selected as endosomes and passed to the Analyze Particles command. Endosome count was normalized to the total stain area determined via Huang auto threshold of the auto-scaled (equivalent to brightness and contrast > auto in FIJI) raw Nile red image.

5.2.6 Mitochondria morphology analysis

Differentiated SH-SY5Y cells were stained with 250 nM Mitospy ™ orange for 30 min at 37 °C then washed once with PBS. Cells were then fixed with 4 % para-formaldehyde, before being washed for 5 min with PBS three times and blocked with blocking buffer for 30 min. Mitochondria were then stained with anti-ATP5-alpha antibody (Mouse mono; Abcam, 14748) overnight at 4 °C before being washed 3 times for 5 min with PBS. Nuclei were stained with 1:2000 Hoechst 33342 for 2 min at RT, before secondary antibody incubation with Alexa-488-conjugated goat anti-mouse (Goat mono; Thermo fisher, A11001) for 1 hr at RT and washed 3 times with PBS for 5 min each.

Nuclei, ATP5-alpha and Mitospy™ orange were visualised on a Leica SP8 confocal microscope system at 20 X magnification using the DAPI, Alexa 488 and dye assistant settings. 10 images were taken per culture and laser and detector settings were kept consistent for all images of each marker.

Mitochondria morphology analysis was performed in FIJI (ImageJ) via an automatic analysis pipeline built by me. Full code is available at https://github.com/Bioinformatics-enthusiast/PHD-FIJI/blob/bbf470326836f8e5a6a4e8db3ac7bd456b2d713f/Mitochondria%20analysis.ijm , and in the supplementary section.

Nuclei morphology was analysed as described previously in chapter 3 using the StarDist (https://github.com/stardist/stardist-imagej) deep learning plugin for nuclei ROI creation followed by characteristic analysis and counting by using the measure command.

Preprocessing was performed on all mitochondria stain images as a sequence of: max intensity projection (Z project command); rolling ball background subtraction of radius 5; unsharp mask of radius 0.5 and mask 0.3; enhance local contrast with block size 199, histogram of 256, and maximum of 1.5; and finally median filter of radius 0.5.

Fluorescent stain intensity and area analyses were performed as follows. Intensity was measured on the whole image and on a thresholded selection of mitochondria with min and max pixel values of 40 and 255.

Mitochondria branch morphology was analysed as follows. Mitochondria selective staining was selected via Otsu auto thresholding, followed by skeletonisation using Skeletonize command, and skeleton analysis via the Analyze skeleton (2D/3D) command with prune set to none.

5.2.6 cellular ROS analysis

24-well culture plate (Corning) wells were coated with 300 ml of 8 ml laminin/ml PBS for 2 hr at 37 °C and 5 % CO_2. Equal cultures of WT and DJ-1 KO SH-SY5Y cells were seeded at a density of 20,000 cells in 2 ml of DMEM F-12 glutamax^{tm} media supplemented with FBS and P/S. Cells were then differentiated as previously described, and then treated with 10 nM rotenone or 0.1 %solvent DMSO as control for 24 hr at 37 °C and 5 % CO_2. ROS level was detected via the Abcam Cellular ROS Assay Kit (Red) (ab186027) according to the manufacturer's instructions. Subsequently, ROS dependent staining was visualized via the RFP settings of a Citation 5 microscope system. 6 images were taken per well with consistent exposure and gain for all images.

Quantification of ROS was performed in FIJI (ImageJ) using a semi-automatic pipeline created by me. In short, the Find maxima command was employed to detect stressed cells represented by regions of high pixel intensity. The StarDist (https://github.com/stardist/stardist-imagej) deep learning plugin for nuclei ROI creation and subsequent counting of ROI was used to determine the number of cells per image. Lastly, the counts of stressed cells was normalized against the number of cellsper image.

Statistical analysis was performed in R.

5.3 Results

5.3.1 Rotenone treatments results in different EV responses from differentiated WT and DJ-1 SH-SY5Y

The number of small and large EV was previously analysed in healthy conditions in both WT and DJ-1 KO differentiated SH-SY5Y. Understanding how the differences observed change upon treatment with the parkinsonian toxin rotenone is important to understanding the role of EV in DJ-1 mediated communication under oxidative stress. To this end, the concentration of small and large EV was studied in differentiated WT and DJ-1 KO SH-SY5Y cells with and without rotenone treatment. All analyses of small and large EV number were carried out using the emmeans package in R on a mixed effect model of the form: $\text{EV number} \sim \text{Rotenone Concentration} * \text{Genotype} + (1|\text{batch})$

Interestingly, WT and DJ-1 KO react differently to a range of rotenone concentrations regarding the amount of detected EV. For small EV (<200 nm), EV from WT cells were significantly different from control at treatments of 5 ($p = 0.006$) and 10 ($p = 0.003$) nM rotenone, increasing by factors of 2.25 and 2.36 respectively (Figure 5.1). However, in DJ-1 KO, small EV significantly increased at treatments of 10 ($p < 0.0001$) and 25 ($p = 0.006$) nM rotenone by factors of 3.48 and 2.19 respectively (Figure 5.1). Furthermore at 5 nM rotenone significantly higher numbers of small EV were detected in WT cells, 1.52 times higher than the amount detected in DJ-1 KO EV ($p = 0.05$) (Figure 5.1), whereas this effect is flipped at 10 nM rotenone treatment with 1.56 times more small EV being detected from DJ-1 KO cells compared to WT (Figure 5.1).

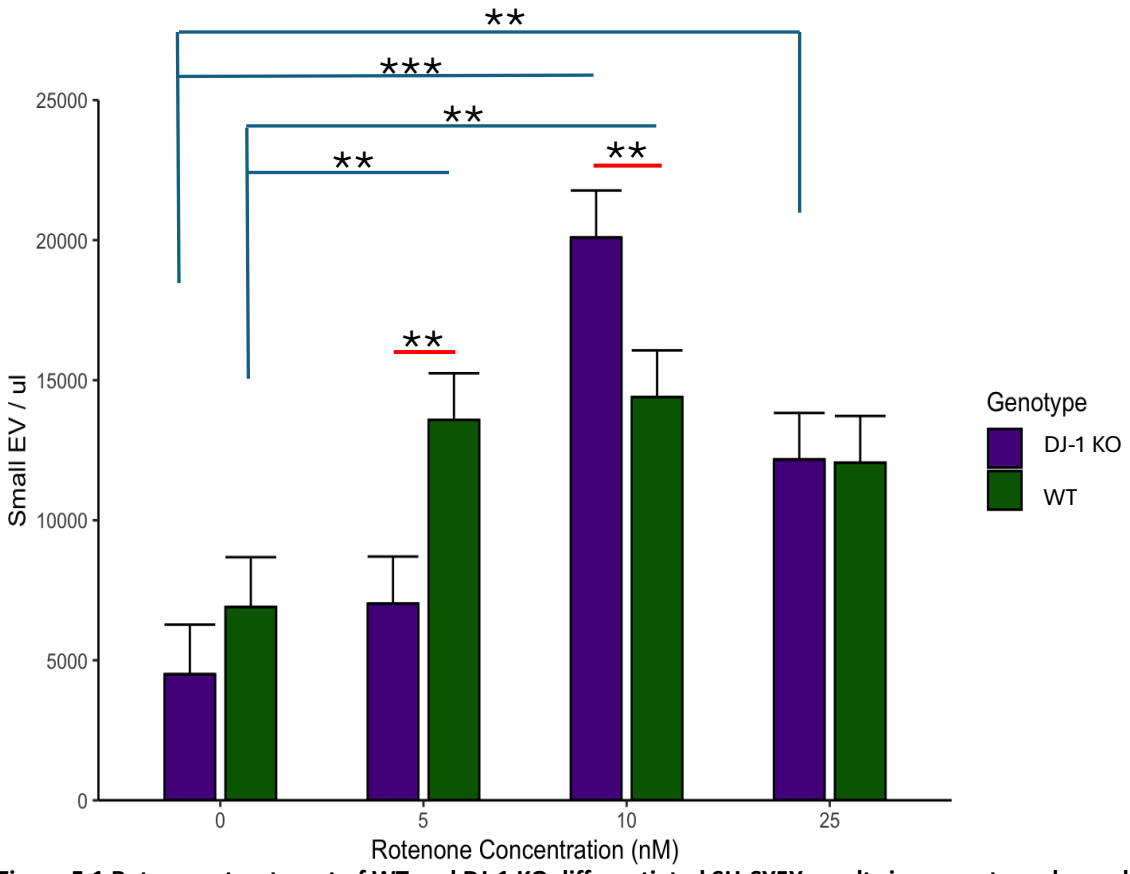

Figure 5.1 Rotenone treatment of WT and DJ-1 KO differentiated SH-SY5Y results in a genotype dependent increase in recovered small (<200 nm diameter) EV. Column chart representing the amount of small EV per ul of media detected by flow cytometry from differentiated WT and DJ-1 KO SH-SY5Y cells with or without various rotenone treatments. Column height = least square mean calculated by the emmeans R package. Error bars = standard error. Genotypes are represented by the colour of the columns with Green = WT and Purple = DJ-1 KO. Significant differences between concentrations represented by blue bars and differences between genotypes by red. "*…" denote p value thresholds; with "*" equaling $p < 0.05$, "**" $p < 0.01$, and "***" $p < 0.001$. EV detected on Cytoflex S system. EV size was assessed by violet-light side scatter. EV events were separated from noise by the fluorescence of Bodipy-FL-SE staining.

As was previously observed in control conditions, the proportion of the EV population designated as large (> 200 nm diameter) is substantially smaller than the small population (Figure 5.2). The general trend in large EV number as a response to rotenone treatment of cells also matched the one observed for the small EV, except for the increased similarity in large EV between genotypes under control conditions compared to small EVcells (Figure 5.2). However, while the trend is visible, due to the increased variation in the number of large EV per μl in each condition there are so significant differences in large EV as a response to rotenone treatment of source cells (Figure 5.2).

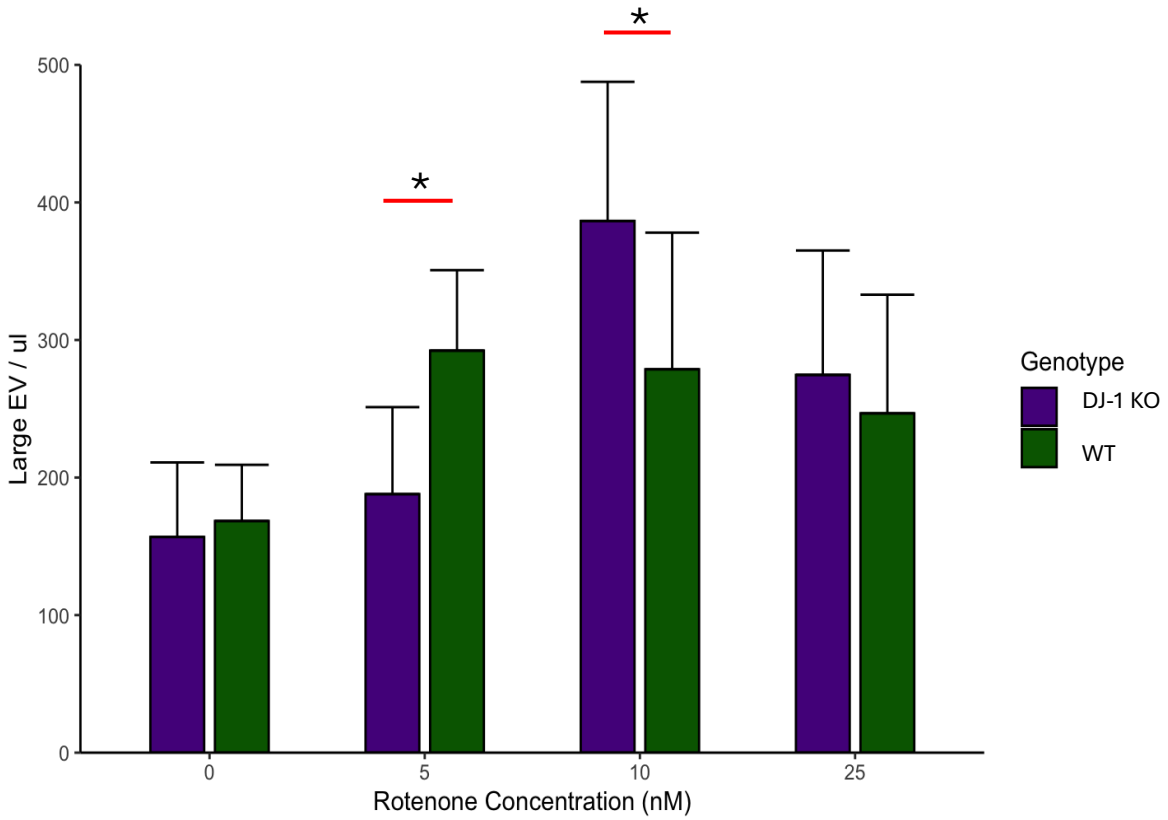

Figure 5.2 Rotenone treatment of WT and DJ-1 KO differentiated SH-SY5Y results in an increase in large EV recoverable from DJ-1 KO. Column chart representing the amount of large EV per ul of media detected by flow cytometry from differentiated WT and DJ-1 KO SH-SY5Y cells with or without various rotenone treatments. Column height = least square mean calculated by the emmeans R package. Error bars = standard error. Genotypes are represented by the colour of the columns with Green = WT and Purple = DJ-1 KO. Significant differences between genotypes by red bars. "*" denotes a p value below the threshold of 0.05. EV detected on Cytoflex S system. EV size was assessed by violet-light side scatter. EV events were separated from noise by the fluorescence of Bodipy-FL-SE staining.

However, differences between the genotypes were still present similarly to the small EV data. At 5 nM rotenone treatment the number of large EV detected was 1.55 times higher from WT cells ($p = 0.0045$) (Figure 5.2). Whereas, at 10 nM rotenone treatment the number of detected EV is 1.39 times higher from DJ-1 KO cells ($p = 0.043$) (Figure 5.2), matching the observed trend of small EV.

As treatment with 10 nM rotenone was the only concentration to result in significant differences compared to control in both genotypes and between genotypes it became the particular treatment of interest for further experimentation.

5.3.2 Rotenone treatments results in genotype dependent changes in endosome size or count per cell

As with previous investigation into EV number described in this thesis, detection and counting of EV by flow cytometry with the employed experimental design is unable to distinguish between the effect of increased production and decreased uptake or vice versa. Similarly to what showed in previous chapters in healthy conditions, the difference in the size and number of endosomes were then analysed as a response to 10 nM rotenone treatment.

To analyse the size and number of endosomes multiple mixed effect models were compared by AIC to determine the most suitable model for further pairwise analysis (tables 5.1 and 5.2). For endosome count the model "$\mathrm{Count} \sim \mathrm{Genotype} * \mathrm{Toxin} + (1|\mathrm{Genotype} + \mathrm{Toxin}|\mathrm{Batch})$" was the most suitable with a AIC value of -167.31 vs the -169.03 of the baseline model "$\mathrm{Count} \sim \mathrm{Genotype} + \mathrm{Toxin} + (1|\mathrm{Batch})$" (Table 5.1). Additionally, the same model was the most suitable for the analysis of endosome size, with an AIC of -69.076 vs -59.89 of the baseline model (p = 0.014) (Table 5.2).

Following selection of the model "$\mathrm{Count} \sim \mathrm{Genotype} * \mathrm{Toxin} + (1|\mathrm{Genotype} + \mathrm{Toxin}|\mathrm{Batch})$", least squares means were calculated for the size and count data by the emmeans R package. Subsequently pairwise contrasts were calculated and their significance determined using emmeans contrast function. Interestingly differentiated WT and DJ-1 KO cells differ greatly in the response to rotenone when investigating endosome size and count.

Table 5.1 AIC of mixed effect models for selection of suitable model for endosome count analysis. Npar = number of parameters contained in the model (higher = more complex). AIC = Akaike information criterion (measure of model fit to data). df = degrees of freedom (0 = model did not converge i.e unusable). Chisq P = Chi squared p value (determinant of suitable model). Genotype + Toxin + (1|batch) = baseline model all others were compared against. "*" indicates p value below 0.05 denoting model has significantly better fit to data than baseline model.

PREDICTIVE MODEL	NPAR	AIC	DF	CHISQ P
GENOTYPE * TOXIN + (1 + GENOTYPE*TOXIN|BATCH)	15	-160.54	4	0.82
GENOTYPE * TOXIN + (1 + GENOTYPE+TOXIN|BATCH)	11	-167.31	1	0.014 (*)
GENOTYPE * TOXIN + (1 + GENOTYPE|BATCH)	10	-162.97	2	1
GENOTYPE * TOXIN + (1 + TOXIN|BATCH)	8	-172.94	0	Null
GENOTYPE + TOXIN + (1 + GENOTYPE+TOXIN|BATCH)	8	-167.31	1	0.77
GENOTYPE + TOXIN + (1 + GENOTYPE|BATCH)	7	-169.23	0	Null
GENOTYPE + TOXIN + (1 + TOXIN|BATCH)	7	-165.06	2	0.98
GENOTYPE + TOXIN + (1|BATCH)	5	-169.03	NA	Baseline

Table 5.2 AIC of mixed effect models for selection of suitable model for endosome size analysis. Npar = number of parameters contained in the model (higher = more complex). AIC = Akaike information criterion (measure of model fit to data). df = degrees of freedom (0 = model did not converge i.e unusable). Chisq P = Chi squared p value (determinant of suitable model). Genotype + Toxin + (1|batch) = baseline model all others were compared against. "*" indicates p value below 0.05 denoting model has significantly better fit to data than baseline model.

PREDICTIVE MODEL	NPAR	AIC	DF	CHISQ P
GENOTYPE * TOXIN + (1 + GENOTYPE*TOXIN|BATCH)	15	-66.4	4	0.82
GENOTYPE * TOXIN + (1 + GENOTYPE+TOXIN|BATCH)	11	-69.076	1	0.014 (*)
GENOTYPE * TOXIN + (1 + GENOTYPE|BATCH)	10	-59.23	2	1
GENOTYPE * TOXIN + (1 + TOXIN|BATCH)	8	-74.44	0	Null
GENOTYPE + TOXIN + (1 + GENOTYPE+TOXIN|BATCH)	8	-60.581	1	0.77
GENOTYPE + TOXIN + (1 + GENOTYPE|BATCH)	7	-64.88	0	Null
GENOTYPE + TOXIN + (1 + TOXIN|BATCH)	7	-56.12	2	0.99
GENOTYPE + TOXIN + (1|BATCH)	5	-59.89	NA	Baseline

The only significant difference in endosome count per cell detected was between DJ-1 KO cells treated with 10 nM rotenone and respective control (p = 0.038), where in rotenone treated cells the number of endosomes was 87 % of that detected in control (Figure 5.3). On the other hand, the only difference in endosome area was detected between WT cells treated with rotenone and its control (p = 0.006), where the endosomes of toxin treated cells were 91 % of the size of control endosomes (Figure 5.3).

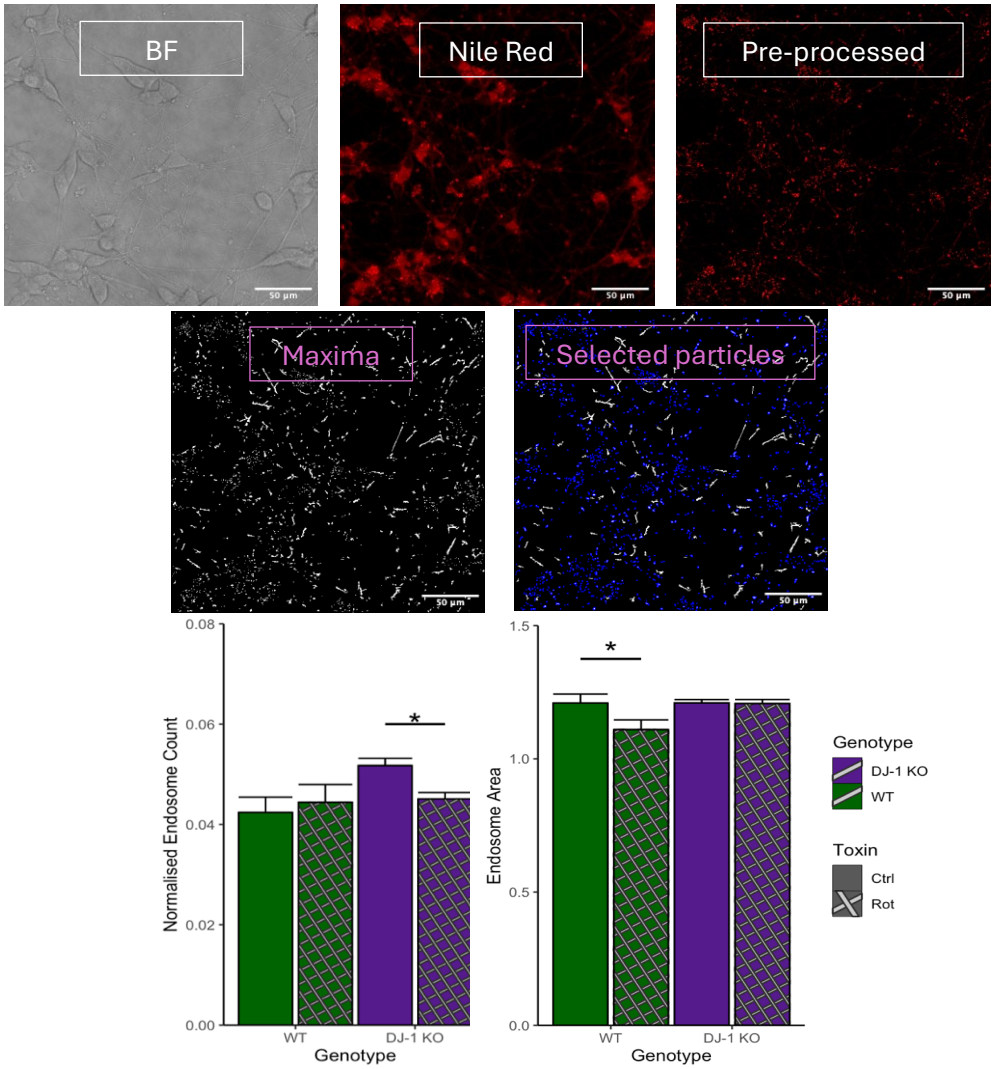

Figure 5.3 Rotenone treatment (10nM) of differentiated WT and DJ-1 KO SH-SY5Y affects endosome size or count in a genotype dependent manner. Images showing the processing and analysis pipeline through which raw images of Nile red staining are passed to generate quantitative data, and columns plots of quantitative data. Images: BF = bright-field (PMT trans); Nile red = raw Nile red staining; Pre-processed = image after pre-processing has been performed; Maxima = output of Find Maxima FIJI command; Selected particles = particles selected and analysed via Analyze Particles FIJI command. Bottom graphs = column charts of normalized endosome count (left) and area (right). Columns = least squares mean. Error bars = standard error. Significant difference indicated by horizontal black bars with "*" above. "*" denotes p value < 0.05.

5.3.3 Rotenone treatment results in genotype dependent changes in mitochondria morphology

The results obtained so far on EV response and endosome number and morphology upon rotenone treatment, required a more reliable readout for the effect of rotenone on cell health .This was particularly relevant to the concentration of 10 nM rotenone used. . To assess the mitochondrial stress the toxin should induce, a double readout of mitochondria stress was devised employing the polarised (healthy) mitochondria selective dye Mitospy™ and immunofluorescent staining of the mitochondrial protein ATP5-alpha, a protein subunit known to undergo changes upon oxidative stress.

From a qualitative standpoint both readouts were a success. Confocal microscopy of both ATP5-alpha and mitospy™ orange revealed strong and clear staining of mitochondrial structures at both 20 and 40 X magnification in control conditions of WT and DJ-1 KO differentiated SH-SY5Y (Figures 5.4/5). Additionally, in control conditions DJ-1 KO cells appeared to have reduced fluorescence intensity of both markers. Similarly, a decrease in fluorescence was observed upon rotenone treatment in both genotypes (Figure 5.4) However, as this was just a qualitative observation, a method of quantifying the observed trend and further mitochondria morphology was desired.

To quantitatively analyse the intensity of mitochondria staining both via ATP5-alpha immunofluorescence and Mitospy™ orange fluorescence an imaging processing method was employed to isolate mitochondria staining for further analysis (Figure 5.6). This method resulted in markedly better distinction between mitochondria and non-mitochondria staining and improved resolution of the physical structure and networks (Figure 5.6). The improved resolution of mitochondria structure and networks appeared to be greatest in images of mitochondria employing Mitospy™ orange, thus network analysis was performed primarily on these images (Figure 5.6).

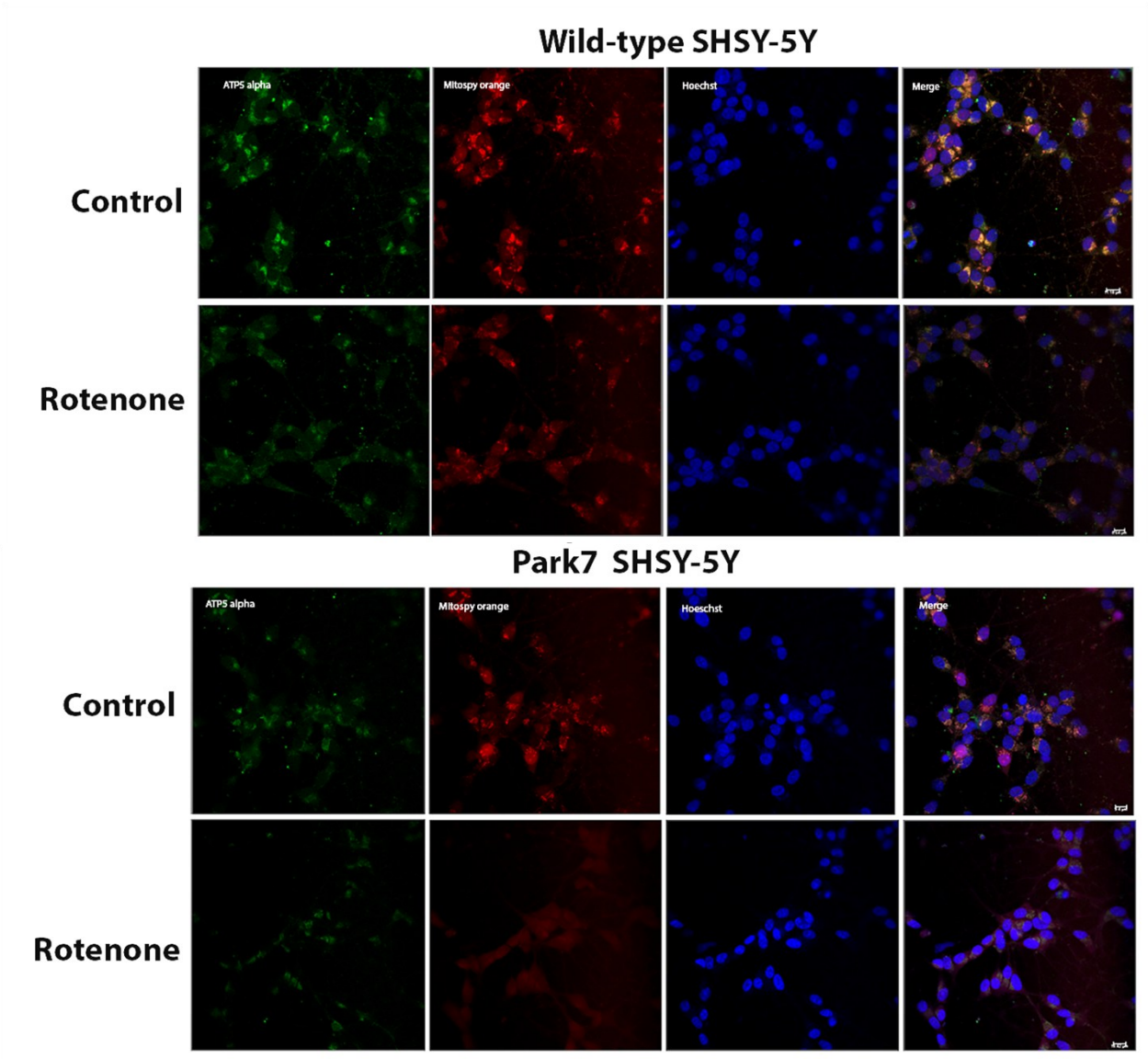

Figure 5.4 Confocal microscopy of labelled mitochondria in differentiated WT and DJ-1 KO SH-SY5Y reveals an effect of 10 nM rotenone treatment. Images of WT and DJ-1 KO differentiated SH-SY5Y nuclei and mitochondria with or without rotenone treatment captured on a Leica SP8 confocal microscope. Top 8 panels = WT, bottom DJ-1 KO. Columns from right to left: ATP5-alpha, Mitospy™ orange, Hoechst 33342, merged. Top row of each set of 8 images = control, and bottom row = 10 nM rotenone treated cells.

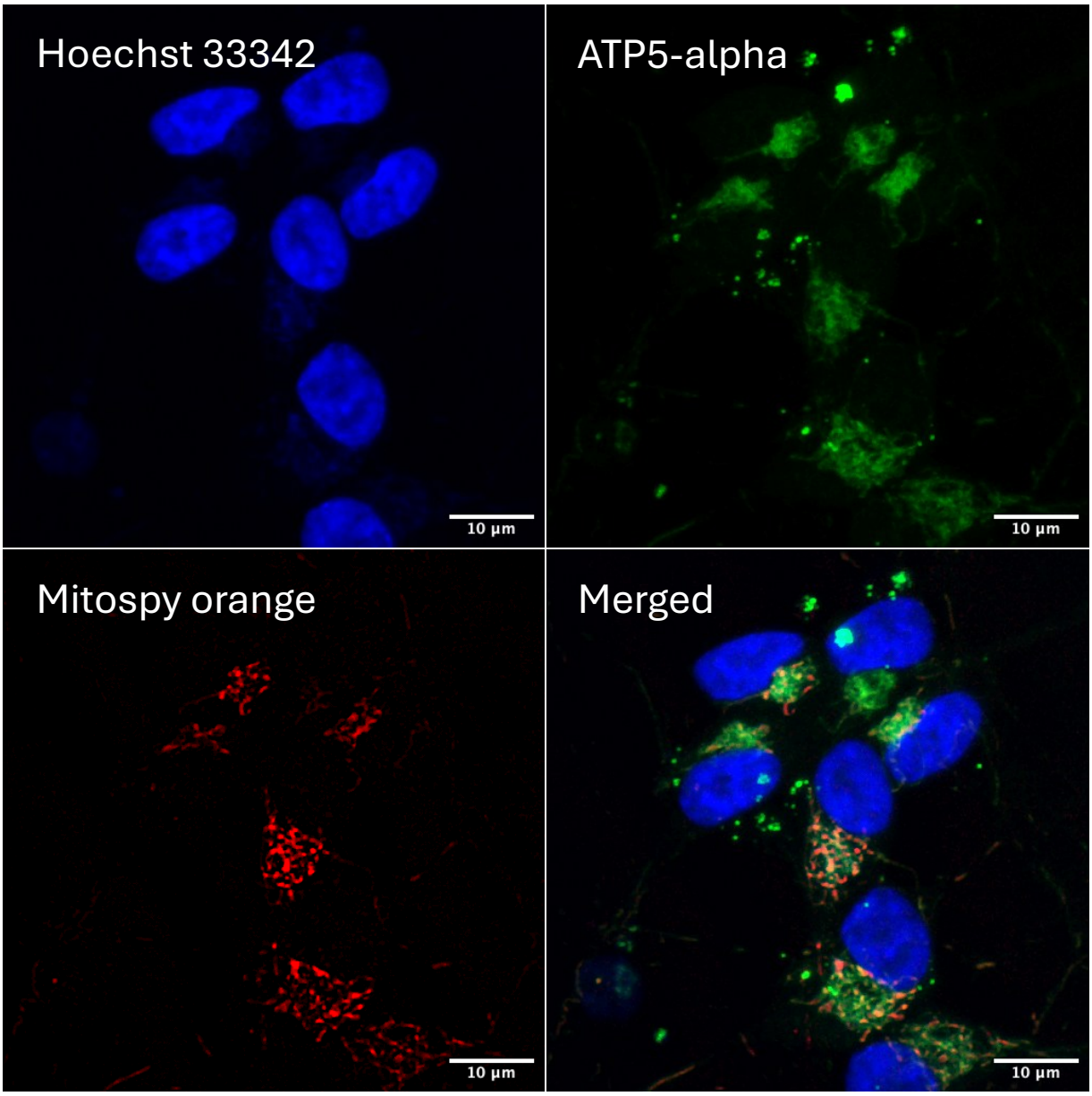

Figure 5.5 Processed max intensity stacks of 3D WT differentiated SH-SY5Y mitochondria images at 40 X magnification under control conditions. 40 X magnification images of WT control mitochondria and nuclei passed through analysis pre-processing pipeline, i.e max intensity stack, background subtraction, unsharp mask, CLAHE contrast enhancement, and median filter. Top left: Nuclei stained with Hoechst 33342. Top right: ATP5-alpha immunofluorescence. Bottom left: Mitospy™ orange staining of mitochondria. Bottom right: Merged image.

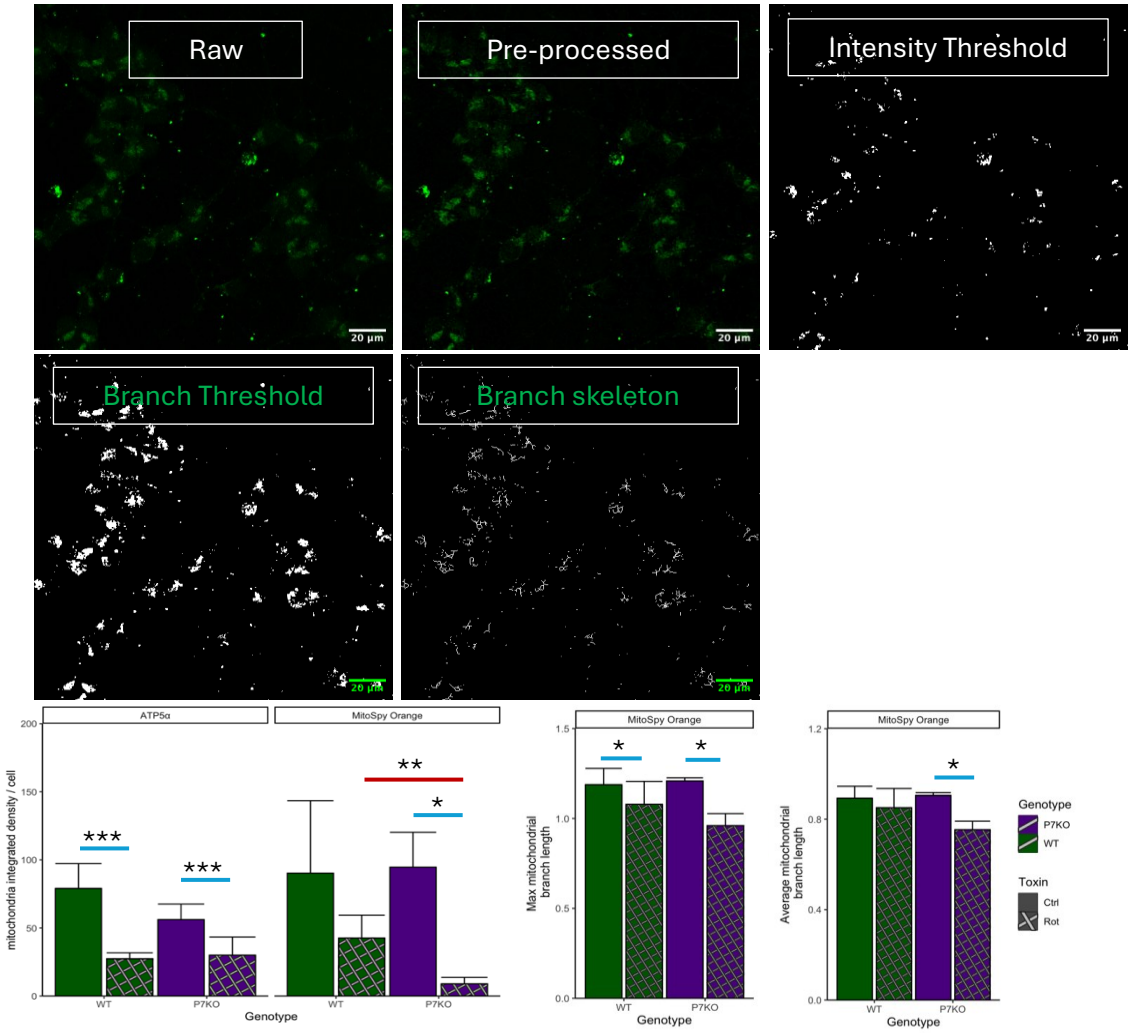

Figure 5.6 Quantification of Mitochondria ATP5-alpha and Mitospy^{TM} orange staining reveals an effect of 10 nM rotenone treatment on mitochondria health. Images representing the analysis pipeline for both ATP5-alpha and Mitospy^{TM} orange staining of differentiated SH-SY5Y mitochondria and graphs of quantified results. Images are as follows: top left = war image as captured on the microscope; top middle = raw image after preprocessing, i.e max intensity stack, background subtraction, unsharp mask, CLAHE contrast enhancement, and median filter; top right = binary threshold of processed image for intensity measurement; bottom left = binary threshold of processed image for branch analysis; bottom middle = Skeleton branch analysis threshold upon which branch analysis was performed. Graphs are as follows: left = integrated density per cell of isolated mitochondria staining by threshold; middle and right = maximum and mean branch length of selected Mitospy^{TM} orange staining skeletons.

Analysis of fluorescence intensity of isolated mitochondria staining by thresholding revealed several significant differences, largely matching the observed trends. Significant differences were determined via the mixed effect models $\text{IntDen per cell} \sim \text{Genotype} + \text{Toxin} + (1|\text{Batch})$ for ATP5- alpha and $\text{IntDen per cell} \sim \text{Genotype} * \text{Toxin} + (1 + \text{Genotype} + \text{Toxin}|\text{Batch})$ for Mitospy^{TM} orange with post

hoc Tukey tests via the emmeans R package. Models were selected as most appropriate for each marker via AIC with Chi squared p values of NA for ATP5-alpha (baseline simplest model = best) and of 0.02 for Mitospy™ orange.

ATP5-alpha immunofluorescence integrated density per cell decreased 2.88-fold in WT and 1.87-fold DJ-1 KO differentiated SH-SY5Y when treated with rotenone (p = 0.0065 for both) (Figure 5.6). Whereas for Mitospy™, integrated density per cell only decreased in DJ-1 KO cells upon rotenone treatment, decreasing 10.53-fold (p = 0. 036) (Figure 5.6). However, with Mitospy™ staining, there is also a 4.74-fold decrease in Integrated density per cell in DJ-1 KO cells compared to WT when treated with rotenone (p = 0.01) (Figure 5.6).

Similarly for mitochondria network branch analysis via Mitospy™ orange staining, the most appropriate models were selected via AIC. For average branch length the best model was the baseline simplest mixed effect model of the form $\text{mean branch length} \sim \text{Genotype} + \text{Toxin} + (1|\text{Batch})$ with no other models providing significantly better fit. For maximum branch length the most appropriate model was of the form $\text{Max branch length} \sim \text{Genotype} * \text{Toxin} + (1 + \text{Genotype}|\text{Batch})$ with a Chi squared p value of 0.043. Several significant differences were detected employing both models and the post hoc Tukey tests via the emmeans R package. Firstly, a decrease was detected in mean branch length upon rotenone treatment in both genotypes, with a fold change of 0.89 in both genotypes (p = 0.89) (Figure 5.6). Additionally, rotenone treatment of DJ-1 KO cells reduced the maximum mitochondria branch length, with a fold change of 0.79 (p = 0.03) (Figure 5.6).

5.3.4 Rotenone treatment induces an increase of ROS in WT and DJ-1 KO differentiated SH-SY5Y in a single experiment (N = 1)

As a possible alternative to the analysis of mitochondria health and morphology as a readout of the effects of rotenone, the level of reactive oxygen species was also assessed. This was achieved by microscopy of WT and DJ-1 KO differentiated SH-SY5Y treated with a fluorescent ROS sensing molecule. While the analysis of only a single replicate was performed due to the success of mitochondrial assessment, treatment with rotenone appeared to increase ROS levels in both genotypes with a stronger increase in DJ-1 KO (Figure 5.7). The percentage of cells stressed increased from 5.8 to 7 % in WT and 5 to 8 % in DJ-1 KO (Figure 5.7).

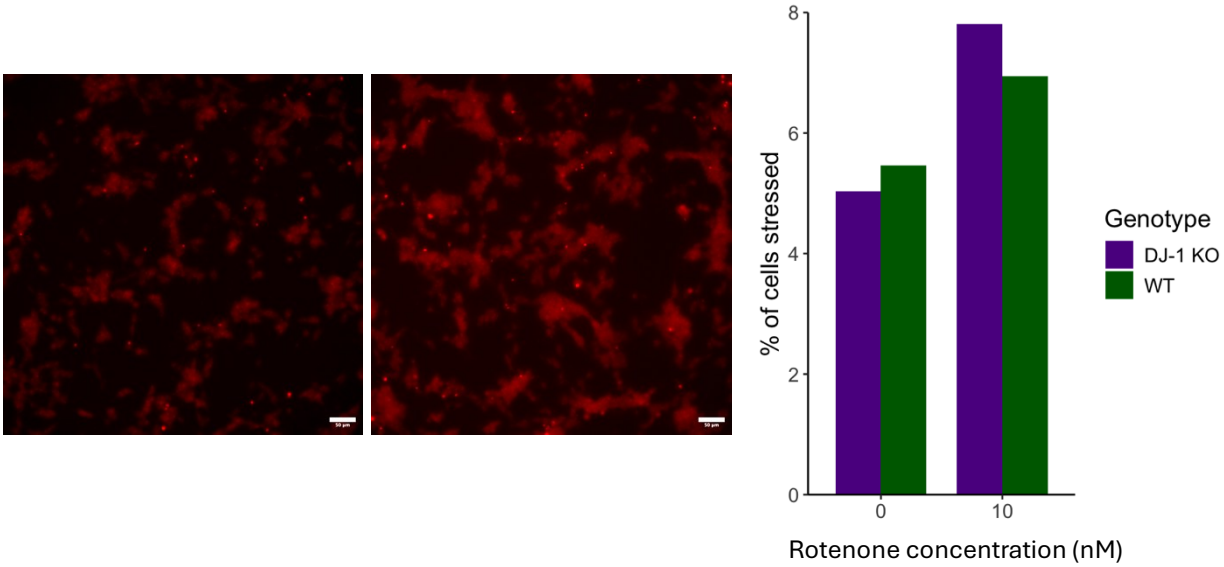

Figure 5.7 nM rotenone induces oxidative stress at a cellular level in differentiated WT and DJ-1 SH-SY5Y. Representative images of ROS detection in WT and DJ-1 differentiated SH-SY5Y, and quantification of the level of ROS / oxidative stress. Cells were determined to be stressed if "relatively" high intensity inclusions were observed. Images were captured on a Cytation 5 microscope system.

5.3.5 Verification of EV population differences in an iPSC derived neuronal system

The results of experimentation on the SH-SY5Y cell line were particularly intriguing, so the effect of rotenone on EV populations was also studied in iPSC-derived neuronal cells, allowing verification of the observations in a cellular model not derived from cancer cell lines.

Firstly, the number of EV was investigated in neural precursor cells derived from human iPSC with a 1bp deletion in the PARK7 gene, B-10, and the isogenic control, both kindly provided by Dr Mark Cookson, NIH. Only one experiment (N = 1) was carried out on these cells as a proof of concept as they are an intermediate to the cells of interest, iPSC derived neurons. In these neural precursor cells, it was observed that in the DJ-1 KO line B-10, detected small EV was 52.8 % compared to their isogenic control when normalised to cell lysate protein mass as a proxy of cell number (Figure 5.8).

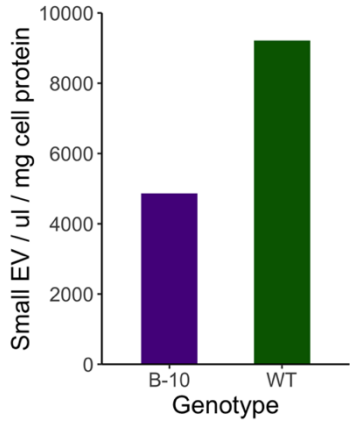

Figure 5.8 Wild-type iPSC derived neural precursors presented with increased small EV / mg protein compared to DJ-1 KO. Graph describing the number of small EV per mg of cell lysate protein detected by flow cytometry on a Cytoflex S system. EV size was assessed by violet-light side scatter. EV events were separated from noise by the fluorescence of Bodipy-FL-SE staining.

Secondly, the number of EV was assessed in neurons derived from B-10 and isogenic control iPSCs. both in control and rotenone treated cells. To this end a suitable rotenone concentration to be used on iPSC-derived neurons was required as differences in cell sensitivity compared to SHSY5Y were expected. B-10 and wild-type ln5 control iPSC-derived neurons were thus treated with varying concentrations of rotenone for 24 hr and the number of necrotic cells was analysed as described in chapter 4 by microscopy of membrane-impermeable fluorescent dye. Of the treatments tested 1 uM rotenone appeared the most suitable both by visual observation of cultures and assessment of necrotic percentage as it had small but minimal effect on the death of B-10 iPSC-derived neurons (Figure 5.9).

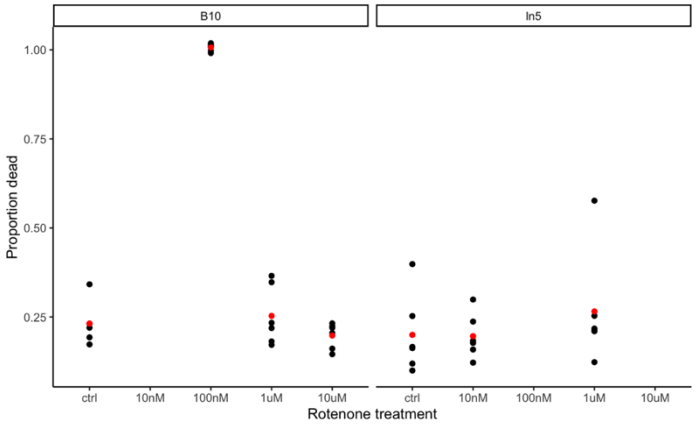

Figure 5.9 1 Rotenone concentration selected as the treatment for iPSC derived neurons. Proportion of cell nuclei that were necrotic as determined by staining with lipid membrane impermeable dye. Each black dot = 1 culture in 1 well of a culture plate. Red dot = mean. Left panel = B-10 derived cells. Right panel = ln5 derived cells

After selection of 1 μM rotenone as the treatment of choice, the number of EV per iPSC derived cortical neuron in untreated/treated B-10 and isogenic control cultures (MAP2 positive, Sox2 negative) was assessed via flow cytometry on a NanoFCM nanoanalyser system. The effect of 1 μM rotenone was observed as an increase of detected EV in isogenic control neurons compared to control, and no increase in the EV of B-10 cells. Specifically, rotenone treatment increased the number of detected EV in isogenic control cultures by a factor of 2.25 from 177 to 399 ($p = 0.013$ t test, Bonferroni corrected) (Figure 5.10). This effect on the isogenic control EV coupled with the lack of effect in B-10 cultures resulted in 185 more EV per cell in rotenone treated control compared to B10 ($p = 0.035$ t test, Bonferroni corrected) (Figure 5.10).

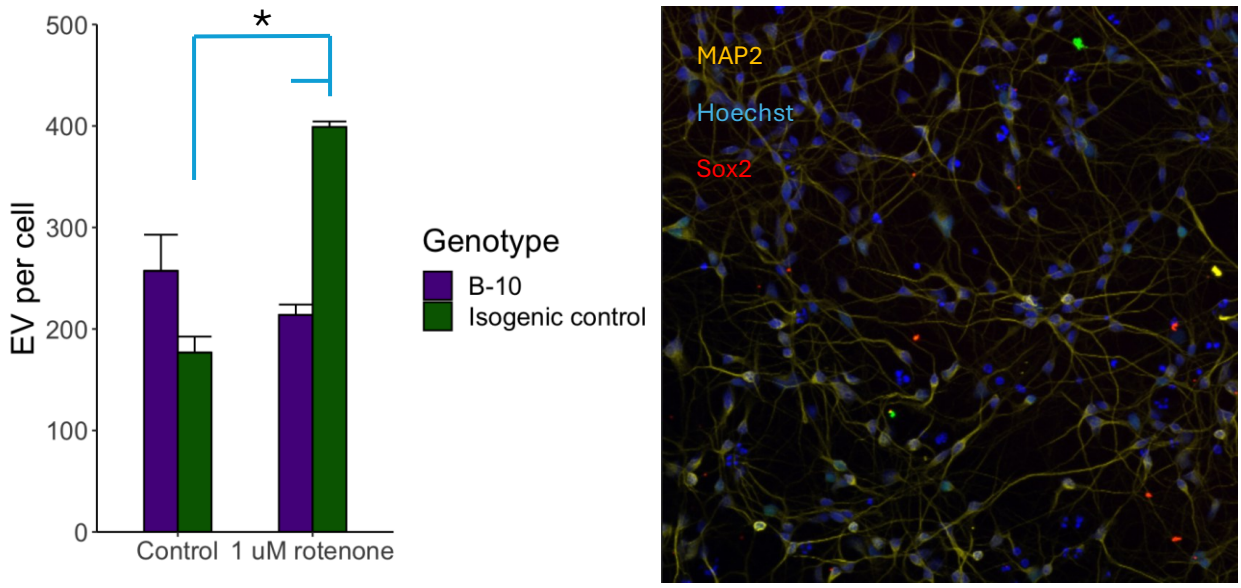

Figure 5.10 Rotenone treatment of iPSC derived neurons reveals genotype linked differences in the EV response. Left: graph of the number of EV per cell detected on a NanoFCM nanoanalyser system. Genotypes identified by colour (purple = B-10, green = isogenic control. Significant difference indicated by blue bars, with degree of significance represented by "*" = p =< 0.05. Right: Image of isogenic-control iPSC-derived glutamatergic neurons, captured of Leica sp8 confocal microscope; with fluorescence labeling of nuclei (Hoechst 33342, blue), MAP2 (immunostaining, yellow), Sox2 (immunostaining, red).

5.4 Discussion

5.4.1 Rotenone treatment affects EV count and endosome count and morphology in a DJ-1 dependent manner

The primary interest of the research project described by this thesis is the link between DJ-1 and EV-mediated intercellular communication. Thus, the principal piece of knowledge that was required was whether EV number/cargo is different between WT and DJ-1 KO cells in an environment of heightened oxidative stress, a situation under which DJ-1 should be active.

The effect of oxidative stress on EV production/uptake

Oxidative stress is a known predictor of detection of increased numbers of EV in a variety of cells (Chiaradia, 2021), such as epithelial RPE-1 (Takasugi, 2017), fibroblasts (Vatsyayan, 2013) HEK293 (Manček-Keber, 2015), WIF-B9 rat hepatocytes (Van Meteren, 2019), and endothelial cells (Vatsyayan, 2013). However, some variation occurs dependent on the chosen inducer of oxidative stress, cell type and whether one investigates specific EV populations only, such as Tissue-factor positive (Chiaradia, 2021). At least in the case of rat hepatocytes, this increase in EV was proven to be linked to oxidative stress: it was observed that incubation of cells with polycyclic aromatic hydrocarbons resulted in a smaller increase in EV when paired with antioxidants than alone (Van Meteren, 2019). Thus, it would not be strange to assume that treatment with rotenone would also increase the amount of EV from differentiated SH-SY5Y cells, as rotenone induces oxidative stress via inhibition of mitochondria complex 1 of the electron transport chain (Heinz, 2017).

The expected increase in EV upon rotenone was in fact observed in both WT and DJ-1 KO differentiated SH-SY5Y when looking specifically at small EV (Figure 5.1). However, what was immediately striking was that DJ-1 KO cells required a higher concentration of rotenone to present with increased small EV than WT cells. Specifically, 10 nM rotenone was the minimum concentration to observe increased small EV counts in DJ-1 KO cells compared to 5 nM for WT. At 10 nM rotenone, DJ-1 KO cells present with increased small EV compared to the relevant control and WT cells at the same concentration. Thus, it is

likely that DJ-1 is not primarily directly involved in EV production or uptake in response to oxidative stress. Instead, the more likely explanation is that DJ-1 is responsible for sensing lower levels of oxidative stress and regulating the response pathways involved. A role that would be somehow supplanted by a separate pathway at the higher concentrations of rotenone allowing for the response in DJ-1 KO cells under this assumption.

Similar to in prior investigations, determining whether increased EV production or decreased EV uptake is occurring when presented with increased EV number is difficult. Further insight into how rotenone can affect EV biogenesis/uptake pathways can be identified by comparing rotenone to Doxorubicin, which potentially shines light onto the answer to this question of production vs uptake. Doxorubicin is a compound used as a chemotherapy drug and known to induce oxidative stress, potentially via the inhibition of mitophagy resulting in accumulation of damaged mitochondria (Bartlett, 2017; Chiaradia, 2021). Alongside this activity it also has the effect of activating p53 (Liu, 2008) in a manner which results in upregulation of multi-vesicular body formation via tumour suppression-activated pathway 6 (TSAP6) (Lespagnol, 2008), a key step in exosome biogenesis (Gurung, 2021). The damage to mitochondria also induces increased cytosolic Ca^{2+}, which induces MVB plasma membrane fusion and membrane blebbing thus promoting EV release (Record, 2018). Thus, doxorubicin results in an increase of MVB formation and their fusion induced exosome release.

Interestingly, rotenone as a toxin has similar activity to Doxorubicin, both increasing free cytosolic Ca^{2+} via mitochondrial damage (Wang, 2005), and activating p53 (Gonçalves, 2011). Whether the activation of p53 in this case presents with the activation of MVB formation via TSAP6 is unknown, especially as the activation of P53 is DNA damage independent in the case of rotenone contrary to that of doxorubicin which induces double strand breaks (Lin, 2018). However, TSAP6 is a well-known direct target of activated p53, so activation of this pathway could be assumed (Passer, 2003). This could explain the observed increases in EV number at 5 and 10 nM treatments in WT and 10 nM in DJ-1 KO cells. However, it still left the question of why DJ-1 KO cells didn't present with increased small EV at 5 nM rotenone treatment in SH-SY5Y and 1 uM treatment in iPSC-derived neurons, contrary to WT. Does DJ-1 interact with the shared pathways of doxorubicin and rotenone which potentially explain the changes in EV number?

What is the role of DJ-1?

While it is clear that the different EV response to rotenone observed in differentiated SH-SY5Y and in iPSC derived neurons was DJ-1 dependent, the precise role of DJ-1 in this pathway is debatable.

DJ-1 is a known interactor and regulator of p53 (Dolgacheva, 2019), a protein implicated in the increase of EV production via regulation of TSAP6 (Passer, 2003; Lespagnol, 2008) and known to be activated via rotenone treatment (Gonçalves, 2011). Rotenone does not directly interact with p53, instead its effects are an indirect response to the toxin's actions (Feng, 2015). The specific known effects on p53 via rotenone treatment include increased p53 transcription, phosphorylation, and nuclear localization (Gonçalves, 2011; Feng, 2015).

DJ-1 modulation of the p53 pathway overlaps substantially with these effects of rotenone treatment (Dolgacheva, 2019). DJ-1 is known to inhibit p53 mediated apoptosis (Bretaud, 2007; Fan, 2008), and overexpression of DJ-1 has been shown to reduce p53 expression (Ottolini, 2013). DJ-1 is also involved in post translational modification of p53, suppressing SUMOylation (Shinbo, 2005), and potentially suppressing acetylation via masking of the binding sites (Fan, 2008). Furthermore, DJ-1 suppresses p53 mediated apoptosis by inhibiting the p53 bax-caspase pathway, and can directly inhibit p53 binding to specific DNA promoter regions (Fan, 2008; Kato, 2013). However, p53 regulation by DJ-1 is DJ-1 cys106 residue oxidation state dependant resulting in a highly complex web of possible outcomes (Kato, 2013). Thus, the most likely role of DJ-1 in the EV release pathway as a response to rotenone is the sensing of the ROS and oxidative stress induced damage and subsequent regulation of p53 activity. This idea was further confirmed by the observation that mitochondrial stress was higher in DJ-1 KO differentiated SH-SY5Y compared to wild-type at 10 nM rotenone, and there is no logic in assuming the same pattern wouldn't have existed at 5 nM, yet no increase in EV occurred in DJ-1 KO.

Furthermore, DJ-1 is a known regulator of autophagy (Liu, 2023). Autophagy is a process in which dysfunctional components of the cell, are degraded by a lysosome dependant pathway (Ichimiya, 2020). Interestingly exosome biogenesis and autophagy are tightly linked, as conditions that impair autophagy promote MVB fusion with the plasma membrane (Hessvik, 2016), whereas those that promote autophagy promote MVB lysosome fusion (Fader, 2007, Biaxauli, 2014). Rotenone has been reported as an inhibitor of autophagic flux, inhibiting the degradation of autophagic vacuoles via the lysosome (Mader, 2012). While not reported on specifically with rotenone, other drugs that block autophagic flux

and inhibit lysosomal degradation such as doxorubicin, bafilomycin A, and chloroquine induce exosome release as expected (Alvarez-Erviti, 2011; Ortega, 2019; Chiaradia, 2021). Thus, EV release may represent a compensatory mechanism for blockades of autophagic flux.

However, regulation of autophagy by DJ-1 seems to be incredibly complex and has been and still is a controversial topic (Liu, 2023). Decreased levels of DJ-1 have been reported to result in an induction of autophagy under conditions of oxidative stress (Thomas, 2011). This effect appears to be dependent on the oxidation state of DJ-1 cys106 and thus on the level of oxidative stress. DJ-1 with cys106-sulphinate (moderate oxidation) has been reported to activate autophagy and cys106-sulphonate (high oxidation) to induce apoptosis (Cao, 2014). Decreased DJ-1 expression also resulted in a decrease in mitochondria membrane potential (Chen, 2021), in agreement with the data obtained in in the work described herein (figure 5.6) However, decreased mitochondria membrane potential due to lower DJ-1 expression was reported to instead impair lysosomal activity and autophagy, contrary to other reports (Chen, 2021). Furthermore, KO of DJ-1 has also been reported to reduce autophagy under conditions of oxidative stress, suggesting that KO of DJ-1 may have different effects (Petrucelli, 2010).

Further evidence for changes in autophagic flux can be seen in the mitochondria network branch data described in fig 5.6. Mitochondria fission/fragmentation results in an increase in discrete smaller mitochondria and promotes mitophagy, autophagy of mitochondria (Adebayo, 2021). Analysis of mitochondria networks found that average branch length decreased in both WT and DJ-1 KO differentiated SH-SY5Y upon treatment with 10 nM rotenone, while maximum branch length decreased in DJ-1 KO cells. Intriguingly, average branch length decreased more in DJ-1 KO, suggesting an increased level of fission that correlates with the level of mitochondria depolarisation observed. These changes may suggest an increase in mitophagy under these conditions (Adebayo, 2021).

The role of DJ-1 in autophagy regulation may explain the changes in small EV that were observed. However, due to the contradictory reports of directionality of effect and apparent dependence on the level of oxidative stress and DJ-1 oxidation (Liu, 2023), further specific study of autophagy under the specific conditions of interest would be required. This could be achieved via the use of pharmacological methods of autophagy and or lysosome inhibition such as the chemical doxorubicin etc discussed previously in this section; particularly in iPSC derived neurons, as the variance in the effect of DJ-1 on autophagy across cell types compels the use of the best possible model system. If autophagy changes are indeed contributing to the observed phenomena of increased EV count upon rotenone treatment,

then it supports the idea that the number of EV is increasing as a means of waste/damaged component removal (Ichimiya, 2020).

Thinking of a wider cellular context, this does not preclude the possibility of a signalling role for DJ-1 involving surrounding cells in the CNS such as astrocytes or microglia, both of which are cell types heavily implicated in Parkinson's disease (Joe, 2018). Thus, for future studies it would be extremely important to clarify how these cells react to increased levels of stress induced EV from neurons.

The data obtained in this study show that the EV response to rotenone is clearly DJ-1 dependant at 5 nM in differentiated SH-SY5Y and 1 uM in iPSC- derived neurons. However, the same cannot be true of the increases in small EV observed at 10 nM rotenone in differentiated DJ-1 KO SH-SY5Y. At this concentration the DJ-1 KO cells showed increased depolarisation and mitochondria network changes as expected due to the lack of the protective functions of DJ-1. Furthermore, an increase in EV compared to the relevant controls was observed proportional to the level of mitochondrial depolarisation and thus level of oxidative stress. While the increase in small EV may be DJ-1 dependant in WT cells, it cannot be in DJ-1 KO suggesting the possibility of either 2 distinct pathways that both result in increased EV upon induction of oxidative stress, or initiation into the same pathway independent of DJ-1.

What is particularly interesting is the genotype dependent changes in endosome morphology. Nile red staining is a crude but effective method of analysing endosome count and size without the nuance of specific populations, as shown by work described in chapter 3. Via this method it was discovered that upon treatment with 10 nM rotenone, WT differentiated SH-SY5Y cells presented with a decrease in average endosome size while showing parity of count with DJ-1 KO. There are 2 real possibilities for what this represents: 1) an increased release of exosomes via fusion of multivesicular bodies with the plasma membrane and 2) reduced uptake of secreted EV.

As MVB are by far the largest type of endosome and the method does not allow for distinguishment of the smaller internal MVB intraluminal vesicles, faster release of exosomes and thus MVB could present as a decrease in size (Huotari, 2011). However, one would expect that this would be coupled with a decrease in endosome counts due to increased secretion which did not happen in WT cells but did in DJ-1 KO. An increase in endocytosis or shift away from MVB formation could also present as a decrease in average size due to an increase in smaller endosomes or decrease in the larger MVBs, but does not explain the increase in EV observed. Due to the mechanics of exosome biogenesis, a decrease in size and count could also both be associated with increased exosome production (Gurung, 2021). It could thus be

assumed that increased exosome production is happening in both genotypes matching the EV data but that other effects on the endo/lysosomal pathways are potentially masking the effects or that the method of analysis is insufficient to elucidate the true effects. Furthermore, the observed DJ-1 dependent changes in endosome count and morphology may be related to the regulation of autophagy by DJ-1 previously described (Liu, 2023). Further stating the importance of understanding the dynamics of exosome production and autophagy.

Unfortunately, the limitations of the method of endosome analysis preclude absolute statements on what is occurring as it was not possible to distinguish different types of endosomes. Thus, it was not possible to identify the effect of rotenone on different endosome populations and pathways. An improved methodology to rectify this issue would likely involve: increasing the magnification to increase spatial resolution; employing membrane dyes with intensity sensitive to pH, as the pH changes throughout the endosomal pathway and in distinct populations (Wang, 2016); or attempting fluorescence lifetime imaging of Nile red if the lifetime of the dye is found to be dependent on endosomal subpopulation, and finally investigating specific markers of autophagy. Simultaneously, investigation of the proteins of the proposed pathway leading from rotenone treatment to increased amounts of EV could shed light on whether it is truly increased production of EV occurring and not reduced uptake, and whether autophagy plays a role.

Ultimately, no matter why the amount of EV changes, this information on its own does not tell the full story. To truly understand what effects an increase or decrease in the number of EV has, cargo and functional analysis of how EV affect other cells is required.

Chapter 6: Proteomics analysis of EV from WT and DJ-1 KO differentiated SH-SY5Y reveals distinct cargo protein signatures and changes in proteins of interest.

6.1 Introduction

In the previous chapter, investigations into the effect of oxidative stress via rotenone treatment on EV production/uptake were reported and discussed. Understanding whether there is increased demand for the function of EV under conditions of oxidative stress, as measured by their number, is interesting on its own. However, to truly understand the role of EV and their link to DJ-1, knowledge of the functional molecule carried by EV and the actual effects of EV on distinct cell types must be obtained.

Oxidative stress through a variety of inducing chemicals and across a variety of cell types and lines has been reported to alter EV production (Chiaradia, 2021). However, further to this effect, changes in EV cargo have also been described under similar conditions of oxidative stress (Benedikter, 2019). Generally, oxidative stress can affect EV cargo in 3 ways: addition or removal of specific cargo such as anti-oxidants; altering the concentration of cargo, or chemical modification of cargo such as oxidative modification of proteins or other indirect post-translational modifications (Chiaradia, 2021). All 3 of these potential changes could influence the signalling output of EV by altering their targeting or effects. Furthermore, these changes are not limited to the proteome and affect lipids, nucleic acid and other metabolite content (Corsello, 2019). However, for the purposes of the research described herein, only the changes in proteomics are of interest.

Research into the effect of oxidative stress has reported in EV from CSE-treated airway epithelial cells that 33 % of the proteome was differentially expressed (Benedikter, 2019). Within the differential proteins, enrichment of biological processes related to intercellular communication, immune system regulation and platelet activity / coagulation was observed (Benedikter, 2019), supporting the role of oxidative stress in inducing EV release with specific purpose rather than simple waste removal. Though due to the heterogeneity of EV populations, this does not preclude the possibility of both signaling and waste removal (Sharma, 2020), or even signaling via waste removal. Indeed, damaged molecules and cellular components are incredibly important signals in immune system regulation (Weismann, 2012).

Within this chapter are reported the investigations performed to understand the protein cargo of EV from WT differentiated SH-SY5Y under oxidative stress conditions, and how said cargo changes without the presence of DJ-1. To this aim, mass spectrometry was employed to investigate changes in the proteome signature, generating a picture of the changes that may be occurring and allowing for the identification of specific proteins of interest that can be targeted for further research.

6.2 Methodology

6.2.1 Cell source and growth conditions

The SH-SY5Y cells employed and their culture conditions throughout the works described in this chapter are identical to those described in detail in sections 2:2:1 and 2:2:2.

6.2.2 SH-SY5Y differentiation

The differentiation method employed throughout the works described herein this chapter is identical to that described in detail in section 2:2:3.

6.2.3 Toxin prep for SH-SY5Y treatments

Toxin preparation and treatments were performed identically to those methods described in chapter 4 section 4.2.3.

6.2.4 EV sample preparation and isolation

EV were sourced from differentiated WT and DJ-1 KO SH-SY5Y grown in T-75 flasks seeded at a density of 800,000 cells per flask. 3 EV samples per condition were prepared by pooling the growth media of 5 T-75 flasks per sample, spread equally across 3 weeks.

EV were isolated via the following method from. Growth media was harvested and cells were spun down at 300 x g for 5 min at 4 °C. Supernatant was collected and debris spun down at 2000 x g for 20 min at

4 °C. Supernatant was harvested and concentrated to 500 ml via centrifugation in Amicon 30 K centrifugal filter units at 3260 x g at 4 °C. EV were then purified via IZON qEV size exclusion chromatography columns according to the manufacturer's instructions. Pure EV samples were then concentrated again via centrifugation in Amicon 30 K centrifugal filter units at 3260 x g at 4 °C from 3 ml to ~ 100 ml and placed on ice.

6.2.5 Preparation of EV protein cargo samples

EV samples were lysed at 65 °C in 1 X Laemmli SDS sample buffer (Alfa Aesar, J61337) for 6 min. SDS-PAGE was subsequently performed on samples in running buffer (30.3 g Tris-base, 144.4 g glycine and 10 g SDS in 1 L H_2O) with gel compositions as follows: running gel = 3.87 ml H_2O 2.12 ml Acrylamide, 2.16 ml 1.5 M Tris (pH 8.8), 83.3 µl 10 % SDS, 83.3 µl 10 % APS, 8.3 µl TEMED; stacking gel = 2.62 ml H_2O, 0.416 ml Acrylamide, 1.07 ml 0.5 M Tris (pH 6.8), 41.6 µl 10 % SDS, 41.6 µl 10 % APS, 4.16 µl TEMED. Upon completion, the gel was stained with Coomassie blue G-250 (0.5% w/v in 40% aqueous methanol and 10% glacial acetic acid) overnight. The gel was then rinsed with H_2O until the majority of free Coomassie blue was removed, then destained with destaining solution until the majority of gel bound Coomassie blue was removed and only protein bound remained. Each lane of the gel was cut into 5 sections based on protein mass ranges, and each section of gel was further cut into ~ equal sized small pieces to promote future access of protease.

Gel pieces were further destained via the following method. Expand gel pieces with 6 mM ABC (H_2O solvent) for 30 min on a hot shaker set to 40 °C. 100 % MeOH was added to a final concentration of 60 % 6 mM ABC and 40 % MeOH and samples were sonicated in a sonic cleaner for 15 min. Solvent was removed and sonication repeated in 50:50 MeOH:H_2O twice. Solvent was removed and 100 % MeOH was added and vortexed for 30 sec, repeating 3 times. Solvent was then replaced with 6mM ABC in H_2O.

Destaining of gel pieces was followed by drying via the following steps. Solvent was removed and replaced with 60:40 6mM ABC:MeOH and shook for 15 min. Solvent was removed and the following step was repeated 3 times: pieces were shrunk with ACN while shaking for 2 min, then ACN was replaced with 6 mM ABC and shook for 2 min. Solvent was removed and samples dried in a speed vac. In gel digestion was subsequently performed with trypsin (200 µg / 40 µl 6 mM ABC) overnight. Gel pieces were centrifuged at 10000 x g for 5 min and supernatant harvested. Gel pieces were then treated with 2 %: 1 % CAN:Hac in H_2O, and shook for 30 min. Gel pieces were centrifuged at 10000 x g for 30 min and

supernatant harvested and pooled with previous harvest. Harvested supernatant samples containing digested proteins were dried using a speed vac and frozen at -20 °C overnight, then resuspended in 2 %: 1 % CAN:Hac in H_2O before analysis on a mass spectrometry instrument.

6.2.6 Mass spectrometry analysis and data processing.

For LC-MS analysis, the dried samples were reconstituted in 30 µL of 1% aqueous acetonitrile with 0.1% formic acid for liquid chromatography-tandem mass spectrometry (LC-MS/MS). Peptide samples (5 µL) were injected onto a trap column (nanoEase M/Z Symmetry C18 Trap Column, 100Å, 5 µm, 180 µm × 20 mm, Waters, UK) on an nUPLC system (Acquity M Class, Waters, UK) operating in single-pump trapping mode at a flow rate of 5 µL/min using eluent B (acetonitrile in aqueous 0.1% formic acid). Peptides were separated at a flow rate of 0.5 µL/min on an analytical column (nanoEase M/Z ACQUITY UPLC BEH C18, 1.7 µm, 100 Å, 75 µm × 150 mm, Waters, UK) with the following gradient of eluent B: 0–45 minutes, 1–45% B; 45–49 minutes, 45–90% B; 49–52 minutes, 90% B; 52–67 minutes, 1% B. Peptide electrospray was formed at 2200 V using a PicoTip™ emitter (New Objective, Germany), and charged peptides were analyzed on a 5600 TripleTOF mass spectrometer (AB Sciex, Framingham, MA, USA) in information-dependent acquisition mode. The 10 most intense ions from each high-resolution MS survey scan were selected for high-sensitivity MS/MS, with a 30-second exclusion window for previously acquired peptide ions. The mass spectrometer was calibrated before acquisition to ensure high mass accuracy at both MS and MS/MS levels.

Relative protein quantification was performed using Progenesis QI for proteomics software (version 4.1, Nonlinear Dynamics, Newcastle, UK). Each sample sub-group (within the same molecular weight range) was aligned on a retention time vs *m*/*z* plot, ensuring the alignment of identical peptides across different samples. Data was further in-silico normalized (based on the peptide distribution) to allow for the high-accuracy relative quantification. All sub-groups were combined using a multi-fraction setup to build up

representative samples. Relative quantification included only protein-unique peptides. Merged data were exported as an .mgf file to Mascot search engine (Mascot Daemon platform, ver 2.5) which was searched against the curated SwissProt database with the following parameters: mass tolerance of 0.1 Da for MS and 0.5 Da for MS/MS spectra, a maximum of two trypsin missed-cleavages, *Homo Sapiens* taxonomy, and variable modifications of methionine oxidation and cysteine carbamidomethylation. Mascot searches were filtered to include peptides identified with minimum of 95% confidence including only scores with confirmed peptide identity (usually 31 or higher). Identified peptide list was exported back to Progenesis for the protein relative quantification between the samples. All keratins were treated as contamination and were excluded from the analysis.

6.2.7 Bioinformatic analysis of the EV proteome

Unsupported learning: data clustering methods

Principal component analysis was carried out on EV samples using their protein quantity signatures to form the principal components via the R programming language.

Kmeans clustering was carried out via the package ClusterR in the R programming language. The mini batch kmeans algorithm was employed with a kmeans ++ initialiser. Optimal centroids were decided by running kmeans algorithms with increasing cluster numbers until substantial diminishing returns in the decreasing “sum of squares” was observed (elbow method).

GO term analysis

GO term enrichment and fold change compared to the uniprot total Homo sapiens dataset and between analysed conditions was analysed via the Funrich software (Pathan, 2015.).

Pathway analysis

Protein interaction and pathway analysis were performed via String-db. Clustering of the protein interaction network was performed via MCL algorithm with an inflation parameter of 3 (Szklarczyk D, 2019.). Functional GO term enrichment was performed per protein interaction network cluster by string-db.

Protein candidate identification

Protein candidates of interest for further research were identified via multiple methods: 1) manual searching of significantly differently expressed proteins from the proteomic dataset for proteins known to be involved in pathways of interest; 2) identification of significantly differently expressed proteins associated with significantly enriched GO terms of interest; and 3) identification of significantly differently expressed proteins involved in pathways of interest picked out via string-db pathway analysis (Szklarczyk D, 2019.).

6.2.8 Protein candidate analysis

Immunostaining

WT and DJ-1 KO SH-SY5Y were seeded at a density of 20,000 cells on UV sterilized coverslips, and grown and differentiated as previously described. Differentiated cells were either treated with 10 nM rotenone of 0.1 % DMSO as solvent control for 24 hrs.

Cells were then fixed with 4 % paraformaldehyde for 20 min, followed by 1 quick wash and 3 5-minute washes with PBS. Fixed cells were blocked for 30 min at room temp on a rocking table in blocking buffer (1 % w/w BSA (Sigma-Aldrich, A3059), 0.2 % v/v Triton™ (Sigma-Aldrich, X-100), in PBS (Calcium and magnesium negative; Gibco, 20012019)). Cells were then treated with either 1:100 anti-Rab7 antibody (Rabbit mono; Cell Signalling, 9367) and 1:200 anti-EEA1 antibody (Mouse mono; BD transduction, 610457), 10 μg/ml anti-synaptotagmin-11 (Mouse mono; Novus Biologicals, H00023208-M03) and 1:100 anti-RUVBL2 (Rabbit poly; Invitrogen, PA5-29871) , or 1:100 anti-ZNF451 (Rabbit poly; Proteintech, 25228-1-AP) primary antibodies in blocking buffer overnight at 4 °C. After 3 5-min washes with PBS, cell

nuclei were stained with Hoechst 33342 (Life Technologies, H3570) at a dilution of 1:2000 in PBS for 5 min, followed by secondary antibody staining with Alexa-488-conjugated goat anti-mouse (Goat mono; Thermo fisher, A11001) or Alexa-647-conjugated goat anti-rabbit (Goat mono; Thermo fisher, A11034) in blocking buffer for 1 hr at room temp, then washed with PBS for 5 min 3 times. Stained coverslips were then mounted with Mowiol on glass microscope slides. Mounted cells were then imaged on a Leica SP8 confocal microscope employing DAPI, Alexa 488 and Alexa 647 dye assistant settings.

Western blotting

Protein candidates were analysed via western blotting in both the EV samples employed in the mass spectrometry analysis described above and in the differentiated SH-SY5Y cells themselves.

EV preparation

EV were lysed and prepared for SDS-PAGE as described above.

Cell preparation

WT and DJ-1 KO cells were seeded at a density of 100,000 cells in Corning 6-well culture plates coated with laminin as previously described. Half of the cell cultures per genotype were treated with rotenone and half with 0.1 % DMSO as solvent control for 24 hrs. Culture medium was aspirated and cells washed with PBS, followed by treatment with Lysis buffer (20 mM Trizma® Acetate; 0.27 M sucrose; 1 mM EDTA; 1 mM EGTA; 50 mM NaF; 5 mM Sodium pyrophosphate decahydrate; 1 mM Sodium orthovanadate; 10 mM beta-sodium glycerophosphate; 1 mM DTT; 1 % Triton x-100; 1X Cocktail Roche) and detachment of cells via cell scraper. Lysate samples were then spun down at 2000 x g for 20 min at 4 degrees C and stored at -80 °C.

SDS-PAGE and western blotting

β-mercaptoethanol was added to 4X loading buffer (62.5 mM Tris-HCL pH 6.8, 2% w/w Sodium-dodecyl-sulphate, 0.1 % w/w Bromophenol blue, 10 % w/w Glycerol) at a final concentration of 9 % v/v. Protein samples we diluted in lysis buffer to equal volumes containing 10 μg protein and placed on ice. 4X

loading buffer was added to each sample in such volume to be diluted to 1X in the final sample volume. Samples were then heated in a heating block at 95 °C for 6 min. Samples were loaded at a volume of 12 μl containing 10 μg protein into Biorad mini TGX 4:20 gradient stain free gels with Tris-Glycine-SDS running buffer (pH 8.3). Precision plus protein™ standards (Biorad, 161-0374) were employed as molecular weight markers at 6 μl volume. Any Empty wells were filled with 75 % lysis buffer and 25 % complete 4X loading buffer with β-mercaptoethanol. SDS-PAGE was carried out in a mini-Protean vertical chamber at constant 100 V for 90 min. Total protein load was visualized via activation of the stain free gel protein stains via UV light on a Biorad Chemidoc system.

Proteins were then transferred to nitrocellulose membranes by using a Trans-blot Turbo Transfer System (Biorad, #1604150). After which the membranes were treated with Biorad EveryBlot blocking buffer™ for 30 min. After blocking Membranes were washed 3 times for 5 min with TBS-T followed by primary antibody incubation on a rocking table overnight in Biorad EveryBlot™ blocking Buffer (Biorad, 12010020) at 4 °C. Protein candidate primary antibodies were as follows: 1:100 anti-RUBVL2 (Rabbit poly; Invitrogen, PA5-29871), or 1:100 anti-ZNF451 (Rabbit poly; Proteintech, 25228-1-AP). Loading controls, their antibodies and dilutions were as follows: GAPDH (mouse mono; Santa Cruz sc-265062; 1:500 dilution. Membranes were then washed 3 times for 5 min with TBS-T, before treatment for 1 hr at room temp with a 1:10000 dilution of horseradish-peroxidase-conjugated secondary goat anti-mouse igG (Vector Laboratories, P-2000-1) or goat anti-rabbit igG (Vector laboratories, P-1000-1) antibodies. Peroxidase activity was visualized via WestDura substrate treatment for 2 minutes. Imagining took place on a Biorad Chemidoc system.

Quantification of protein load was performed in ImageJ (FIJI).

6.3 Results

6.3.1 Analysis of the total Mass spectrometry proteomics dataset reveals distinct protein signatures in EV from WT and DJ-1 KO SH-SY5Y

Analysis of the mass spectrometry outputs via progenesis QI of the EV proteome from WT and DJ-1 KO cells successfully identified 574 distinct proteins.

The first job that needed to be completed was the qualitative analysis of the entire identified EV proteome. Specifically, the analysis of the enriched "cellular compartment" GO terms, which allowed for verification that the identified set was truly of the EV. Previous investigations into EV purification using the methods employed herein were described in chapter 3 and as such confidence in EV purity was high, but verifying this fact via another method provided greater strength to our results.

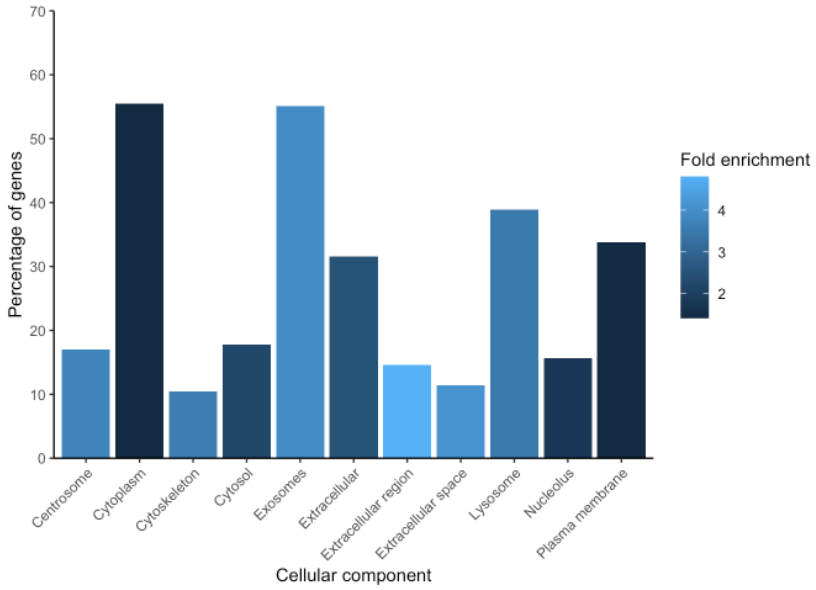

Figure 6.1 Cellular component GO term enrichment analysis of all detected proteins supports isolation and analysis of pure EV. Fold enrichment of cellular component terms in the total identified protein set. Y axis = percentage of genes i.e proteins in the total protein set that possess the associated term. Colour gradient = fold enrichment compared to Uniprot background human protein dataset.

Strikingly, within the significantly enriched terms ($P < 0.05$, Bonferroni adjusted), the “Exosomes” cellular compartment GO term was the joint most common term in the total dataset along with “Cytoplasm” at 55 % of proteins (Fig 6.1). However, the “Exosomes” term showed a substantially higher enrichment compared to the background dataset than cytoplasm, with a fold enrichment of 3.9 vs 1.4 (Fig 6.1). Furthermore, other significantly enriched terms linked to EV were present, including “Extracellular”, “Extracellular region”, “Extracellular space”, “Plasma membrane”, and “Lysosome” with fold enrichments of 2.5, 4.8, 4.1, 1.4, and 3.5 respectively (Fig 6.1).

The second goal was to determine whether EV from WT and DJ-1 KO cells presented distinct protein signatures. This was achieved via a principal components analysis (PCA) where each protein quantity in each sample contributed to the principal components. The EV samples of WT and DJ-1 KO cells separated into distinct groups primarily along PC1 with a standard deviation of 79877.6 and to a lesser extent PC2 with a standard deviation 9143.2 (Fig 6.2). Furthermore, between the EV of WT and DJ-1 KO, of the total 574 identified proteins, 116 or 20.2 % possessed significantly different quantities ($P < 0.05$) (Fig 6.2). Of these 116 significantly different proteins, 50 were overexpressed in DJ-1 KO and 66 in WT (Fig 6.2)

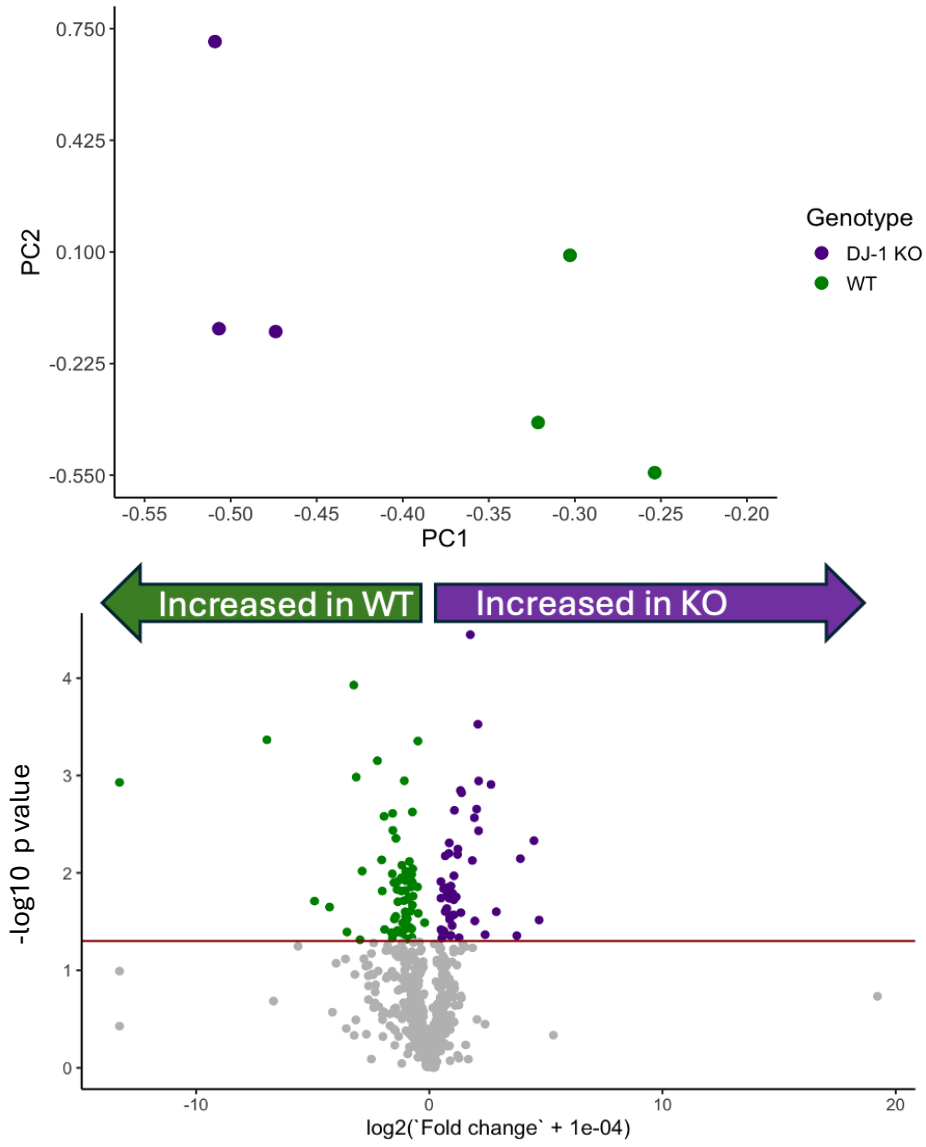

Figure 6.2 Mass spectrometry of EV from WT and DJ-1 KO differentiated SH-SY5Y treated with 10 nM rotenone reveals distinct protein profiles. Top graph: grouping of EV samples via principal components analysis of the total identified protein dataset for WT and DJ-1 KO EV; WT samples in green and DJ-1 KO in purple; data input = protein quantities. Bottom graph: volcano plot of protein fold changes between in DJ-1 KO compared to WT EV; log2 fold change +0.0001 (+ 0.0001 removes errors for proteins with quantity of 0 in DJ-1 KO) on x axis and -log10 p value on y axis; red line = p value threshold, proteins above line have p value < 0.05, thus are significantly different.

Analysis of significantly different proteins

To analyse the functional nature of the observed changes, GO term analysis was performed on the whole significantly different protein dataset. Specifically, rather than investigating enrichment of terms vs the Uniprot background dataset as described above, the change of terms between DJ-1 KO and WT EV was investigated.

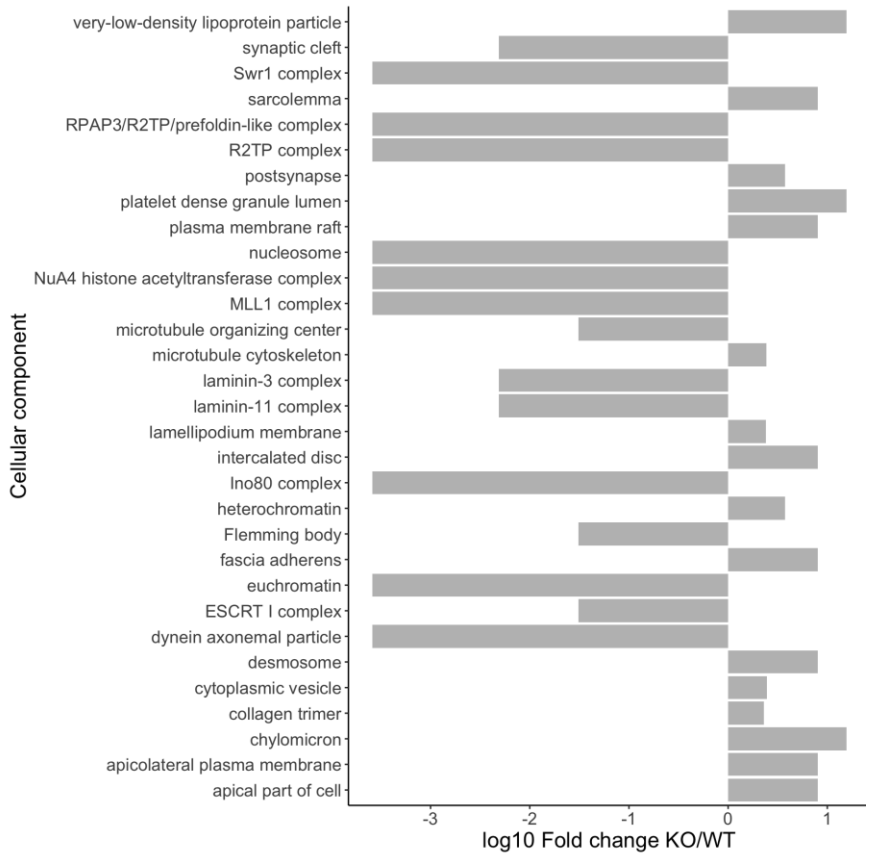

Figure 6.3 Wholistic cellular component GO term enrichment analysis of proteins in DJ-1 KO vs WT. Analysis of cellular component GO term change between DJ-1 KO and WT performed in funrich. Terms with a log10 fold change above 1 are enriched in DJ-1 KO compared to WT and those with a value below 1 depleted in DJ-1 KO. Graph shows top 30 changes in either direction.

Looking at the biological processes (Fig. 6.4) an immediate standout is the plethora of DNA related terms in the top changed terms. The majority of these terms are consequence of the standout protein RUVBL2, the only protein which is significantly different and completely non-present in all DJ-1 KO EV samples.

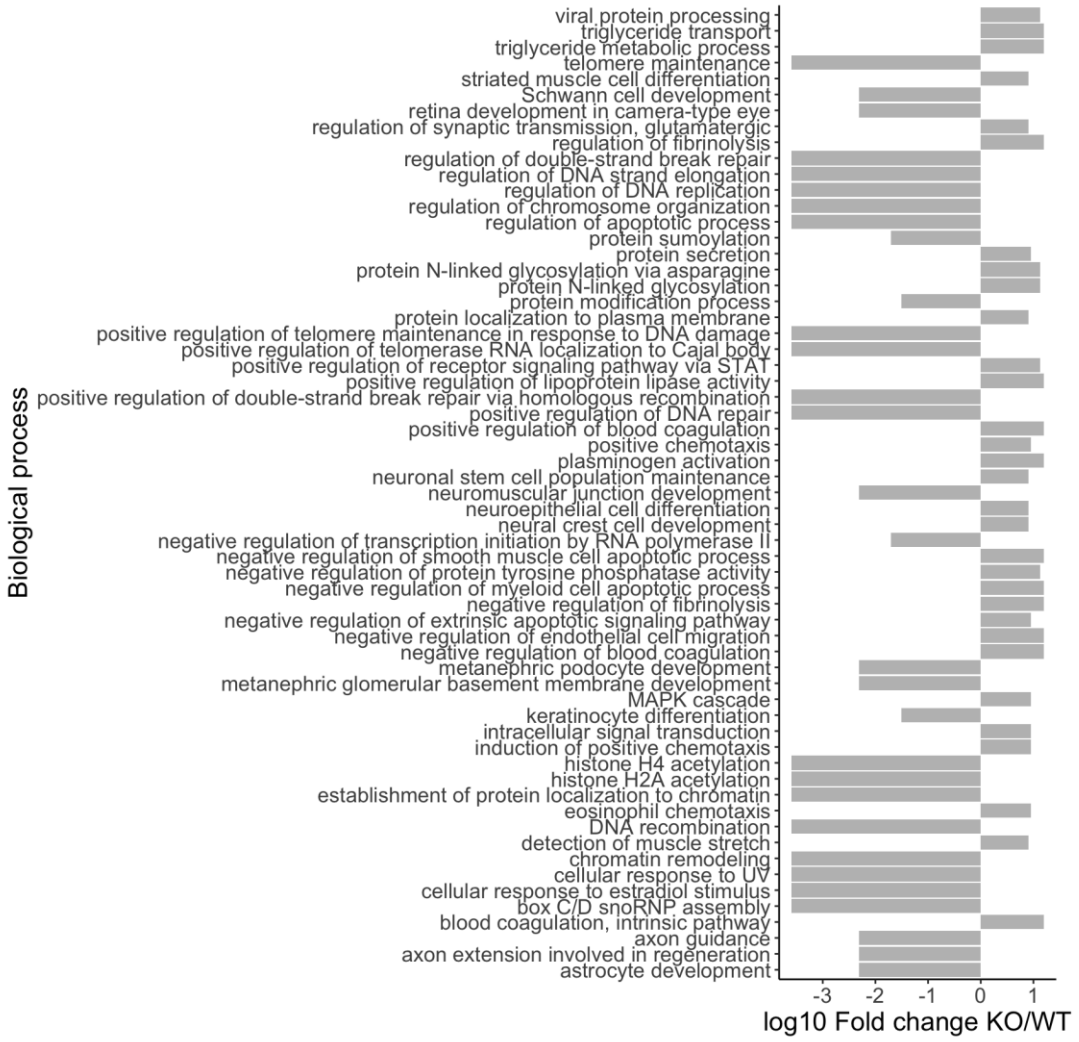

Figure 6.4 Wholistic Biological process GO term enrichment analysis of proteins in DJ-1 KO vs WT. Analysis of biological process GO term change between DJ-1 KO and WT performed in funrich. Terms with a log10 fold change above 1 are enriched in DJ-1 KO compared to WT and those with a value below 1 depleted in DJ-1 KO. Graph shows top 60 significant changes in either direction.

Non-RUVBL2-associated GO terms in the top 30 cellular component terms or 60 biological process terms of particular interest due to their functional grouping included:" regulation of synaptic transmission, glutamatergic", synaptic cleft and post synapse; protein secretion, protein localization to plasma membrane, ESCRT 1 complex, cytoplasmic vesicle, microtubule organizing center, microtubule cytoskeleton, and dynein axonemal particle; and the laminin-3/11 complexes; protein modification process, protein sumoylation, protein N-linked glycosylation; axon guidance and axon extension involved in regeneration; and astrocyte development and neuronal stem cell population maintenance (Fig 6.3).

An interesting observation on the significantly different protein dataset is that the vast majority of significantly enriched biological process terms are associated with only 1 protein in the dataset. For biological process 234 terms are only associated to 1 protein dropping to 54 for 2 proteins and 14, 10, 3 and 1 for 3, 4, and 5 proteins respectively. This is less apparent in cellular component with 47 terms are associated with 1 protein, 15, 7, 11, 2, and 19 with 2, 3, 4, 5 and >= 6 proteins respectively.

6.3.2 Proteins can be grouped based on fold change to generate cluster with distinct functional features

Wholistic analysis of the significantly different protein dataset GO terms resulted in interesting observations but generated incredibly large and hard to interpret datasets. To reduce the issues observed via this method, similar analysis but on distinct smaller clusters of proteins was attempted.

To this end, significantly different proteins were clustered based on fold change via a kmeans algorithm with a kmeans ++ initializer, following the logic that proteins with similar fold changes are regulated similarly in terms of expression or EV localization and thus share functional similarity.

Firstly, the number of clusters to create needed to be identified. This was achieved by running a kmeans clustering algorithm with increasing numbers of clusters and recording the total sum of squares of each cluster as a measure of variation, with lower total sum of squares representing a better fit to the data (Fig 6.5). A decrease in total sum of squares was observed until 5 clusters after which an essentially flat relationship was observed (Fig 6.5). Thus, 5 clusters were chosen as the optimal number of clusters to group significantly different proteins (Fig 6.5).

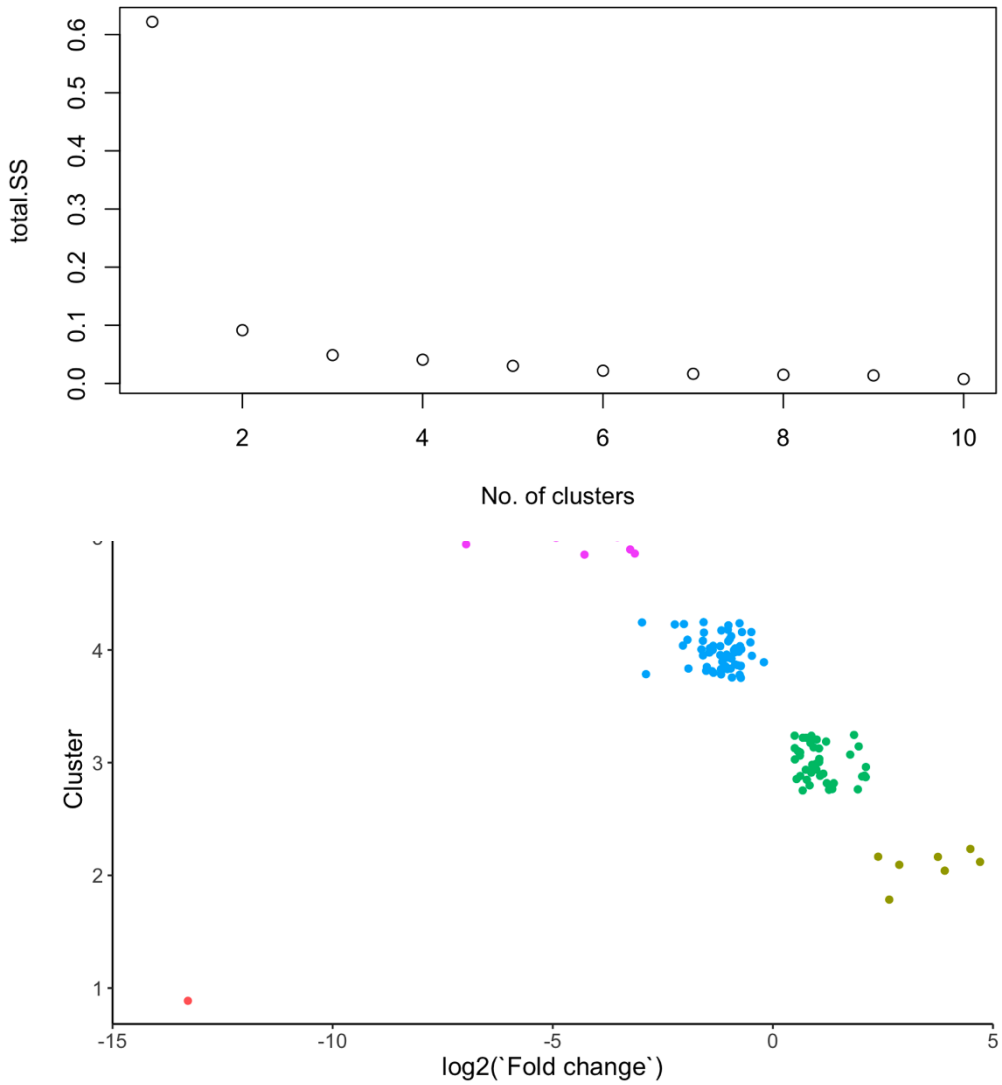

Figure 6.5 Kmeans clustering of significantly different proteins by grouping on fold change. Top graph: comparison of total sum of squares of the clustered proteins at increasing numbers of clusters. Bottom graph: significantly different proteins clustered by mini-batch kmeans algorithm with kmeans++ initializer; clusters on y axis and log2 fold change on x axis; each point = 1 protein.

Clustering the significantly different proteins via kmeans resulted in 5 clusters as follows: cluster 1, 1 protein (RUVBL2); cluster 2, 7 proteins; cluster 3, 43 proteins; cluster 4, 59 proteins; and cluster 5, 6 proteins (Fig 6.5). Cluster 1 represents the singular non-present proteins in DJ-1 KO RUVBL2. Clusters 2, 3, 4 and 5 represent proteins relatively highly enriched in DJ-1 KO, lowly enriched in DJ-1, lowly enriched in WT, and highly enriched in WT with centroid log10 fold changes of 1.17, 0.23, -0.35, and -1.48 respectively (Fig 6.5). The vast majority of proteins were either in cluster 3 or 4 which together represent

87.9 % of significantly different proteins. Thus, the vast majority of proteins were only relatively lowly enriched in either genotype (Fig 6.5).

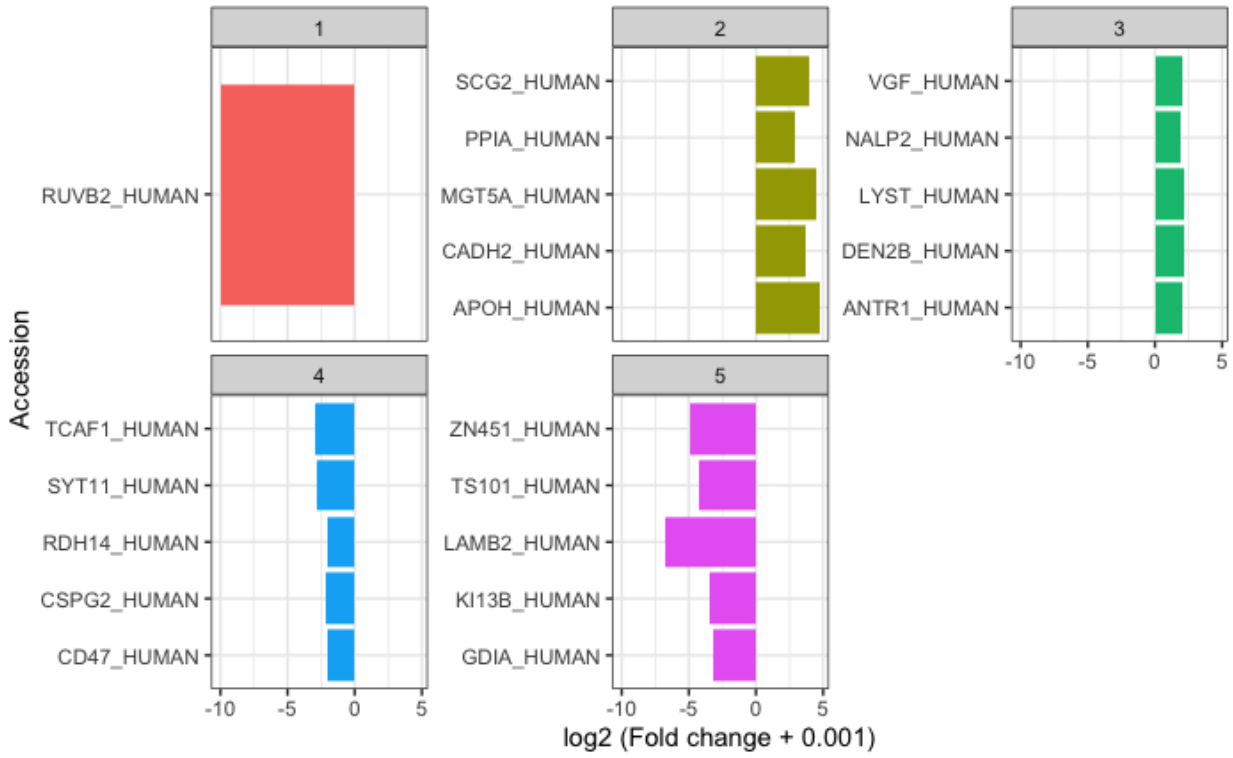

Figure 6.6 Top 5 proteins based on fold change for each Kmeans defined cluster. Top 5 proteins ranked by log2 (fold change +0.001) for each kmeans defined cluster. Proteins represented by their Accessions on the y axis and log2 (fold change + 0.001) on the x axis. Coloured according to cluster colours from Kmeans clustering graph in fig 6.5.

Once clustering of proteins was achieved via kmeans, functional analysis of each cluster was desired. Firstly, the top 5 proteins ranked by log2 (fold change + 0.001) were isolated (Fig 6.6). Secondly GO term enrichment was performed for the proteins in each cluster against the background dataset (Fig 6.7), and finally fold changes in GO terms were investigated between DJ-1 KO and WT EV proteins (Fig 6.8).

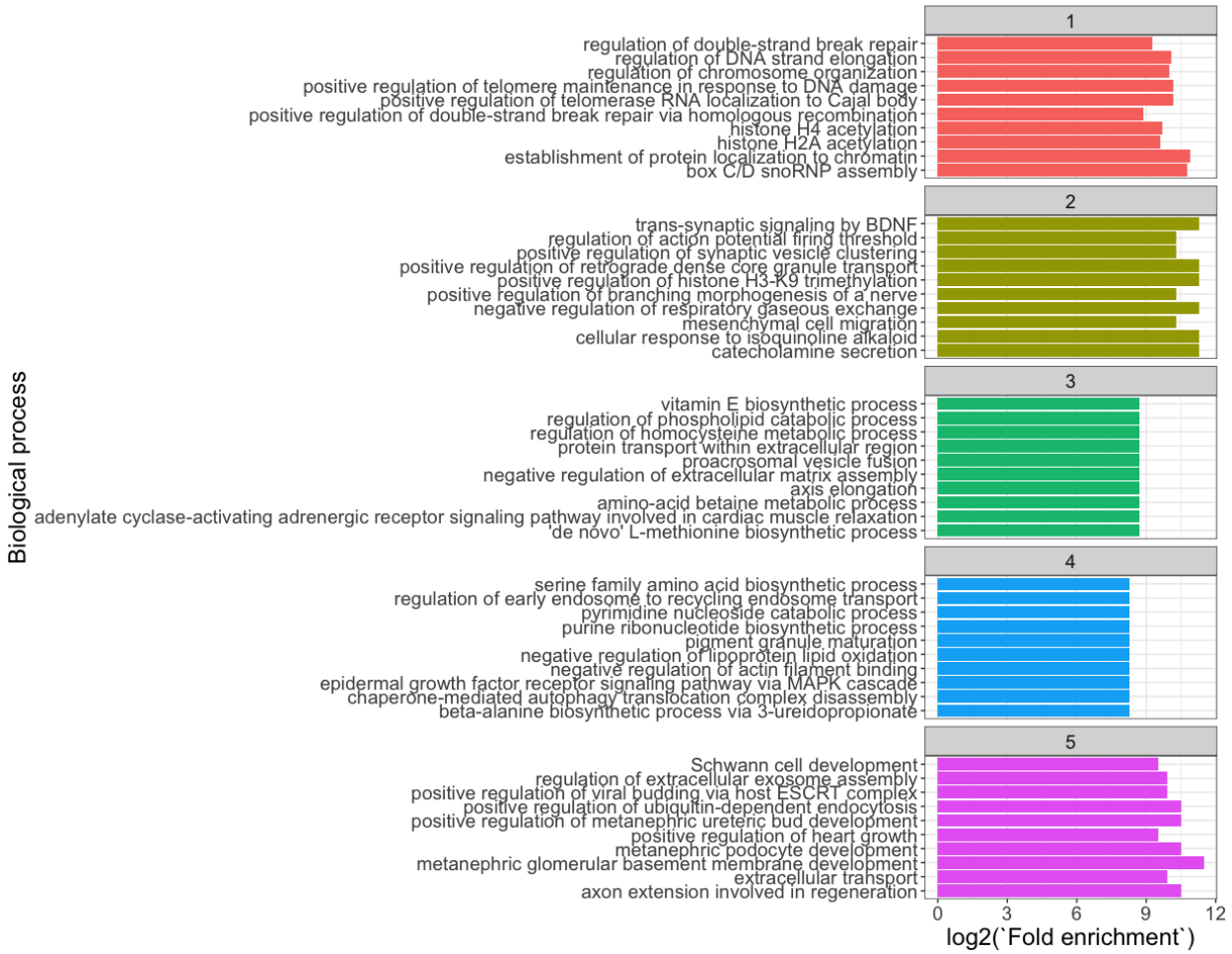

Figure 6.7 Top 10 enriched Biological process GO terms for each Kmeans defined cluster. Analysis of biological process GO term enrichment against Uniprot human protein database per protein cluster performed in funrich. Terms with a log10 fold change above 1 are enriched in DJ-1 KO compared to WT and those with a value below 1 depleted in DJ-1 KO. Graph shows top 10 most enriched terms per cluster.

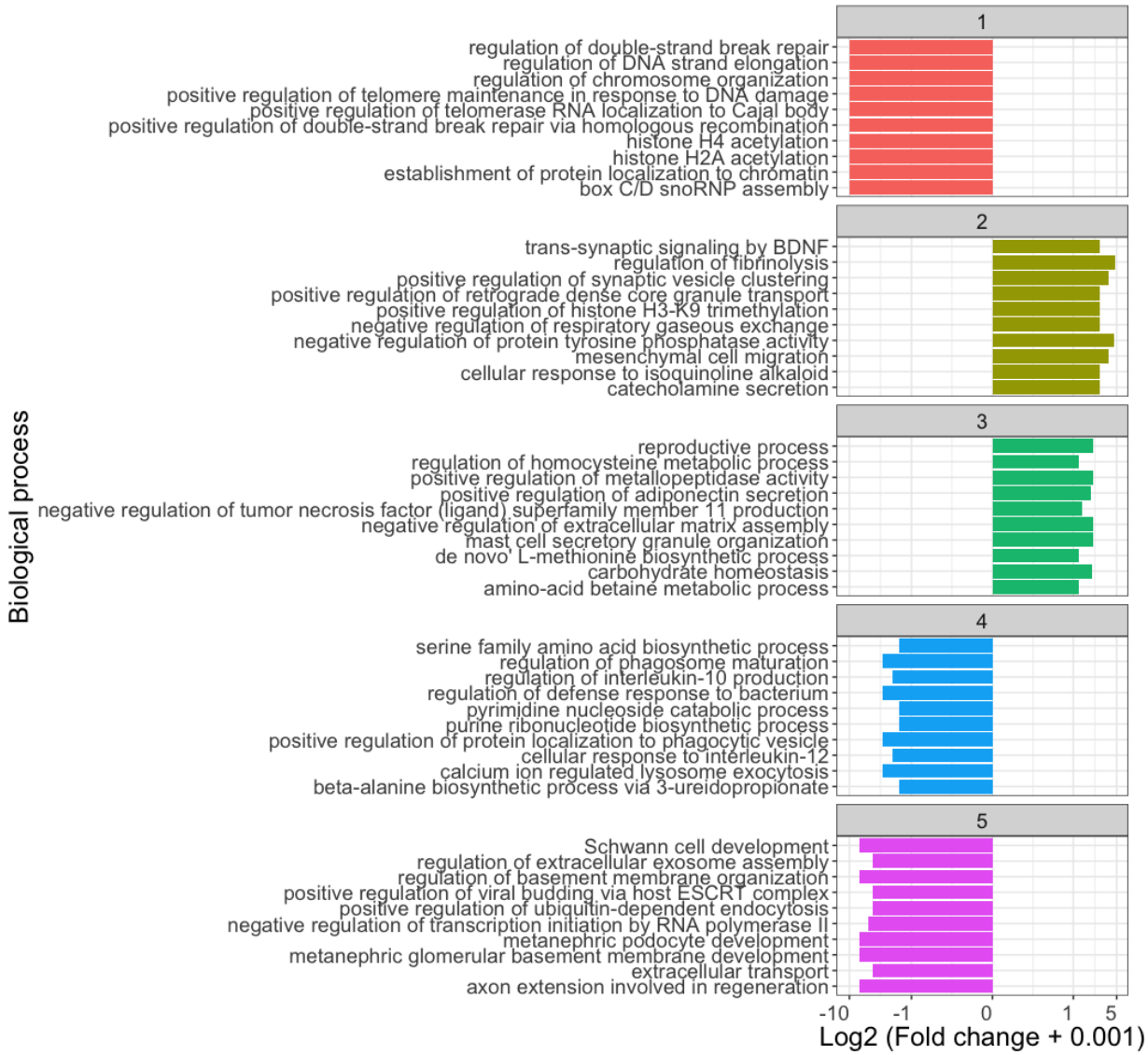

Figure 6.8 Top 10 Biological process GO terms by absolute value fold change in DJ-1 KO vs WT for each Kmeans defined cluster. Analysis of biological process GO term change between DJ-1 KO and WT per cluster performed in funrich. Terms with a log10 fold change above 1 are enriched in DJ-1 KO compared to WT and those with a value below 1 depleted in DJ-1 KO. Graph shows top 10 most different terms per cluster.

Each cluster of significantly different proteins was investigated for proteins of interest. Searching occurred by extracting proteins associated with GO terms of interest such as those related to synapse and neurotransmitter release and manual searching for known relevant proteins. Ultimately several proteins were picked out for further research, including RUVBL2, Synaptotagmin 11 (SYT11), zinc finger 451 (ZNF451), CD47, and cadherin-2. Further research into CD47 and cadherin-2 was performed by other

members of the lab group and thus is not included in this thesis. However, further analysis of RUVBL2, SYT11 and ZNF451 is reported in a later section of this chapter.

6.3.3 Protein-proteins interaction analysis via string db

Functional analysis of the significantly different protein dataset was performed using string db, a protein-protein interaction and functional database. A clustered protein-protein interaction map was generated via MCL clustering with an inflation parameter of 3. (Fig 6.9) 21 individual clusters were identified ranging from 19 proteins to 1 per cluster (Table 6.1). Two very interesting outputs were derived from this clustering: cluster 1 with 19 proteins presenting with a primary function description of “Blood microparticle” and secondary description of “Complement and coagulation cascades, and Protein-lipid complex”; and cluster 5 presenting with 5 proteins and a primary description of “Regulation of extracellular exosome assembly”.

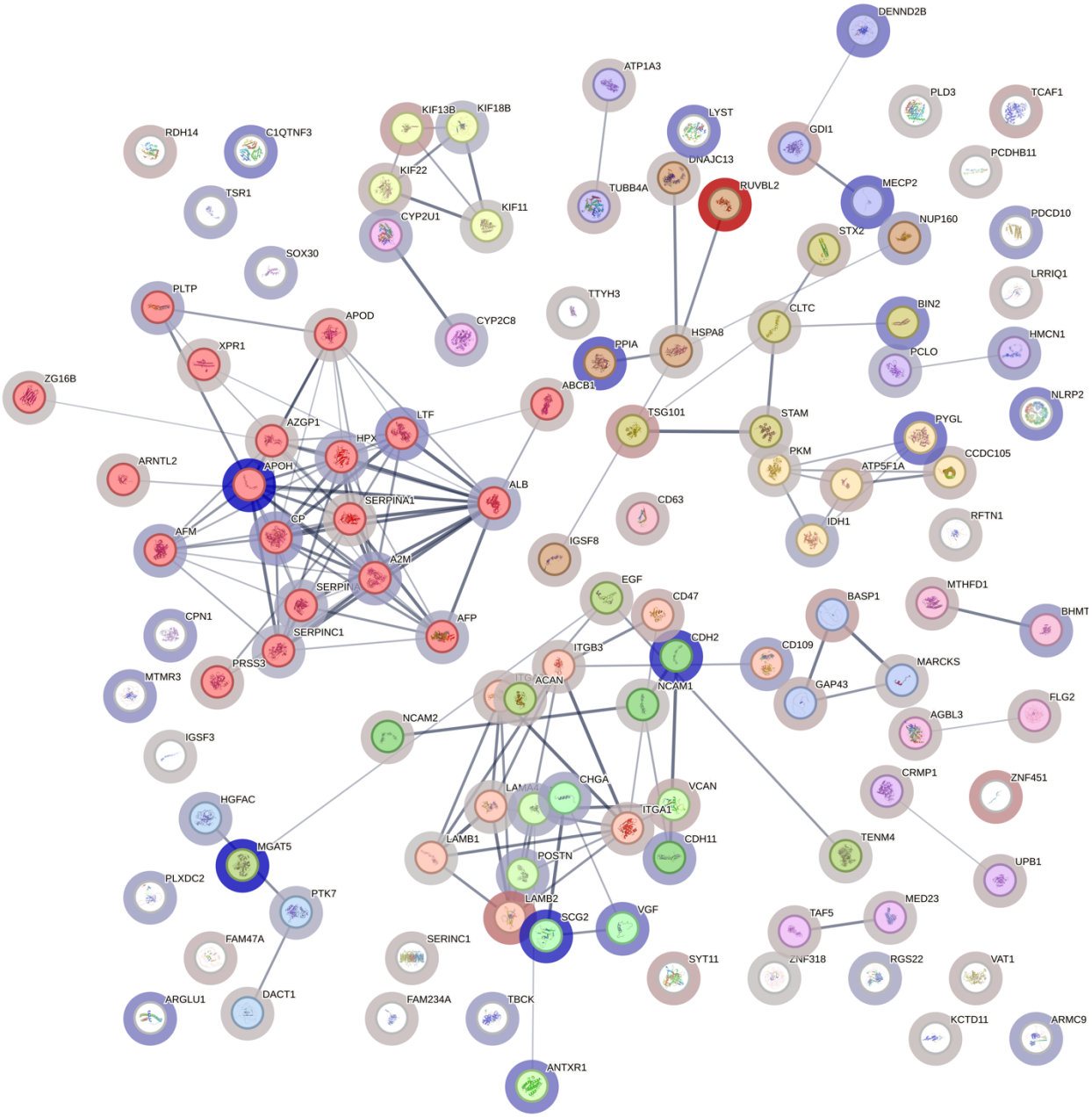

Figure 6.9 String interaction network of all significantly different proteins and associated MCL clusters. Clustered protein-protein interaction map of significantly different proteins generated in string db via MCL clustering. Each node = 1 protein. Node colour indicates cluster and within cluster links are mapped as lines between nodes. Node outer ring colour and saturation = log2 fold change, depleted in DJ-1 KO = red ring, enriched in DJ-1 KO = blue ring, higher saturation = larger change.

Table 6.1 Description of MCL clusters derived from String interaction network of significantly different proteins.

Cluster color = colour of cluster on protein-protein interaction map in fig 6. (-) indicates no functional enrichment.

cluster numb	gene count	primary description	secondary description	protein names
1	19	Blood microparticle	Complement and coagulation cascades, and Protein-lipid complex	APOD, APOH, CP, SERPINA7, AFM, A2M, HPX, AZGP1, PLTP, SERPINA1, AFP, ALB, SERPINC1, LTF, ABCB1, ARNTL2, ZG16B, XPR1, PRSS3
2	8	ECM-receptor interaction	Protein complex involved in cell adhesion	LAMB1, LAMB2, ITGA3, ITGB3, ITGA1, LAMA4, CD47, CD109
3	6	Mixed, incl. Chaperone cofactor-dependent protein refolding, and DnaJ homolog subfamily A member 1/2-like	-	HSPA8, DNAJC13, PPIA, IGSF8, NUP160, RUVBL2
4	5	-	-	PYGL, ATP5F1A, IDH1, PKM, CCDC105
5	5	Regulation of extracellular exosome assembly	ESCRT complex	TSG101, CLTC, STAM, STX2, BIN2
6	4	Kinesins	-	KIF22, KIF13B, KIF18B, KIF11
7	4	-	-	EGF, ACAN, MGAT5, TENM4
8	4	-	-	POSTN, FBN1, VCAN, ANTXR1
9	4	Prion, and Neural cell adhesion	-	NCAM1, CDH11, CDH2, NCAM2
10	3	Mixed, incl. Chromogranin A/B/C, and Protein localization to secretory granule	-	CHGA, VGF, SCG2
11	3	-	-	DACT1, PTK7, HGFAC
12	3	MARCKS family, and Regulation of metanephric ureteric bud development	-	GAP43, BASP1, MARCKS
13	3	-	-	GDI1, DENND2B, MECP2
14	2	Dystonia	-	TUBB4A, ATP1A3
15	2	-	-	HMCN1, PCLO
16	2	-	-	CRMP1, UPB1
17	2	-	-	MED23, TAF5
18	2	Synthesis of (16-20)-hydroxyeicosatetraenoic acids (HETE)	-	CYP2C8, CYP2U1
19	2	-	-	FLG2, AGBL3
20	2	Methionine biosynthetic process	One carbon pool by folate, and Amino-acid betaine catabolic process	MTHFD1, BHMT
21	1	-	-	CD63

6.3.4 Further investigations into identified proteins of interest.

Further investigation into the proteins of interest RUVBL2, SYT11 and ZNF451 were performed via immunostaining and confocal microscopy and qualitative analysis. Regarding RUVBl2, rotenone treated WT showed the highest expression in cells. Furthermore, its non-presence in DJ-1 KO EV from rotenone treated cells was verified in cells, with minimal if any expression being visible (Fig 6.6/10).

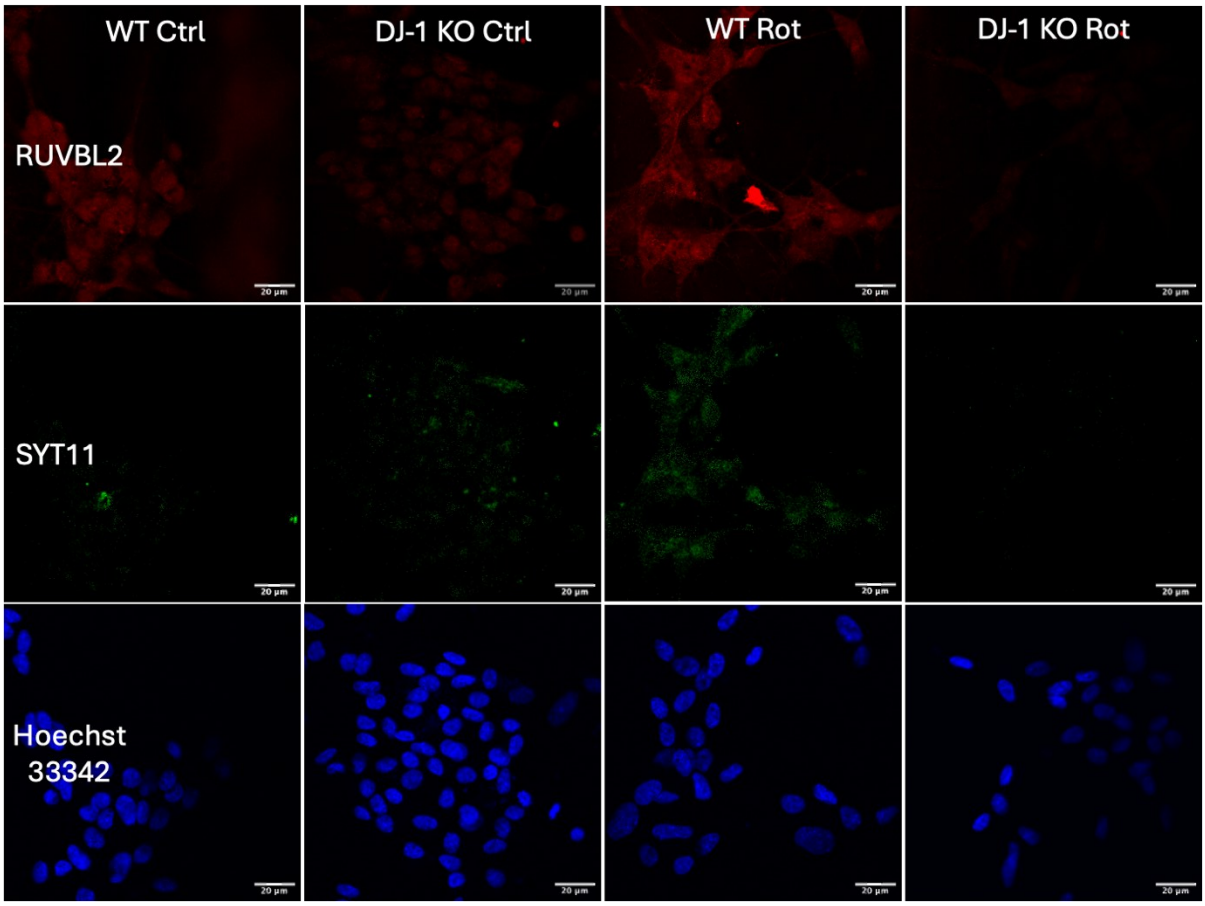

Figure 6.10 Further investigation into RUVBL2 and SYT11 expression in cells via immunofluorescence and confocal microscopy. Representative images taken of a Leica SP8 confocal microscope showing the expression of immunostained RUVBL2 and SYT11 in WT and DJ-1 differentiated SH-SY5Y, with and without 10 nM rotenone treatment. Nuclei stained with Hoechst 33342. Scale bar= 20 μm.

An interesting observation was that in control condition , RUVBL2 was present in both genotypes but with a much stronger signal in wild type cells than in DJ-1 KO cells, and this difference between the two genotypes was even stronger upon rotenone treatment thus reflecting what observed in the EV cargo(Fig 6.10).It also appears that treatment with 10 nM rotenone induces a change in RUVBL2

localisation, as it appears to be less localized to the nuclei in rotenone treated WT cells. On the other hand, SYT11 was incredibly difficult to detect in cells of all conditions except rotenone treated WT cells (Fig 6.10). However, this still confirms the change seen in EV as SYT11 was depleted in EV from rotenone treated DJ-1 KO cells (Fig 6.1).

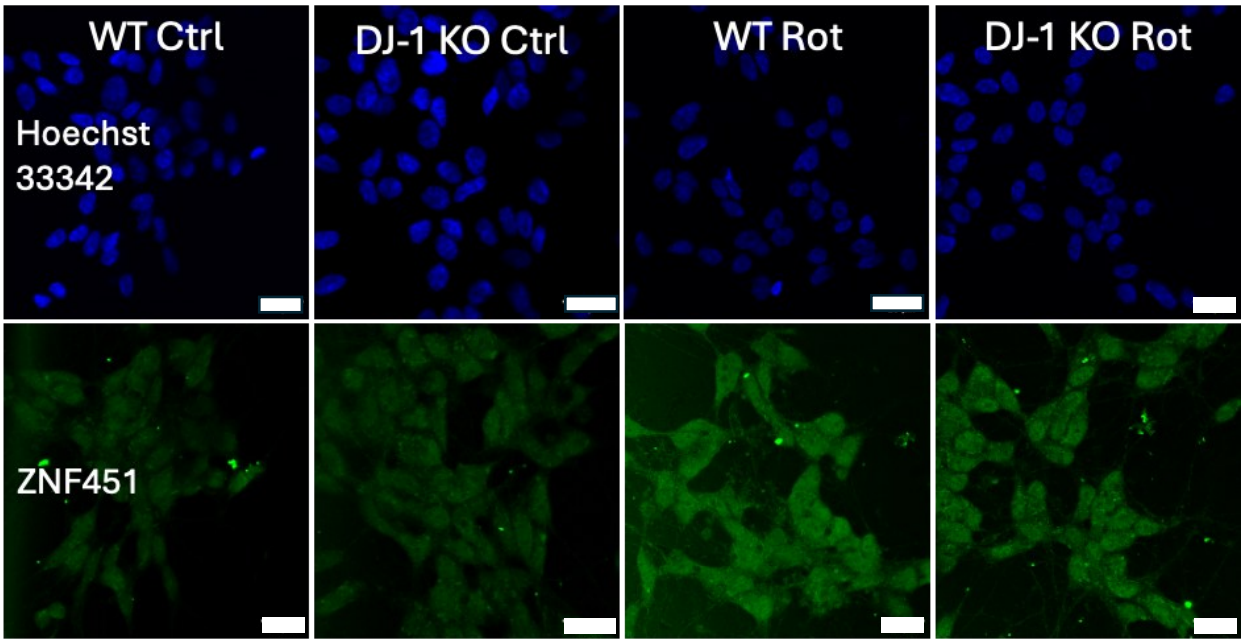

Figure 6.11 Further investigation into ZNF451 expression in cells via immunofluorescence confocal microscopy. Representative images taken of a Leica sp8 confocal microscope showing the expression of immunostained ZNF451 in WT and DJ-1 differentiated SH-SY5Y with and without 10 nM rotenone treatment. Nuclei stained with Hoechst 33342. Scale bars = 20 μm.

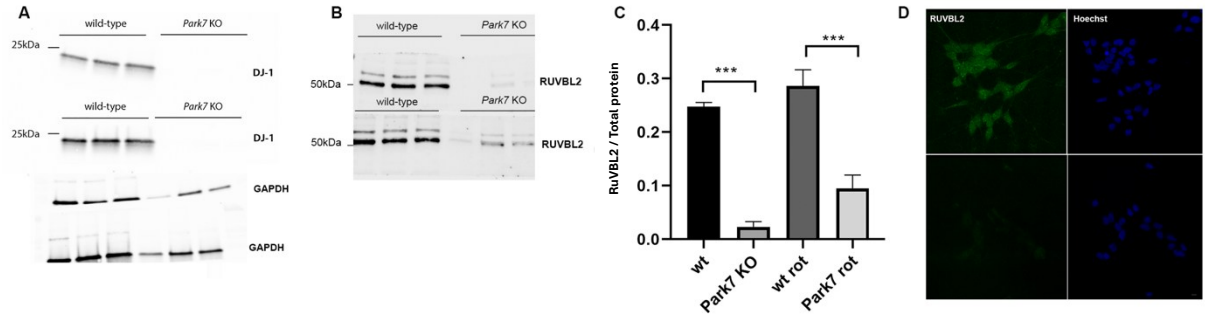

Figure 6.11 Cellular RUVBL2 expression changes in differentiated SH-SY5Y both due to DJ-1 KO and rotenone-induced oxidative stress. Western blots and immunofluorescence of RUVBL2 expression in differentiated WT and DJ-1 KO SH-SY5Y cells in control and oxidative stress conditions.A: WB confirmation of DJ-1 KO , . GAPDH was used as loading control. B: RUVBL2 western blot for the two genotypes. C: RUVBL2 quantification based on stain free gel total protein as loading control, in all westerns the top row = control, bottom = rotenone treated. D: RUVBL2 immunofluorescence upon rotenone treatment in wild type cells (upper panel) and Park7 KO cells (lower panel)

Further investigation into RUVBL2 was performed via western blotting and the data clearly confirmed what previously observed by immunofluorescence: a strong difference in protein level between wild-type and KO cells in control condition (90% decrease in Park7) as well as in oxidative stress (60% decrease in Park7). Interestingly, a small increase in RUVBL2 was observed upon rotenone treatment in both genotypes compared to their respective controls...

6.4 Discussion

6.4.1 DJ-1 KO induces a distinct EV proteomic profile in rotenone-treated differentiated SH-SY5Y

In the previous chapter it was reported that DJ-1 KO resulted in a 1.56-fold increase in the amount of small EV at 10 nM rotenone treatment compared to WT (Fig 5.1). Herein this chapter evidence is presented that DJ-1 KO also alters the EV proteome, changing the concentration of 20.2 % of the identified EV proteins (Fig 6.2), with a slight propensity towards depletion in DJ-1 KO EV. Indeed, 50 proteins were enriched in DJ-1 KO vs 66 depleted.

Oxidative stress has been reported to alter the EV proteome in only 1 known study so far (Benedikter, 2019). Given the role of DJ-1 in responding to oxidative stress (Di Nottia, 2017), it is perhaps not surprising to see that DJ-1 alters the EV proteome. However, this is the first[t] report on the effect of DJ-1 KO on the EV proteome, and as such these effects were a truly novel discovery.

EV cargo in non-stressed conditions was not studied as part of this project and as oxidative stress can change the EV proteome (Benedikter, 2019) the question arises as what proportion of the changes observed herein are due to direct action by DJ-1 and what proportion are indirect effects caused by increased oxidative stress due to DJ-1 absence? From an overall functional and pathology perspective the answer to this question may be ultimately irrelevant. An indirect effect is still an effect of DJ-1 KO and its functional outputs of interest occur all the same. However, to truly understand the underlying mechanisms of DJ-1 EV interaction, studying the EV proteome in non-stressed conditions and at 5 nM rotenone where no increase of EV in DJ-1 KO was observed will likely be necessary.

In the previous chapter it was discussed how DJ-1 regulates autophagy (Thomas, 2011). Autophagy is closely linked to exosome production through the endolysosomal pathways (Huotari, 2011). There appears to be a decision point in the degradation of cellular components at the MVB stage, where their fate can be altered from autophagic degradation to extracellular release via exosomes (Baixauli, 2014). Could DJ-1 regulate this decision point? If so, this would suggest that an unknown proportion of the significantly different proteins observed were present in EV as a way to increase removal of damaged proteins. However, this does not rule out signaling roles, especially to support and immune cells such as astrocytes and microglia which can react to damaged proteins as signals and generate a protective response (Weismann, 2012; Gao, 2023; Verkhratsky, 2023). If this explanation is correct and the reason for increased EV in DJ-1 ko cells was removal of damaged proteins, it would logically be expected that

functional overlap across the significantly different proteins would be low. This is indeed what was observed with 84 % of biological process GO terms only being associated with 1 significantly different protein. However, to truly understand what proportion of protein changes are due to increased removal of damaged proteins, proteomic analysis of known oxidative damage protein modifications such as residue oxidation and carbonylation should be analysed (Kehm, 2021).

Despite the low overlap of GO terms across the significantly different proteins, there are several functional themes that could be derived from both fold change analysis and string db clustered protein groups.

Investigation of the biological process GO terms of the fold change derived protein groupings determined that each cluster possessed a relevant theme of interest. Cluster 1 was represented by a single protein, RUVBL2, involved in regulation of DNA transcription and repair, and histone and chromatin modification. Cluster 2 highlighted the theme of blood coagulation, a theme shared with the largest group derived from string db protein-protein interaction clustering, and a secondary theme of synaptic regulation containing a protein of interest, cadherin-2. Cluster 3 was enriched in proteins involved in immunoregulation and protein localisation/transport;cluster 4 presented proteins playing a role in immunoregulation and synaptic vesicle regulation, containing the proteins of interest CD47 and SYT11. Finally, cluster 5 showed the themes of cell adhesion and differentiation. Additional functional themes derived from string db protein-protein interaction terms included: cell adhesion, both to the extracellular matrix and other cells; chaperone activity; exosome assembly and ESCRT complex activity; kinesin activity; MARCKS and axonal regeneration/development; and lipid metabolism.

Interestingly, every functional theme identified from the significantly different proteins can be linked to Parkinson's disease.

Blood coagulation is the largest detected theme with most proteins being enriched in rotenone-treated-DJ-1 KO EV. Issues and dysfunction related to vascular tissues and blood coagulation/fibrinolysis are well known features of Parkinson's disease as highlighted by vascular Parkinsonism and its shared clinical presentation with Parkinson's disease (Korczyn, 2015; Sharma, 2021). Blood coagulation is clearly linked to oxidative stress both through oxidative damage of vascular endothelial tissue and red blood cells (Wang, 2020; Li, 2023). Indeed, the only other known proteomics analysis of EV from oxidatively stressed CSE-treated airway epithelial cells reported that functional terms related to platelet activity and blood coagulation were significantly enriched (Benedikter, 2019), in agreement with the work described herein.

This same EV proteomics study also reported significant enrichment of immune system regulation functional terms (Benedikter, 2019), confirmed in the results described in this chapter. Though, while immune regulation changes are reported in both cases, the specifics of the changes may be different and result in distinct functional pathways. Parkinson's disease has a complicated link to immune system regulation and particularly dysregulation of inflammation (Tansey, 2022). Changes in intestinal inflammation and neuroinflammation, circulating pro-inflammatory cytokines, innate and adaptive immune cell activation and frequency, and blood-brain barrier permeability and infiltration of peripheral immune cells into the CNS are all reported as hallmarks of Parkinson's disease (Tansey, 2022). Furthermore, patients affected by several auto-immune disorders have been reported to have a 33 % increased risk of Parkinson's disease development. Namely, multiple sclerosis, Grave's disease (hyperthyroidism), Hashimoto disease (hypothyroidism), pernicious anaemia or polymyalgia rheumatica (Li, 2012), indicating that excessive levels of inflammation can damage cells propagating neurodegeneration away from the original source (Tansey, 2022).

Cell adhesion, both of cells to the extracellular matrix and between cells, has been identified by genome-wide association and gene expression studies of SNPs in Parkinson's disease as a relevant pathway (Myers, 2012). Herein reported, DJ-1 KO affected the EV concentration of proteins involved in both cell to extracellular matrix adhesion, and neuron-neuron adhesion particularly relating to synaptic connections. Affected proteins relating to neuron-ECM adhesion identified in this work (Table 6.1) included integrins alpha 1/3 and integrin beta 3 (Denda, 2009), and laminin (Aumailley, 2013). Whereas those related to synaptic connections included NCAM1 and 2, and cadherin 2 and 11. Cell adhesion is intricately linked to synaptic activity and plasticity, which is known to be dysregulated in Parkinson's disease (Chapman, 2014). In fact, the significantly different proteins described NCAM1, NCAM2, CADH2 and CADH11 are all known to be regulators of synaptic plasticity (Kim, 2021; Bartelt-Kirbach, 2011). However, the NCAMs are downregulated in DJ-1 KO EV and CADHs upregulated, suggesting a potentially nuanced change.

Cell adhesion both to the ECM and between cells at synapses is incredibly important in neurons as detachment causes death via anoikis in the case ECM detachment (Reddig, 2005) and apoptosis in the case of sufficient synaptic connection loss (Brady, 2010). Furthermore, cell adhesion is important for axon growth and regeneration, another functional theme discovered in the significantly different proteins of this work, represented by string cluster 12 (Sami, 2020). GAP43, MARCKS, and BASP1 are all proteins heavily implicated in axonal growth and regeneration (El Amri, 2018; Chung, 2020). This is particularly interesting as axon regeneration is widely believed to not occur in the CNS, outside of

controversial reports on specific neuron groups such as the serotonergic neurons of the rostral raphe nuclei (Xu, 1995; Huebner, 2009). However, this research was carried out in SH-SY5Y cells differentiated into a dopaminergic-neuron-like phenotype. They are not true dopaminergic CNS neurons, and as such may present with features such as a capability to regenerate axons similarly to PNS neurons that are not relevant to the true biological system of interest. Nevertheless, the proteins GAP43, MARCKS and BASP1 may present interesting targets for tests of regenerative treatment.

Regulation of synaptic activity was also a detected functional theme via terms relating to synaptic vesicle recycling. Synaptic vesicle recycling is an essential process for maintaining the release-ready neurotransmitter-containing vesicles, and has been reported as dysfunctional in Parkinson's disease (Zou, 2021). Synaptic and axonal degeneration is believed to be one of the earliest recognisable morphological changes of degenerating neurons in Parkinson's disease (Gcwensa, 2021). Synaptic degeneration can be caused by synaptic vesicle recycling dysfunction, and the dopaminergic neurons of the substantia nigra are particularly vulnerable to this dysfunction (Cao, 2017). This vulnerability is in part caused by dopamine, as cytosolic dopamine is an oxidative stressor and cytosolic dopamine increases under conditions of synaptic vesicle recycling dysfunction (Chen, 2008; Zou, 2021). Interestingly, packaging of dopamine into synaptic vesicles is ATP reliant as the vesicular monoamine transporter is a proton pump secondary transporter of dopamine (Eiden, 2004). ATP synthesis appeared to be deficient in rotenone treated differentiated WT and DJ-1 KO SH-SY5Y as expression of the ATP5α subunit was reduced compared to control, as reported in chapter 5. This feature was also observed in rotenone treated DJ-1 KO EV compared to WT in the current chapter as ATP5α was significantly depleted in DJ-1 KO EV (Table 6.1).

Synaptic vesicle recycling is tightly linked to the cell endosomal trafficking pathways. Both pathways interface in the secretion to and internalization from the extracellular space, and shuffling of proteins between sub cellular compartments and the plasma membrane (Ivanova, 2022). Several functional themes were detected in the significantly different proteins that are involved in both pathways. Namely, string clusters 5, 6 and 10, presented as "exosome assembly", "kinesins", and "protein localisation to dense core granule". EV production is known to be altered by oxidative stress (Chiaradia, 2021), a key feature of Parkinson's disease (Jenner, 2003), but disruption of protein trafficking and localisation have also been reported (Hunn, 2015). Particularly, the degradation of ubiquitinated proteins via autosomal pathways is known to be affected (Ebrahimi-Fakhari, 2012).

String Cluster 5 contains the proteins TSG101, STAM, CLTC, STX2, BIN2, with all but BIN2 being depleted in DJ-1 KO EV. TSG101 (Tumor susceptibility gene 101 protein) is the most heavily depleted protein in the cluster (fold change = 0.051) and is substantially involved in the regulation of exosome biogenesis (Gurung, 2021). Interestingly, both STAM and TSG101 are involved in ESCRT-0 complex sorting of ubiquitinated proteins into multi-vesicular bodies (Mayers, 2011; Coudert, 2021). This may suggest that the sorting of proteins destined for degradation is altered in DJ-1 KO. Interestingly, BIN2 is known to primarily regulate membrane curvature and is known for its role in creation of cellular membrane protrusions called podosomes in leukocytes (Soldati, 2012). Alterations in membrane curvature are required for endocytosis (Zhao, 2017; Cail, 2022) but also for the formation of microvesicles by membrane budding (Tricarico, 2016). Thus, changes in BIN2 may represent alterations in a non ESCRT related / exosome extracellular release pathway. This potential shift of EV production pathway is lent credence by BIN2 being heavily enriched in DJ-1 KO EV (fold change = 3.59) compared to the depletion of STAM and TSG101. Alternatively, it may represent alterations in endocytosis, which DJ-1 has been reported to linked to.

String Cluster 6 contains 4 kinesin-like proteins, KIF11, KIF13B, KIF18B and KIF22. Interestingly, KIF13B appears to be involved primarily in axonemal transport of proteins, and thus is involved in maintaining healthy axons and synapses (Yu, 2020; Yoshimura, 2023). However, KIF11, 18B and 22 are all primarily known as proteins involved in mitotic spindle control (Stout, 2011; Waitzman, 2013; Almeida, 2018), a process that does not occur in terminally differentiated neurons (Wilcock, 2007). This feature thus suggested that these proteins have unreported roles in neurons, that they are important for signaling to non-neuronal cells such as astrocytes and microglia, or that their presence is an artifact due to SH-SY5Y being a neuroblastoma derived cell line.

String Cluster 10 is represented by 3 proteins, SCG2, VGF and CHGA. All 3 proteins are involved in the formation of dense core secretory granules (Gentile, 2004; Kim, 2005; Courel, 2010). In neurons dense core secretory granules are involved in the secretion of neuropeptides such as enkephalin, and dynorphin, as well as other neurotrophic factors (Merighi, 2018). While similar to synaptic vesicles, dense core vesicles are indeed separate structures (Liu, 1994; Merighi, 2018). Whether a dysfunction in the dense core granule pathways in dopaminergic neurons may be involved in the development of PD has yet to be understood, but a proteomic study of MPP+ treated undifferentiated SH-SY5Y secretory granule vesicles found that 556 proteins were differentially expressed (Wen, 2021), and among these

protein VGF and secretogranins also identified in the current work. However, the secretogranin reported to be different in the reported study was 3 rather than 2 as reported in this chapter's work (Wen, 2021).

The final identified functional theme was "lipid metabolism". Dysfunctional lipid metabolism is particularly tightly linked to Parkinson's disease. α-synuclein has showed preferential binding to specific lipid molecular species, and there is a close link between α-synuclein oligomerisation and aggregation and its interaction with the lipid (Alecu, 2019). Genetically, mutations in the Parkinson's disease associated genes GBA, SMPD1, GALC, PLA2G6, and SCARB2 are all related to lipid metabolism (Alecu, 2019). Furthermore, the platelet dysfunction reported as a key feature of Parkinson's disease can be regulated by lipid mediators such as "platelet activating factors" (Seet, 2010). Lipid mediators are also involved in immune system regulation either directly or indirectly via the stabilisation and regulation of membrane proteins exposed extracellularly such as CD47 (Palsdottir, 2004).

It is interesting that all of these features identified by EV cargo analysis upon oxidative stress are related to Parkinson's disease and appear to be modulated by the presence / absence of DJ-1. However, determining what functional changes are occurring is difficult: these functional pathways may have changed due to changes in cell expression e.g increased cellular expression of proteins leading to higher presence in EV, or due to true selective changes in localisation of proteins to EV.

Furthermore, it is unknown from these bioinformatic analyses whether the proteins observed to be differentially present in EV are even in a functional state, or whether they are damaged, e.g oxidatively modified. The function of EV is also dependent on their interaction with other cells, do they exert effects by binding with a membrane protein to a cell surface receptor, or by internalisation with or without cargo release (Mulcahy, 2014)? Which cells would they affect assuming the true in vivo system: other neurons, astrocytes, oligodendrocytes, or microglia? All of these cell types have been reported to react to neuronal EV, and thus could be important for resolving the overall function of neuronal EV (Ogaki, 2021; Ahmad, 2022; La Torre, 2022).

If it is the case that many of the different proteins are damaged and thus released from the cell, it stands to reason that microglia would play an important role in clearing the extracellular environment and degrading such proteins as the CNS resident phagocytic macrophages (Gao, 2023). However, astrocytes and oligodendrocytes also have roles in maintaining the stability and health of the CNS, particularly of the sensitive neuronal axons and synapses (Jäkel, 2017). It is possible that EV from DJ-1 containing cells

prime an oxidative stress protective response in surrounding cells, preventing or inhibiting the spread of damage.

Ultimately to truly understand the functional implications of the observed changes, functional assays of EV treatment of specific cell types must be performed (described in following chapter).

6.4.2 A deep-dive into the potential role of RUVBl2

In the last part of the results section of this chapter, 3 proteins identified in EV were investigated in differentiated SHSY5y cells in control condition and upon rotenone treatment, to better understand differences in such candidates between the EV and the cellular compartment. These proteins were: RUVBL2, SYT11 and ZNF451.

RUVBL2 was chosen as a protein of great interest because it was the only significant protein undetectable in DJ-1 KO EV. RUVBL2 is an interesting and highly complex protein of diverse functions, primarily acting in complex with the closely related RUVBl1 (Dauden, 2021). Diverse quaternary complexes can be formed between RUVBL1/2, but the most functional has been reported to be the hetero hexameric ring RUVBl1 (Dauden, 2021). It is these quarternary complexes upon which RUVBL2 functions, providing a scaffold for more complex protein structures such as the Fanconi anemia core complex involved in DNA repair to form RUVBl1 (Rajendra, 2014; Dauden, 2021). RUVBL1/2 complexes are also essential for chromatin remodeling as the scaffolding of INO80 family and TIP60 containing complexes (Willhoft, 2020). These functions would require RUVBL2 to be localised to the nucleus of cells to provide access to DNA, which is in agreement to with the nuclear localisation of RUVBL2 observed in control, but not rotenone-treated WT and DJ-1 KO cells via immunofluorescence in the works described herein.

Interestingly, upon rotenone treatment, RUVBL2 expression in cells maintained the severe depletion in DJ-1 KO, but its localisation appeared clearly cytoplasmic in WT cells rather than being confined to the nucleus. This suggests an altered role of RUVBl2 under conditions of oxidative stress. RUVBL1/2 heteromeric complexes have not just been reported to be involved in DNA related functions. They have also been reported to be a part of a large cochaperone complex R2TP or PAQosome involving HSP90, RNA polymerase 2-associated 3 (RPAP3) and PIH1 domain-containing protein 1 (PIH1D1) which may explain changes in localisation (Kakihara, 2012; Houry, 2018).

The “PAQosome or particle for arrangement of quaternary structure” is a large multi protein complex primarily involved in regulating and stabilising the formation of functionally diverse multiprotein complexes via the binding of specific modules or protein adaptors to its scaffold (Houry, 2018). Several of the known complexes formed via this pathway are involved in the eukaryotic translation machinery such as L7AeRNPs, U5 snRNP, RNAPs and some PIKKs (Houry, 2018). Thus, these complexes are localised outside of the nucleus. The altered localisation of RUVBL2 may therefore represent an increased demand of cochaperone activity. This would be expected under conditions of oxidative stress as oxidative modification severely impacts translation through RNA modification (Kong, 2010), protein folding (Cao, 2014) and quaternary structure formation (Dahl, 2015). Indeed, the expression of many cochaperones are redox stress sensitive highlighting the increased demand of their function (Kumsta, 2009). The work described herein showed that in differentiated DJ-1 KO SH-SY5Y cells, RUVBL2 was significantly depleted compared to WT with and without rotenone treatment, suggesting a possible deficiency in both DNA repair, chromatin remodeling and cochaperone activity even in healthy conditions which may play a role in the development of DJ-1 associated Parkinson’s disease through the slow accumulation of DNA, protein, and organelle damage.

This may help to explain the role of RUVBL2 in cells, but why was it detected in EV, and why only RUVBL2 if RUVBL2 complexes primarily with RUVBL1? Interestingly the ratio of RUVBL2 between DJ-1 KO and WT was different in EV compared to cells. In EV RUVBL2 was completed absent in all samples, whereas in cells the ratio of WT RUVBL2 to DJ-1 KO upon rotenone treatment was ~ 1:3 as quantified by western blotting. Despite the relatively low abundance of RUVBL2 in WT EV detected by mass spectrometry, this implies an altered packaging of RUVBL2 into EV as other similarly low abundance proteins were present in the EV of both genotypes. However, RUVBL1, RUVBL2 major complex partner was not detected at all in EV. RUVBL1 and RUVBL2 have been reported to have some antagonistic roles in non-human models, suggesting that their complexing is not necessary for all functions (Diop, 2008). Specifically, these antagonistic roles have been reported in their homologs in Drosophila development and DNA transcription via their association with distinct complexes (Diop, 2008). The low abundance of RUVBL2 in differentiated WT SH-SY5Y EV doesn’t provide confidence in the likelihood of a functional role. Another possible reasoning was perhaps that RUVBL2 was present in EV without RUVBL1 because RUVBL2 (+) RUVBL1 (-) complexes are more susceptible to oxidation-induced damage and thus degradation, resulting in packaging of degradation-fated RUVBL2 into EV for removal. The lack of RUVBL2 in DJ-1 KO EV could then be explained by the altered packaging / targeting of degradation-fated proteins or activation of a separate EV biogenesis pathway previously discussed. However, this is intense speculation

based on heavy assumptions. RUVBL2 requires extensive further investigations to elucidate the reasoning behind its inclusion in EV and what functions it may play in Parkinson's disease.

Other than RUVBL2, the other 2 proteins of interest studied were SYT11 and ZNF451. However, during the period covered by this thesis only 1 preliminary immunofluorescence experiment was performed on these proteins. Therefore, while changes in both proteins were observed in DJ-1 KO cells and upon rotenone treatment, no conclusion can be drawn without further experimentation and further study of RUVBL2, SYT11 and ZNF451 will follow on from this work.

Chapter 7: DJ-1 KO alters the function of differentiated SH-SY5Y-derived EV in control and rotenone treated conditions.

7.1 Introduction

In previous chapters the effects of DJ-1 KO and / or oxidative stress on the number and protein content of EV produced by differentiated SH-SY5Y cells was studied, and it was found that both oxidative stress induced by rotenone and DJ-1 KO resulted in changes to the number of EV. This may be explained by changes to the autophagic degradation pathways of the cells (Chiaradia, 2021) Subsequently, the EV proteome was reported to be altered in EV derived from DJ-1 KO differentiated SH-SY5Y treated with rotenone compared to WT. The idea that protein degradation via autophagy was altered in DJ-1 KO cells in combination with the proteome changes presented an interesting dilemma. If many changes in the proteome are due to altered degradation pathways, what functional state are these proteins in and thus how relevant are the expected functions from pathway analysis? Ultimately, the only way to verify the relevance of EV changes induced by DJ-1 KO was to perform functional assays, treating cells of interest with EV isolated from WT and DJ-1 KO cells under healthy and oxidative stress conditions.

In the introductory chapter of this thesis the functional roles of EV in the CNS were discussed at length in chapter 1, section 1.2.2 “Extracellular vesicles in the CNS”. Briefly, EV derived from many cells of the CNS including both neurons and glia have been reported to show diverse functionality in the CNS. Neurons (Chivet, 2014), oligodendrocytes (Barres, 2013), microglia (Guo, 2020) and astrocytes (Venturini, 2019) have all been reported to produce EV with specific functions related to the cell type of origin. EV function appears to be incredibly important in the CNS as neurons (Chivet, 2014), oligodendrocytes (Barres, 2013), astrocytes (Bianco, 2009) and microglia (Antonucci, 2012) all release EV as a response to neuronal activity via neurotransmitter release.

Indeed, EV release from neurons was largely reported to be associated with synapses where they are involved in synaptic plasticity and homeostasis of the synaptic cleft via interactions with pre/post-synaptic neurons and astrocytes (Bianco, 2009; Morel, 2013; Chivet, 2014; Lee, 2018; Pastuzyn, 2018). However, neuron derived EV are also released from neurites, suggesting a broader role than initially reported (Goldie, 2014). Interestingly, rat cortical neuron-derived EV have been reported to promote an anti-inflammatory phenotype in rat primary microglia (Peng, 2021). Thus, neuron-derived EV, analogous

to differentiated SH-SY5Y derived EV in our studies, appear to show diverse functional capacity in line with the known heterogeneity of EV populations.

The known functions of neuron-derived EV involve synaptic plasticity regulation, synaptic cleft homeostasis, and immunoregulation (Morel, 2013; Chivet, 2014; Venturini, 2019; Peng, 2021). Synapse and immune system regulation were also observed as enriched in the significantly different proteins between DJ-1 KO and WT derived EV in the proteomics study reported in chapter 6. These are features which are of particular interest to Parkinson's disease as synaptic dysfunction and a dysregulated immune system are both believed to be involved in Parkinson's disease pathology (Soukup, 2018; Tansey, 2022). Thus, it was decided that the functional effects of WT and DJ-1 KO differentiated SH-SY5Y EV under healthy conditions and oxidative stress would be studied when applied to human astrocytes and to a macrophage model cell line as preliminary investigations.

7.2 Methodology.

7.2.1 Tissue culture conditions

SH-SY5Y

SH-SY5Y cells were cultured as previously described in chapter 2 section 2.2.2.

Human astrocytes

Human astrocytes (ScienCell: SC-1800-Kit) were acquired from Caltag Medsystems.

Astrocytes were cultured according to the manufacturer's instructions. Briefly, growth surfaces were coated with 2 μg/cm^2 poly-L-lysine (ScienCell: SC-0403) in ddH_2O overnight at 37 °C, and astrocytes seeded at a density of 3000 cells/cm^2 in complete Human astrocyte growth medium (ScienCell: SC-1801 + SC-1852 supplement + SC-0503 Pen/strep + SC-0113 TNS).

THP-1 monocytes

Human THP-1 monocytes (ATCC; LGC Standards, Middlesex, UK) were cultured in 'complete' RPMI 1640 medium (Sigma Aldrich, UK) (10% (v/v) Foetal Bovine Serum (Gibco, UK), 1% Penicillin–Streptomycin and 1% L-glutamine solution (Sigma Aldrich, UK)) and incubated at 37 °C and 5% CO_2. Fresh media was added upon expansion to a cell density of 5×10^5–1×10^6/ml. THP-1 monocytes were differentiated into macrophage-like cells by the following method: THP-1 cells were centrifuged at 300 xg for 5 min, then resuspended in fresh complete RPMI 1640 medium at a density of 5×10^5cells/ml; subsequently differentiation was stimulated with 100 nM dihydroxyvitamin D3 (VD3; Enzo Life Sciences, UK) and incubation at 37 °C for 48 h to allow for complete differentiation into macrophage-like cells.

7.2.2 SH-SY5Y EV sample generation

Cell cultures

In experiments utilising EV from undifferentiated SH-SY5Y, undifferentiated cells were seeded at a density of 800,000 cells in T75 flasks and expanded over 5 days. Standard SH-SY5Y tissue culturing practice was followed during this process.

Where relevant, SH-SY5Y cells were differentiated as described in chapter 2 section 2.2.3.

Rotenone preparation and treatments were performed identically as described in chapter 4 section 4.2.3.

EV samples were isolated and purified via the following method. Cells were removed by centrifugation at 300 x g for 5 min at 4 °C, and the supernatant harvested. EV-containing supernatant was centrifuged at 2000 x g for 20 min at 4 °C to remove cellular debris and the supernatant harvested. For astrocyte functional assays only, EV were stained with 5 μM Bodipy-FL-SE overnight at 4 °C. Concentration of the sample to a volume of 500 μL via a 30 kDa Amicon vertical centrifugal filter column at 4 °C then occurred. EV were purified from the resulting supernatant and free dye via size exclusion chromatography (qEV 70 nm columns, IZON science) according to the manufacturer's instructions. Pure EV samples were subsequently concentrated to ~ 150 μl via a 30 kDa Amicon vertical centrifugal filter column at 4 °C.

7.2.3 THP-1-derived macrophage Migration assay

THP-1 monocytes were differentiated into macrophages via 48 hour treatment with 100 nM vitamin D3 at a cell density of 1*10^6 cells/ml. 80,000 macrophages were subsequently seeded into each porous transwell insert in 300 μl serum-free RPMI media, with each transwell situated in a well of 24 well Corning tissue culture plate containing 700 μl of EV (derived from WT or DJ-1 KO differentiated SH-SY5Y in control or 10 nM rotenone treated conditions), or negative control (Serum-free RPMI). 80,000 THP-1 derived macrophages were also seeded directly into wells in 700 ul serum-free RPMI without transwell insert as positive controls.

Vertical migration of THP-1 derived macrophages was monitored on a Cytation 5 automatic microscope system. Positive controls were used to define the focal height employed for all imaging by focussing on the macrophages directly seeded into the wells and thus residing at the migration finish focal height. Bright-field images were captured at 4 X magnification for 12 hrs with 4 images being captured per well every 30 min.

Each set of 4 images was subsequentially stitched together. A minimum pixel intensity threshold of 3000 was applied to generate a mask, holes in masks were filled and touching objects split. Cells were defined as objects with a diameter ranging from 10 to 50 μm, and cell counts generated.

For this experiment N = 3 individual cultures.

7.2.4 Assay of the effects of differentiated SH-SY5Y EV on Astrocytes

Glass coverslips were coated with 2 μg/cm^2 poly-L-lysine (ScienCell: SC-0403) in ddH_2O overnight at 37 °C. Subsequently, astrocytes were seeded at a density of 3000 cells/cm^2 onto coated coverslips in a 24-well corning tissue culture plate, in complete Human astrocyte growth medium (ScienCell: SC-1801 + SC-1852 supplement + SC-0503 Pen/strep + SC-0113 TNS). Astrocytes were then expanded until 70% confluency at 37 °C and 5 % CO_2.

After expansion, astrocyte cultures were treated with 20 μl of EV samples or DPBS (EV sample solvent) as negative control for 24 hours at 37 °C and 5 % CO_2. Astrocytes were then fixed with 4 % paraformaldehyde for 20 min, followed by 1 quick wash and 3 5-minute washes with PBS (Calcium and magnesium negative; Gibco, 20012019). Fixed cells were blocked for 30 min at room temp in blocking buffer (1 % w/w BSA (Sigma-Aldrich, A3059), 0.2 % v/v Triton™ (Sigma-Aldrich, X-100), in 1 X PBS). Astrocyte cultures were treated with the following primary antibodies for markers of interest: 1:200 anti-GFAP (Mouse monoclonal; Millipore, MAB360); 1:4000 anti-DJ-1 (mouse monoclonal; Novus Biologicals, NBP1-92715); S100 β (Rb monoclonal; Abcam, ab52642) in blocking buffer overnight at 4 °C. Cultures were either stained for GFAP alone or DJ-1 and S100. After primary antibody incubation, cells were washed 3 times with PBS for 5 min. Cell nuclei were then stained with 1:2000 Hoechst 33342 for 5 min at room temperature, and then washed 3 times for 5 min with PBS. Nuclei staining was followed by treatment with the following secondary antibodies in blocking buffer for 1 hr at room temperature, dependent on the species of the primary antibody animal source: mouse primaries were stained with alexa 555-conjugated donkey anti-mouse secondary antibody (Donkey mono, Invitrogen; A31572); rabbit primaries were stained with alexa-647-conjugated donkey anti-rabbit secondary antibody (Donkey mono, Invitrogen; A31571). Cells were finally washed 3 times with PBS for 5 min, and mounted onto glass microscope slides using Mowiol.

Stained astrocytes were imaged on a Leica SP8 Falcon confocal microscope system, employing the DAPi, alexa 488, alexa 555 and alexa 647 dye assistant settings for Hoechst-stained nuclei, EV, GFP, and S-100/DJ-1 staining respectively. 5 images per stain were captured with constant gain and laser power for all images of a specific marker.

Stain intensity, area and integrated density was analysed for GFAP, S-100 and DJ-1 staining in FIJI (ImageJ). Nuclei morphology was characterised via the Stardist deep-learning plugin for nucleus ROI

detection in FIJI. This process was automated via imageJ macro scripts written by me and available in thesupplementary section and at Github https://github.com/Bioinformatics-enthusiast/PHD-FIJI/blob/ecf1554bc45758d7d5f37d3f8d26a4f9041e8d0b/Astrocyte%20Nuclear%20morphol%20%2B%20GFAP.ijm + https://github.com/Bioinformatics-enthusiast/PHD-FIJI/blob/ecf1554bc45758d7d5f37d3f8d26a4f9041e8d0b/Astrocyte%20Nuclear%20morphol%20%2B%20C3%2B4%20stain.ijm.

Statistical analysis was carried out in R.

For this experiment N = 2.

7.3 Results.

7.3.2 Promotion of macrophage migration by EV is dependent on DJ-1 and rotenone-induced oxidative stress in EV source cells

The goal of the work described in this chapter was to elucidate any functional changes in EV from WT and DJ-1 differentiated SH-SY5Y under healthy conditions and conditions of oxidative stress. This was principally analysed by assessing promotion of THP-1-derived macrophage migration by EV from each condition.

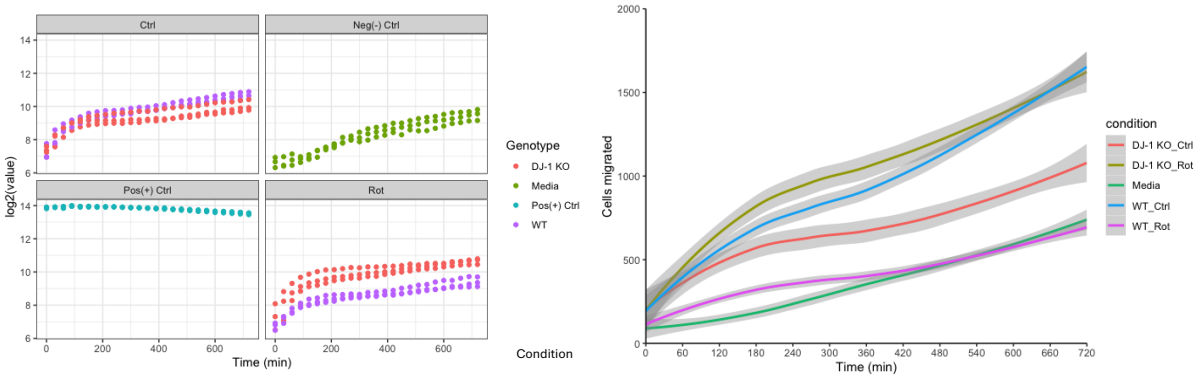

Figure 7.1 Promotion of macrophage migration by EV is dependent on DJ-1 KO and rotenone-induced oxidative stress in EV source cells. Plots of THP-1-derived macrophage migration promoted by EV from WT and DJ-1 KO differentiated SH-SY5Y under conditions of healthy and rotenone-induced oxidative stress. Left graph: migration (y axis = migrated cells, log2 transformed) in individual replicates including positive control; colour indicates condition; panels = top left – EV from healthy control cells, top right – negative control, bottom left – positive control, bottom right – EV from rotenone treated cells. Right graph: LOESS smoothing of migrated cell counts on time for each condition excluding positive control; colour indicates condition; error indicated by grey region surrounding lines.

Differences in the trend line intercepts and overall rate of migration between all conditions bar positive control, were assessed via a mixed effect model of the following form:

$$\text{Migrated cells} \sim \text{polynomial}(\text{Time}, 2\text{nd degree}) * \text{condition} + (1 + \text{polynomial}(\text{Time}, 2\text{nd degree})|\text{culture})$$

Firstly, conditions other than positive control were compared to negative control. Regarding intercepts, all conditions except for EV from rotenone treated WT cells were significantly different from negative control (Table 7.1/2, Figure 7.1). On the other hand, only EV from WT ctrl and rotenone-treated DJ-1 KO cells promoted a significantly different overall rate of migration compared to negative control (Table 7.3/4, Figure 7.1).

Table 7.1 Estimated marginal means for each migration assay condition. Condition = migration promoter condition; emmean = estimated marginal mean (i.e model intercept); SE = standard error of the mean; df = degrees of freedom; lower.CL and upper.CL 95 % confidence limits. Calculated via emmeans R package.

condition	emmean	SE	df	lower.CL	upper.CL
DJ-1 KO Ctrl EV	700	75.7	10	531	869
DJ-1 KO Rot EV	1087	75.7	10	918	1256
WT Ctrl EV	952	75.7	10	783	1121
WT Rot EV	416	75.7	10	247	585
Neg control	343	75.7	10	174	585

Table 7.2 Estimated marginal mean contrasts between assessed conditions of interest. Contrast = conditions compared and order of comparison; difference = difference in estimated marginal means between conditions as defined in contrast; SE = standard error of the estimate; df = degrees of freedom; p.value = FDR adjusted p value. Contrasts calculated via Dunnet's test using emmeans R package.

contrast	difference	SE	df	t.ratio	p.value (FDR)
DJ-1 KO Ctrl EV – neg control	357.1	107	10	3.336	0.0101
DJ-1 KO Rot EV – neg control	743.9	107	10	6.95	0.0002
WT Ctrl EV – neg control	608.9	107	10	5.689	0.0004
WT Rot EV – neg control	73.1	107	10	0.683	0.5103
DJ-1 KO ctrl EV – DJ-1 KO rot EV	-387	116	10	-3.322	0.0210
DJ-1 KO ctrl EV – WT ctrl EV	-252	116	10	-2.163	0.0750
DJ-1 KO ctrl EV – WT rot EV	284	116	10	2.439	0.061
DJ-1 KO rot EV – WT ctrl EV	135	116	10	1.159	0.2797
DJ-1 KO rot EV – WT rot EV	671	116	10	5.761	0.0025
WT ctrl EV – WT rot EV	536	116	10	4.601	0.0053

Table 7.3 Estimated marginal mean coefficients of the effect of time on migration (rate of migration) for each condition. Condition = migration promoter condition; Time.trend = effect of time on migration (migration rate); SE = standard error of mean; df = degrees of freedom; lower and upper.CL, 95 % confidence limits. Calculated via emmeans R package.

condition	Time.trend	SE	df	lower.CL	upper.CL
DJ-1 KO Ctrl EV	0.993	0.164	10	0.628	1.36
DJ-1 KO Rot EV	1.691	0.164	10	1.326	2.06
WT Ctrl EV	1.805	0.164	10	1.441	2.17
WT Rot EV	0.697	0.164	10	0.332	1.06
Neg control	0.928	0.164	10	0.564	1.29

Table 7.4 Estimated marginal mean coefficient contrasts between assessed conditions of interest. Contrast = conditions compared and order of comparison; difference = difference in estimated marginal mean coefficient between conditions as defined in contrast; SE = standard error of the estimate; df = degrees of freedom. Contrasts calculated via Dunnet's test using emmeans R package.

contrast	difference	SE	df	t.ratio	p.value (FDR)
DJ-1 KO Ctrl EV – neg control	0.0647	0.232	10	0.280	0.7855
DJ-1 KO Rot EV – neg control	0.7621	0.232	10	3.291	0.0163
WT Ctrl EV – neg control	0.877	0.232	10	3.788	0.0142
WT Rot EV – neg control	-0.2315	0.232	10	-1	0.4547
DJ-1 KO ctrl EV – DJ-1 KO rot EV	-0.697	0.232	8	-3.01	0.0252
DJ-1 KO ctrl EV – WT ctrl EV	-0.812	0.232	8	-3.506	0.016
DJ-1 KO ctrl EV – WT rot EV	0.296	0.232	8	1.279	0.2842
DJ-1 KO rot EV – WT ctrl EV	-0.115	0.232	8	-0.496	0.6332
DJ-1 KO rot EV – WT rot EV	0.994	0.232	8	4.289	0.008
WT ctrl EV – WT rot EV	1.108	0.232	8	4.785	0.008

Furthermore, comparisons between the intercepts and rate of migration in each EV-containing condition were assessed via the same method. In terms of intercept, half of the comparisons were significantly different: DJ-1 KO Ctrl vs DJ-1 KO Rot EV; DJ-1 KO Rot EV vs WT Rot EV; and WT Ctrl EV vs WT Rot EV

(Table 7.1/2, Figure 7.1). When investigating rate of migration, it was observed that 4 out of 6 comparisons showed significantly different rates of migration: DJ-1 KO Ctrl EV vs DJ-1 KO Rot EV and WT Ctrl EV; DJ-1 KO Rot EV vs WT Rot EV; and WT Ctrl EV vs WT Rot EV (Table 7.3/4, Figure 7.1).

7.3.2 Treatment with EV from WT and DJ-1 KO SH-SY5Y cells alters the phenotypic profile of human astrocytes in a preliminary study.

Towards a more complete understanding of the functional effects of SH-SY5Y EV, their effects on human astrocytes were studied in a preliminary study of N = 2 replicates. Due to the preliminary nature and low replicate number, this work was not analysed statistically.

Changes in astrocyte phenotype upon EV treatment were assessed via the markers GFAP, S100 and DJ-1. The total study was broken down into 2 sub studies, one where EV from differentiated WT SH-SY5Y under healthy and oxidative stress conditions were employed, and one where EV from undifferentiated WT and DJ-1 KO SH-SY5Y under oxidative stress conditions only were employed.

Investigations into the effects of EV from WT differentiated SH-SY5Y on human astrocytes

As first result, bodipy-stained EV could be observed in cell cultures where treatment occurred and not in the no EV treatment control (Figure 2A), thus, validating correct treatment procedure. Furthermore, it was observed that while S100 and DJ-1 immunofluorescent signal was present throughout the majority of astrocytes (Figure 2B.), GFAP showed substantially higher specificity to singular cells with the majority appearing to be GFAP negative in contrast to S100 and DJ-1 (Figure 7.2).

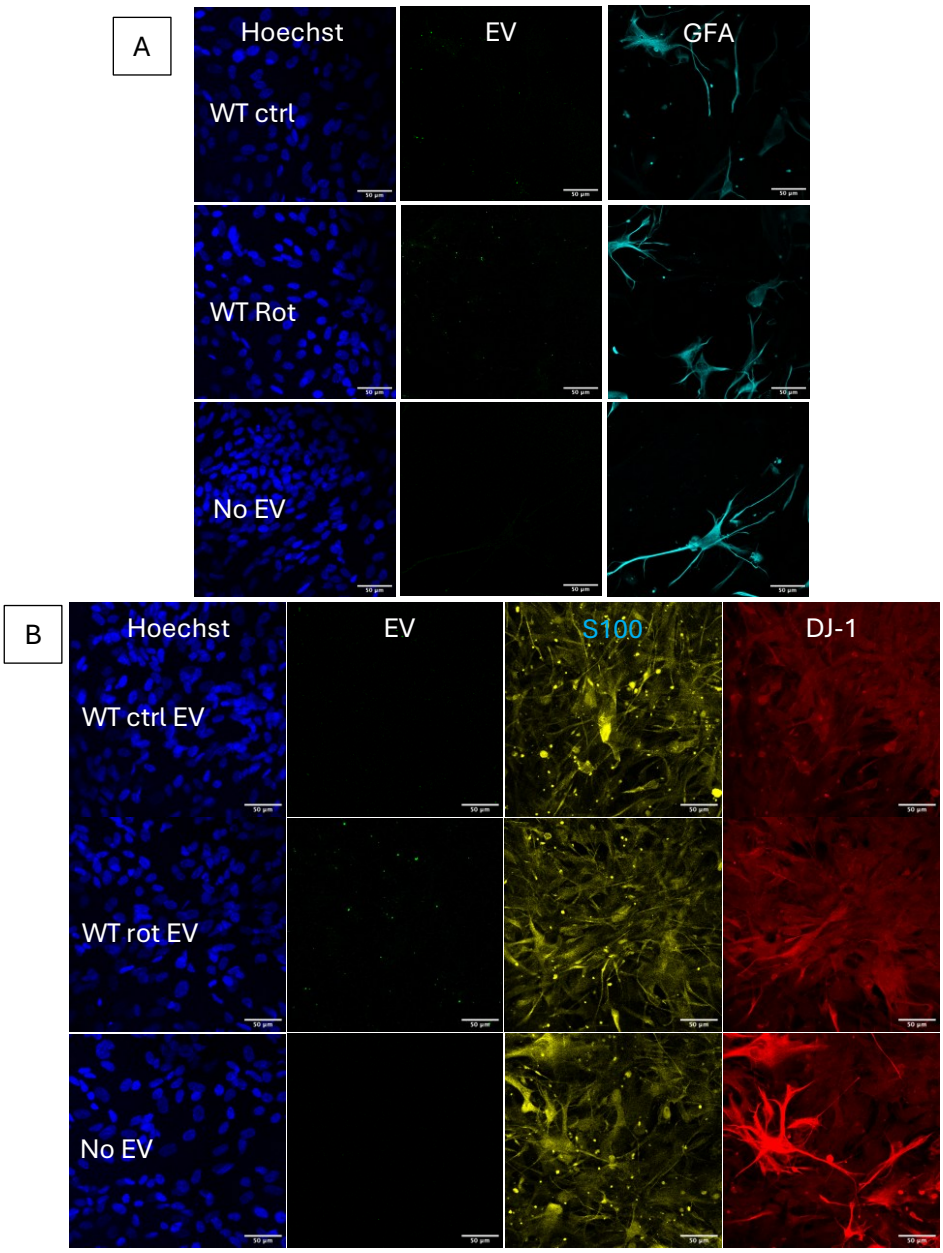

Figure 7.2 Confocal microscopy of Astrocyte markers of interest with or without treatment with WT differentiated SH-SY5Y EV. Sub figure A: Images of astrocyte cultures stained for GFAP; rows equate to treatment conditions and columns to nuclei, EV and GFAP fluorescence. Sub figure B: Images of astrocyte cultures stained for S100 and DJ-1; rows equate to treatment conditions and columns to nuclei, EV, S100 and DJ-1 fluorescence. All images were captured on a Leica SP8 confocal microscope platform.

To assess phenotypic changes in human astrocytes upon treatment with EV from WT differentiated SH-SY5Y, nuclei size (a measure of transcriptional activity), and marker fluorescence was assessed.

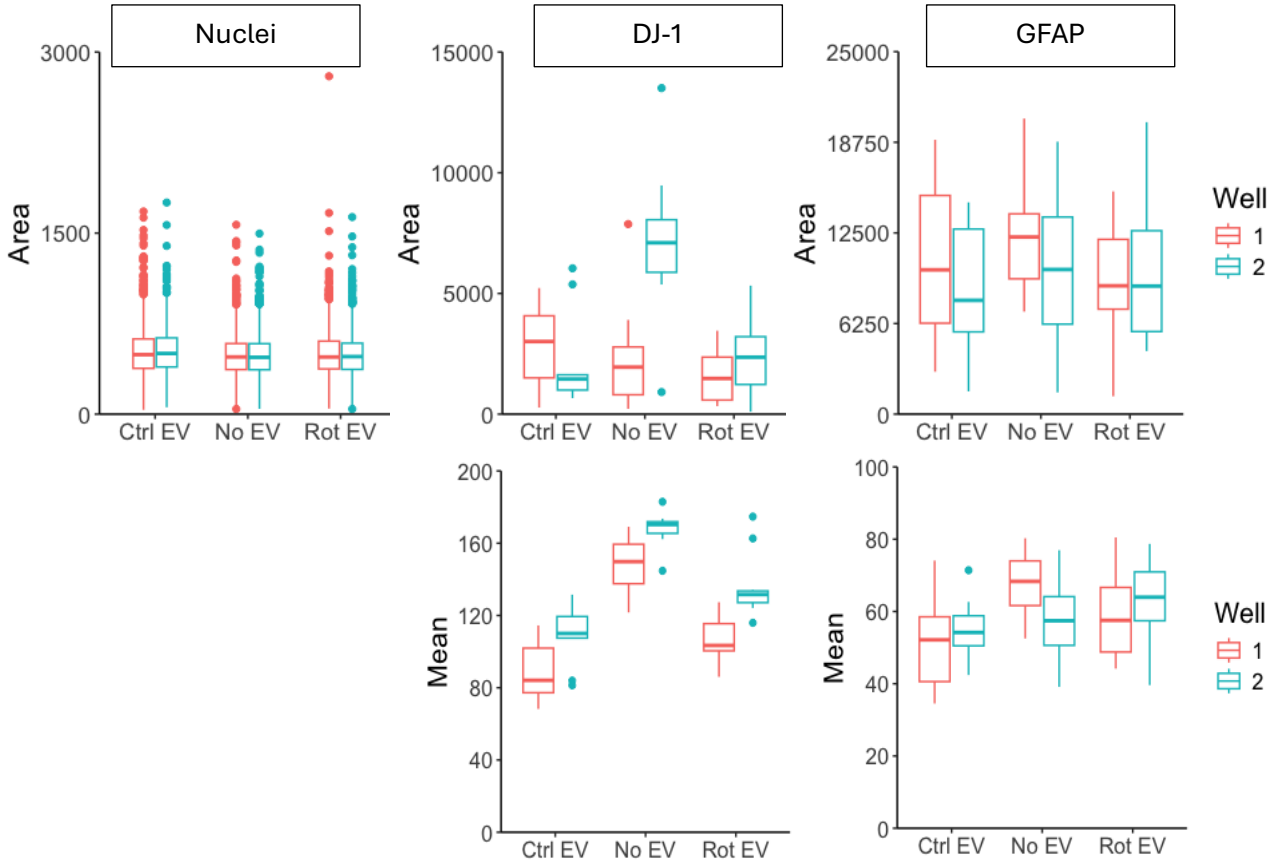

Figure 7.3 Quantification of nuclei area, and GFAP and DJ-1 fluorescence mean and area in human astrocytes upon treatment with WT differentiated SH-SY5Y EV. Quantification of nuclei area in column 1, DJ-1 features in column 2, and GFAP features in column 3 respectively. Quantification carried out in FIJI (ImageJ). Boxplots represent variation in parameter values within the image sets (10 images) of each well. Individual wells per condition are represented via colouration.

Interestingly, via quantification it was observed that both treatment with EV from healthy and rotenone-treated WT differentiated SH-SY5Y presented with higher DJ-1 fluorescence intensity without corresponding increase in area outside of well 2 (Figure 7.3). This confirmed what previously observed by eye in the raw images (Figure 7.2). On the other hand, no differences in nuclei area were observed. Regarding GFAP staining a small observable effect was observed wherein fluorescence intensity increased in both EV treatments.

Investigations into the effects of EV from rotenone-treated undifferentiated WT and DJ-1 KO SH-SY5Y on human astrocytes

Similarly to the above-described investigation into the effects of EV on astrocytes, the markers GFAP, S100 and DJ-1 were investigated in human astrocytes. However, rather than treating astrocytes with EV from differentiated WT SH-SY5Y, astrocytes were treated with EV from rotenone-treated undifferentiated WT and DJ-1 KO SH-SY5Y.

Interestingly, the strong increase in DJ-1 mean intensity in non-EV-treated astrocytes compared to EV treated astrocytes observed in the previous experiment did not manifest when employing EV from undifferentiated cells. However, EV treated astrocytes showed a DJ-1 area distribution with a larger righthand tail, thus a higher number of images with high DJ-1 stain area. Furthermore, regarding GFAP staining, DJ-1 KO EV treatment resulted in a similar GFAP stain area to that of no EV treatment in astrocytes, with both conditions showing substantially different GFAP stain area to that of WT EV treated astrocytes.

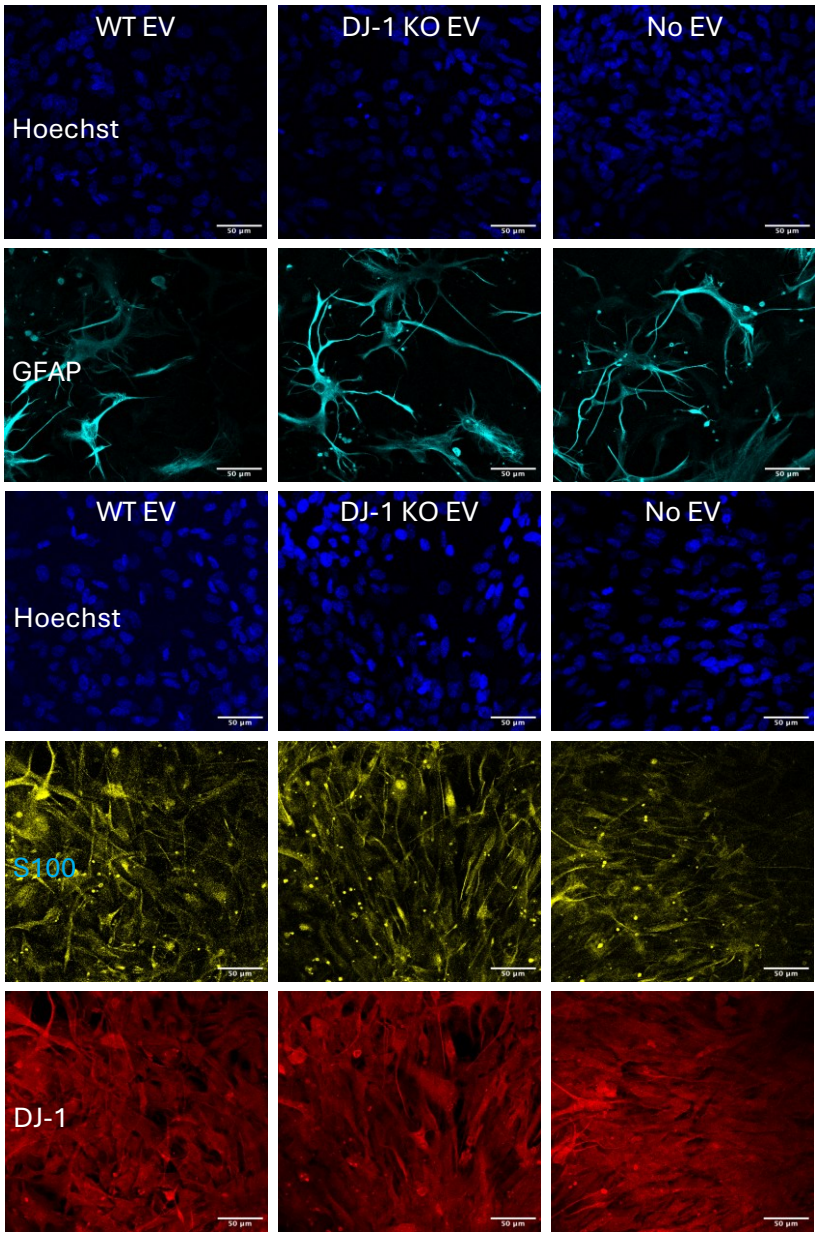

Figure 7.4 Images of astrocyte cultures stained for GFAP, S100 and DJ-1. Columns represent treatment conditions. Rows from top to bottom: 1 = Nuclei staining for GFAP stained cells; 2 = GFAP staining; 3 = Nuclei staining for S100 and DJ-1 stained cells; 4 S100 staining; 5 = DJ-1 staining. All images were captured on a Leica SP8 confocal microscope platform.

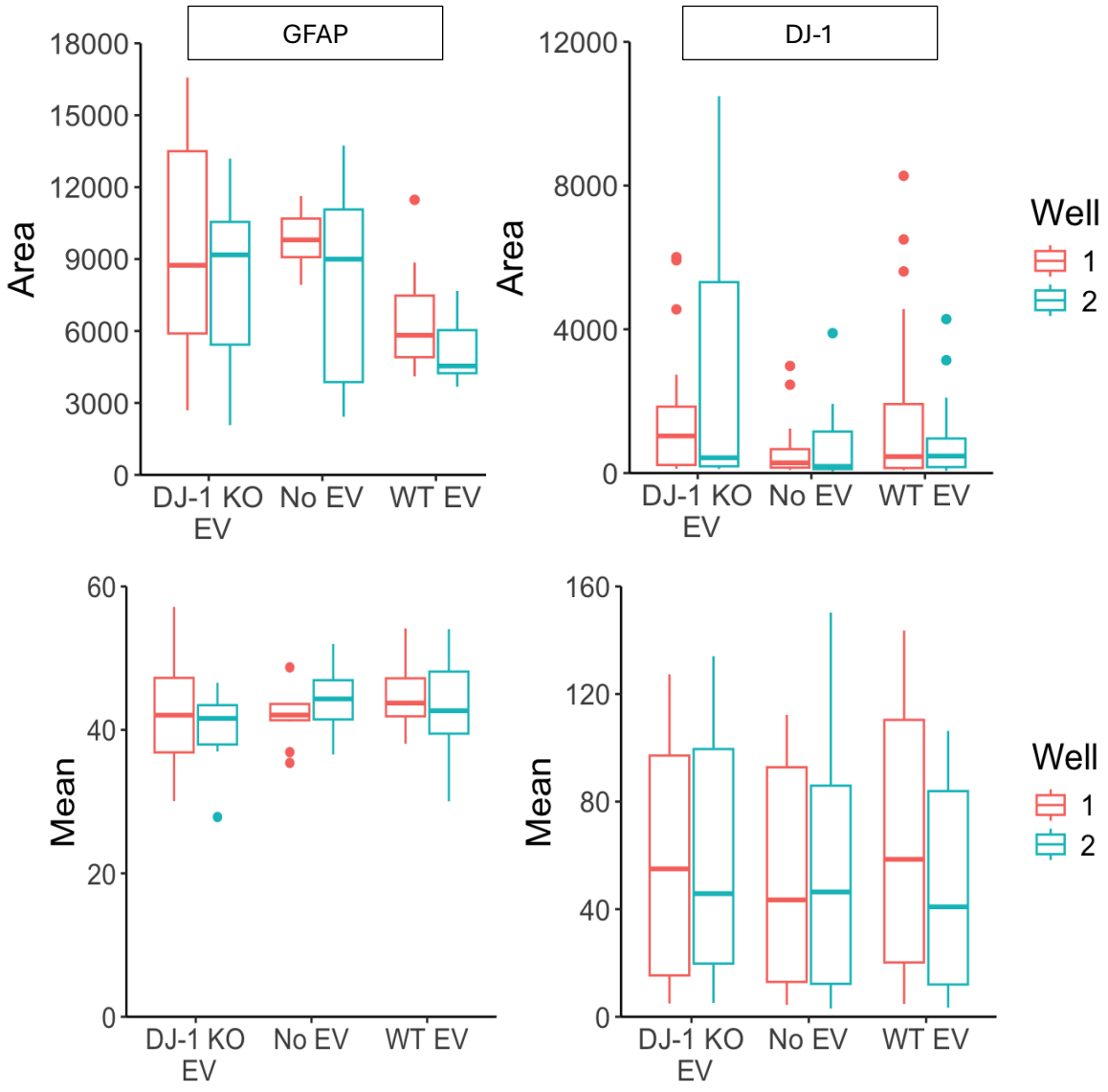

Figure 7.5 Quantification of GFAP features in column 1, and DJ-1 features in column 2 respectively. Quantification carried out in FIJI (ImageJ). Boxplots represent variation in parameter values within the image sets (10 images) of each well. Individual wells per condition are represented by different colours.

7.4 Discussion

7.4.1 Promotion of monocyte-derived macrophage migration by SH-SY5Y EV is dependent on DJ-1 and rotenone-treatment of source cells

Towards an understanding of how neuronal EV may interface with the wider CNS under conditions of oxidative stress and DJ-1 KO, both features linked to or causative of Parkinson's disease, the effects of SHSY5Y EV were investigated on macrophage migration and astrocyte phenotype.

Macrophage migration in the case of the CNS is relevant primarily to the motile actions of microglia (Perry, 2013), the CNS resident macrophage population. However, research has also shown that infiltration of monocyte-derived macrophages into the CNS can occur under certain conditions (Perry, 2013)

Interestingly in the migration assay reported in this chapter, it was observed that only EV from rotenone-treated WT SH-SY5Y did not promote migration of monocyte-derived macrophages in a distinct manner from the negative control. Also, EV from rotenone treated differentiated SH-SY5Y produced the opposite effect on migration in DJ-1 KO vs WT. Both rotenone-treated DJ-1 KO EV and healthy WT EV promoted the highest level of migration and were not significantly different from each other.

Several aspects were considered as explanations for the differential effect of EV from rotenone treated wild type and DJ-1 KO cells. An increased amount of EV would increase promotion of macrophage migration through increase of signal quantity. However, known quantities of EV in these employed conditions from previous chapters suggested that both control conditions present with the lowest level of EV and the rotenone treated with the most. Notably, rotenone treatment does not consistently increase EV promotion of migration as it did EV number, thus EV number can be ruled out as a mechanism. This experiment also suggested that oxidative stress would consistently reduce migration levels, as both DJ-1 KO without rotenone treatment and rotenone treatment of WT cells reduced EV promotion of migration. However, this theory breaks down when both DJ-1 KO and rotenone are applied together wherein the highest level of promotion was observed, equal to that of WT control EV, leaving the interesting divergent response to rotenone in DJ-1 KO and WT cells. This may potentially represent a threshold of oxidative damage accumulation before an alternate pathway or alternate pathway entry point is employed, that is only reached under such conditions.

Multiple CNS disease states have been associated with increased microglia migration and monocyte-derived macrophage infiltration and migration (Gao, 2023). However, while microglia migration in disease states appears to be linked to an inflammatory phenotype, there is evidence that peripheral monocyte-derived macrophage infiltration is linked to tissue repair and inflammation resolution (Park, 2022; Gao, 2023). Rotenone-treated DJ-1 KO EV and healthy WT EV should represent the opposite ends of the spectrum in terms of disease relevance, yet both conditions stimulate the highest level of migration. Why, and how does this fact match the currently understood role of microglia and infiltrating macrophages in CNS disease? This interestingly observation is further complicated by the fact that EV from "healthy" DJ-1 KO SH-SY5Y stimulated a middling level of migration, and that rotenone-treated WT EV stimulated none.

The effect of EV effects on macrophage migration is clearly complicated and doesn't explain the whole story without further investigation into the difference in peripheral monocyte and microglial migration. It is potentially possible that while two conditions may stimulate the same level of monocyte derived macrophage migration, they would not do so for microglia, a nuance that would not have been detected by this study.

Furthermore, the disease relevant functional effects of EV are likely also mediated by alteration of the inflammatory phenotype, independently from any changes to migration (Keren-Shaul, 2017; Yin, 2017). Migration is known to not be associated with either pro or anti-inflammatory phenotypes. Rotenone-treated DJ-1 KO EV could for example cause the known anti-inflammatory phenotype of the infiltrating macrophages to switch to a pro-inflammatory phenotype similar to disease-relevant microglia states (Keren-Shaul, 2017; Park, 2022; Gao, 2023), whereas healthy WT EV may promote this pro-repair and anti-inflammatory phenotype. Similarly, the lower level of migration induced by "healthy" DJ-1 KO EV could result in an imbalance in pro and anti-inflammatory macrophages/microglia due to lower infiltration, and may represent a deficiency in macrophage homeostatic function (Yin, 2017), a situation which could contribute to Parkinson's progression via inflammation induced cell damage, synaptic pruning dysfunction, and or dysfunction clearance of cellular waste/debris.

However, this still leaves the issue of rotenone-treated WT EV, a condition which promoted no migration. Further studies are thus heavily required to truly understand the effects of these EV on macrophages and inflammation. Particularly it is important to understand the phenotype of these monocyte derived macrophages, whether they are inflammatory m1 or pro-repair m2. Furthermore, it would be interesting to investigate if promotion of migration differs in microglia compared to monocyte derived

macrophages, and again test for difference in inflammatory phenotype specifically in microglia. This is particularly important in the case of rotenone-treated WT EV where no migration occurred, as migration may not play as important a role in the activity of microglia which show more prominent migration in the CNS during development (Smolders, 2019).

Mechanistically speaking, at least in the case of rotenone-treated cell-derived EV, a more specific conclusion can be derived based on the EV proteomics dataset generated as part of this project. In accordance with these data, the primary influencer of migration promotion could indeed be the presence or absence of CD47 on EV. CD47 is a membrane protein with an extracellularly exposed region that is known to prevent phagocytosis of cells by macrophages (Takimoto, 2019). It has particularly high relevance in cancers where it correlates with an aggressive phenotype via the causation of immune evasion (Takimoto, 2019).

What is particularly interesting about CD47 is that in work performed by a colleague, inhibition of EV-localised CD47 activity via blocking antibody resulted in an increase in migration promotion by EV (unpublished results; Butler}. This is particularly relevant to the research described herein as CD47 was severely depleted in rotenone-treated DJ-1 KO EV compared to rotenone-treated WT EV in the proteomics study reported in chapter 6. Rotenone-treated DJ-1 KO EV presented with the highest promotion of migration and rotenone-treated WT with the least, suggesting that this severe difference in migration promotion could be mediated by CD47. In future studies it would be of interest to understand whether the anti-phagocytosis function of CD47 on cells also applies to EV (Takimoto, 2019). If phagocytosis of EV is altered, the functional effects of EV on macrophages can be modified, as phagocytosis is a known mechanism through which effects can be exerted (Mulcahy, 2014). Under conditions of phagocytosis and migration impairment together the ability of EV to functionally affect macrophages would logically be heavily impaired or removed.

A further avenue of study may also be to restrict the statistical analysis of migration rate to a specified time window. The data obtained in this work showed that between 0 and 300 minutes the highest rates of migration were observed in all conditions. Furthermore, this time frame showed a difference in migration rate between rotenone-treated WT EV and negative control, not present when considering a longer time of analysis. If true, this may provide another aspect to consider in relation to macrophage functionality.

Ultimately, despite the lack of understanding regarding some of the changes in migration reported herein, this work highlights a novel, so far unknown function of DJ-1in inter-cellular communication. DJ-1 was originally identified as ROS sensor protein involved in the protective response against oxidative stress. Later work has reported DJ-1 function in the regulation of the immune system (Zhang, 2020). Our results build on this specific role of DJ-1, showing that it can influence macrophage migration via an altered EV response. Whether this is an indirect or direct effect is debatable, but the importance of DJ-1 is self-evident and represents a previously unknown functional mechanism for DJ-1 action on the immune system.

7.4.2 Treatment of human astrocytes with EV from WT and DJ-1 KO SH-SY5Y appears to alter their phenotype

The CNS is a complex interconnected system, consisting of multiple distinct cell types all with their own complex functions (Zeng, 2018). Thus, it was imperative to not only focus on a single cell type in the preliminary investigations into EV function that are described in this chapter. The secondary cell type of interest for an investigation into EV functionality was the astrocytes. A preliminary investigation into the effects of EV treatment on GFAP, DJ-1 and S100 in human astrocytes was thus performed. However, this was a decidedly preliminary investigation into the feasibility of study and as such must be interpreted under the limitation of an insufficient N number.

While this was the case, there are several outputs, primarily around the feasibility of the assay that can be confidently asserted. Firstly, EV presence in treated astrocyte cultures was observed, potentially representing the capability to study EV uptake as a predictor of functional changes. Secondly, all 3 markers of interest, GFAP, DJ-1 and S100 were detectable via immunofluorescence microscopy. Thirdly and finally, it was possible to quantify the fluorescence intensity and morphological features such as area of the markers.

Despite the insufficient N number, and thus statistical analysis for confident assertions, several interesting observations were made. In the experiment in which the EV of differentiated WT SH-SY5Y were employed to treat astrocytes, it was observed that DJ-1 mean intensity appeared to be different between all conditions. From highest to lowest the conditions were “no EV”, “rotenone-treated WT EV”,

“healthy WT EV”. Interestingly, both EV treatments reduced DJ-1 mean intensity, potentially representing a more active/stressed astrocyte state due to a lack of expected signals from other cell types. On the other hand, when investigating the quantification of markers in astrocytes treated with undifferentiated SH-SY5Y EV, the changes observed upon differentiated SH-SY5Y EV treatment were not seen. Instead, a decrease in GFAP stain area occurred under treatment with DJ-1 KO rotenone treated EV only.

At this juncture, the overall feasibility of the method appeared to be good and verified. However, results showed higher inconsistency than expected between images, wells and batches. These experiments thus provide a solid baseline for further study into the functional effects of EV on human astrocytes but does require further fine tuning of the method for an optimal use case.

Chapter 8: Conclusions.

Over the course of this thesis, novel advances in understanding the link between DJ-1 and EV has been reported on and discussed in detail. Several novel discoveries were made into the involvement of DJ-1 in the pathways of EV uptake, and biogenesis and packaging under conditions of oxidative stress. These discoveries have ultimately revealed the imperative function of DJ-1 in correct response to oxidative stress via EV, creating new understanding of DJ-1-linked Parkinson's disease and opening new avenues of research into the role of EV and DJ-1 in oxidative stress responses and Parkinson's disease pathology. Overall, the discoveries made can be broken down into 3 major features.

Firstly, DJ-1 KO results in distinct reaction pattern to increasing concentrations of rotenone treatment. Rotenone treatment in both WT and DJ-1 KO increased the amount of EV detected (Fig 5.1). This likely represents a true increase in production of EV as described in previous work by other researcher groups reporting on EV production under oxidative stress (Record, 2018). However, in DJ-1 KO cells a higher concentration of rotenone was required to elicit a response (Fig 5.1). This may be due to the decreased ability of DJ-1 KO cells to sense low levels of oxidative stress. Indeed, DJ-1 function is altered via oxidative modification of its Cys106 residue sidechain. Cys106 is a sulphur containing side chain wherein the pKa is depressed to the low value of 5.4 maintaining thiolate anion via the stabilising effect of hydrogen bonds to surrounding residues (Witt, 2009; Wilson, 2011). This state renders the residue incredibly susceptible to oxidation and thus underpins the role of DJ-1 in the sensing of low concentration ROS (Witt, 2009). Furthermore, this increase in EV production may represent the outcome of overwhelmed or blockaded autophagic degradation pathways, both of which are known to occur due to toxins which act similarly to rotenone and have been reported to induce EV production (Chiaradia, 2021). However, it is clear that while DJ-1 is necessary for this effect at low levels of ROS, it is not required for this effect at relatively higher concentrations of ROS, suggesting that an alternate pathway is employed or that the same pathway is activated via a different mechanism in place of DJ-1, such as a reaction to oxidative damage to intracellular components rather than the direct reaction to ROS mediated by DJ-1. The impairment of internal cellular component degradation and thus EV production increase leads nicely into the second discovered feature.

Under conditions of oxidative stress induced by rotenone treatment wherein both WT and DJ-1 KO show increased EV number, the proteomic content of EV is altered (Fig 6.2). Whether it is correct that impaired

autophagic degradation is responsible for the changes in EV number and protein cargo is debateable, however the importance of DJ-1 in protein packaging into EV under oxidative stress is evident. DJ-1 KO under sufficient rotenone treatment resulted in a distinct set of functional enrichments in differentially expressed proteins compared to a previous study of EV components under oxidative stress (Chapter 6) (Benedikter, 2019). These results highlight the role of DJ-1 in correct intercellular signalling under oxidative stress and indicate that the reported effects are not simply due to increased levels of oxidative stress when lacking DJ-1. With both the amount and protein cargo of EV being altered under sufficient oxidative stress and DJ-1 KO, it would be expected that these EV should behave differently. Which brings the final feature into light.

In both healthy and oxidatively stressed conditions DJ-1 KO changed the functionality of EV regarding their ability to promote macrophage migration (Fig 7.1). Under rotenone treated conditions, EV produced from WT cells did not stimulate migration, whereas those from DJ-1 KO cells stimulated the highest rate of migration (Fig 7.1). Interestingly this was potentially explainable by the presence or absence of CD47 on the EV, a protein which inhibits macrophage migration promotion by EV (Butler, unpublished results) and phagocytosis of cells by macrophages (Takimoto, 2019). EV from WT cells treated with rotenone showed relatively high levels of CD47, and did not promote migration (Fig 6.6; Proteomics results, supplementary section). EV from DJ-1 KO cells treated with rotenone showed relatively low levels of CD47 and stimulated a high level of migration (Fig 6.6; Proteomics results, supplementary section; Fig 7.1). If CD47 is indeed responsible for the difference this raises an interesting question, is phagocytosis of EV impaired if CD47 is present at a high concentration? If so EV from WT cells would likely not be destined to affect macrophages at all, and would explain the lack of migration stimulation. On the other hand, EV from DJ-1 KO cells may both promote macrophage migration and be phagocytosed by macrophages. This could represent a means of disposing of increased levels of damaged proteins produced due to autophagy impairment in a safe manner, but may also contribute to inflammation.

Overall, it is interesting that the major features of DJ-1 KO that were observed are all related to intracellular trafficking and packaging via vesicular pathways. Mutations in genes involved in lipid metabolism such as GBA1 (Sidransky, 2009), VSP35 (Zavodszky, 2014) and PINK1 (Valente, 2004) have been known to be causative of familial Parkinson's disease for many years now. However, lipidopathy has received substantially less interest than proteinopathy as an aspect of Parkinson's disease but has recently been highlighted in an in-depth review by Manuel Florel-Leon and Tiago Fleming Outeiro

(Flores-Leon, 2023). Altered lipid homeostasis may be an interesting avenue of research to pursue in the case of DJ-1 as it would link the features of impaired intracellular vesicular trafficking and degradation, and mitochondria dysfunction observed (Florel-Leon, 2023).

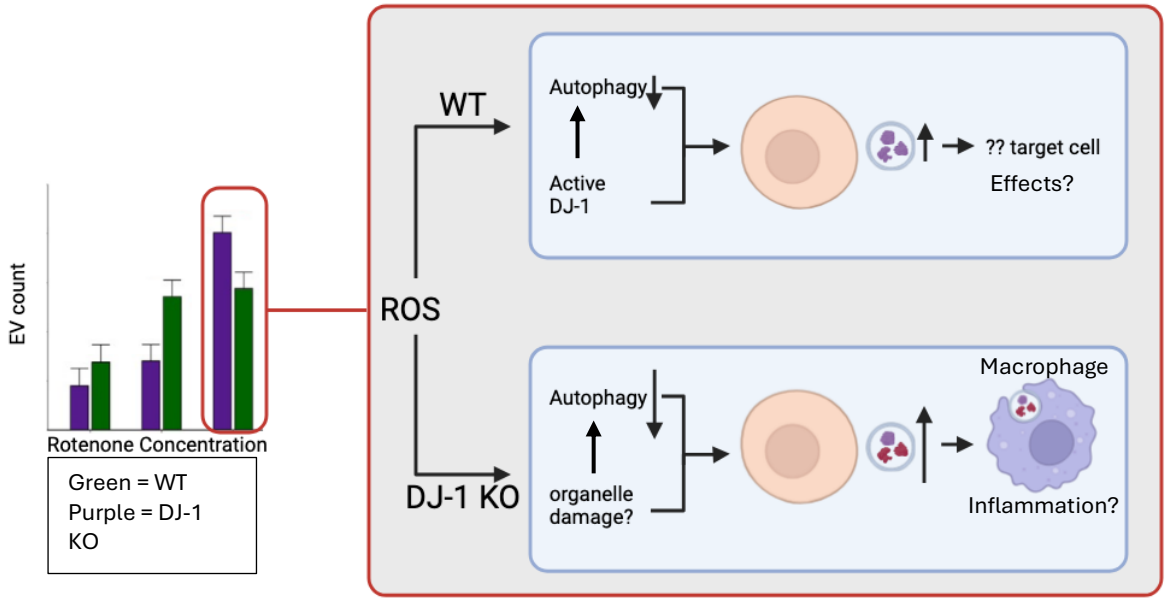

Figure 8.1 Graphical abstract of conclusions derived from reported works. A diagram briefly described the reported effects of DJ-1 KO on EV and proposed methods of action. Made in Biorender.

References

Abbas, M. M., et al. (2016). "Early Onset Parkinson's disease due to DJ1 mutations: An Indian study." Parkinsonism & Related Disorders 32: 20-24DOI: 10.1016/j.parkreldis.2016.04.024.

Abou-Sleiman, P. M., et al. (2003). "The role of pathogenicDJ-1 mutations in Parkinson's disease." Annals of Neurology 54(3): 283-286DOI: 10.1002/ana.10675.

Adebayo, M., et al. (2021). "Mitochondrial fusion and fission: The fine-tune balance for cellular homeostasis." The FASEB Journal 35(6)DOI: 10.1096/fj.202100067R.

Ahmad, S., et al. (2022). "Role of Extracellular Vesicles in Glia-Neuron Intercellular Communication." Frontiers in Molecular Neuroscience 15DOI: 10.3389/fnmol.2022.844194.

Akers, J. C., et al. (2013). "Biogenesis of extracellular vesicles (EV): exosomes, microvesicles, retrovirus-like vesicles, and apoptotic bodies." Journal of Neuro-Oncology 113(1): 1-11DOI: 10.1007/s11060-013-1084-8.

Alam, Z. I., et al. (2002). "Oxidative DNA Damage in the Parkinsonian Brain: An Apparent Selective Increase in 8-Hydroxyguanine Levels in Substantia Nigra." Journal of Neurochemistry 69(3): 1196-1203DOI: 10.1046/j.1471-4159.1997.69031196.x.

Alecu, I. and S. A. L. Bennett (2019). "Dysregulated Lipid Metabolism and Its Role in α-Synucleinopathy in Parkinson's Disease." Frontiers in Neuroscience 13DOI: 10.3389/fnins.2019.00328.

Aleyasin, H., et al. (2007). "The Parkinson's disease gene DJ-1 is also a key regulator of stroke-induced damage." Proceedings of the National Academy of Sciences 104(47): 18748-18753DOI: 10.1073/pnas.0709379104.

Aliakbari, F., et al. (2024). "A methodological primer of extracellular vesicles isolation and characterization via different techniques." Biology Methods and Protocols 9(1)DOI: 10.1093/biomethods/bpae009.

Almeida, A. C. and H. Maiato (2018). "Chromokinesins." Current Biology 28(19): R1131-R1135DOI: 10.1016/j.cub.2018.07.017.

Alvarez-Erviti, L., et al. (2011). "Lysosomal dysfunction increases exosome-mediated alpha-synuclein release and transmission." Neurobiology of Disease 42(3): 360-367DOI: 10.1016/j.nbd.2011.01.029.

Amor, S., et al. (2010). "Inflammation in neurodegenerative diseases." Immunology 129(2): 154-169DOI: 10.1111/j.1365-2567.2009.03225.x.

Anda, F. C. d., et al. (2016). "Cortical neurons gradually attain a post-mitotic state." Cell Research 26(9): 1033-1047DOI: 10.1038/cr.2016.76.

Ando, H., et al. (2013). "Positive feedback loop via astrocytes causes chronic inflammation in virus-associated myelopathy." Brain 136(9): 2876-2887DOI: 10.1093/brain/awt183.

Annesi, G., et al. (2005). "DJ-1 mutations and parkinsonism-dementia-amyotrophic lateral sclerosis complex." Annals of Neurology 58(5): 803-807DOI: 10.1002/ana.20666.

Antonucci, F., et al. (2012). "Microvesicles released from microglia stimulate synaptic activity via enhanced sphingolipid metabolism." The EMBO Journal 31(5): 1231-1240DOI: 10.1038/emboj.2011.489.

Arnold, D. B. and D. E. Clapham (1999). "Molecular Determinants for Subcellular Localization of PSD-95 with an Interacting K+ Channel." Neuron 23(1): 149-157DOI: 10.1016/s0896-6273(00)80761-8.

Arshadi, C., et al. (2021). "SNT: a unifying toolbox for quantification of neuronal anatomy." Nature Methods 18(4): 374-377DOI: 10.1038/s41592-021-01105-7.

Aumailley, M. (2014). "The laminin family." Cell Adhesion & Migration 7(1): 48-55DOI: 10.4161/cam.22826.

Babst, M., et al. (2002). "Escrt-III: an endosome-associated heterooligomeric protein complex required for mvb sorting." Dev Cell 3(2): 271-282DOI: 10.1016/s1534-5807(02)00220-4.

Babst, M., et al. (2002). "Endosome-associated complex, ESCRT-II, recruits transport machinery for protein sorting at the multivesicular body." Dev Cell 3(2): 283-289DOI: 10.1016/s1534-5807(02)00219-8.

Baixauli, F., et al. (2014). "Exosomes and Autophagy: Coordinated Mechanisms for the Maintenance of Cellular Fitness." Frontiers in Immunology 5DOI: 10.3389/fimmu.2014.00403.

Bakhti, M., et al. (2011). "Inhibition of Myelin Membrane Sheath Formation by Oligodendrocyte-derived Exosome-like Vesicles." Journal of Biological Chemistry 286(1): 787-796DOI: 10.1074/jbc.M110.190009.

Balaji, S. (2024). "Major Imaging Challenges in Microscopy and How to Solve Them." Microscopy Today 32(3): 22-27DOI: 10.1093/mictod/qaae033.

Bandyopadhyay, S. and M. R. Cookson (2004). "Evolutionary and functional relationships within the DJ1 superfamily." BMC Evolutionary Biology 4(1): 6-6DOI: 10.1186/1471-2148-4-6.

Barres, B. A., et al. (2013). "Neurotransmitter-Triggered Transfer of Exosomes Mediates Oligodendrocyte–Neuron Communication." PLOS Biology 11(7)DOI: 10.1371/journal.pbio.1001604.

Bartelt-Kirbach, B., et al. (2011). "Different Regulation of N-Cadherin and Cadherin-11 in Rat Hippocampus." Cell Communication & Adhesion 17(4-6): 75-82DOI: 10.3109/15419061.2010.549977.

Bartlett, J. J., et al. (2017). "Autophagic dysregulation in doxorubicin cardiomyopathy." Journal of Molecular and Cellular Cardiology 104: 1-8DOI: 10.1016/j.yjmcc.2017.01.007.

Batelli, S., et al. (2015). "The Parkinson's Disease-Related Protein DJ-1 Protects Dopaminergic Neurons in vivo and Cultured Cells from Alpha-Synuclein and 6-Hydroxydopamine Toxicity." Neurodegenerative Diseases 15(1): 13-23DOI: 10.1159/000367993.

Benedikter, B. J., et al. (2019). "Proteomic analysis reveals procoagulant properties of cigarette smoke-induced extracellular vesicles." Journal of Extracellular Vesicles 8(1)DOI: 10.1080/20013078.2019.1585163.

Benedikter, B. J., et al. (2017). "Cigarette smoke extract induced exosome release is mediated by depletion of exofacial thiols and can be inhibited by thiol-antioxidants." Free Radical Biology and Medicine 108: 334-344DOI: 10.1016/j.freeradbiomed.2017.03.026.

Bianco, F., et al. (2009). "Acid sphingomyelinase activity triggers microparticle release from glial cells." The EMBO Journal 28(8): 1043-1054DOI: 10.1038/emboj.2009.45.

Biedler, J. L., et al. (1978). "Multiple neurotransmitter synthesis by human neuroblastoma cell lines and clones." Cancer Res 38(11 Pt 1): 3751-3757

Björkblom, B., et al. (2013). "Parkinson Disease Protein DJ-1 Binds Metals and Protects against Metal-induced Cytotoxicity." Journal of Biological Chemistry 288(31): 22809-22820DOI: 10.1074/jbc.M113.482091.

Blackinton, J., et al. (2009). "Formation of a Stabilized Cysteine Sulfinic Acid Is Critical for the Mitochondrial Function of the Parkinsonism Protein DJ-1." Journal of Biological Chemistry 284(10): 6476-6485DOI: 10.1074/jbc.M806599200.

Bonifati, V., et al. (2003). "Mutations in the DJ-1 Gene Associated with Autosomal Recessive Early-Onset Parkinsonism." Science 299(5604): 256-259DOI: 10.1126/science.1077209.

Boukouris, S. and S. Mathivanan (2015). "Exosomes in bodily fluids are a highly stable resource of disease biomarkers." PROTEOMICS - Clinical Applications 9(3-4): 358-367DOI: 10.1002/prca.201400114.

Braak, H., et al. (2003). "Staging of brain pathology related to sporadic Parkinson's disease." Neurobiology of Aging 24(2): 197-211DOI: 10.1016/s0197-4580(02)00065-9.

Brady, S. and G. Morfini (2010). "A Perspective on Neuronal Cell Death Signaling and Neurodegeneration." Molecular Neurobiology 42(1): 25-31DOI: 10.1007/s12035-010-8128-2.

Brenna, S., et al. (2021). "Brain-Derived Extracellular Vesicles in Health and Disease: A Methodological Perspective." International Journal of Molecular Sciences 22(3)DOI: 10.3390/ijms22031365.

Bretaud, S., et al. (2006). "p53-dependent neuronal cell death in a DJ-1-deficient zebrafish model of Parkinson's disease." Journal of Neurochemistry 100(6): 1626-1635DOI: 10.1111/j.1471-4159.2006.04291.x.

Bu, M., et al. (2021). "Dynamic control of the dopamine transporter in neurotransmission and homeostasis." npj Parkinson's Disease 7(1)DOI: 10.1038/s41531-021-00161-2.

Bucher, M. L., et al. (2020). "Acquired dysregulation of dopamine homeostasis reproduces features of Parkinson's disease." npj Parkinson's Disease 6(1)DOI: 10.1038/s41531-020-00134-x.

Bultron, G., et al. (2010). "The risk of Parkinson's disease in type 1 Gaucher disease." Journal of Inherited Metabolic Disease 33(2): 167-173DOI: 10.1007/s10545-010-9055-0.

Burns, R. S., et al. (1983). "A primate model of parkinsonism: selective destruction of dopaminergic neurons in the pars compacta of the substantia nigra by N-methyl-4-phenyl-1,2,3,6-tetrahydropyridine." Proceedings of the National Academy of Sciences 80(14): 4546-4550DOI: 10.1073/pnas.80.14.4546.

Butcher, J. (2000). "Scientists suggest a link between rotenone and Parkinson's disease." The Lancet 356(9242)DOI: 10.1016/s0140-6736(05)70367-6.

Buzas, E. I. (2022). "The roles of extracellular vesicles in the immune system." Nature Reviews Immunology 23(4): 236-250DOI: 10.1038/s41577-022-00763-8.

Caby, M.-P., et al. (2005). "Exosomal-like vesicles are present in human blood plasma." International Immunology 17(7): 879-887DOI: 10.1093/intimm/dxh267.

Cail, R. C., et al. (2022). "Induced nanoscale membrane curvature bypasses the essential endocytic function of clathrin." Journal of Cell Biology 221(7)DOI: 10.1083/jcb.202109013.

Camussi, G., et al. (2020). "Cryo-electron microscopy of extracellular vesicles from cerebrospinal fluid." PLoS ONE 15(1)DOI: 10.1371/journal.pone.0227949.

Canet-Avilés, R. M., et al. (2004). "The Parkinson's disease protein DJ-1 is neuroprotective due to cysteine-sulfinic acid-driven mitochondrial localization." Proceedings of the National Academy of Sciences 101(24): 9103-9108DOI: 10.1073/pnas.0402959101.

Cao, J., et al. (2014). "The Oxidation States of DJ-1 Dictate the Cell Fate in Response to Oxidative Stress Triggered by 4-HPR: Autophagy or Apoptosis?" Antioxidants & Redox Signaling 21(10): 1443-1459DOI: 10.1089/ars.2013.5446.

Cao, M., et al. (2017). "Parkinson Sac Domain Mutation in Synaptojanin 1 Impairs Clathrin Uncoating at Synapses and Triggers Dystrophic Changes in Dopaminergic Axons." Neuron 93(4): 882-896.e885DOI: 10.1016/j.neuron.2017.01.019.

Cao, S. S. and R. J. Kaufman (2014). "Endoplasmic Reticulum Stress and Oxidative Stress in Cell Fate Decision and Human Disease." Antioxidants & Redox Signaling 21(3): 396-413DOI: 10.1089/ars.2014.5851.

Cerri, S., et al. (2021). "GBA Mutations Influence the Release and Pathological Effects of Small Extracellular Vesicles from Fibroblasts of Patients with Parkinson's Disease." International Journal of Molecular Sciences 22(4)DOI: 10.3390/ijms22042215.

Chang, C., et al. (2013). "Exosomes of BV-2 cells induced by alpha-synuclein: Important mediator of neurodegeneration in PD." Neuroscience Letters 548: 190-195DOI: 10.1016/j.neulet.2013.06.009.

Chapman, M. A. (2014). "Interactions between cell adhesion and the synaptic vesicle cycle in Parkinson's

disease." Medical Hypotheses 83(2): 203-207DOI: 10.1016/j.mehy.2014.04.029.

Chen, L., et al. (2008). "Unregulated Cytosolic Dopamine Causes Neurodegeneration Associated with Oxidative Stress in Mice." The Journal of Neuroscience 28(2): 425-433DOI: 10.1523/jneurosci.3602-07.2008.

Chen, W. T.-L., et al. (2021). "Serum DJ-1 Is a Biomarker of Colorectal Cancer and DJ-1 Activates Mitophagy to Promote Colorectal Cancer Progression." Cancers 13(16)DOI: 10.3390/cancers13164151.

Chen, Y., et al. (2020). "The role of astrocytes in oxidative stress of central nervous system: A mixed blessing." Cell Proliferation 53(3)DOI: 10.1111/cpr.12781.

Chiaradia, E., et al. (2021). "Extracellular Vesicles under Oxidative Stress Conditions: Biological Properties and Physiological Roles." Cells 10(7)DOI: 10.3390/cells10071763.

Chivet, M., et al. (2014). "Exosomes secreted by cortical neurons upon glutamatergic synapse activation specifically interact with neurons." Journal of Extracellular Vesicles 3(1)DOI: 10.3402/jev.v3.24722.

Choi, D.-J., et al. (2019). "A Parkinson's disease gene, DJ-1, regulates anti-inflammatory roles of astrocytes through prostaglandin D2 synthase expression." Neurobiology of Disease 127: 482-491DOI: 10.1016/j.nbd.2019.04.003.

Choi, D. J., et al. (2020). "Critical roles of astrocytic-CCL2-dependent monocyte infiltration in a DJ-1 knockout mouse model of delayed brain repair." Glia 68(10): 2086-2101DOI: 10.1002/glia.23828.

Chun, C., et al. (2021). "Astrocyte-derived extracellular vesicles enhance the survival and electrophysiological function of human cortical neurons in vitro." Biomaterials 271DOI: 10.1016/j.biomaterials.2021.120700.

Chung, D., et al. (2020). "GAP-43 and BASP1 in Axon Regeneration: Implications for the Treatment of Neurodegenerative Diseases." Frontiers in Cell and Developmental Biology 8DOI: 10.3389/fcell.2020.567537.

Chunna, A. and X.-P. Pu (2017). Role of DJ-1 in Fertilization. DJ-1/PARK7 Protein: 61-66DOI: 10.1007/978-981-10-6583-5_5.

Cleeter, M. W. J., et al. (2006). "Irreversible Inhibition of Mitochondrial Complex I by 1-Methyl-4-Phenylpyridinium: Evidence for Free Radical Involvement." Journal of Neurochemistry 58(2): 786-789DOI: 10.1111/j.1471-4159.1992.tb09789.x.

Corsello, T., et al. (2019). "Cigarette Smoke Condensate Exposure Changes RNA Content of Extracellular Vesicles Released from Small Airway Epithelial Cells." Cells 8(12)DOI: 10.3390/cells8121652.

Coudert, L., et al. (2021). "The ESCRT-0 subcomplex component Hrs/Hgs is a master regulator of myogenesis via modulation of signaling and degradation pathways." BMC Biology 19(1)DOI: 10.1186/s12915-021-01091-4.

Courel, M., et al. (2010). "Pro-hormone Secretogranin II Regulates Dense Core Secretory Granule

Biogenesis in Catecholaminergic Cells." Journal of Biological Chemistry 285(13): 10030-10043DOI: 10.1074/jbc.M109.064196.

Croese, T. and R. Furlan (2018). "Extracellular vesicles in neurodegenerative diseases." Molecular Aspects of Medicine 60: 52-61DOI: 10.1016/j.mam.2017.11.006.

Dahl, J.-U., et al. (2015). "Protein Quality Control under Oxidative Stress Conditions." Journal of Molecular Biology 427(7): 1549-1563DOI: 10.1016/j.jmb.2015.02.014.

Dahlstroem, A. and K. Fuxe (1964). "Evidence for the Existence of Monoamine-Containing Neurons in the Central Nervous System. I. Demonstration of Monoamines in the Cell Bodies of Brain Stem Neurons." Acta Physiol Scand Suppl: SUPPL 232:231-255

Daneman, R., et al. (2021). "Extracellular DJ-1 induces sterile inflammation in the ischemic brain." PLOS Biology 19(5)DOI: 10.1371/journal.pbio.3000939.

Danzer, K. M., et al. (2012). "Exosomal cell-to-cell transmission of alpha synuclein oligomers." Molecular Neurodegeneration 7(1)DOI: 10.1186/1750-1326-7-42.

Darvish, H., et al. (2013). "Detection of copy number changes in genes associated with Parkinson's disease in Iranian patients." Neuroscience Letters 551: 75-78DOI: 10.1016/j.neulet.2013.07.013.

Dauden, M. I., et al. (2021). "RUVBL1–RUVBL2 AAA-ATPase: a versatile scaffold for multiple complexes and functions." Current Opinion in Structural Biology 67: 78-85DOI: 10.1016/j.sbi.2020.08.010.

Davidson, B., et al. (2008). "Expression and clinical role of DJ-1, a negative regulator of PTEN, in ovarian carcinoma." Human Pathology 39(1): 87-95DOI: 10.1016/j.humpath.2007.05.014.

Davies, L. C., et al. (2013). "Tissue-resident macrophages." Nature Immunology 14(10): 986-995DOI: 10.1038/ni.2705.

De Luca, C., et al. (2018). "Neuro-Immune Hemostasis: Homeostasis and Diseases in the Central Nervous System." Frontiers in Cellular Neuroscience 12DOI: 10.3389/fncel.2018.00459.

Denda, S. and L. F. Reichardt (2007). Studies on Integrins in the Nervous System. Integrins: 203-221DOI: 10.1016/s0076-6879(07)26010-0.

Desplats, P., et al. (2009). "Inclusion formation and neuronal cell death through neuron-to-neuron transmission of α-synuclein." Proceedings of the National Academy of Sciences 106(31): 13010-13015DOI: 10.1073/pnas.0903691106.

Di Nottia, M., et al. (2017). "DJ-1 modulates mitochondrial response to oxidative stress: clues from a novel diagnosis of PARK7." Clinical Genetics 92(1): 18-25DOI: 10.1111/cge.12841.

Dickens, A. M., et al. (2017). "Astrocyte-shed extracellular vesicles regulate the peripheral leukocyte response to inflammatory brain lesions." Science Signaling 10(473)DOI: 10.1126/scisignal.aai7696.

Diop, S. B., et al. (2008). "Reptin and Pontin function antagonistically with PcG and TrxG complexes to

mediate Hox gene control." EMBO reports 9(3): 260-266DOI: 10.1038/embor.2008.8.

Dolgacheva, L. P., et al. (2019). "Role of DJ-1 in the mechanism of pathogenesis of Parkinson's disease." Journal of Bioenergetics and Biomembranes 51(3): 175-188DOI: 10.1007/s10863-019-09798-4.

Doonan, F. and T. G. Cotter (2008). "Morphological assessment of apoptosis." Methods 44(3): 200-204DOI: 10.1016/j.ymeth.2007.11.006.

Doyle, L. and M. Wang (2019). "Overview of Extracellular Vesicles, Their Origin, Composition, Purpose, and Methods for Exosome Isolation and Analysis." Cells 8(7)DOI: 10.3390/cells8070727.

Dugger, B. N. and D. W. Dickson (2017). "Pathology of Neurodegenerative Diseases." Cold Spring Harbor Perspectives in Biology 9(7): a028035-a028035DOI: 10.1101/cshperspect.a028035.

Eberhard, D. and E. Lammert (2017). The Role of the Antioxidant Protein DJ-1 in Type 2 Diabetes Mellitus. DJ-1/PARK7 Protein: 173-186DOI: 10.1007/978-981-10-6583-5_11.

Ebrahimi-Fakhari, D., et al. (2012). "Protein degradation pathways in Parkinson's disease: curse or blessing." Acta Neuropathologica 124(2): 153-172DOI: 10.1007/s00401-012-1004-6.

Eiden, L. E., et al. (2004). "The vesicular amine transporter family (SLC18): amine/proton antiporters required for vesicular accumulation and regulated exocytotic secretion of monoamines and acetylcholine." Pfl□gers Archiv European Journal of Physiology 447(5): 636-640DOI: 10.1007/s00424-003-1100-5.

Ekert, P. G. and D. L. Vaux (1997). "Apoptosis and the immune system." British Medical Bulletin 53(3): 591-603DOI: 10.1093/oxfordjournals.bmb.a011632.

Emery, B., et al. (2020). "Oligodendrocytes support axonal transport and maintenance via exosome secretion." PLOS Biology 18(12)DOI: 10.1371/journal.pbio.3000621.

Encinas, M., et al. (2002). "Sequential Treatment of SH-SY5Y Cells with Retinoic Acid and Brain-Derived Neurotrophic Factor Gives Rise to Fully Differentiated, Neurotrophic Factor-Dependent, Human Neuron-Like Cells." Journal of Neurochemistry 75(3): 991-1003DOI: 10.1046/j.1471-4159.2000.0750991.x.

Erer, S., et al. (2016). "Mutation analysis of the PARKIN, PINK1, DJ1, and SNCA genes in Turkish early-onset Parkinson's patients and genotype-phenotype correlations." Clinical Neurology and Neurosurgery 148: 147-153DOI: 10.1016/j.clineuro.2016.07.005.

Escrevente, C., et al. (2011). "Interaction and uptake of exosomes by ovarian cancer cells." BMC Cancer 11: 108DOI: 10.1186/1471-2407-11-108.

Feng, D., et al. (2010). "Cellular internalization of exosomes occurs through phagocytosis." Traffic 11(5): 675-687DOI: 10.1111/j.1600-0854.2010.01041.x.

Feng, Y., et al. (2015). "Rotenone affects p53 transcriptional activity and apoptosis via targeting SIRT1

and H3K9 acetylation in SH-SY5Y cells." Journal of Neurochemistry 134(4): 668-676DOI: 10.1111/jnc.13172.

Fink, S. L. and B. T. Cookson (2005). "Apoptosis, Pyroptosis, and Necrosis: Mechanistic Description of Dead and Dying Eukaryotic Cells." Infection and Immunity 73(4): 1907-1916DOI: 10.1128/iai.73.4.1907-1916.2005.

Fitzner, D., et al. (2011). "Selective transfer of exosomes from oligodendrocytes to microglia by macropinocytosis." Journal of Cell Science 124(3): 447-458DOI: 10.1242/jcs.074088.

Fitzner, D., et al. (2011). "Selective transfer of exosomes from oligodendrocytes to microglia by macropinocytosis." J Cell Sci 124(Pt 3): 447-458DOI: 10.1242/jcs.074088.

Flores-Leon, M. and T. F. Outeiro (2023). "More than meets the eye in Parkinson's disease and other synucleinopathies: from proteinopathy to lipidopathy." Acta Neuropathologica 146(3): 369-385DOI: 10.1007/s00401-023-02601-0.

Follett, J., et al. (2014). "The Vps35 D620N Mutation Linked to Parkinson's Disease Disrupts the Cargo Sorting Function of Retromer." Traffic 15(2): 230-244DOI: 10.1111/tra.12136.

Forster, J. I., et al. (2016). "Characterization of Differentiated SH-SY5Y as Neuronal Screening Model Reveals Increased Oxidative Vulnerability." J Biomol Screen 21(5): 496-509DOI: 10.1177/1087057115625190.

Frøyset, A. K., et al. (2018). "Astroglial DJ-1 over-expression up-regulates proteins involved in redox regulation and is neuroprotective in vivo." Redox Biology 16: 237-247DOI: 10.1016/j.redox.2018.02.010.

Fu, K., et al. (2011). "DJ-1 inhibits TRAIL-induced apoptosis by blocking pro-caspase-8 recruitment to FADD." Oncogene 31(10): 1311-1322DOI: 10.1038/onc.2011.315.

Fulda, S. and K. M. Debatin (2006). "Extrinsic versus intrinsic apoptosis pathways in anticancer chemotherapy." Oncogene 25(34): 4798-4811DOI: 10.1038/sj.onc.1209608.

Gao, C., et al. (2023). "Microglia in neurodegenerative diseases: mechanism and potential therapeutic targets." Signal Transduction and Targeted Therapy 8(1)DOI: 10.1038/s41392-023-01588-0.

Gassama, Y. and A. Favereaux (2021). "Emerging Roles of Extracellular Vesicles in the Central Nervous System: Physiology, Pathology, and Therapeutic Perspectives." Frontiers in Cellular Neuroscience 15DOI: 10.3389/fncel.2021.626043.

Gcwensa, N. Z., et al. (2021). "Molecular Mechanisms Underlying Synaptic and Axon Degeneration in Parkinson's Disease." Frontiers in Cellular Neuroscience 15DOI: 10.3389/fncel.2021.626128.

Gentile, F., et al. (2004). "The neuroendocrine protein VGF is sorted into dense-core granules and is secreted apically by polarized rat thyroid epithelial cells." Experimental Cell Research 295(1): 269-280DOI: 10.1016/j.yexcr.2004.01.010.

Ghazavi, F., et al. (2011). "PRKN, DJ-1, and PINK1 screening identifies novel splice site mutation in PRKN and two novel DJ-1 mutations." Movement Disorders 26(1): 80-89DOI: 10.1002/mds.23417.

Ginhoux, F., et al. (2013). "Origin and differentiation of microglia." Frontiers in Cellular Neuroscience 7DOI: 10.3389/fncel.2013.00045.

Goldie, B. J., et al. (2014). "Activity-associated miRNA are packaged in Map1b-enriched exosomes released from depolarized neurons." Nucleic Acids Research 42(14): 9195-9208DOI: 10.1093/nar/gku594.

Gómez-Benito, M., et al. (2020). Modeling Parkinson's Disease With the Alpha-Synuclein Protein. Frontiers in Pharmacology, Frontiers Media S.A. 11DOI: 10.3389/fphar.2020.00356.

Gonçalves, A. P., et al. (2011). "Involvement of p53 in cell death following cell cycle arrest and mitotic catastrophe induced by rotenone." Biochimica et Biophysica Acta (BBA) - Molecular Cell Research 1813(3): 492-499DOI: 10.1016/j.bbamcr.2011.01.006.

Goncalves, M. B., et al. (2019). "Regulation of Myelination by Exosome Associated Retinoic Acid Release from NG2-Positive Cells." The Journal of Neuroscience 39(16): 3013-3027DOI: 10.1523/jneurosci.2922-18.2019.

Gonzalez-Hunt, C. P. and L. H. Sanders (2020). "DNA damage and repair in Parkinson's disease: Recent advances and new opportunities." Journal of Neuroscience Research 99(1): 180-189DOI: 10.1002/jnr.24592.

Görner, K., et al. (2007). "Structural Determinants of the C-terminal Helix-Kink-Helix Motif Essential for Protein Stability and Survival Promoting Activity of DJ-1." Journal of Biological Chemistry 282(18): 13680-13691DOI: 10.1074/jbc.M609821200.

Grey, M., et al. (2015). "Acceleration of α-Synuclein Aggregation by Exosomes." Journal of Biological Chemistry 290(5): 2969-2982DOI: 10.1074/jbc.M114.585703.

Guo, J.-F., et al. (2008). "Mutation analysis of Parkin , PINK1 , DJ-1 and ATP13A2 genes in Chinese patients with autosomal recessive early-onset Parkinsonism." Movement Disorders 23(14): 2074-2079DOI: 10.1002/mds.22156.

Guo, M., et al. (2020). "Microglial exosomes facilitate α-synuclein transmission in Parkinson's disease." Brain 143(5): 1476-1497DOI: 10.1093/brain/awaa090.

Gurung, S., et al. (2021). "The exosome journey: from biogenesis to uptake and intracellular signalling." Cell Communication and Signaling 19(1)DOI: 10.1186/s12964-021-00730-1.

H. Rashed, M., et al. (2017). "Exosomes: From Garbage Bins to Promising Therapeutic Targets." International Journal of Molecular Sciences 18(3)DOI: 10.3390/ijms18030538.

Hague, S., et al. (2003). "Early-onset Parkinson's disease caused by a compound heterozygous DJ-1 mutation." Annals of Neurology 54(2): 271-274DOI: 10.1002/ana.10663.

Hällqvist, J., et al. (2024). "Plasma proteomics identify biomarkers predicting Parkinson's disease up to 7 years before symptom onset." Nature Communications 15(1)DOI: 10.1038/s41467-024-48961-3.

Hanagasi, H. A., et al. (2016). "A novel homozygous DJ1 mutation causes parkinsonism and ALS in a Turkish family." Parkinsonism & Related Disorders 29: 117-120DOI: 10.1016/j.parkreldis.2016.03.001.

Haraszti, R. A., et al. (2016). "High-resolution proteomic and lipidomic analysis of exosomes and microvesicles from different cell sources." J Extracell Vesicles 5: 32570DOI: 10.3402/jev.v5.32570.

Harding, C., et al. (1983). "Receptor-mediated endocytosis of transferrin and recycling of the transferrin receptor in rat reticulocytes." J Cell Biol 97(2): 329-339DOI: 10.1083/jcb.97.2.329.

Hashemi, S. H., et al. (2003). "SSR2(a) receptor expression and adrenergic/cholinergic characteristics in differentiated SH-SY5Y cells." Neurochem Res 28(3-4): 449-460DOI: 10.1023/a:1022848718109.

Heinz, S., et al. (2017). "Mechanistic Investigations of the Mitochondrial Complex I Inhibitor Rotenone in the Context of Pharmacological and Safety Evaluation." Scientific Reports 7(1)DOI: 10.1038/srep45465.

Henderson, M. X., et al. (2019). "α-Synuclein pathology in Parkinson's disease and related α-synucleinopathies." Neuroscience Letters 709DOI: 10.1016/j.neulet.2019.134316.

Hering, R., et al. (2004). "Novel homozygous p.E64D mutation in DJ1 in early onset Parkinson disease (PARK7)." Human Mutation 24(4): 321-329DOI: 10.1002/humu.20089.

Hessvik, N. P., et al. (2016). "PIKfyve inhibition increases exosome release and induces secretory autophagy." Cellular and Molecular Life Sciences 73(24): 4717-4737DOI: 10.1007/s00018-016-2309-8.

Higgins, J. D. S. and J. T. Greenamyre (1996). "[3H]Dihydrorotenone Binding to NADH: Ubiquinone Reductase (Complex I) of the Electron Transport Chain: An Autoradiographic Study." The Journal of Neuroscience 16(12): 3807-3816DOI: 10.1523/jneurosci.16-12-03807.1996.

Ho, D. H., et al. (2014). "Increased DJ-1 in Urine Exosome of Korean Males with Parkinson's Disease." BioMed Research International 2014: 1-8DOI: 10.1155/2014/704678.

Hod, Y. (2004). "Differential control of apoptosis by DJ-1 in prostate benign and cancer cells." Journal of Cellular Biochemistry 92(6): 1221-1233DOI: 10.1002/jcb.20159.

Houry, W. A., et al. (2018). "The PAQosome, an R2TP-Based Chaperone for Quaternary Structure Formation." Trends in Biochemical Sciences 43(1): 4-9DOI: 10.1016/j.tibs.2017.11.001.

Hsu, D.-H., et al. (2003). "Exosomes as a Tumor Vaccine: Enhancing Potency Through Direct Loading of Antigenic Peptides." Journal of Immunotherapy 26(5): 440-450DOI: 10.1097/00002371-200309000-

00007.

Huang, S., et al. (2017). "Increased miR-124-3p in microglial exosomes following traumatic brain injury inhibits neuronal inflammation and contributes to neurite outgrowthviatheir transfer into neurons." The FASEB Journal 32(1): 512-528DOI: 10.1096/fj.201700673r.

Huebner, E. A. and S. M. Strittmatter (2009). Axon Regeneration in the Peripheral and Central Nervous Systems. Cell Biology of the Axon: 305-360DOI: 10.1007/400_2009_19.

Hunn, B. H. M., et al. (2015). "Impaired intracellular trafficking defines early Parkinson's disease." Trends in Neurosciences 38(3): 178-188DOI: 10.1016/j.tins.2014.12.009.

Huotari, J. and A. Helenius (2011). "Endosome maturation." EMBO J 30(17): 3481-3500DOI: 10.1038/emboj.2011.286.

Hurley, J. H. and P. I. Hanson (2010). "Membrane budding and scission by the ESCRT machinery: it's all in the neck." Nat Rev Mol Cell Biol 11(8): 556-566DOI: 10.1038/nrm2937.

Ichimiya, T., et al. (2020). "Autophagy and Autophagy-Related Diseases: A Review." International Journal of Molecular Sciences 21(23)DOI: 10.3390/ijms21238974.

Ishikawa, S., et al. (2009). "Oxidative Status of DJ-1-dependent Activation of Dopamine Synthesis through Interaction of Tyrosine Hydroxylase and 4-Dihydroxy-l-phenylalanine (l-DOPA) Decarboxylase with DJ-1." Journal of Biological Chemistry 284(42): 28832-28844DOI: 10.1074/jbc.M109.019950.

Ivanova, D. and M. A. Cousin (2022). "Synaptic Vesicle Recycling and the Endolysosomal System: A Reappraisal of Form and Function." Frontiers in Synaptic Neuroscience 14DOI: 10.3389/fnsyn.2022.826098.

Jahn, R., et al. (2003). "Membrane fusion." Cell 112(4): 519-533DOI: 10.1016/s0092-8674(03)00112-0.

Jäkel, S. and L. Dimou (2017). "Glial Cells and Their Function in the Adult Brain: A Journey through the History of Their Ablation." Frontiers in Cellular Neuroscience 11DOI: 10.3389/fncel.2017.00024.

Jan, A., et al. (2021). "The Prion-Like Spreading of Alpha-Synuclein in Parkinson's Disease: Update on Models and Hypotheses." International Journal of Molecular Sciences 22(15)DOI: 10.3390/ijms22158338.

Jankovic, J. (2008). "Parkinson's disease: clinical features and diagnosis." Journal of Neurology, Neurosurgery & Psychiatry 79(4): 368-376DOI: 10.1136/jnnp.2007.131045.

Jenner, P. (2003). "Oxidative stress in Parkinson's disease." Annals of Neurology 53(S3): S26-S38DOI: 10.1002/ana.10483.

Ji, Y.-J., et al. (2020). "Down-regulation of DJ-1 Augments Neuroinflammation via Nrf2/Trx1/NLRP3 Axis

in MPTP-induced Parkinson's Disease Mouse Model." Neuroscience 442: 253-263DOI: 10.1016/j.neuroscience.2020.06.001.

Joe, E.-H., et al. (2018). "Astrocytes, Microglia, and Parkinson's Disease." Experimental Neurobiology 27(2): 77-87DOI: 10.5607/en.2018.27.2.77.

Jung, S. H., et al. (2014). "DJ-1 protein regulates CD3+ T cell migration via overexpression of CXCR4 receptor." Atherosclerosis 235(2): 503-509DOI: 10.1016/j.atherosclerosis.2014.05.955.

Junn, E., et al. (2005). "Interaction of DJ-1 with Daxx inhibits apoptosis signal-regulating kinase 1 activity and cell death." Proc Natl Acad Sci U S A 102(27): 9691-9696DOI: 10.1073/pnas.0409635102.

Kakihara, Y. and W. A. Houry (2012). "The R2TP complex: Discovery and functions." Biochimica et Biophysica Acta (BBA) - Molecular Cell Research 1823(1): 101-107DOI: 10.1016/j.bbamcr.2011.08.016.

Kasten M, Hartmann C, Hampf J, Schaake S, Westenberger A, Vollstedt EJ, Balck A, Domingo A, Vulinovic F, Dulovic M, Zorn I, Madoev H, Zehnle H, Lembeck CM, Schawe L, Reginold J, Huang J, König IR, Bertram L, Marras C, Lohmann K, Lill CM, Klein C. Genotype-Phenotype Relations for the Parkinson's Disease Genes Parkin, PINK1, DJ1: MDSGene Systematic Review. Mov Discord. 2018 May;33(5):730-741. doi: 10.1002/mds.27352.

Kato, I., et al. (2023). "Oxidized DJ-1 Inhibits p53 by Sequestering p53 from Promoters in a DNA-Binding Affinity-Dependent Manner." Molecular and Cellular Biology 33(2): 340-359DOI: 10.1128/mcb.01350-12.

Kawate, T., et al. (2017). Expression of DJ-1 in Cancer Cells: Its Correlation with Clinical Significance. DJ-1/PARK7 Protein: 45-59DOI: 10.1007/978-981-10-6583-5_4.

Kehm, R., et al. (2021). "Protein oxidation - Formation mechanisms, detection and relevance as biomarkers in human diseases." Redox Biology 42DOI: 10.1016/j.redox.2021.101901.

Keren-Shaul, H., et al. (2017). "A Unique Microglia Type Associated with Restricting Development of Alzheimer's Disease." Cell 169(7): 1276-1290.e1217DOI: 10.1016/j.cell.2017.05.018.

Kerr, J. F., et al. (1972). "Apoptosis: a basic biological phenomenon with wide-ranging implications in tissue kinetics." Br J Cancer 26(4): 239-257DOI: 10.1038/bjc.1972.33.

Khounlo, R., et al. (2021). "Membrane Binding of α-Synuclein Stimulates Expansion of SNARE-Dependent Fusion Pore." Frontiers in Cell and Developmental Biology 9DOI: 10.3389/fcell.2021.663431.

Kim, J.-h., et al. (2013). "DJ-1 facilitates the interaction between STAT1 and its phosphatase, SHP-1, in brain microglia and astrocytes: A novel anti-inflammatory function of DJ-1." Neurobiology of Disease 60: 1-10DOI: 10.1016/j.nbd.2013.08.007.

Kim, J.-M., et al. (2016). "DJ-1 deficiency impairs glutamate uptake into astrocytes via the regulation of flotillin-1 and caveolin-1 expression." Scientific Reports 6(1)DOI: 10.1038/srep28823.

Kim, K. S., et al. (2013). "DJ-1 Associates with lipid rafts by palmitoylation and regulates lipid rafts-dependent endocytosis in astrocytes." Human Molecular Genetics 22(23): 4805-4817DOI: 10.1093/hmg/ddt332.

Kim, R. H., et al. (2005). "Hypersensitivity of DJ-1-deficient mice to 1-methyl-4-phenyl-1,2,3,6-tetrahydropyrindine (MPTP) and oxidative stress." Proceedings of the National Academy of Sciences 102(14): 5215-5220DOI: 10.1073/pnas.0501282102.

Kim, T. (2005). "Chromogranin A: a surprising link between granule biogenesis and hypertension." Journal of Clinical Investigation 115(7): 1711-1713DOI: 10.1172/jci25706.

Kim, W., et al. (2021). "Spatiotemporal processing of neural cell adhesion molecules 1 and 2 by BACE1 in vivo." Journal of Biological Chemistry 296DOI: 10.1016/j.jbc.2021.100372.

Kim, Y.-C., et al. (2009). "Oxidation of DJ-1-dependent cell transformation through direct binding of DJ-1 to PTEN." International Journal of Oncology 35(06)DOI: 10.3892/ijo_00000451.

Kinumi, T., et al. (2004). "Cysteine-106 of DJ-1 is the most sensitive cysteine residue to hydrogen peroxide-mediated oxidation in vivo in human umbilical vein endothelial cells." Biochemical and Biophysical Research Communications 317(3): 722-728DOI: 10.1016/j.bbrc.2004.03.110.

Kong, Q. and C.-l. G. Lin (2010). "Oxidative damage to RNA: mechanisms, consequences, and diseases." Cellular and Molecular Life Sciences 67(11): 1817-1829DOI: 10.1007/s00018-010-0277-y.

Korczyn, A. D. (2015). "Vascular parkinsonism—characteristics, pathogenesis and treatment." Nature Reviews Neurology 11(6): 319-326DOI: 10.1038/nrneurol.2015.61.

Krämer-Albers, E.-M. (2020). "Extracellular vesicles in the oligodendrocyte microenvironment." Neuroscience Letters 725DOI: 10.1016/j.neulet.2020.134915.

Krishna, A., et al. (2014). "Systems genomics evaluation of the SH-SY5Y neuroblastoma cell line as a model for Parkinson's disease." BMC Genomics 15(1)DOI: 10.1186/1471-2164-15-1154.

Kristiansen, M. and J. Ham (2014). "Programmed cell death during neuronal development: the sympathetic neuron model." Cell Death & Differentiation 21(7): 1025-1035DOI: 10.1038/cdd.2014.47.

Kumsta, C. and U. Jakob (2009). "Redox-Regulated Chaperones." Biochemistry 48(22): 4666-4676DOI: 10.1021/bi9003556.

Kurzawa-Akanbi, M., et al. (2021). "Altered ceramide metabolism is a feature in the extracellular vesicle-mediated spread of alpha-synuclein in Lewy body disorders." Acta Neuropathologica 142(6): 961-984DOI: 10.1007/s00401-021-02367-3.

Kwok, Z. H., et al. (2021). "Extracellular Vesicle Transportation and Uptake by Recipient Cells: A Critical Process to Regulate Human Diseases." Processes (Basel) 9(2)DOI: 10.3390/pr9020273.

Kyung, J. W., et al. (2018). "DJ-1 deficiency impairs synaptic vesicle endocytosis and reavailability at

nerve terminals." Proceedings of the National Academy of Sciences 115(7): 1629-1634DOI: 10.1073/pnas.1708754115.

La Forge, F. H., HL; Smith, LE (1933). "The Determination of the structure of rotenone." Chemical Reviews 18(2): 181-213DOI: 10.1021/cr60042a001.

La Torre, M. E., et al. (2022). "Extracellular Vesicles Cargo in Modulating Microglia Functional Responses." Biology 11(10)DOI: 10.3390/biology11101426.

Lachenal, G., et al. (2011). "Release of exosomes from differentiated neurons and its regulation by synaptic glutamatergic activity." Molecular and Cellular Neuroscience 46(2): 409-418DOI: 10.1016/j.mcn.2010.11.004.

Laster, S. M., et al. (1988). "Tumor necrosis factor can induce both apoptic and necrotic forms of cell lysis." The Journal of Immunology 141(8): 2629-2634DOI: 10.4049/jimmunol.141.8.2629.

Lee, S. H., et al. (2018). "Reciprocal control of excitatory synapse numbers by Wnt and Wnt inhibitor PRR7 secreted on exosomes." Nature Communications 9(1)DOI: 10.1038/s41467-018-05858-2.

Lekshmi, A., et al. (2017). "A quantitative real-time approach for discriminating apoptosis and necrosis." Cell Death Discovery 3(1)DOI: 10.1038/cddiscovery.2016.101.

Lespagnol, A., et al. (2008). "Exosome secretion, including the DNA damage-induced p53-dependent secretory pathway, is severely compromised in TSAP6/Steap3-null mice." Cell Death & Differentiation 15(11): 1723-1733DOI: 10.1038/cdd.2008.104.

Lev, N., et al. (2009). "DJ-1 Changes in G93A-SOD1 Transgenic Mice: Implications for Oxidative Stress in ALS." Journal of Molecular Neuroscience 38(2): 94-102DOI: 10.1007/s12031-008-9138-7.

Li, M., et al. (2021). "Isolation of Exosome Nanoparticles from Human Cerebrospinal Fluid for Proteomic Analysis." ACS Applied Nano Materials 4(4): 3351-3359DOI: 10.1021/acsanm.0c02622.

Li, P., et al. (2024). "Understanding thrombosis: the critical role of oxidative stress." Hematology 29(1): 2301633DOI: 10.1080/16078454.2023.2301633.

Li, T., et al. (2021). "Role of Glia-Derived Extracellular Vesicles in Neurodegenerative Diseases." Frontiers in Aging Neuroscience 13DOI: 10.3389/fnagi.2021.765395.

Li, X., et al. (2012). "Subsequent Risks of Parkinson Disease in Patients with Autoimmune and Related Disorders: A Nationwide Epidemiological Study from Sweden." Neurodegenerative Diseases 10(1-4): 277-284DOI: 10.1159/000333222.

Lin, R.-W., et al. (2018). "P53 enhances apoptosis induced by doxorubicin only under conditions of severe DNA damage." Cell Cycle 17(17): 2175-2186DOI: 10.1080/15384101.2018.1520565.

Liu, J., et al. (2008). "ERKs/p53 signal transduction pathway is involved in doxorubicin-induced apoptosis in H9c2 cells and cardiomyocytes." American Journal of Physiology-Heart and Circulatory Physiology

295(5): H1956-H1965DOI: 10.1152/ajpheart.00407.2008.

Liu, S., et al. (2023). "Importance of DJ-1 in autophagy regulation and disease." Arch Biochem Biophys 743: 109672DOI: 10.1016/j.abb.2023.109672.

Liu, Y., et al. (1994). "Preferential localization of a vesicular monoamine transporter to dense core vesicles in PC12 cells." The Journal of cell biology 127(5): 1419-1433DOI: 10.1083/jcb.127.5.1419.

Lizarraga-Valderrama, L. R. and G. K. Sheridan (2021). "Extracellular vesicles and intercellular communication in the central nervous system." FEBS Letters 595(10): 1391-1410DOI: 10.1002/1873-3468.14074.

Lombardi, M., et al. (2019). "Detrimental and protective action of microglial extracellular vesicles on myelin lesions: astrocyte involvement in remyelination failure." Acta Neuropathologica 138(6): 987-1012DOI: 10.1007/s00401-019-02049-1.

Long, X., et al. (2020). "Astrocyte-derived exosomes enriched with miR-873a-5p inhibit neuroinflammation via microglia phenotype modulation after traumatic brain injury." Journal of Neuroinflammation 17(1)DOI: 10.1186/s12974-020-01761-0.

Lopes, F. M., et al. (2010). "Comparison between proliferative and neuron-like SH-SY5Y cells as an in vitro model for Parkinson disease studies." Brain Research 1337: 85-94DOI: 10.1016/j.brainres.2010.03.102.

Luarte, A., et al. (2020). "Astrocyte-Derived Small Extracellular Vesicles Regulate Dendritic Complexity through miR-26a-5p Activity." Cells 9(4)DOI: 10.3390/cells9040930.

Lucas, J. I. and I. Marin (2006). "A New Evolutionary Paradigm for the Parkinson Disease Gene DJ-1." Molecular Biology and Evolution 24(2): 551-561DOI: 10.1093/molbev/msl186.

Luk, B., et al. (2015). "A Physical Interaction between the Dopamine Transporter and DJ-1 Facilitates Increased Dopamine Reuptake." PLoS ONE 10(8)DOI: 10.1371/journal.pone.0136641.

Luk, K. C., et al. (2012). "Pathological α-Synuclein Transmission Initiates Parkinson-like Neurodegeneration in Nontransgenic Mice." Science 338(6109): 949-953DOI: 10.1126/science.1227157.

Maas, S. L. N., et al. (2017). "Extracellular Vesicles: Unique Intercellular Delivery Vehicles." Trends in Cell Biology 27(3): 172-188DOI: 10.1016/j.tcb.2016.11.003.

Macedo, M. G., et al. (2009). "Genotypic and phenotypic characteristics of Dutch patients with early onset Parkinson's disease." Movement Disorders 24(2): 196-203DOI: 10.1002/mds.22287.

Mader, B. J., et al. (2012). "Rotenone Inhibits Autophagic Flux Prior to Inducing Cell Death." ACS Chemical Neuroscience 3(12): 1063-1072DOI: 10.1021/cn300145z.

Magalhães, M., et al. (2016). "DJ-1 linked parkinsonism (PARK7) is associated with Lewy body

pathology." Brain 139(6): 1680-1687DOI: 10.1093/brain/aww080.

Malgieri, G. and D. Eliezer (2008). "Structural effects of Parkinson's disease linked DJ-1 mutations." Protein Science 17(5): 855-868DOI: 10.1110/ps.073411608.

Manček-Keber, M., et al. (2015). "Toll-like receptor 4 senses oxidative stress mediated by the oxidation of phospholipids in extracellular vesicles." Science Signaling 8(381)DOI: 10.1126/scisignal.2005860.

Mappouras, D., et al. (1990). "Purification and characterization of L-DOPA decarboxylase from human kidney." Molecular and Cellular Biochemistry 94(2): 147-156DOI: 10.1007/bf00214121.

Marostica, G., et al. (2021). "Extracellular Vesicles in Neuroinflammation." Frontiers in Cell and Developmental Biology 8DOI: 10.3389/fcell.2020.623039.

Martin, E. R., et al. (2022). "A novel method for generating glutamatergic SH-SY5Y neuron-like cells utilizing B-27 supplement." Front Pharmacol 13: 943627DOI: 10.3389/fphar.2022.943627.

Martins, J. B., et al. (2013). "Differential effects of methyl-4-phenylpyridinium ion, rotenone, and Paraquat on differentiated SH-SY5Y cells." Journal of Toxicology 2013DOI: 10.1155/2013/347312.

Masato, A., et al. (2019). "Impaired dopamine metabolism in Parkinson's disease pathogenesis." Mol Neurodegener 14(1): 35DOI: 10.1186/s13024-019-0332-6.

Matsuda, W., et al. (2009). "Single Nigrostriatal Dopaminergic Neurons Form Widely Spread and Highly Dense Axonal Arborizations in the Neostriatum." The Journal of Neuroscience 29(2): 444-453DOI: 10.1523/jneurosci.4029-08.2009.

Mayers, J. R., et al. (2011). "ESCRT-0 Assembles as a Heterotetrameric Complex on Membranes and Binds Multiple Ubiquitinylated Cargoes Simultaneously." Journal of Biological Chemistry 286(11): 9636-9645DOI: 10.1074/jbc.M110.185363.

Meiser, J., et al. (2013). "Complexity of dopamine metabolism." Cell Communication and Signaling 11(1)DOI: 10.1186/1478-811x-11-34.

Merighi, A. (2018). "Costorage of High Molecular Weight Neurotransmitters in Large Dense Core Vesicles of Mammalian Neurons." Frontiers in Cellular Neuroscience 12DOI: 10.3389/fncel.2018.00272.

Meulener, M., et al. (2005). "Drosophila DJ-1 Mutants Are Selectively Sensitive to Environmental Toxins Associated with Parkinson's Disease." Current Biology 15(17): 1572-1577DOI: 10.1016/j.cub.2005.07.064.

Mihoub, M., et al. (2017). Protein Repair from Glycation by Glyoxals by the DJ-1 Family Maillard Deglycases. DJ-1/PARK7 Protein: 133-147DOI: 10.1007/978-981-10-6583-5_9.

Milkovic NM, Catazaro J, Lin J, et al. Transient sampling of aggregation-prone conformations causes

pathogenic instability of a parkinsonian mutant of DJ-1 at physiological temperature. Protein Science : a Publication of the Protein Society. 2015 Oct;24(10):1671-1685. DOI: 10.1002/pro.2762.

Min, H. K., et al. (2022). "DJ-1 controls T cell differentiation and osteoclastogenesis in rheumatoid arthritis." Sci Rep 12(1): 12767DOI: 10.1038/s41598-022-16285-1.

Miura, E., et al. (2014). "VPS35 dysfunction impairs lysosomal degradation of α-synuclein and exacerbates neurotoxicity in a Drosophila model of Parkinson's disease." Neurobiology of Disease 71: 1-13DOI: 10.1016/j.nbd.2014.07.014.

Miyajima, Y., et al. (2010). "Prognostic significance of nuclear DJ-1 expression in astrocytoma." Anticancer research 30(1): 265-269

Montecalvo, A., et al. (2012). "Mechanism of transfer of functional microRNAs between mouse dendritic cells via exosomes." Blood 119(3): 756-766DOI: 10.1182/blood-2011-02-338004.

Moore, A. E., et al. (2001). "Parkinsonian Motor Deficits Are Reflected by Proportional A9/A10 Dopamine Neuron Degeneration in the Rat." Experimental Neurology 172(2): 363-376DOI: 10.1006/exnr.2001.7823.

Morel, L., et al. (2013). "Neuronal Exosomal miRNA-dependent Translational Regulation of Astroglial Glutamate Transporter GLT1." Journal of Biological Chemistry 288(10): 7105-7116DOI: 10.1074/jbc.M112.410944.

Mosley, R. L., et al. (2013). "Triggering of Inflammasome by Aggregated α–Synuclein, an Inflammatory Response in Synucleinopathies." PLoS ONE 8(1)DOI: 10.1371/journal.pone.0055375.

Muddapu, V. R. and V. S. Chakravarthy (2021). "Influence of energy deficiency on the subcellular processes of Substantia Nigra Pars Compacta cell for understanding Parkinsonian neurodegeneration." Scientific Reports 11(1)DOI: 10.1038/s41598-021-81185-9.

Mulcahy, L. A., et al. (2014). "Routes and mechanisms of extracellular vesicle uptake." J Extracell Vesicles 3DOI: 10.3402/jev.v3.24641.

Muralidharan-Chari, V., et al. (2009). "ARF6-regulated shedding of tumor cell-derived plasma membrane microvesicles." Curr Biol 19(22): 1875-1885DOI: 10.1016/j.cub.2009.09.059.

Muzio, L., et al. (2021). "Microglia in Neuroinflammation and Neurodegeneration: From Understanding to Therapy." Frontiers in Neuroscience 15DOI: 10.3389/fnins.2021.742065.

Myers, A. J., et al. (2012). "Comprehensive Research Synopsis and Systematic Meta-Analyses in Parkinson's Disease Genetics: The PDGene Database." PLoS Genetics 8(3)DOI: 10.1371/journal.pgen.1002548.

Nagakubo, D., et al. (1997). "DJ-1, a Novel Oncogene Which Transforms Mouse NIH3T3 Cells in Cooperation withras." Biochemical and Biophysical Research Communications 231(2): 509-513DOI: 10.1006/bbrc.1997.6132.

Nanbo, A., et al. (2013). "Exosomes derived from Epstein-Barr virus-infected cells are internalized via caveola-dependent endocytosis and promote phenotypic modulation in target cells." J Virol 87(18): 10334-10347DOI: 10.1128/JVI.01310-13.

Naoi, M., et al. (1988). "Effect of 1-methyl-4-phenylpyridinium ion (MPP+) on catecholamine levels and activity of related enzymes in clonal rat pheochromocytoma PC12h cells." Life Sciences 43(18): 1485-1491DOI: 10.1016/0024-3205(88)90261-5.

Nature (1933). "Rotenone as an insecticide." Nature 132(167)DOI: https://doi.org/10.1038/132167b0.

Newman, L. A., et al. (2022). "Circulating cell-specific extracellular vesicles as biomarkers for the diagnosis and monitoring of chronic liver diseases." Cellular and Molecular Life Sciences 79(5)DOI: 10.1007/s00018-022-04256-8.

Ni, A. and C. Ernst (2022). "Evidence That Substantia Nigra Pars Compacta Dopaminergic Neurons Are Selectively Vulnerable to Oxidative Stress Because They Are Highly Metabolically Active." Frontiers in Cellular Neuroscience 16DOI: 10.3389/fncel.2022.826193.

Nirmala, J. G. and M. Lopus (2019). "Cell death mechanisms in eukaryotes." Cell Biology and Toxicology 36(2): 145-164DOI: 10.1007/s10565-019-09496-2.

Nuytemans, K., et al. (2010). "Genetic etiology of Parkinson disease associated with mutations in the SNCA, PARK2, PINK1, PARK7, and LRRK2 genes: a mutation update." Human Mutation 31(7): 763-780DOI: 10.1002/humu.21277.

Ogaki, A., et al. (2021). "Extracellular Vesicles Taken up by Astrocytes." International Journal of Molecular Sciences 22(19)DOI: 10.3390/ijms221910553.

Oh, S. E. and M. M. Mouradian (2018). "Cytoprotective mechanisms of DJ-1 against oxidative stress through modulating ERK1/2 and ASK1 signal transduction." Redox Biology 14: 211-217DOI: 10.1016/j.redox.2017.09.008.

Oh, S. E., et al. (2018). "The Parkinson's disease gene product DJ-1 modulates miR-221 to promote neuronal survival against oxidative stress." Redox Biology 19: 62-73DOI: 10.1016/j.redox.2018.07.021.

Olney, J. W., et al. (1990). "Excitotoxicity of L-dopa and 6-OH-dopa: implications for Parkinson's and Huntington's diseases." Exp Neurol 108(3): 269-272DOI: 10.1016/0014-4886(90)90134-e.

Orimo, S., et al. (2011). "Unmyelinated axons are more vulnerable to degeneration than myelinated axons of the cardiac nerve in Parkinson's disease." Neuropathology and Applied Neurobiology 37(7): 791-802DOI: 10.1111/j.1365-2990.2011.01194.x.

Ortega, F. G., et al. (2019). "Interfering with endolysosomal trafficking enhances release of bioactive exosomes." Nanomedicine: Nanotechnology, Biology and Medicine 20DOI: 10.1016/j.nano.2019.102014.

Ottolini, D., et al. (2013). "The Parkinson disease-related protein DJ-1 counteracts mitochondrial impairment induced by the tumour suppressor protein p53 by enhancing endoplasmic reticulum-mitochondria tethering." Human Molecular Genetics 22(11): 2152-2168DOI: 10.1093/hmg/ddt068.

Pahlman, S., et al. (1984). "Retinoic acid-induced differentiation of cultured human neuroblastoma cells: a comparison with phorbolester-induced differentiation." Cell Differ 14(2): 135-144DOI: 10.1016/0045-6039(84)90038-1.

Palsdottir, H. and C. Hunte (2004). "Lipids in membrane protein structures." Biochimica et Biophysica Acta (BBA) - Biomembranes 1666(1-2): 2-18DOI: 10.1016/j.bbamem.2004.06.012.

Pan, B. T., et al. (1985). "Electron microscopic evidence for externalization of the transferrin receptor in vesicular form in sheep reticulocytes." J Cell Biol 101(3): 942-948DOI: 10.1083/jcb.101.3.942.

Pardo, M., et al. (2006). "The characterization of the invasion phenotype of uveal melanoma tumour cells shows the presence of MUC18 and HMG-1 metastasis markers and leads to the identification of DJ-1 as a potential serum biomarker." International Journal of Cancer 119(5): 1014-1022DOI: 10.1002/ijc.21942.

Park, K. W., et al. (2022). "Delayed Infiltration of Peripheral Monocyte Contributes to Phagocytosis and Transneuronal Degeneration in Chronic Stroke." Stroke 53(7): 2377-2388DOI: 10.1161/strokeaha.122.038701.

Parolini, I., et al. (2009). "Microenvironmental pH is a key factor for exosome traffic in tumor cells." J Biol Chem 284(49): 34211-34222DOI: 10.1074/jbc.M109.041152.

Passer, B. J., et al. (2003). "The p53-inducible TSAP6 gene product regulates apoptosis and the cell cycle and interacts with Nix and the Myt1 kinase." Proceedings of the National Academy of Sciences 100(5): 2284-2289DOI: 10.1073/pnas.0530298100.

Pastuzyn, E. D., et al. (2018). "The Neuronal Gene Arc Encodes a Repurposed Retrotransposon Gag Protein that Mediates Intercellular RNA Transfer." Cell 172(1-2): 275-288.e218DOI: 10.1016/j.cell.2017.12.024.

Peng, H., et al. (2021). "Neuron-Derived Extracellular Vesicles Modulate Microglia Activation and Function." Biology 10(10)DOI: 10.3390/biology10100948.

Peng, L., et al. (2020). "DJ-1 exerts anti-inflammatory effects and regulates NLRX1-TRAF6 via SHP-1 in stroke." Journal of Neuroinflammation 17(1)DOI: 10.1186/s12974-020-01764-x.

Pennypacker, K. R., et al. (1989). "Changes in expression of tyrosine hydroxylase immunoreactivity in human SMS-KCNR neuroblastoma following retinoic acid or phorbol ester-induced differentiation." Molecular Brain Research 5(4): 251-258DOI: 10.1016/0169-328x(89)90059-4.

Perrett, R. M., et al. (2015). "The endosomal pathway in Parkinson's disease." Molecular and Cellular Neuroscience 66: 21-28DOI: 10.1016/j.mcn.2015.02.009.

Perry, V. H. and J. Teeling (2013). "Microglia and macrophages of the central nervous system: the contribution of microglia priming and systemic inflammation to chronic neurodegeneration." Seminars in Immunopathology 35(5): 601-612DOI: 10.1007/s00281-013-0382-8.

Petrucelli, L., et al. (2010). "Reduced Basal Autophagy and Impaired Mitochondrial Dynamics Due to Loss of Parkinson's Disease-Associated Protein DJ-1." PLoS ONE 5(2)DOI: 10.1371/journal.pone.0009367.

Pfeifer, G. P. (2024). "DNA Damage and Parkinson's Disease." International Journal of Molecular Sciences 25(8)DOI: 10.3390/ijms25084187.

Pifl, C., et al. (1993). "Dopamine transporter expression confers cytotoxicity to low doses of the parkinsonism-inducing neurotoxin 1-methyl-4-phenylpyridinium." J Neurosci 13(10): 4246-4253DOI: 10.1523/JNEUROSCI.13-10-04246.1993.

Pissadaki, E. K. and J. P. Bolam (2013). "The energy cost of action potential propagation in dopamine neurons: clues to susceptibility in Parkinson's disease." Frontiers in Computational Neuroscience 7DOI: 10.3389/fncom.2013.00013.

Poole, L. B. (2015). The basics of thiols and cysteines in redox biology and chemistry. Free Radical Biology and Medicine, Elsevier Inc. 80: 148-157DOI: 10.1016/j.freeradbiomed.2014.11.013.

Puspita, L., et al. (2017). "Oxidative stress and cellular pathologies in Parkinson's disease." Molecular Brain 10(1)DOI: 10.1186/s13041-017-0340-9.

Qi, Z., et al. (2014). "Rotenone and paraquat perturb dopamine metabolism: A computational analysis of pesticide toxicity." Toxicology 315(1): 92-101DOI: 10.1016/j.tox.2013.11.003.

Rajendra, E., et al. (2014). "Abundance of the Fanconi anaemia core complex is regulated by the RuvBL1 and RuvBL2 AAA+ ATPases." Nucleic Acids Research 42(22): 13736-13748DOI: 10.1093/nar/gku1230.

Ramsey, C. P. and B. I. Giasson (2010). "L10p and P158DEL DJ-1 mutations cause protein instability, aggregation, and dimerization impairments." Journal of Neuroscience Research 88(14): 3111-3124DOI: 10.1002/jnr.22477.

Raninga, P. V., et al. (2017). The Multifaceted Roles of DJ-1 as an Antioxidant. DJ-1/PARK7 Protein: 67-87DOI: 10.1007/978-981-10-6583-5_6.

Record, M., et al. (2018). "Extracellular vesicles: lipids as key components of their biogenesis and

functions." Journal of Lipid Research 59(8): 1316-1324DOI: 10.1194/jlr.E086173.

Reddig, P. J. and R. L. Juliano (2005). "Clinging to life: cell to matrix adhesion and cell survival." Cancer and Metastasis Reviews 24(3): 425-439DOI: 10.1007/s10555-005-5134-3.

Reitz, C., et al. (2011). "Epidemiology of Alzheimer disease." Nature Reviews Neurology 7(3): 137-152DOI: 10.1038/nrneurol.2011.2.

Repici, M. and F. Giorgini (2019). "DJ-1 in Parkinson's Disease: Clinical Insights and Therapeutic Perspectives." Journal of Clinical Medicine 8(9): 1377-1377DOI: 10.3390/jcm8091377.

Rose, R., et al. (2022). "Chromatin compaction precedes apoptosis in developing neurons." Communications Biology 5(1)DOI: 10.1038/s42003-022-03704-2.

Ross, R. A., et al. (1983). "Coordinate morphological and biochemical interconversion of human neuroblastoma cells." J Natl Cancer Inst 71(4): 741-747

Ruan, Z., et al. (2021). "Alzheimer's disease brain-derived extracellular vesicles spread tau pathology in interneurons." Brain 144(1): 288-309DOI: 10.1093/brain/awaa376.

Salama, M. and O. Arias-Carrión (2011). "Natural toxins implicated in the development of Parkinson's disease." Therapeutic Advances in Neurological Disorders 4(6): 361-373DOI: 10.1177/1756285611413004.

Sami, A., et al. (2020). "Advances in the Signaling Pathways Downstream of Glial-Scar Axon Growth Inhibitors." Frontiers in Cellular Neuroscience 14DOI: 10.3389/fncel.2020.00174.

Sampson, T. R., et al. (2016). "Gut Microbiota Regulate Motor Deficits and Neuroinflammation in a Model of Parkinson's Disease." Cell 167(6): 1469-1480.e1412DOI: 10.1016/j.cell.2016.11.018.

Sarnowska, A. (2002). "Application of organotypic hippocampal culture for study of selective neuronal death." Folia Neuropathol 40(2): 101-106

Sartori-Rupp, A., et al. (2019). "Correlative cryo-electron microscopy reveals the structure of TNTs in neuronal cells." Nature Communications 10(1)DOI: 10.1038/s41467-018-08178-7.

Savitt, D. and J. Jankovic (2019). "Targeting α-Synuclein in Parkinson's Disease: Progress Towards the Development of Disease-Modifying Therapeutics." Drugs 79(8): 797-810DOI: 10.1007/s40265-019-01104-1.

Schildknecht, S., et al. (2015). "Preferential Extracellular Generation of the Active Parkinsonian Toxin MPP+by Transporter-Independent Export of the Intermediate MPDP+." Antioxidants & Redox Signaling 23(13): 1001-1016DOI: 10.1089/ars.2015.6297.

Seet, R. C. S., et al. (2010). "Oxidative damage in Parkinson disease: Measurement using accurate

biomarkers." Free Radical Biology and Medicine 48(4): 560-566DOI: 10.1016/j.freeradbiomed.2009.11.026.

Sekito, A., et al. (2005). "Stimulation of transforming activity of DJ-1 by Abstrakt, a DJ-1-binding protein." International Journal of Oncology 26(3): 685-689

Sevlever, D., et al. (2008). "Cathepsin D Is the Main Lysosomal Enzyme Involved in the Degradation of α-Synuclein and Generation of Its Carboxy-Terminally Truncated Species." Biochemistry 47(36): 9678-9687DOI: 10.1021/bi800699v.

Sharma, A., et al. (2021). "Comprehensive Profiling of Blood Coagulation and Fibrinolysis Marker Reveals Elevated Plasmin-Antiplasmin Complexes in Parkinson's Disease." Biology 10(8)DOI: 10.3390/biology10080716.

Sharma, S., et al. (2020). "Impact of isolation methods on the biophysical heterogeneity of single extracellular vesicles." Scientific Reports 10(1)DOI: 10.1038/s41598-020-70245-1.

Shinbo, Y., et al. (2005). "DJ-1 restores p53 transcription activity inhibited by Topors/p53BP3." Int J Oncol 26(3): 641-648

Sidransky, E., et al. (2009). "Multicenter Analysis of Glucocerebrosidase Mutations in Parkinson's Disease." New England Journal of Medicine 361(17): 1651-1661DOI: 10.1056/NEJMoa0901281.

Silva, M. T. (2010). "Secondary necrosis: The natural outcome of the complete apoptotic program." FEBS Letters 584(22): 4491-4499DOI: 10.1016/j.febslet.2010.10.046.

Smolders, S. M.-T., et al. (2019). "Microglia: Brain cells on the move." Progress in Neurobiology 178DOI: 10.1016/j.pneurobio.2019.04.001.

Soldati, T., et al. (2012). "Bin2 Is a Membrane Sculpting N-BAR Protein That Influences Leucocyte Podosomes, Motility and Phagocytosis." PLoS ONE 7(12)DOI: 10.1371/journal.pone.0052401.

Soukup, S. F., et al. (2018). "Parkinson's disease: convergence on synaptic homeostasis." The EMBO Journal 37(18)DOI: 10.15252/embj.201898960.

Stathakis, D. G., et al. (1997). "Human Postsynaptic Density-95 (PSD95): Location of the Gene (DLG4) and Possible Function in Nonneural as Well as in Neural Tissues." Genomics 44(1): 71-82DOI: 10.1006/geno.1997.4848.

Stefanova, N., et al. (2011). "Toll-Like Receptor 4 Promotes α-Synuclein Clearance and Survival of Nigral Dopaminergic Neurons." The American Journal of Pathology 179(2): 954-963DOI: 10.1016/j.ajpath.2011.04.013.

Stephenson, S. E. M., et al. (2019). "Familial early onset Parkinson's disease caused by a homozygous frameshift variant in PARK7: Clinical features and literature update." Parkinsonism & Related Disorders 64: 308-311DOI: 10.1016/j.parkreldis.2019.03.013.

Stogsdill, J. A. and C. Eroglu (2017). "The interplay between neurons and glia in synapse development and plasticity." Current Opinion in Neurobiology 42: 1-8DOI: 10.1016/j.conb.2016.09.016.

Stout, J. R., et al. (2011). "Kif18B interacts with EB1 and controls astral microtubule length during mitosis." Molecular Biology of the Cell 22(17): 3070-3080DOI: 10.1091/mbc.e11-04-0363.

Stuendl, A., et al. (2016). "Induction of α-synuclein aggregate formation by CSF exosomes from patients with Parkinson's disease and dementia with Lewy bodies." Brain 139(2): 481-494DOI: 10.1093/brain/awv346.

Surmeier, D. J. (2018). "Determinants of dopaminergic neuron loss in Parkinson's disease." The FEBS Journal 285(19): 3657-3668DOI: 10.1111/febs.14607.

Svensson, K. J., et al. (2013). "Exosome uptake depends on ERK1/2-heat shock protein 27 signaling and lipid Raft-mediated endocytosis negatively regulated by caveolin-1." J Biol Chem 288(24): 17713-17724DOI: 10.1074/jbc.M112.445403.

Taghavi, S., et al. (2018). "A Clinical and Molecular Genetic Study of 50 Families with Autosomal Recessive Parkinsonism Revealed Known and Novel Gene Mutations." Molecular Neurobiology 55(4): 3477-3489DOI: 10.1007/s12035-017-0535-1.

Taguchi, K., et al. (2018). "Expression of α-synuclein is regulated in a neuronal cell type-dependent manner." Anatomical Science International 94(1): 11-22DOI: 10.1007/s12565-018-0464-8.

Taira, T., et al. (2004). "DJ-1 has a role in antioxidative stress to prevent cell death." EMBO reports 5(2): 213-218DOI: 10.1038/sj.embor.7400074.

Takahashi-Niki, K., et al. (2017). Transcriptional Regulation of DJ-1. DJ-1/PARK7 Protein: 89-95DOI: 10.1007/978-981-10-6583-5_7.

Takasugi, M., et al. (2017). "Small extracellular vesicles secreted from senescent cells promote cancer cell proliferation through EphA2." Nature Communications 8(1)DOI: 10.1038/ncomms15728.

Takimoto, C. H., et al. (2019). "The Macrophage 'Do not eat me' signal, CD47, is a clinically validated cancer immunotherapy target." Annals of Oncology 30(3): 486-489DOI: 10.1093/annonc/mdz006.

Tansey, M. G., et al. (2022). "Inflammation and immune dysfunction in Parkinson disease." Nature Reviews Immunology 22(11): 657-673DOI: 10.1038/s41577-022-00684-6.

Tarantino, P., et al. (2009). "Compound heterozygosity in DJ-1 gene non-coding portion related to parkinsonism." Parkinsonism & Related Disorders 15(4): 324-326DOI: 10.1016/j.parkreldis.2008.07.001.

Taylor-Whiteley, T. R., et al. (2019). "Recapitulating Parkinson's disease pathology in a three-dimensional human neural cell culture model." Disease Models & MechanismsDOI: 10.1242/dmm.038042.

Teixeira, M., et al. (2021). "Alpha-Synuclein and the Endolysosomal System in Parkinson's Disease: Guilty

by Association." Biomolecules 11(9)DOI: 10.3390/biom11091333.

Teng, F. and M. Fussenegger (2020). "Shedding Light on Extracellular Vesicle Biogenesis and Bioengineering." Advanced Science 8(1)DOI: 10.1002/advs.202003505.

Théry, C., et al. (2018). "Minimal information for studies of extracellular vesicles 2018 (MISEV2018): a position statement of the International Society for Extracellular Vesicles and update of the MISEV2014 guidelines." Journal of Extracellular Vesicles 7(1)DOI: 10.1080/20013078.2018.1535750.

Thomas, K. J., et al. (2011). "DJ-1 acts in parallel to the PINK1/parkin pathway to control mitochondrial function and autophagy." Human Molecular Genetics 20(1): 40-50DOI: 10.1093/hmg/ddq430.

Tian, M., et al. (2008). "Proteomic analysis identifies MMP-9, DJ-1 and A1BG as overexpressed proteins in pancreatic juice from pancreatic ductal adenocarcinoma patients." BMC Cancer 8(1): 241-241DOI: 10.1186/1471-2407-8-241.

Tortolici, F., et al. (2021). "Ionizing Radiation-Induced Extracellular Vesicle Release Promotes AKT-Associated Survival Response in SH-SY5Y Neuroblastoma Cells." Cells 10(1)DOI: 10.3390/cells10010107.

Trajkovic, K., et al. (2008). "Ceramide triggers budding of exosome vesicles into multivesicular endosomes." Science 319(5867): 1244-1247DOI: 10.1126/science.1153124.

Trams, E. G., et al. (1981). "Exfoliation of membrane ecto-enzymes in the form of micro-vesicles." Biochim Biophys Acta 645(1): 63-70DOI: 10.1016/0005-2736(81)90512-5.

Tremblay, M.-E., et al. (2019). "Glial phagocytic clearance in Parkinson's disease." Molecular Neurodegeneration 14(1)DOI: 10.1186/s13024-019-0314-8.

Tricarico, C., et al. (2016). "Biology and biogenesis of shed microvesicles." Small GTPases 8(4): 220-232DOI: 10.1080/21541248.2016.1215283.

Trudler, D., et al. (2014). "DJ-1 deficiency triggers microglia sensitivity to dopamine toward a pro-inflammatory phenotype that is attenuated by rasagiline." Journal of Neurochemistry 129(3): 434-447DOI: 10.1111/jnc.12633.

Usunoff, K. G., et al. (2010). "Neuromelanin in the Human Brain: A Review and Atlas of Pigmented Cells in the Substantia Nigra." Archives of Physiology and Biochemistry 110(4): 257-369DOI: 10.1076/apab.110.4.257.11827.

Valente, E. M., et al. (2004). "Hereditary Early-Onset Parkinson's Disease Caused by Mutations in PINK1." Science 304(5674): 1158-1160DOI: 10.1126/science.1096284.

van Meteren, N., et al. (2019). "Polycyclic Aromatic Hydrocarbons Can Trigger Hepatocyte Release of Extracellular Vesicles by Various Mechanisms of Action Depending on Their Affinity for the Aryl Hydrocarbon Receptor." Toxicological Sciences 171(2): 443-462DOI: 10.1093/toxsci/kfz157.

van Niekerk, E. A., et al. (2022). "Methods for culturing adult CNS neurons reveal a CNS conditioning effect." Cell Reports Methods 2(7)DOI: 10.1016/j.crmeth.2022.100255.

Vatsyayan, R., et al. (2013). "4-Hydroxy-2-Nonenal Enhances Tissue Factor Activity in Human Monocytic Cells via p38 Mitogen-Activated Protein Kinase Activation-Dependent Phosphatidylserine Exposure." Arteriosclerosis, Thrombosis, and Vascular Biology 33(7): 1601-1611DOI: 10.1161/atvbaha.113.300972.

Venturini, A., et al. (2019). "Exosomes From Astrocyte Processes: Signaling to Neurons." Frontiers in Pharmacology 10DOI: 10.3389/fphar.2019.01452.

Verkhratsky, A., et al. (2023). "Astrocytes in human central nervous system diseases: a frontier for new therapies." Signal Transduction and Targeted Therapy 8(1)DOI: 10.1038/s41392-023-01628-9.

Visanji, N. P., et al. (2013). "The prion hypothesis in Parkinson's disease: Braak to the future." Acta Neuropathologica Communications 1(1)DOI: 10.1186/2051-5960-1-2.

Vonk, L. A., et al. (2018). "Mesenchymal Stromal/stem Cell-derived Extracellular Vesicles Promote Human Cartilage Regeneration In Vitro." Theranostics 8(4): 906-920DOI: 10.7150/thno.20746.

Vornov, J. J., et al. (1998). "Regional vulnerability to endogenous and exogenous oxidative stress in organotypic hippocampal culture." Exp Neurol 149(1): 109-122DOI: 10.1006/exnr.1997.6673.

Voss, A. K. and A. Strasser (2020). "The essentials of developmental apoptosis." F1000Research 9DOI: 10.12688/f1000research.21571.1.

Waitzman, J. S. and S. E. Rice (2013). "Mechanism and regulation of kinesin-5, an essential motor for the mitotic spindle." Biology of the Cell 106(1): 1-12DOI: 10.1111/boc.201300054.

Wang, C., et al. (2017). "Investigation of endosome and lysosome biology by ultra pH-sensitive nanoprobes." Advanced Drug Delivery Reviews 113: 87-96DOI: 10.1016/j.addr.2016.08.014.

Wang, K., et al. (2017). "TNF-α promotes extracellular vesicle release in mouse astrocytes through glutaminase." Journal of Neuroinflammation 14(1)DOI: 10.1186/s12974-017-0853-2.

Wang, Q. and R. Zennadi (2020). "Oxidative Stress and Thrombosis during Aging: The Roles of Oxidative Stress in RBCs in Venous Thrombosis." International Journal of Molecular Sciences 21(12)DOI: 10.3390/ijms21124259.

Wang, T., et al. (2020). "DJ-1 Regulates Microglial Polarization Through P62-Mediated TRAF6/IRF5 Signaling in Cerebral Ischemia-Reperfusion." Frontiers in Cell and Developmental Biology 8DOI: 10.3389/fcell.2020.593890.

Wang, X., et al. (2009). "Genomic and biochemical approaches in the discovery of mechanisms for selective neuronal vulnerability to oxidative stress." BMC Neurosci 10: 12DOI: 10.1186/1471-2202-10-12.

Wang, X.-J. and J.-X. Xu (2005). "Possible involvement of Ca2+ signaling in rotenone-induced apoptosis in human neuroblastoma SH-SY5Y cells." Neuroscience Letters 376(2): 127-132DOI: 10.1016/j.neulet.2004.11.041.

Wang, Z.-X., et al. (2023). "DNA Damage-Mediated Neurotoxicity in Parkinson's Disease." International Journal of Molecular Sciences 24(7)DOI: 10.3390/ijms24076313.

Weismann, D. and C. J. Binder (2012). "The innate immune response to products of phospholipid peroxidation." Biochimica et Biophysica Acta (BBA) - Biomembranes 1818(10): 2465-2475DOI: 10.1016/j.bbamem.2012.01.018.

Welsh, J. A., et al. (2024). "Minimal information for studies of extracellular vesicles (MISEV2023): From basic to advanced approaches." Journal of Extracellular Vesicles 13(2)DOI: ARTN e12404 10.1002/jev2.12404.

Wen, G., et al. (2021). "Proteomic characterization of secretory granules in dopaminergic neurons indicates chromogranin/secretogranin-mediated protein processing impairment in Parkinson's disease." Aging 13(16): 20335-20358DOI: 10.18632/aging.203415.

Wilcock, A. C., et al. (2007). "Mitotic spindle orientation distinguishes stem cell and terminal modes of neuron production in the early spinal cord." Development 134(10): 1943-1954DOI: 10.1242/dev.002519.

Wilde, G. J., et al. (1997). "Differential vulnerability of the CA1 and CA3 subfields of the hippocampus to superoxide and hydroxyl radicals in vitro." J Neurochem 69(2): 883-886DOI: 10.1046/j.1471-4159.1997.69020883.x.

Willhoft, O. and D. B. Wigley (2020). "INO80 and SWR1 complexes: the non-identical twins of chromatin remodelling." Current Opinion in Structural Biology 61: 50-58DOI: 10.1016/j.sbi.2019.09.002.

Wilson, M. A. (2011) The Role of Cysteine Oxidation in DJ-1 Function and Dysfunction. Antioxid Redox Signal. 15(1): 111-112. DOI: 10.1089/ars.2010.3481

Wilson, M. A., et al. (2003). "The 1.1-Å resolution crystal structure of DJ-1, the protein mutated in autosomal recessive early onset Parkinson's disease." Proceedings of the National Academy of Sciences 100(16): 9256-9261 DOI: 10.1073/pnas.1133288100.

Witt, A. C., et al. (2008). "Cysteine pKa depression by a protonated glutamic acid in human DJ-1." Biochemistry 47(28): 7430-7440DOI: 10.1021/bi800282d.

Wollert, T. and J. H. Hurley (2010). "Molecular mechanism of multivesicular body biogenesis by ESCRT complexes." Nature 464(7290): 864-869DOI: 10.1038/nature08849.

Xiao, B., et al. (2022). "Mitophagy and reactive oxygen species interplay in Parkinson's disease." npj Parkinson's Disease 8(1) DOI: 10.1038/s41531-022-00402-y.

Xiao, Y., et al. (2021). "Role of extracellular vesicles in neurodegenerative diseases." Progress in

Neurobiology 201DOI: 10.1016/j.pneurobio.2021.102022.

Xicoy, H., et al. (2017). "The SH-SY5Y cell line in Parkinson's disease research: a systematic review." Molecular Neurodegeneration 12(1) DOI: 10.1186/s13024-017-0149-0.

Xie, F., et al. (2022). "Breast cancer cell-derived extracellular vesicles promote CD8+ T cell exhaustion via TGF-β type II receptor signaling." Nature Communications 13(1) DOI: 10.1038/s41467-022-31250-2.

Xu, X. M., et al. (1995). "A Combination of BDNF and NT-3 Promotes Supraspinal Axonal Regeneration into Schwann Cell Grafts in Adult Rat Thoracic Spinal Cord." Experimental Neurology 134(2): 261-272DOI: 10.1006/exnr.1995.1056.

Yanagisawa, D., et al. (2008). "DJ-1 Protects against Neurodegeneration Caused by Focal Cerebral Ischemia and Reperfusion in Rats." Journal of Cerebral Blood Flow & Metabolism 28(3): 563-578DOI: 10.1038/sj.jcbfm.9600553.

Yin, Z., et al. (2020). "Neuron-derived exosomes with high miR-21-5p expression promoted polarization of M1 microglia in culture." Brain, Behavior, and Immunity 83: 270-282DOI: 10.1016/j.bbi.2019.11.004.

Yoshimura, Y., et al. (2023). "Par1b/MARK2 Phosphorylates Kinesin-Like Motor Protein GAKIN/KIF13B To Regulate Axon Formation." Molecular and Cellular Biology 30(9): 2206-2219DOI: 10.1128/mcb.01181-09.

Yu, H.-L., et al. (2020). "Myosin X Interaction with KIF13B, a Crucial Pathway for Netrin-1-Induced Axonal Development." The Journal of Neuroscience 40(48): 9169-9185DOI: 10.1523/jneurosci.0929-20.2020.

Yuan, A., et al. (2017). "Neurofilaments and Neurofilament Proteins in Health and Disease." Cold Spring Harbor Perspectives in Biology 9(4)DOI: 10.1101/cshperspect.a018309.

Yuen, H. F., et al. (2008). "DJ-1 Could Predict Worse Prognosis in Esophageal Squamous Cell Carcinoma." Cancer Epidemiology Biomarkers & Prevention 17(12): 3593-3602DOI: 10.1158/1055-9965.EPI-08-0214.

Yuyama, K., et al. (2020). "Lysosomal-associated transmembrane protein 4B regulates ceramide-induced exosome release." The FASEB Journal 34(12): 16022-16033DOI: 10.1096/fj.202001599R.

Yuyama, K., et al. (2014). "Decreased Amyloid-β Pathologies by Intracerebral Loading of Glycosphingolipid-enriched Exosomes in Alzheimer Model Mice." Journal of Biological Chemistry 289(35): 24488-24498DOI: 10.1074/jbc.M114.577213.

Zaborowski, M. P., et al. (2015). "Extracellular Vesicles: Composition, Biological Relevance, and Methods of Study." Bioscience 65(8): 783-797DOI: 10.1093/biosci/biv084.

Zavodszky, E., et al. (2014). "Mutation in VPS35 associated with Parkinson's disease impairs WASH complex association and inhibits autophagy." Nature Communications 5(1)DOI: 10.1038/ncomms4828.

Zeng, N., et al. (2022). "DJ-1 depletion prevents immunoaging in T-cell compartments." EMBO reports 23(3)DOI: 10.15252/embr.202153302.

Zeng, Z., et al. (2018). "Revealing cellular and molecular complexity of the central nervous system using single cell sequencing." Stem Cell Research & Therapy 9(1)DOI: 10.1186/s13287-018-0985-z.

Zhang, L., et al. (2020). "Role of DJ-1 in Immune and Inflammatory Diseases." Frontiers in Immunology 11DOI: 10.3389/fimmu.2020.00994.

Zhang, S., et al. (2018). "Intercellular transfer of pathogenic α-synuclein by extracellular vesicles is induced by the lipid peroxidation product 4-hydroxynonenal." Neurobiology of Aging 61: 52-65DOI: 10.1016/j.neurobiolaging.2017.09.016.

Zhao, N., et al. (2022). "DJ-1 activates the Atg5-Atg12-Atg16L1 complex via Sirt1 to influence microglial polarization and alleviate cerebral ischemia/reperfusion-induced inflammatory injury." Neurochemistry International 157DOI: 10.1016/j.neuint.2022.105341.

Zhao, W., et al. (2017). "Nanoscale manipulation of membrane curvature for probing endocytosis in live cells." Nature Nanotechnology 12(8): 750-756DOI: 10.1038/nnano.2017.98.

Zhou, T., et al. (2019). "α-synuclein accumulation in SH-SY5Y cell impairs autophagy in microglia by exosomes overloading miR-19a-3p." Epigenomics 11(15): 1661-1677DOI: 10.2217/epi-2019-0222.

Zhou, T., et al. (2022). "Effects of miRNAs in exosomes derived from α-synuclein overexpressing SH-SY5Y cells on autophagy and inflammation of microglia." Cellular Signalling 89DOI: 10.1016/j.cellsig.2021.110179.

Zhou, Y., et al. (2017). "DJ-1/Park7 Sensitive Na+/H+Exchanger 1 (NHE1) in CD4+T Cells." Journal of Cellular Physiology 232(11): 3050-3059DOI: 10.1002/jcp.25516.

Zhu, G., et al. (2022). "Crosstalk Between the Oxidative Stress and Glia Cells After Stroke: From Mechanism to Therapies." Frontiers in Immunology 13DOI: 10.3389/fimmu.2022.852416.

Zhu, X.-L., et al. (2010). "DJ-1: A novel independent prognostic marker for survival in glottic squamous cell carcinoma." Cancer Science 101(5): 1320-1325DOI: 10.1111/j.1349-7006.2010.01531.x.

Zou, L., et al. (2021). "Dysfunction of Synaptic Vesicle Endocytosis in Parkinson's Disease." Frontiers in Integrative Neuroscience 15DOI: 10.3389/fnint.2021.619160.

Zwaal, R. F. and A. J. Schroit (1997). "Pathophysiologic implications of membrane phospholipid asymmetry in blood cells." Blood 89(4): 1121-1132

Supplementary

Mass spectrometry data

Accession	Uniprot Entry	Gene Names (primary)	WT mean	DJ-1 KO mean	Fold change	P t.test
APOH_HUMAN	P02749	APOH	17.129	447.083	26.102	0.030
MGT5A_HUMAN	Q09328	MGAT5	1.689	37.847	22.411	0.005
SCG2_HUMAN	P13521	SCG2	18.617	278.749	14.973	0.007
CADH2_HUMAN	P19022	CDH2	23.987	322.496	13.445	0.044
PPIA_HUMAN	P62937	PPIA	508.275	3718.484	7.316	0.025
MECP2_HUMAN	P51608	MECP2	547.134	3418.532	6.248	0.001
PYGL_HUMAN	P06737	PYGL	1.919	10.068	5.246	0.043
LYST_HUMAN	Q99698	LYST	1216.269	5262.960	4.327	0.001
DEN2B_HUMAN	P78524	DENND2B	22.520	97.147	4.314	0.004
ANTR1_HUMAN	Q9H6X2	ANTXR1	2215.598	9381.200	4.234	0.000
VGF_HUMAN	O15240	VGF	1364.564	5565.972	4.079	0.002
NALP2_HUMAN	Q9NX02	NLRP2	445.502	1721.351	3.864	0.031
C1QT3_HUMAN	Q9BXJ4	C1QTNF3	194.435	741.125	3.812	0.003
BIN2_HUMAN	Q9UBW5	BIN2	154.760	555.386	3.589	0.007
ARGL1_HUMAN	Q9NWB6	ARGLU1	17100.672	57768.397	3.378	0.000
TRFL_HUMAN	P02788	LTF	5066.782	13212.617	2.608	0.002
MTMR3_HUMAN	Q13615	MTMR3	510.755	1301.277	2.548	0.026
PDC10_HUMAN	Q9BUL8	PDCD10	145.814	367.843	2.523	0.001
CBPN_HUMAN	P15169	CPN1	448.435	1085.677	2.421	0.046
BHMT1_HUMAN	Q93088	BHMT	141.052	329.370	2.335	0.006
CERU_HUMAN	P00450	CP	35.530	82.111	2.311	0.006
CAD11_HUMAN	P55287	CDH11	426.576	944.051	2.213	0.018
HMCN1_HUMAN	Q96RW7	HMCN1	1980.435	4167.647	2.104	0.002
CD109_HUMAN	Q6YHK3	CD109	1610.494	3343.372	2.076	0.011
ARMC9_HUMAN	Q7Z3E5	ARMC9	806.021	1667.453	2.069	0.027
TBCK_HUMAN	Q8TEA7	TBCK	1894.551	3917.256	2.068	0.019
AFAM_HUMAN	P43652	AFM	980.258	1954.984	1.994	0.016

PXDC2_HUMAN	Q6UX71	PLXDC2	178.567	354.292	1.984	0.027
A2MG_HUMAN	P01023	A2M	109537.504	215784.598	1.970	0.035
TSR1_HUMAN	Q2NL82	TSR1	32379.580	61436.443	1.897	0.014
SOX30_HUMAN	O94993	SOX30	57487.437	108936.247	1.895	0.044
NU160_HUMAN	Q12769	NUP160	795.141	1476.855	1.857	0.044
POSTN_HUMAN	Q15063	POSTN	3837.431	7037.119	1.834	0.029
PLTP_HUMAN	P55058	PLTP	830.500	1519.263	1.829	0.030
HEMO_HUMAN	P02790	HPX	636.656	1149.715	1.806	0.005
CMGA_HUMAN	P10645	CHGA	3819.629	6890.390	1.804	0.018
ALBU_HUMAN	P02768	ALB	486388.346	866818.398	1.782	0.006
HGFA_HUMAN	Q04756	HGFAC	226.319	385.959	1.705	0.014
CP2U1_HUMAN	Q7Z449	CYP2U1	2505.877	4228.425	1.687	0.017
RGS22_HUMAN	Q8NE09	RGS22	586.416	984.093	1.678	0.023
THBG_HUMAN	P05543	SERPINA7	7822.753	12538.901	1.603	0.007
IDHC_HUMAN	O75874	IDH1	585.412	935.929	1.599	0.025
TVAZ2_HUMAN	A0A0B4J265	TRAV26-2	4133.967	6356.666	1.538	0.039
FBN1_HUMAN	P35555	FBN1	1651.580	2535.208	1.535	0.041
FETA_HUMAN	P02771	AFP	52813.331	80822.424	1.530	0.015
CP2C8_HUMAN	P10632	CYP2C8	40559.214	60347.580	1.488	0.041
PTK7_HUMAN	Q13308	PTK7	149.172	216.550	1.452	0.047
PCLO_HUMAN	Q9Y6V0	PCLO	554.944	784.771	1.414	0.038
ANT3_HUMAN	P01008	SERPINC1	4676.610	6600.531	1.411	0.018
KI18B_HUMAN	Q86Y91	KIF18B	1225.797	1725.731	1.408	0.012
LAMB1_HUMAN	P07942	LAMB1	34266.501	29750.907	0.868	0.032
KIF11_HUMAN	P52732	KIF11	433.268	311.110	0.718	0.026
ZN318_HUMAN	Q5VUA4	ZNF318	456.909	325.213	0.712	0.000
TEN4_HUMAN	Q6N022	TENM4	544.054	381.599	0.701	0.014
IGSF3_HUMAN	O75054	IGSF3	205.918	126.545	0.615	0.017
HSP7C_HUMAN	P11142	HSPA8	4941.305	3005.236	0.608	0.009
KPYM_HUMAN	P14618	PKM	4373.759	2640.787	0.604	0.002
LAMA4_HUMAN	Q16363	LAMA4	1303.718	786.763	0.603	0.021
NCAM1_HUMAN	P13591	NCAM1	1581.695	951.532	0.602	0.012
ZG16B_HUMAN	Q96DA0	ZG16B	847.935	505.334	0.596	0.046
MED23_HUMAN	Q9ULK4	MED23	1909.475	1131.297	0.592	0.037
PLD3_HUMAN	Q8IV08	PLD3	1218.699	720.824	0.591	0.010
STAM1_HUMAN	Q92783	STAM	3463.084	2023.797	0.584	0.014
DACT1_HUMAN	Q9NYF0	DACT1	2447.125	1403.339	0.573	0.025
DJC13_HUMAN	O75165	DNAJC13	545.650	301.728	0.553	0.036
APOD_HUMAN	P05090	APOD	449.924	248.449	0.552	0.008
CLH1_HUMAN	Q00610	CLTC	1626.897	891.449	0.548	0.018
MARCS_HUMAN	P29966	MARCKS	2055.685	1113.148	0.541	0.010
ZA2G_HUMAN	P25311	AZGP1	1560.213	819.026	0.525	0.019
A1AT_HUMAN	P01009	SERPINA1	1803.477	939.677	0.521	0.048

NCAM2_HUMAN	O15394	NCAM2	533.384	276.711	0.519	0.030
S53A1_HUMAN	Q9UBH6	XPR1	696.018	358.450	0.515	0.026
PGCA_HUMAN	P16112	ACAN	326.900	166.414	0.509	0.047
CBPC3_HUMAN	Q8NEM8	AGBL3	609.159	309.207	0.508	0.037
AT1A3_HUMAN	P13637	ATP1A3	4538.910	2252.402	0.496	0.010
PCDBB_HUMAN	Q9Y5F2	PCDHB11	236.274	116.981	0.495	0.028
RFTN1_HUMAN	Q14699	RFTN1	108.650	53.453	0.492	0.012
F234A_HUMAN	Q9H0X4	FAM234A	132.812	64.854	0.488	0.025
MDR1_HUMAN	P08183	ABCB1	2327.324	1136.172	0.488	0.015
KCD11_HUMAN	Q693B1	KCTD11	519.382	250.861	0.483	0.011
ITB3_HUMAN	P05106	ITGB3	148.226	70.357	0.475	0.001
TTYH3_HUMAN	Q9C0H2	TTYH3	1886.172	880.874	0.467	0.019
ITA3_HUMAN	P26006	ITGA3	250.399	113.079	0.452	0.033
FILA2_HUMAN	Q5D862	FLG2	1222.682	543.188	0.444	0.041
TAF5_HUMAN	Q15542	TAF5	134.641	59.607	0.443	0.040
SERC1_HUMAN	Q9NRX5	SERINC1	456.658	201.686	0.442	0.008
EGF_HUMAN	P01133	EGF	527.100	230.204	0.437	0.015
BMAL2_HUMAN	Q8WYA1	BMAL2	586.604	256.064	0.437	0.011
LRIQ1_HUMAN	Q96JM4	LRRIQ1	362.577	142.213	0.392	0.020
ITA1_HUMAN	P56199	ITGA1	1281.633	500.687	0.391	0.012
CD63_HUMAN	P08962	CD63	1226.824	475.108	0.387	0.039
DPYL1_HUMAN	Q14194	CRMP1	69.356	26.547	0.383	0.015
IGSF8_HUMAN	Q969P0	IGSF8	9728.276	3599.732	0.370	0.004
STX2_HUMAN	P32856	STX2	122.666	45.314	0.369	0.041
TRY3_HUMAN	P35030	PRSS3	15221.083	5595.730	0.368	0.028
VAT1_HUMAN	Q99536	VAT1	460.756	162.757	0.353	0.030
TEKL1_HUMAN	Q8IYK2	TEKTL1	99.573	34.813	0.350	0.013
KIF22_HUMAN	Q14807	KIF22	3857.933	1302.096	0.338	0.004
BUP1_HUMAN	Q9UBR1	UPB1	2479.764	832.353	0.336	0.002
FA47A_HUMAN	Q5JRC9	FAM47A	462.604	153.889	0.333	0.047
C1TC_HUMAN	P11586	MTHFD1	205.112	68.124	0.332	0.010
TBB4A_HUMAN	P04350	TUBB4A	84.973	27.602	0.325	0.041
ATPA_HUMAN	P25705	ATP5F1A	839.718	222.087	0.264	0.038
NEUM_HUMAN	P17677	GAP43	587.566	153.004	0.260	0.003
RDH14_HUMAN	Q9HBH5	RDH14	348.141	85.779	0.246	0.015
CD47_HUMAN	Q08722	CD47	204.910	49.668	0.242	0.007
CSPG2_HUMAN	P13611	VCAN	10952.618	2337.187	0.213	0.001
SYT11_HUMAN	Q9BT88	SYT11	1453.751	197.053	0.136	0.010
TCAF1_HUMAN	Q9Y4C2	TCAF1	541.217	68.886	0.127	0.049
BASP1_HUMAN	P80723	BASP1	1608.089	182.708	0.114	0.001
GDIA_HUMAN	P31150	GDI1	175.509	18.535	0.106	0.000
KI13B_HUMAN	Q9NQT8	KIF13B	176.862	15.258	0.086	0.040
TS101_HUMAN	Q99816	TSG101	150.752	7.748	0.051	0.022

ZN451_HUMAN	Q9Y4E5	ZNF451	216.742	7.109	0.033	0.019
LAMB2_HUMAN	P55268	LAMB2	37.580	0.296	0.008	0.000
RUVB2_HUMAN	Q9Y230	RUVBL2	23.270	0.000	0.000	0.001
HEP2_HUMAN	P05546	SERPIND1	536.429	400.572	0.747	0.051
PTN4_HUMAN	P29074	PTPN4	159.855	99.547	0.623	0.052
TBB4B_HUMAN	P68371	TUBB4B	446.322	197.978	0.444	0.052
RFC5_HUMAN	P40937	RFC5	1358.493	258.822	0.191	0.052
ARFG3_HUMAN	Q9NP61	ARFGAP3	399.105	1076.227	2.697	0.053
OMD_HUMAN	Q99983	OMD	771.802	894.411	1.159	0.054
EF1A2_HUMAN	Q05639	EEF1A2	2580.680	745.700	0.289	0.055
LUM_HUMAN	P51884	LUM	29471.436	39312.287	1.334	0.056
IGJ_HUMAN	P01591	JCHAIN	330.179	6.626	0.020	0.057
ACTG_HUMAN	P63261	ACTG1	676.299	1943.941	2.874	0.057
H2A1B_HUMAN	P04908	H2AC4; H2AC8	525.173	1895.794	3.610	0.059
RAB30_HUMAN	Q15771	RAB30	174.610	245.454	1.406	0.059
CD81_HUMAN	P60033	CD81	6303.856	2437.561	0.387	0.060
TRFE_HUMAN	P02787	TF	2064.032	4245.269	2.057	0.060
LIN41_HUMAN	Q2Q1W2	TRIM71	7166.935	5649.191	0.788	0.061
AT1B1_HUMAN	P05026	ATP1B1	4916.445	2263.538	0.460	0.061
PCD16_HUMAN	Q96JQ0	DCHS1	2646.219	3628.189	1.371	0.062
DOP1_HUMAN	Q5JWR5	DOP1A	10195.947	3027.935	0.297	0.062
EMAL2_HUMAN	O95834	EML2	278.617	95.865	0.344	0.062
SERA_HUMAN	O43175	PHGDH	369.358	101.745	0.275	0.063
TIMP2_HUMAN	P16035	TIMP2	137.332	347.178	2.528	0.063
LAMA5_HUMAN	O15230	LAMA5	33111.655	25302.807	0.764	0.063
FA10_HUMAN	P00742	F10	4524.329	2682.038	0.593	0.064
HFM1_HUMAN	A2PYH4	HFM1	538.198	1113.923	2.070	0.065
RS27A_HUMAN	P62979	RPS27A	39359.789	24783.659	0.630	0.067
SAHH_HUMAN	P23526	AHCY	10024.648	4922.697	0.491	0.067
GNAQ_HUMAN	P50148	GNAQ	108.608	19.389	0.179	0.067
ATPB_HUMAN	P06576	ATP5F1B	710.688	261.335	0.368	0.067
4F2_HUMAN	P08195	SLC3A2	726.286	458.049	0.631	0.068
DYH8_HUMAN	Q96JB1	DNAH8	457.724	207.844	0.454	0.069
ASPM_HUMAN	Q8IZT6	ASPM	359.583	167.968	0.467	0.070
PLAK_HUMAN	P14923	JUP	593.117	222.692	0.375	0.070
CTL2_HUMAN	Q8IWA5	SLC44A2	581.422	294.595	0.507	0.071
ITIH2_HUMAN	P19823	ITIH2	87182.114	130765.698	1.500	0.071
BASI_HUMAN	P35613	BSG	403.435	202.891	0.503	0.072
CAP1_HUMAN	Q01518	CAP1	352.845	163.668	0.464	0.072
NFKB2_HUMAN	Q00653	NFKB2	184.303	72.982	0.396	0.073
ITB1_HUMAN	P05556	ITGB1	4104.983	2147.249	0.523	0.075
GDIB_HUMAN	P50395	GDI2	568.295	260.574	0.459	0.075

F163B_HUMAN	P0C2L3	FAM163B	1125.164	160.393	0.143	0.076
SHRM3_HUMAN	Q8TF72	SHROOM3	165.471	13.646	0.082	0.076
AN18A_HUMAN	Q8IVF6	ANKRD18A	2915.663	4623.701	1.586	0.077
ARF5_HUMAN	P84085	ARF5	207.258	108.131	0.522	0.078
ACTN1_HUMAN	P12814	ACTN1	131.315	164.430	1.252	0.078
PML_HUMAN	P29590	PML	325.326	165.720	0.509	0.079
DESM_HUMAN	P17661	DES	404.783	266.522	0.658	0.079
CA2D2_HUMAN	Q9NY47	CACNA2D2	221.699	124.325	0.561	0.079
C4BPA_HUMAN	P04003	C4BPA	1130.478	1553.458	1.374	0.079
2AAA_HUMAN	P30153	PPP2R1A	320.343	265.772	0.830	0.081
KDM5B_HUMAN	Q9UGL1	KDM5B	984.700	531.202	0.539	0.082
MPRI_HUMAN	P11717	IGF2R	14920.933	29405.284	1.971	0.082
TBC16_HUMAN	Q8TBP0	TBC1D16	399.284	503.041	1.260	0.084
AL9A1_HUMAN	P49189	ALDH9A1	260.165	124.178	0.477	0.084
PERM_HUMAN	P05164	MPO	911.426	56.871	0.062	0.085
SMCA4_HUMAN	P51532	SMARCA4	6484.363	4978.790	0.768	0.086
PDIA3_HUMAN	P30101	PDIA3	89.506	14.623	0.163	0.088
IC1_HUMAN	P05155	SERPING1	1542.037	3492.941	2.265	0.088
ILF2_HUMAN	Q12905	ILF2	1044.066	1732.432	1.659	0.090
CTNB1_HUMAN	P35222	CTNNB1	827.411	427.379	0.517	0.091
TCPH_HUMAN	Q99832	CCT7	71.411	10.821	0.152	0.091
SHBG_HUMAN	P04278	SHBG	336.795	281.907	0.837	0.092
Z3H7B_HUMAN	Q9UGR2	ZC3H7B	2154.591	3080.889	1.430	0.094
WDR1_HUMAN	O75083	WDR1	649.917	436.505	0.672	0.094
PDC6I_HUMAN	Q8WUM4	PDCD6IP	3215.059	2097.610	0.652	0.097
MOCS3_HUMAN	O95396	MOCS3	4661.634	7162.142	1.536	0.097
NBEL2_HUMAN	Q6ZNJ1	NBEAL2	51.635	24.692	0.478	0.100
HS90B_HUMAN	P08238	HSP90AB1	2528.445	2002.000	0.792	0.101
GNAS1_HUMAN	Q5JWF2	GNAS	312.079	68.104	0.218	0.102
SBSN_HUMAN	Q6UWP8	SBSN	52.023	0.000	0.000	0.102
STXB1_HUMAN	P61764	STXBP1	496.133	163.758	0.330	0.102
BCD1_HUMAN	Q9NWK9	ZNHIT6	40.721	62.354	1.531	0.103
DPOE1_HUMAN	Q07864	POLE	2816.220	4309.335	1.530	0.105
EMIL1_HUMAN	Q9Y6C2	EMILIN1	41131.298	31060.819	0.755	0.109
GCP6_HUMAN	Q96RT7	TUBGCP6	23.585	4.267	0.181	0.109
GP119_HUMAN	Q8TDV5	GPR119	1850.950	2714.828	1.467	0.110
LACTB_HUMAN	P83111	LACTB	1656.779	2734.651	1.651	0.110
TPD55_HUMAN	Q96J77	TPD52L3	548.337	59.919	0.109	0.110
CYFP1_HUMAN	Q7L576	CYFIP1	59.277	11.182	0.189	0.111
FPRP_HUMAN	Q9P2B2	PTGFRN	874.327	426.082	0.487	0.112
PFKAM_HUMAN	P08237	PFKM	181.775	119.179	0.656	0.113
PR14L_HUMAN	Q5THK1	PRR14L	613.817	227.652	0.371	0.114

JIP4_HUMAN	O60271	SPAG9	95.342	15.540	0.163	0.114
COQA1_HUMAN	Q96A83	COL26A1	159.479	45.903	0.288	0.115
TCPE_HUMAN	P48643	CCT5	642.633	397.211	0.618	0.115
ARPC4_HUMAN	P59998	ARPC4	220.870	354.141	1.603	0.116
METL5_HUMAN	Q9NRN9	METTL5	56.546	19.941	0.353	0.117
SPTN1_HUMAN	Q13813	SPTAN1	4035.944	6477.451	1.605	0.117
CTCFL_HUMAN	Q8NI51	CTCFL	11925.460	6730.746	0.564	0.118
SORCN_HUMAN	P30626	SRI	966.171	558.783	0.578	0.119
LMF1_HUMAN	Q96S06	LMF1	777.804	217.173	0.279	0.120
AKAP9_HUMAN	Q99996	AKAP9	272.243	406.215	1.492	0.120
ASB6_HUMAN	Q9NWX5	ASB6	2151.517	3686.996	1.714	0.122
PGK1_HUMAN	P00558	PGK1	4425.721	8008.588	1.810	0.122
HS71A_HUMAN	P0DMV8	HSPA1A	882.363	391.383	0.444	0.122
IF4A1_HUMAN	P60842	EIF4A1	426.136	215.905	0.507	0.123
CO5_HUMAN	P01031	C5	9513.659	14187.863	1.491	0.124
VCAM1_HUMAN	P19320	VCAM1	288.799	417.859	1.447	0.126
PSA6_HUMAN	P60900	PSMA6	279.308	193.725	0.694	0.127
GSTP1_HUMAN	P09211	GSTP1	670.409	312.921	0.467	0.127
PGS2_HUMAN	P07585	DCN	625.334	348.801	0.558	0.127
CNDP2_HUMAN	Q96KP4	CNDP2	267.225	175.093	0.655	0.129
CTNA1_HUMAN	P35221	CTNNA1	280.885	204.777	0.729	0.129
ARH37_HUMAN	A1IGU5	ARHGEF37	14275.253	17388.483	1.218	0.130
TBA1A_HUMAN	Q71U36	TUBA1A	439.573	247.835	0.564	0.132
DCD_HUMAN	P81605	DCD	9944.435	13977.660	1.406	0.133
CBAR2_HUMAN	Q6ZTR7	CIBAR2	412.693	627.667	1.521	0.136
CADH6_HUMAN	P55285	CDH6	60.380	95.334	1.579	0.137
FBLN1_HUMAN	P23142	FBLN1	13106.811	19663.203	1.500	0.138
WDR54_HUMAN	Q9H977	WDR54	482.847	1009.229	2.090	0.139
EF1A1_HUMAN	P68104	EEF1A1	2533.025	1752.378	0.692	0.140
ATD3A_HUMAN	Q9NVI7	ATAD3A	358.439	72.375	0.202	0.141
CFAB_HUMAN	P00751	CFB	370.622	211.053	0.569	0.141
A1BG_HUMAN	P04217	A1BG	4719.360	6269.573	1.328	0.142
ENPL_HUMAN	P14625	HSP90B1	300.313	217.125	0.723	0.142
A4_HUMAN	P05067	APP	980.269	1867.862	1.905	0.143
CO4A_HUMAN	P0C0L4	C4A	2257.540	3156.436	1.398	0.143
IL8_HUMAN	P10145	CXCL8	146.781	24.045	0.164	0.145
VINC_HUMAN	P18206	VCL	689.991	905.937	1.313	0.147
IGL1_HUMAN	P0DOX8		1843.384	3392.241	1.840	0.148
TENA_HUMAN	P24821	TNC	7581.632	3508.509	0.463	0.151
TBB3_HUMAN	Q13509	TUBB3	206.898	96.759	0.468	0.152
MABP1_HUMAN	O60336	MAPKBP1	48.129	102.252	2.125	0.153
LDHA_HUMAN	P00338	LDHA	3229.512	4542.558	1.407	0.153
TBB5_HUMAN	P07437	TUBB	5072.456	2716.464	0.536	0.154

URP2_HUMAN	Q86UX7	FERMT3	1607.703	1093.122	0.680	0.155
ENOA_HUMAN	P06733	ENO1	6111.816	3751.565	0.614	0.156
IGG1_HUMAN	P0DOX5		1677.009	699.362	0.417	0.156
AB12B_HUMAN	Q7Z5M8	ABHD12B	1300.652	2631.777	2.023	0.159
UBR4_HUMAN	Q5T4S7	UBR4	206.774	81.947	0.396	0.160
SG196_HUMAN	Q9H5K3	POMK	369.420	217.580	0.589	0.160
PRG4_HUMAN	Q92954	PRG4	279.680	55.969	0.200	0.167
VA0D1_HUMAN	P61421	ATP6V0D1	6902.080	12607.412	1.827	0.169
HBB_HUMAN	P68871	HBB	15420.515	30471.319	1.976	0.173
GNAL_HUMAN	P38405	GNAL	575.431	490.170	0.852	0.174
MDGA1_HUMAN	Q8NFP4	MDGA1	411.695	237.617	0.577	0.177
ITIH3_HUMAN	Q06033	ITIH3	38036.987	55631.335	1.463	0.177
P2RX4_HUMAN	Q99571	P2RX4	842.106	1279.532	1.519	0.180
NEBU_HUMAN	P20929	NEB	648.016	493.136	0.761	0.180
MOES_HUMAN	P26038	MSN	2166.340	1788.032	0.825	0.180
PTN9_HUMAN	P43378	PTPN9	123.277	312.889	2.538	0.182
ARP2_HUMAN	P61160	ACTR2	258.230	177.724	0.688	0.184
EXT1_HUMAN	Q16394	EXT1	0.000	60.905	609046.193	0.185
APOB_HUMAN	P04114	APOB	11489.563	20789.371	1.809	0.187
ISLR2_HUMAN	Q6UXK2	ISLR2	138.067	84.963	0.615	0.187
ALDR_HUMAN	P15121	AKR1B1	435.884	270.446	0.620	0.188
CNTN1_HUMAN	Q12860	CNTN1	356.681	728.358	2.042	0.189
LCAT_HUMAN	P04180	LCAT	757.045	1046.904	1.383	0.190
INADL_HUMAN	Q8NI35	PATJ	397.082	1027.297	2.587	0.192
ITIH4_HUMAN	Q14624	ITIH4	12221.078	21187.474	1.734	0.193
CO3_HUMAN	P01024	C3	98826.168	136203.015	1.378	0.194
USH1G_HUMAN	Q495M9	USH1G	1334.742	1924.702	1.442	0.197
NOCT_HUMAN	Q9UK39	NOCT	107.428	17.518	0.163	0.199
UBA1_HUMAN	P22314	UBA1	213.726	146.865	0.687	0.206
ILK_HUMAN	Q13418	ILK	797.600	453.733	0.569	0.206
FA11_HUMAN	P03951	F11	53.148	29.494	0.555	0.207
KCND2_HUMAN	Q9NZV8	KCND2	301.437	2.898	0.010	0.207
TRA2A_HUMAN	Q13595	TRA2A	490.955	340.986	0.695	0.208
EXT2_HUMAN	Q93063	EXT2	25.058	14.917	0.595	0.213
UDB15_HUMAN	P54855	UGT2B15	962.103	446.541	0.464	0.214
MBRL_HUMAN	Q4ZIN3	TMEM259	40.207	7.939	0.197	0.215
HORN_HUMAN	Q86YZ3	HRNR	1676.943	1286.318	0.767	0.216
RET_HUMAN	P07949	RET	2469.841	1800.515	0.729	0.218
O51Q1_HUMAN	Q8NH59	OR51Q1	556.147	712.024	1.280	0.220
CLP1_HUMAN	Q92989	CLP1	4649.315	7813.125	1.680	0.222
DEP1A_HUMAN	Q5TB30	DEPDC1	394.915	277.645	0.703	0.222
H2B1B_HUMAN	P33778	H2BC3	463.409	90.363	0.195	0.223

SOX_HUMAN	Q9P0Z9	PIPOX	1878.695	2373.261	1.263	0.223
MRP_HUMAN	P49006	MARCKSL1	1326.978	3191.977	2.405	0.227
PEPD_HUMAN	P12955	PEPD	240.084	170.554	0.710	0.229
PRKDC_HUMAN	P78527	PRKDC	200.886	432.864	2.155	0.230
ADA21_HUMAN	Q9UKJ8	ADAM21	7956.086	5970.178	0.750	0.231
FETUA_HUMAN	P02765	AHSG	1814.588	1011.585	0.557	0.232
CO6A3_HUMAN	P12111	COL6A3	1339.323	784.911	0.586	0.232
PIP_HUMAN	P12273	PIP	1276.809	621.004	0.486	0.234
NCAN_HUMAN	O14594	NCAN	205.951	45.773	0.222	0.236
MFGM_HUMAN	Q08431	MFGE8	5629.404	3447.454	0.612	0.239
L2GL1_HUMAN	Q15334	LLGL1	188.399	123.091	0.653	0.239
GELS_HUMAN	P06396	GSN	80935.684	113639.882	1.404	0.240
HMGCL_HUMAN	P35914	HMGCL	3703.342	2319.590	0.626	0.241
CO7_HUMAN	P10643	C7	3426.620	5271.804	1.538	0.241
PARK7_HUMAN	Q99497	PARK7	548.381	404.072	0.737	0.241
H4_HUMAN	P62805	H4C1;	1102.652	211.144	0.191	0.241
DESP_HUMAN	P15924	DSP	3322.044	2672.710	0.805	0.242
TRI32_HUMAN	Q13049	TRIM32	2099.950	2321.490	1.105	0.242
GDIR1_HUMAN	P52565	ARHGDIA	540.466	199.495	0.369	0.243
PSB6_HUMAN	P28072	PSMB6	965.171	704.432	0.730	0.246
AP2D_HUMAN	Q7Z6R9	TFAP2D	4619.935	1628.937	0.353	0.248
PLEK_HUMAN	P08567	PLEK	2287.315	1400.944	0.612	0.251
ASIP_HUMAN	P42127	ASIP	225.486	57.904	0.257	0.266
TCPG_HUMAN	P49368	CCT3	239.700	160.644	0.670	0.266
AT1A1_HUMAN	P05023	ATP1A1	1153.880	970.077	0.841	0.266
TEN3_HUMAN	Q9P273	TENM3	207.986	99.914	0.480	0.268
1433F_HUMAN	Q04917	YWHAH	31.792	1.781	0.056	0.269
DAPLE_HUMAN	Q9P219	CCDC88C	101.321	65.385	0.645	0.271
IP3KC_HUMAN	Q96DU7	ITPKC	171.843	124.321	0.723	0.271
SPAG1_HUMAN	Q07617	SPAG1	205.028	255.371	1.246	0.275
RAB35_HUMAN	Q15286	RAB35	71.201	36.889	0.518	0.276
VTNC_HUMAN	P04004	VTN	28114.220	39582.180	1.408	0.279
TBG1_HUMAN	P23258	TUBG1	1669.334	2058.351	1.233	0.279
LYSC_HUMAN	P61626	LYZ	2726.974	847.090	0.311	0.280
CD276_HUMAN	Q5ZPR3	CD276	208.226	80.780	0.388	0.282
CO5A1_HUMAN	P20908	COL5A1	399.134	254.933	0.639	0.284
BAIP2_HUMAN	Q9UQB8	BAIAP2	665.745	414.164	0.622	0.285
C1QT4_HUMAN	Q9BXJ3	C1QTNF4	380.361	94.230	0.248	0.285
ITPR3_HUMAN	Q14573	ITPR3	92.353	60.763	0.658	0.286
CLC11_HUMAN	Q9Y240	CLEC11A	424.976	684.410	1.610	0.287
ZPI_HUMAN	Q9UK55	SERPINA10	138.008	260.833	1.890	0.288
KCRB_HUMAN	P12277	CKB	16872.826	9579.342	0.568	0.288
RALA_HUMAN	P11233	RALA	1538.064	1055.317	0.686	0.289

ANXA2_HUMAN	P07355	ANXA2	1248.602	1895.190	1.518	0.294
RB11A_HUMAN	P62491	RAB11A	4032.796	2784.725	0.691	0.294
DPYL2_HUMAN	Q16555	DPYSL2	672.927	564.247	0.838	0.297
GAN_HUMAN	Q9H2C0	GAN	1317.559	1902.804	1.444	0.299
H3C_HUMAN	Q6NXT2	H3-5	2765.603	1966.536	0.711	0.301
MROH5_HUMAN	Q6ZUA9	MROH5	2326.941	3459.617	1.487	0.305
AT10A_HUMAN	O60312	ATP10A	563.787	324.368	0.575	0.306
IQGA1_HUMAN	P46940	IQGAP1	968.616	632.915	0.653	0.306
ZDBF2_HUMAN	Q9HCK1	ZDBF2	386.608	686.902	1.777	0.311
FIBA_HUMAN	P02671	FGA	1066.705	1591.531	1.492	0.312
HDAC5_HUMAN	Q9UQL6	HDAC5	581.647	259.041	0.445	0.314
ARAP1_HUMAN	Q96P48	ARAP1	4830.272	6906.850	1.430	0.315
TTC7B_HUMAN	Q86TV6	TTC7B	935.106	1444.898	1.545	0.316
SE6L1_HUMAN	Q9BYH1	SEZ6L	142.131	85.281	0.600	0.318
SYQ_HUMAN	P47897	QARS1	310.111	236.534	0.763	0.318
DDX27_HUMAN	Q96GQ7	DDX27	423.809	1744.612	4.117	0.319
RAP2A_HUMAN	P10114	RAP2A	415.654	238.684	0.574	0.320
IGHA1_HUMAN	P01876	IGHA1	1943.478	482.913	0.248	0.321
GNAI3_HUMAN	P08754	GNAI3	204.679	22.999	0.112	0.323
PGFRB_HUMAN	P09619	PDGFRB	115.322	140.911	1.222	0.323
PARP2_HUMAN	Q9UGN5	PARP2	2958.543	2344.725	0.793	0.330
NRAP_HUMAN	Q86VF7	NRAP	6788.178	10051.582	1.481	0.330
FBRS_HUMAN	Q9HAH7	FBRS	1962.815	3035.303	1.546	0.331
ZN844_HUMAN	Q08AG5	ZNF844	6892.500	11231.116	1.629	0.332
RRP12_HUMAN	Q5JTH9	RRP12	666.595	531.733	0.798	0.334
MT25B_HUMAN	Q96FB5	METTL25B	1830.838	2560.376	1.398	0.337
AMY1A_HUMAN	P0DUB6	AMY1A	122.263	253.381	2.072	0.338
NUAK2_HUMAN	Q9H093	NUAK2	488.455	1017.079	2.082	0.339
TPIS_HUMAN	P60174	TPI1	1874.157	2611.208	1.393	0.340
WDR27_HUMAN	A2RRH5	WDR27	4218.399	7174.700	1.701	0.341
LAMC1_HUMAN	P11047	LAMC1	13990.534	11232.936	0.803	0.353
RUND1_HUMAN	Q96C34	RUNDC1	671.654	538.887	0.802	0.354
ACTB_HUMAN	P60709	ACTB	5257.748	7467.907	1.420	0.355
TGM1_HUMAN	P22735	TGM1	59.964	314.160	5.239	0.356
AK1D1_HUMAN	P51857	AKR1D1	1688.479	1942.832	1.151	0.357
MMP2_HUMAN	P08253	MMP2	514.624	655.479	1.274	0.360
OPT_HUMAN	Q9UBM4	OPTC	951.922	1220.916	1.283	0.362
PGBM_HUMAN	P98160	HSPG2	2610.964	3772.466	1.445	0.370
DYHC2_HUMAN	Q8NCM8	DYNC2H1	153.606	47.672	0.310	0.370
TCPQ_HUMAN	P50990	CCT8	302.256	201.376	0.666	0.371
FINC_HUMAN	P02751	FN1	10092.151	11961.337	1.185	0.371
PKP1_HUMAN	Q13835	PKP1	35.128	0.000	0.000	0.374
SPT4H_HUMAN	P63272	SUPT4H1	90.672	55.500	0.612	0.374

KIF3C_HUMAN	O14782	KIF3C	2492.564	2794.713	1.121	0.376
XIRP2_HUMAN	A4UGR9	XIRP2	618.666	1017.029	1.644	0.380
RAE1_HUMAN	P24386	CHM	7348.763	9150.701	1.245	0.381
AMYP_HUMAN	P04746	AMY2A	2258.611	1875.098	0.830	0.383
CDC42_HUMAN	P60953	CDC42	858.510	1114.188	1.298	0.386
ABC3B_HUMAN	Q9UH17	APOBEC3B	3958.908	4823.424	1.218	0.387
HBA_HUMAN	P69905	HBA1;	44341.678	60332.773	1.361	0.388
ACES_HUMAN	P22303	ACHE	813.840	727.725	0.894	0.394
CATG_HUMAN	P08311	CTSG	155.241	13.125	0.085	0.395
FA5_HUMAN	P12259	F5	8553.483	7211.485	0.843	0.395
BMP7_HUMAN	P18075	BMP7	466.911	564.979	1.210	0.396
VPS35_HUMAN	Q96QK1	VPS35	306.527	244.951	0.799	0.399
GNAI2_HUMAN	P04899	GNAI2	243.192	85.346	0.351	0.401
1433E_HUMAN	P62258	YWHAE	5139.000	4240.796	0.825	0.403
MA7D2_HUMAN	Q96T17	MAP7D2	595.853	1107.367	1.858	0.405
APOM_HUMAN	O95445	APOM	1171.704	1413.632	1.206	0.408
HXD8_HUMAN	P13378	HOXD8	53.506	41.128	0.769	0.410
ARRC_HUMAN	P36575	ARR3	1703.687	2162.086	1.269	0.411
FMOD_HUMAN	Q06828	FMOD	774.999	1049.049	1.354	0.411
IGKC_HUMAN	P01834	IGKC	726.713	264.371	0.364	0.414
FIL1L_HUMAN	Q4L180	FILIP1L	323.590	161.559	0.499	0.416
ACSF3_HUMAN	Q4G176	ACSF3	78.296	119.298	1.524	0.423
EFC4A_HUMAN	Q8N4Y2	CRACR2B	3608.737	2618.550	0.726	0.423
RS18_HUMAN	P62269	RPS18	178.113	130.541	0.733	0.426
ENPP2_HUMAN	Q13822	ENPP2	474.639	501.777	1.057	0.428
TLN1_HUMAN	Q9Y490	TLN1	26316.820	34948.053	1.328	0.429
CFAD_HUMAN	P00746	CFD	926.284	1305.350	1.409	0.435
UB2V1_HUMAN	Q13404	UBE2V1	800.045	1100.800	1.376	0.437
AGRIN_HUMAN	O00468	AGRN	319.833	203.928	0.638	0.439
TMCO1_HUMAN	Q9UM00	TMCO1	289.929	208.078	0.718	0.440
MYO6_HUMAN	Q9UM54	MYO6	1341.917	1561.429	1.164	0.443
ANXA5_HUMAN	P08758	ANXA5	290.887	470.378	1.617	0.446
STMN1_HUMAN	P16949	STMN1	21636.997	11866.917	0.548	0.446
LV403_HUMAN	A0A075B6K6	IGLV4-3	139.404	21.422	0.154	0.452
RAB5C_HUMAN	P51148	RAB5C	521.154	670.908	1.287	0.457
RL18_HUMAN	Q07020	RPL18	1033.098	1517.914	1.469	0.458
EF2_HUMAN	P13639	EEF2	1724.031	1552.902	0.901	0.459
IL1AP_HUMAN	Q9NPH3	IL1RAP	152.548	180.100	1.181	0.462
VASP_HUMAN	P50552	VASP	0.266	10.620	39.869	0.463
FRPD1_HUMAN	Q5SYB0	FRMPD1	4841.938	5180.217	1.070	0.464
H2B1A_HUMAN	Q96A08	H2BC1	64.021	6.848	0.107	0.465
RGPD1_HUMAN	P0DJD0	RGPD1	1554.858	2138.726	1.376	0.465
DSG1_HUMAN	Q02413	DSG1	1059.965	775.416	0.732	0.467

PLP2_HUMAN	Q04941	PLP2	65.087	38.617	0.593	0.475
G3P_HUMAN	P04406	GAPDH	15254.404	13656.306	0.895	0.475
H2A1A_HUMAN	Q96QV6	H2AC1	876.968	351.808	0.401	0.476
SEPR_HUMAN	Q12884	FAP	183.826	151.294	0.823	0.477
MRCKA_HUMAN	Q5VT25	CDC42BPA	15.748	3.952	0.251	0.478
SEMG2_HUMAN	Q02383	SEMG2	259.720	351.193	1.352	0.489
GNAO_HUMAN	P09471	GNAO1	77.618	65.623	0.845	0.491
ANXA1_HUMAN	P04083	ANXA1	134.720	156.715	1.163	0.495
PARVB_HUMAN	Q9HBI1	PARVB	488.937	653.956	1.338	0.496
FSCN1_HUMAN	Q16658	FSCN1	206.437	133.245	0.645	0.505
TENR_HUMAN	Q92752	TNR	103329.193	85158.950	0.824	0.508
ITPR1_HUMAN	Q14643	ITPR1	1023.335	927.050	0.906	0.511
SACS_HUMAN	Q9NZJ4	SACS	461.015	576.000	1.249	0.515
ARHG6_HUMAN	Q15052	ARHGEF6	422.245	307.526	0.728	0.515
RAB7A_HUMAN	P51149	RAB7A	3551.560	2912.867	0.820	0.516
APLP2_HUMAN	Q06481	APLP2	788.609	891.095	1.130	0.517
LAMA2_HUMAN	P24043	LAMA2	13.848	18.745	1.354	0.519
PLVAP_HUMAN	Q9BX97	PLVAP	77.400	102.542	1.325	0.523
GFAP_HUMAN	P14136	GFAP	73544.072	65118.935	0.885	0.524
NAR4_HUMAN	Q93070	ART4	116.078	119.001	1.025	0.531
AT2B1_HUMAN	P20020	ATP2B1	149.553	101.642	0.680	0.532
ELOV6_HUMAN	Q9H5J4	ELOVL6	912.392	699.920	0.767	0.534
WDFY4_HUMAN	Q6ZS81	WDFY4	5213.509	6727.962	1.290	0.538
CGNL1_HUMAN	Q0VF96	CGNL1	456.097	574.554	1.260	0.539
ASXL1_HUMAN	Q8IXJ9	ASXL1	1625.073	1400.423	0.862	0.539
PI5L1_HUMAN	Q5T9C9	PIP5KL1	1546.341	992.694	0.642	0.542
PXDN_HUMAN	Q92626	PXDN	3171.259	3762.687	1.186	0.543
GOGB1_HUMAN	Q14789	GOLGB1	310.038	265.839	0.857	0.549
CGAS_HUMAN	Q8N884	CGAS	346.552	298.859	0.862	0.550
SDCB1_HUMAN	O00560	SDCBP	20794.163	17635.059	0.848	0.554
ELNE_HUMAN	P08246	ELANE	1697.672	2165.194	1.275	0.555
SPY4_HUMAN	Q9C004	SPRY4	171.102	264.936	1.548	0.556
GANAB_HUMAN	Q14697	GANAB	72.336	54.293	0.751	0.561
NHRF4_HUMAN	Q86UT5	NHERF4	333.941	224.561	0.672	0.564
F13A_HUMAN	P00488	F13A1	177.661	195.402	1.100	0.569
NRCAM_HUMAN	Q92823	NRCAM	162.957	110.664	0.679	0.572
COMP_HUMAN	P49747	COMP	2306.878	2100.142	0.910	0.573
BIP_HUMAN	P11021	HSPA5	3042.528	3379.491	1.111	0.574
TXK_HUMAN	P42681	TXK	2397.526	1871.138	0.780	0.577
MIME_HUMAN	P20774	OGN	1799.794	2039.075	1.133	0.580
FRM4A_HUMAN	Q9P2Q2	FRMD4A	476.046	441.785	0.928	0.581
SEMG1_HUMAN	P04279	SEMG1	382.053	1125.626	2.946	0.583
CO9_HUMAN	P02748	C9	6452.481	7682.574	1.191	0.585

B4GA1_HUMAN	O43505	B4GAT1	303.583	434.600	1.432	0.586
TSN8_HUMAN	P19075	TSPAN8	114.803	41.061	0.358	0.587
MDHC_HUMAN	P40925	MDH1	578.488	524.791	0.907	0.592
DYHC1_HUMAN	Q14204	DYNC1H1	258.369	221.218	0.856	0.592
JKIP2_HUMAN	Q96AA8	JAKMIP2	4011.269	7296.217	1.819	0.595
G6PI_HUMAN	P06744	GPI	215.869	369.084	1.710	0.599
XPP1_HUMAN	Q9NQW7	XPNPEP1	37.519	20.671	0.551	0.613
MTMR6_HUMAN	Q9Y217	MTMR6	556.852	440.136	0.790	0.615
1433B_HUMAN	P31946	YWHAB	7301.784	9122.231	1.249	0.619
ITIH1_HUMAN	P19827	ITIH1	11579.375	12123.440	1.047	0.621
S10A9_HUMAN	P06702	S100A9	458.928	260.908	0.569	0.621
FRIH_HUMAN	P02794	FTH1	130.520	147.358	1.129	0.621
GSTA5_HUMAN	Q7RTV2	GSTA5	2198.098	2672.824	1.216	0.622
FLNB_HUMAN	O75369	FLNB	65.025	70.929	1.091	0.623
AK1A1_HUMAN	P14550	AKR1A1	1140.125	1494.002	1.310	0.631
DPOLB_HUMAN	P06746	POLB	5018.257	5429.957	1.082	0.635
TSP3_HUMAN	P49746	THBS3	523.678	482.786	0.922	0.637
RAB10_HUMAN	P61026	RAB10	1312.171	1509.887	1.151	0.641
DOPO_HUMAN	P09172	DBH	1025.230	933.224	0.910	0.642
CASPE_HUMAN	P31944	CASP14	208.908	150.850	0.722	0.645
DPYL5_HUMAN	Q9BPU6	DPYSL5	103.675	122.936	1.186	0.658
RL21_HUMAN	P46778	RPL21	318.727	350.104	1.098	0.658
COG3_HUMAN	Q96JB2	COG3	332.209	305.203	0.919	0.660
1433G_HUMAN	P61981	YWHAG	1936.510	2334.105	1.205	0.660
CO8B_HUMAN	P07358	C8B	1079.372	1237.748	1.147	0.664
IFT80_HUMAN	Q9P2H3	IFT80	839.686	932.155	1.110	0.664
LG3BP_HUMAN	Q08380	LGALS3BP	73691.560	64670.697	0.878	0.665
PGAM1_HUMAN	P18669	PGAM1	142.200	199.005	1.399	0.672
TTC9B_HUMAN	Q8N6N2	TTC9B	97.783	91.680	0.938	0.672
PEDF_HUMAN	P36955	SERPINF1	45603.023	52009.340	1.140	0.675
KNOP1_HUMAN	Q1ED39	KNOP1	5497.753	5840.123	1.062	0.675
PSMD2_HUMAN	Q13200	PSMD2	50.265	46.930	0.934	0.677
QOR_HUMAN	Q08257	CRYZ	110.491	123.709	1.120	0.679
RAB6A_HUMAN	P20340	RAB6A	111.879	108.365	0.969	0.684
MO4L2_HUMAN	Q15014	MORF4L2	1296.067	1244.974	0.961	0.686
1433Z_HUMAN	P63104	YWHAZ	2497.132	1996.924	0.800	0.686
GOLM1_HUMAN	Q8NBJ4	GOLM1	199.548	207.616	1.040	0.687
FAAH2_HUMAN	Q6GMR7	FAAH2	157.439	138.225	0.878	0.689
COAA1_HUMAN	Q03692	COL10A1	669.983	771.221	1.151	0.694
ABHD8_HUMAN	Q96I13	ABHD8	1420.650	1135.440	0.799	0.696
CAMP_HUMAN	P49913	CAMP	327.969	315.245	0.961	0.697
IMB1_HUMAN	Q14974	KPNB1	595.229	623.536	1.048	0.705
TNKS2_HUMAN	Q9H2K2	TNKS2	8564.490	8933.420	1.043	0.706

TSP4_HUMAN	P35443	THBS4	2061.147	2332.225	1.132	0.708
UBAC2_HUMAN	Q8NBM4	UBAC2	2839.328	2967.489	1.045	0.721
SEM3C_HUMAN	Q99985	SEMA3C	261.372	274.921	1.052	0.721
CO1A1_HUMAN	P02452	COL1A1	566.781	297.618	0.525	0.722
APOA1_HUMAN	P02647	APOA1	2587.036	2134.026	0.825	0.724
PLS3_HUMAN	Q9NRY6	PLSCR3	1534.818	1792.309	1.168	0.728
LAMA1_HUMAN	P25391	LAMA1	98.302	96.786	0.985	0.729
TBA4A_HUMAN	P68366	TUBA4A	25421.360	21291.491	0.838	0.730
CA2D1_HUMAN	P54289	CACNA2D1	738.615	891.404	1.207	0.730
PMGE_HUMAN	P07738	BPGM	156.214	165.545	1.060	0.735
PSA1_HUMAN	P25786	PSMA1	34.248	79.155	2.311	0.746
IF2A_HUMAN	P05198	EIF2S1	176.684	157.585	0.892	0.747
XYLT1_HUMAN	Q86Y38	XYLT1	243.218	225.930	0.929	0.758
PRDX2_HUMAN	P32119	PRDX2	401.273	375.145	0.935	0.758
HS90A_HUMAN	P07900	HSP90AA1	10632.693	10194.144	0.959	0.759
PIAS1_HUMAN	O75925	PIAS1	5956.758	6843.936	1.149	0.761
AN36B_HUMAN	Q8N2N9	ANKRD36B	160.140	375.138	2.343	0.768
ATS13_HUMAN	Q76LX8	ADAMTS13	352.004	361.188	1.026	0.769
CALM1_HUMAN	P0DP23	CALM1	633.292	684.384	1.081	0.770
HRG_HUMAN	P04196	HRG	840.603	880.865	1.048	0.773
NP1L2_HUMAN	Q9ULW6	NAP1L2	306.298	218.014	0.712	0.781
FLNA_HUMAN	P21333	FLNA	7336.529	6737.042	0.918	0.781
LRP1_HUMAN	Q07954	LRP1	2312.938	2279.089	0.985	0.783
OR2W3_HUMAN	Q7Z3T1	OR2W3	321.993	354.921	1.102	0.787
ILEU_HUMAN	P30740	SERPINB1	309.240	272.332	0.881	0.795
FKBP8_HUMAN	Q14318	FKBP8	172.367	167.964	0.974	0.797
CSPG4_HUMAN	Q6UVK1	CSPG4	10.570	25.507	2.413	0.797
COL11_HUMAN	Q9BWP8	COLEC11	1537.100	1660.366	1.080	0.809
DDAH2_HUMAN	O95865	DDAH2	118.587	123.870	1.045	0.809
RAC1_HUMAN	P63000	RAC1	144.283	125.181	0.868	0.810
RHOA_HUMAN	P61586	RHOA	46.907	8.355	0.178	0.814
TENX_HUMAN	P22105	TNXB	4.385	13.962	3.184	0.817
APOE_HUMAN	P02649	APOE	80522.977	77013.324	0.956	0.821
NID1_HUMAN	P14543	NID1	4641.283	4541.727	0.979	0.824
AMPL_HUMAN	P28838	LAP3	3108.287	3341.946	1.075	0.826
SYT5_HUMAN	O00445	SYT5	128.036	133.406	1.042	0.827
FPPS_HUMAN	P14324	FDPS	3174.127	3435.503	1.082	0.833
LDHB_HUMAN	P07195	LDHB	3350.620	3079.859	0.919	0.836
CATZ_HUMAN	Q9UBR2	CTSZ	473.581	501.241	1.058	0.839
GPC2_HUMAN	Q8N158	GPC2	83.463	86.297	1.034	0.841
KDIS_HUMAN	Q9ULH0	KIDINS220	11225.468	11482.892	1.023	0.843
CAPZB_HUMAN	P47756	CAPZB	1646.403	1585.195	0.963	0.844

THRB_HUMAN	P00734	F2	200.367	370.861	1.851	0.847
LC1L1_HUMAN	Q5VSP4	LCN1P1	696.324	790.637	1.135	0.854
H2B1C_HUMAN	P62807	H2BC4;	532.584	666.409	1.251	0.863
CLIC1_HUMAN	O00299	CLIC1	529.915	500.062	0.944	0.865
L1CAM_HUMAN	P32004	L1CAM	142.219	136.463	0.960	0.868
HMGC2_HUMAN	Q8TB92	HMGCLL1	1855.019	1795.922	0.968	0.874
SGPL1_HUMAN	O95470	SGPL1	670.324	671.657	1.002	0.878
PKD1_HUMAN	P98161	PKD1	1114.050	1074.956	0.965	0.884
RSSA_HUMAN	P08865	RPSA	132.114	155.239	1.175	0.887
TAGL2_HUMAN	P37802	TAGLN2	3951.654	3807.574	0.964	0.902
BPIB1_HUMAN	Q8TDL5	BPIFB1	194.503	85.620	0.440	0.904
COIA1_HUMAN	P39060	COL18A1	730.767	816.204	1.117	0.908
TSP1_HUMAN	P07996	THBS1	58329.472	59218.517	1.015	0.908
ANXA6_HUMAN	P08133	ANXA6	51.684	48.973	0.948	0.912
MYH9_HUMAN	P35579	MYH9	5519.417	5140.111	0.931	0.922
APLD1_HUMAN	Q96LR9	APOLD1	6798.946	6948.056	1.022	0.925
FANCI_HUMAN	Q9NVI1	FANCI	891.168	888.193	0.997	0.931
BLMH_HUMAN	Q13867	BLMH	56.614	55.800	0.986	0.932
B4GT1_HUMAN	P15291	B4GALT1	38.632	35.394	0.916	0.933
ALDOA_HUMAN	P04075	ALDOA	658.267	590.217	0.897	0.933
TRPV3_HUMAN	Q8NET8	TRPV3	1665.561	1628.375	0.978	0.935
FIBB_HUMAN	P02675	FGB	4448.296	4242.547	0.954	0.935
PEBP1_HUMAN	P30086	PEBP1	1505.020	1592.570	1.058	0.936
HSPB1_HUMAN	P04792	HSPB1	212.297	193.813	0.913	0.951
RAP1A_HUMAN	P62834	RAP1A	4191.846	4407.582	1.051	0.952
CO6A1_HUMAN	P12109	COL6A1	9200.508	9120.803	0.991	0.955
PRDX1_HUMAN	Q06830	PRDX1	353.839	423.295	1.196	0.958
PIMT_HUMAN	P22061	PCMT1	237.080	254.461	1.073	0.964
MNS1_HUMAN	Q8NEH6	MNS1	642.507	665.680	1.036	0.967
RSU1_HUMAN	Q15404	RSU1	1202.463	1221.554	1.016	0.971
COF1_HUMAN	P23528	CFL1	2069.800	2023.717	0.978	0.974
DHSO_HUMAN	Q00796	SORD	197.815	182.078	0.920	0.975
CRBG3_HUMAN	Q68DQ2	CRYBG3	18879.978	18326.199	0.971	0.977
1433T_HUMAN	P27348	YWHAQ	369.519	435.711	1.179	0.988
TBB1_HUMAN	Q9H4B7	TUBB1	2897.959	3214.313	1.109	0.992

ImageJ code

Nile_red_endosome_counter.ijm

```
macro "Nile Red endosome counter"(

	/*

	 All images to be analysed should be in one folder in tiff format.

	 Multi channel is acceptable as long as endosome stain channel is consistent across all images.

	 Selection of channel occurs at later step and will be promted by messgae box.

	*/


	//get input + output directories from user

	in_directory = getDirectory("Choose input directory");

	out_directory = getDirectory("Choose output directory");


	//get list of files from input directory

	in_file_list = getFileList(in_directory);


	//Ask user whether images are multi channel and if so which channel is to be analysed.

	Multichannel_boolean = getBoolean("Are your images multichannel?");


	//if images are multichannel, ask user which channel is to be analysed. default = 1

	Analysis_channel = getNumber("Which channel should be analysed?", 1);
```

```
//loop over all files in input directory
for(i = 0; i < in_file_list.length; i++)(
	//open current file
	current_file_path = in_directory + in_file_list[i];
	open(current_file_path);

	//get current file name without extension
	image_name = File.getNameWithoutExtension(current_file_path);
	current_file = in_file_list[i];

	//show current progress
	showProgress(i+1 , in_file_list.length+1);

	//if multichannel, run multi channel preprocess function to isolate desired channel

	if(Multichannel_boolean)(
		//select correct channel
		Stack.setChannel(Analysis_channel);
	}

	//change LUT to "Yellow Hot".
	run("Yellow Hot");

	//run analysis function on current file
	Analysis();

};
```

```
//save summary table once all images analysed
	selectWindow("Summary");
	saveAs(
		"txt",
		out_directory + "Summary.txt"
	);
	close("Summary.txt");

//define analysis function
function Analysis()(
	//Ask user to perform background subtraction if deemed necessary
	waitForUser(
		"Background subtraction checkpoint",
		"Run Subtract Background now if desired.\nEnsure that parameters are
		recorded if ran!\n\nClick OK when ready to continue!"
	);

	//ask for user to run Find Maxima and click OK to continue
	waitForUser(
		"Find Maxima checkpoint",
		"Open 'Find Maxima' window.\nSelect strict, exclude edge, preview
		parameters,\nand desired noise value.\nEnsure prominence value is
		recorded!\n\nClick OK when ready to continue "
	);

	//select maxima image. name format dependant on whether image is multichannel
	if(Multichannel_boolean)(
		maxima_image_name = "C" + Analysis_channel + "-" + current_file + "
Maxima";
	} else (
```

```
		maxima_image_name = current_file + " Maxima";
	};
	//force image to binary to prevent errors
	run("Make Binary");

	//set summary measurements
	run("Set Measurements...", "area mean min center fit shape integrated median
area_fraction redirect=maxima_image_name decimal=3");

	//run analyze particles on maxima image
	run(
		"Analyze Particles...",
		"size=0-4 circularity=0.2-1.00 show=Overlay display exclude summarize
overlay"
	);

	//ask user if analysis is ok before continuing. Allow them to redo if not.
	particle_analysis_check = getBoolean("Has the particle analysis ran correctly?");

	//Delete particle analysis related outputs if ran incorrectly and ask user to rerun
	if(!particle_analysis_check)(
		close("Results");
		Table.deleteRows(i, i, "Summary");

		waitForUser("Re-run 'Analyze Particles' with desired parameters until
correct");
	}

	//Save Results table to output directory
	selectWindow("Results");
```

```
                saveAs(
                        "txt",
                        out_directory + image_name + "_Results.txt"
                );
                close("Results");
                close("*");
        };
}
```

Toxin Prelim fluor nuclei counter.ijm

```
/*
Sript to fully automate counting of fluorescent cell nuclei.

Current form designed to work for parkinsonian toxin preliminary data
with DAPI and GFP spectrum fluorescence only!!
 */

 macro "Fluorescent cell nuclei counter" (
        // Images should all be stored in one folder with distinct images for each channel.

        //get input + output directories from user
        in_directory = getDirectory("Choose input directory");
        out_directory = getDirectory("Choose output directory");

        //get list of files from input directory
        in_file_list = getFileList(in_directory);

        //ask user for find-maxima prominence-value settings to use for for each channel
```

```
DAPI_prominence = getNumber("State find-maxima prominence for DAPI channel", 5000);
GFP_prominence = getNumber("State find-maxima prominence for GFP channel", 12000);

count = 0;
//loop over all input images
for (i = 0; i < in_file_list.length; i++) (

    //Identify and set correct process based on image
    if (in_file_list[i].matches(".*DAPI.*")) (
        Prominence = DAPI_prominence;
        current_file_path = in_directory + in_file_list[i];
        open(current_file_path);

        run("Find Maxima...", "prominence=DAPI_prominence strict exclude
        output=Count");

        setResult("Image", count, getTitle());
        close("*");
        count = count + 1;
    } else if (in_file_list[i].matches(".*GFP.*"))(
        Prominence = GFP_prominence;
        current_file_path = in_directory + in_file_list[i];
        open(current_file_path);

        run("Find Maxima...", "prominence=GFP_prominence strict exclude
        output=Count");

        setResult("Image", count, getTitle());
        close("*");
```

```
                count = count + 1;
            };
        };

        //Save Results table to output directory
            selectWindow("Results");
            saveAs(
                "txt", out_directory + "Results.txt"
            );
            close("Results");
}
```

Diff SHSY Nuclear morphology analysis.ijm

```
/*
Script to automate the assessment of cell nuclear morphology in
one fluorescent channel via StarDist plugin in images of single channel tiff format.

Currently does not support semi-automatic or headless format

Optimised for Differentiated SH-SY5Y cells.
Do not use for other cells without adjustment of parameters.

Adjustments may be made in future to accomodate other formats.
*/
setBatchMode(true);
macro "Cell Nuclear Morphology" (
        //Ask user for input and output directories.
        /*
        Images should all be stored in one folder!
```

```
	Folder may contain images that will not be processed as selection of desrired files will occur.

	*/

	in_directory = getDirectory("Choose input directory");

	out_directory = getDirectory("Choose output directory");

	//get list of files from input directory

	in_file_list = getFileList(in_directory);

	//Ask user for string identifier of images to be processed from input directory

	process_file_identifier = getString(

		"Regular expression indentifying files to be processed. Leave blank if all.", ""

	);

	//Ask user for output file name

	output_file_name = getString(

		"Please state output file name", "Nuclear morphology Results"

	);

	//loop over all files in folder and process images matching desired identifier

	Processed_image_counter = 0; //Counter for processed images. Starts at 0, increments by 1 per image. 0 = first image.

	for (i = 0; i < in_file_list.length; i++) (

		//Decide whether to proccess current file

		if (in_file_list[i].matches(process_file_identifier)) (
```

```
                Process();
            };
        };

        //Save Results to output directory

        selectWindow("All_results");
        saveAs("text", out_directory + output_file_name);

        close("*");
        close("ROI Manager");
        close(output_file_name);

        //define analysis function
        function Process() (

            //Select image to be processed and open
            current_file_path = in_directory + in_file_list[i];
            open(current_file_path);
            current_image = getTitle();
            //run StarDist on image with described parameters
            run(
                "Command From Macro",
                "command=[de.csbdresden.stardist.StarDist2D], args=['input':
"+current_image+", 'modelChoice':'Versatile (fluorescent nuclei)', 'normalizeInput':'true',
'percentileBottom':'0.0', 'percentileTop':'100.0', 'probThresh':'0.4', 'nmsThresh':'0.4',
'outputType':'ROI Manager', 'nTiles':'1', 'excludeBoundary':'2', 'roiPosition':'Automatic',
'verbose':'false', 'showCsbdeepProgress':'false', 'showProbAndDist':'false'], process=[false]"
            );
```

```
//Measure morphology parameters and summarise
if(roiManager("count") > 1) (
	roiManager("Measure");
	run("Summarize");

	//Generate overall result table if not present, i.e at start of loop iteration
	if (isOpen("All_results")==false) (
		//get headings from results table to be used in conjoined table
		selectWindow("Results");
		Headings = split(Table.headings);
		//create all result table
		Table.create("All_results");
		selectWindow("All_results");
		for (i = 0; i < Headings.length; i++) (
			Table.set(Headings[i],0, "");
		};
	} else (
		Headings = split(Table.headings);
	};

	//Append results data to all result table

	selectWindow("Results");
	for (i = 0; i < Headings.length; i++) (
			selectWindow("Results");
			if(i == 0 || i == Headings.length-1) (
				cur_result = getResultString(Headings[i], nResults -
4);
			} else (
```

```
                                        cur_result = getResult(Headings[i], nResults - 4);
                                    };
                                    selectWindow("All_results");
                                    Table.set(Headings[i], Processed_image_counter,
cur_result);
                            };
                            selectWindow("All_results");
                            // add nuclei count data to count column of all results
                            Table.set("Count", Processed_image_counter, nResults-4);
                            Table.set("Image", Processed_image_counter, current_image);



                            selectWindow("All_results");
                            Table.update;

                            close("Results");
                            roiManager("delete");

                            Processed_image_counter++;
                    };
                    close("*");
            };
};
setBatchMode(false);
```

Endosome analyser.ijm

```
/*
 * Endosome analyser ( size and number )
 *
```

```
*/

// select input and output directories

input_dir = getDirectory("Choose input directory");
output_dir = getDirectory("Choose output directory");

// make necessary folder in output directory
File.makeDirectory(output_dir+"Pre-processed_Tiffs");
File.makeDirectory(output_dir+"Maxima");
File.makeDirectory(output_dir+"analysed overlays");
File.makeDirectory(output_dir+"Results");

//Get file list
Files = getFileList(input_dir);

//initialise img counter
img_count = 0;

//loop over all files
for (i = 0; i < lengthOf(Files); i++) (
	//detect and continue only if file ends with .tiff
	cur_file = Files[i];
	if(endsWith(cur_file, ".tiff"))(
		//increment counter and open image
		img_count++;
		open(input_dir+cur_file);
		//get image name and print to log which image is currently being analysed
		base_image_name = getTitle();
```

```
                print("Running analysis... Currently analysing: " + "\"" + base_image_name + "\"");

                // split channels and delete PMT trans image
                run("Split Channels");
                close("C2-" + base_image_name);

                if(nSlices > 1)(
                // convert z stack to max intensity stack
                run("Z Project...", "projection=[Max Intensity]");
                cur_image = "MAX_C1-"+base_image_name;
                } else (
                        cur_image = "C1-"+base_image_name;
                };
                //run analysis function
                selectImage(cur_image);
                endosome_analyser();

        };

};
selectWindow("Summary");
saveAs("txt", output_dir+"Results/Summarised.txt");

close("*");
close("Results");
close("Summarised.txt");
close("Roi Manager");
print("Analysis Complete!");
```

```
function endosome_analyser() (
	// first run total stain analysis
	// set huang threshold and measure stain area
	AutoScaler();
	print("                                Generating total stain Area value...");
	setAutoThreshold("Huang dark");
	total_stain_area = getValue("Area limit");
	//reset threshold to prepare for further anlaysis
	resetThreshold;

	// secondly analyse size and number of endosomes
	// preprocess image
	print("                                Pre-processing...");
	run("Top Hat...", "radius=1.5");
	saveAs("tiff", output_dir+"Pre-processed_Tiffs/"+"pre_proc_"+base_image_name);

	//get threshold values for find maxima prominece setting
	setAutoThreshold();
	getThreshold(lower, upper);
	prominence = lower;
	resetThreshold;

	//run find maxima to isoalte structures
	print("                                Finding Maxima...");
	run("Find Maxima...", "exclude strict prominence=" + prominence+" output=[Maxima Within
Tolerance]");
	saveAs("tiff", output_dir+"Maxima/"+ "Maxima_"+base_image_name + ".tiff");

	//run analyse particles to isolate and analyse endosomes
```

```
	print("                                analysing particles...");
	run("Analyze Particles...", "size=0-10 circularity=0.50-1.00 display exclude clear summarize add");
	selectWindow("Results");
	saveAs("txt", output_dir+"Results/"+ base_image_name +"_results.txt");

	roiManager("Show All without labels");
	run("Flatten");
	saveAs("tiff", output_dir+"analysed overlays/"+ "overlay_"+base_image_name);
	roiManager("delete");

	//add total stain area to summary table
	selectWindow("Summary");
	Table.set("Total stain area", img_count-1, total_stain_area);

	close("*");
	print("Done analysing: " + "\"" + base_image_name + "\"" + "\n" + img_count + "/" + lengthOf(Files) + " images analysed");

};

function AutoScaler()(
	AUTO_THRESHOLD = 5000;
	getRawStatistics(pixcount);
	limit = pixcount/10;
	threshold = pixcount/AUTO_THRESHOLD;
	nBins = 256;
	getHistogram(values, histA, nBins);
	i = -1;
```

```
        found = false;
        do (
    counts = histA[++i];
    if (counts > limit) counts = 0;
    found = counts > threshold;
        } while ((!found) && (i < histA.length-1))
        hmin = values[i];

        i = histA.length;
        do (
    counts = histA[--i];
    if (counts > limit) counts = 0;
    found = counts > threshold;
        } while ((!found) && (i > 0))
        hmax = values[i];

        setMinAndMax(hmin, hmax);
        run("Apply LUT");

};
```

Mitochondria analysis.ijm

```
/*
 * Macro Carrying out mitochondrial analysis, i.e fluoresence intensity of mito channels, Co-localisation of mito channels,
 * and branching analysis of mito channels
 *
 */
```

```
// Set Path

Path = getDir("Choose working Directory");
In_Path = getDir("Choose input folder");
File.makeDirectory(Path+"Nuclei_Morphology");
File.makeDirectory(Path+"Mito_Pre-processed_tiffs");
File.makeDirectory(Path+"Mito_post_analysis_tiffs");
File.makeDirectory(Path+"Mito_results");
File.makeDirectory(Path+"Mito_Binaries");

run("Set Measurements...", "area mean shape integrated display limit redirect=None decimal=3");

// Get list of image files in input
Files = getFileList(In_Path);



img_count = 0
//Open and run on all images
for (i = 0; i < lengthOf(Files); i++) ( // loop over all files in Path
	cur_file = Files[i]; // get current file name
	if(endsWith(cur_file, ".tiff"))(
		img_count++;
		open(In_Path+cur_file); // open current file
		raw_cur_image = getTitle(); // get current image name
		print("Currently analysing: "+raw_cur_image+" ....");

		// If z stack convert to max intensity. Each image has 3 channels so if nslice > 4 then must be Z stack
```

```
		if(nSlices > 4)(
			run("Z Project...", "projection=[Max Intensity]");
			cur_image = "MAX_"+raw_cur_image;
		} else (
			cur_image = raw_cur_image;
		};

		// Split channels
		run("Split Channels"); // Further codes assumes 3 channels, 1 Nuclei stain and 2 mitochondria

		// Run seperate process and analysis functions for each channel (Functions are designed specifically for this exp and
		// their respective channel only

		for(cur_channel = 1; cur_channel < 4; cur_channel++)(//loop over each channel
			if(cur_channel == 1)(
				print("\t\t\t\t\tProcessing: Nuclei morphology ....");
				C1_Nuclei_processor();
				print("\t\t\t\t\tProcessing: Nuclei morphology Done!");
			} else (
				selectImage("C"+cur_channel+"-"+cur_image);
				print("\t\t\t\t\tProcessing: Mitochondria: Channel_"+cur_channel);
				Mito_preprocessor();
				print("\t\t\t\t\t\t\tPreprocessing Mitochondria Done!: Channel_"+cur_channel);
				selectImage("C"+cur_channel+"-"+cur_image);
				Mito_Measurer();
				print("\t\t\t\t\t\t\tMitochondria Measuring Done!: Channel_"+cur_channel);
```

```
                                selectImage("C"+cur_channel+"-"+cur_image);
                                Mito_branch_analyser();
                                print("\t\t\t\t\t\t\tMitochondria Bracnch Analysis Done!: Channel_"+cur_channel);
                                print("\t\t\t\t\tProcessing Mitochondria: Channel_"+cur_channel+" Done!");
                        };
                };
                close("*");
                print("Done analysing: "+raw_cur_image);

        };
        close("*");
        close("ROI Manager");
};

function C1_Nuclei_processor() (
        selectImage("C1-"+cur_image);
        saveAs("tiff", Path+"Nuclei_Morphology/C1-"+cur_image);
        //run background subtraction
                run("Subtract Background...", "rolling = 50");
        //run stardist nuclei detection
        run(
                "Command From Macro",
                "command=[de.csbdresden.stardist.StarDist2D], args=['input':C1-"+cur_image+", 'modelChoice':'Versatile (fluorescent nuclei)', 'normalizeInput':'true', 'percentileBottom':'1.0', 'percentileTop':'99.0', 'probThresh':'0.8', 'nmsThresh':'0.3', 'outputType':'Both', 'nTiles':'1', 'excludeBoundary':'2', 'roiPosition':'Automatic', 'verbose':'false', 'showCsbdeepProgress':'false', 'showProbAndDist':'false'], process=[false]"
                );
        selectImage("Label Image");
```

```
		run("Flatten");
		saveAs("tiff",Path+"Nuclei_Morphology/"+"Label_Image"+raw_cur_image);
		//Measure morphology parameters
			if(roiManager("count") > 1) (
				roiManager("Measure");


				selectWindow("Results");
				Table.save(Path+"Nuclei_Morphology/"+raw_cur_image+"_Results.txt");


				close("Results");
				roiManager("delete");


			};
};


function Mito_preprocessor() (
		//run background subtraction
		run("Subtract Background...", "rolling = 5");
		//run unsharp mask
		run("Unsharp Mask...","radius=1 mask = 0.30");
		//run CLAHE
		run("Enhance Local Contrast (CLAHE)", "blocksize=199 histogram=256 maximum=1.50
mask=*None*");
		//run median filter
		run("Median...", "radius=0.5");
		//save processed image for referance
		saveAs("tiff", Path+"Mito_Pre-processed_tiffs/C"+cur_channel+"-"+cur_image);
};
```

```
function Mito_Measurer()(
	//measure on pre-processed and thresholded
	run("Duplicate...","  ");
	rename("C"+cur_channel+"-"+cur_image+"_measured");
	run("Measure");
	setThreshold(40, 255);
	rename("Threshold_measured_"+"C"+cur_channel+"-"+cur_image);
	run("Measure");
	selectImage("Threshold_measured_"+"C"+cur_channel+"-"+cur_image);
	run("Convert to Mask");
	saveAs("tiff", Path+"Mito_Binaries/"+getTitle());

	selectWindow("Results");
	Table.save(Path+"Mito_results/C"+cur_channel+"-
"+raw_cur_image+"_Measure_Results.txt");
	close("Results");

	close("C"+cur_channel+"-"+cur_image+"Threshold_measured");

};

function Mito_branch_analyser()(
	//run mitochodnrial branching analysis
	selectImage("C"+cur_channel+"-"+cur_image);
	setAutoThreshold("Otsu dark no-reset");
	setOption("BlackBackground", true);
	run("Convert to Mask");

	saveAs("tiff", Path+"Mito_Binaries/Otsu-Threshold_"+getTitle());
```

```
	run("Skeletonize");
	saveAs("tiff", Path+"Mito_Binaries/Skeleton_"+getTitle());
	run("Analyze Skeleton (2D/3D)", "prune=none display");
	//save image with plugin output overlay
	selectImage("Tagged skeleton");
	run("Flatten");
	saveAs("tiff", Path+"Mito_post_analysis_tiffs/Tag_skel_"+"C"+cur_channel+"-
"+raw_cur_image);
	close("Tagged skeleton");
	//save results
	selectWindow("Results");
	Table.save(Path+"Mito_results/"+raw_cur_image+"_C"+cur_channel+"_Results.txt");
	close("Results");
};
```

Astrocyte Nuclear morphol + GFAP.ijm

```
macro "astro nuc morphol and C3+4 staining" (
	//Ask user for input and output directories.
	/*
	Images should all be stored in one folder!
	Folder may contain images that will not be processed as selection of desrired files will
occur.
	*/

	in_directory = getDirectory("Choose input directory");
	out_directory = getDirectory("Choose output directory");

	//make dirs in out for preprocessed and overlays
	File.makeDirectory(out_directory+"preprocessed");
```

```
File.makeDirectory(out_directory+"Overlays");
File.makeDirectory(out_directory+"thresholded");
File.makeDirectory(out_directory+"Nuc_Results");
File.makeDirectory(out_directory+"POI_Results");

//get list of files from input directory
in_file_list = getFileList(in_directory);

//Ask user for string identifier of images to be processed from input directory
process_file_identifier = getString(
        "Regular expression indentifying files to be processed. Leave '.*' if all.", ".*"
);



//loop over all files in folder and process images matching desired identifier

Processed_image_counter = 0; //Counter for processed images. Starts at 0, increments by 1 per image. 0 = first image.

for (i = 0; i < in_file_list.length; i++) (

        //Decide whether to proccess current file
        if (in_file_list[i].matches(process_file_identifier)) (
                //Select image to be processed and open
                current_file_path = in_directory + in_file_list[i];
                open(current_file_path);
                rename(replace(getTitle(), " ", "_"));

                current_image = getTitle();
```

```
                print("Currently analysing: " + current_image);

                //split and select channel
                run("Split Channels");

                print("    Currently preforming nuclear morphology analysis...");
                Process_Nuc_morphol();
                print("    Currently preforming POI analysis...");
                Process_POI("C3");
                print("Completed analysis of: " + current_image);

                close("*");
            };

        };

        close("*");
        close("ROI Manager");
        close("Results");
        print("All analyses completed!!!");

        function Process_Nuc_morphol () (

            run("Set Measurements...", "area mean standard min shape integrated display
redirect=None decimal=3");

            //select nuc channel
            selectImage("C1-"+current_image);
```

```
		run("Blue");

		//run background subtraction

		run("Subtract Background...", "rolling = 50");


		//run CLAHE (local contrast enhancer

		run("Enhance Local Contrast (CLAHE)", "blocksize=50 histogram=256
maximum=4");

		//save preprocessed

		saveAs("tiff", out_directory+"Preprocessed/"+"C1-Preprocessed_"+current_image);


		//run StarDist on image with described parameters

		run("Command From Macro",

			"command=[de.csbdresden.stardist.StarDist2D], args=['input':"+"C1-
Preprocessed_"+current_image+", 'modelChoice':'Versatile (fluorescent nuclei)',
'normalizeInput':'true', 'percentileBottom':'0.19999999999999998', 'percentileTop':'99.8',
'probThresh':'0.6', 'nmsThresh':'0.4', 'outputType':'Both', 'nTiles':'1', 'excludeBoundary':'2',
'roiPosition':'Automatic', 'verbose':'false', 'showCsbdeepProgress':'false', 'showProbAndDist':'false'],
process=[false]"

			);

		selectImage("Label Image");

		run("Flatten");

		saveAs("tiff", out_directory+"Overlays/"+"overlay_"+current_image);


		//Measure morphology parameters

		if(roiManager("count") > 1) (

			roiManager("Measure");


			selectWindow("Results");

			Table.save(out_directory+"Nuc_Results/"+"Nuc_result_"+current_image);


			close("Results");
```

```
                roiManager("delete");


        };
};


function Process_POI(channel) (
        //select POI channel
        selectImage(channel+"-"+current_image);
        run("Green");
        //run background subtraction
        run("Subtract Background...", "rolling = 50");


        //run CLAHE (local contrast enhancer
        run("Enhance Local Contrast (CLAHE)", "blocksize=50 histogram=256
maximum=4");
        //save preprocessed
        saveAs("tiff", out_directory+"Preprocessed/"+channel+"-
Preprocessed_"+current_image);


        run("Set Measurements...", "area mean standard min integrated limit display
redirect=None decimal=3");
        //measure without threshold
        setThreshold(0, 255);
        run("Measure");


        //measure with threshold
                setThreshold(20, 255);
        run("Measure");
        run("Convert to Mask");
```

```
		saveAs("tiff", out_directory+"thresholded/"+channel+"-
thresholded_"+current_image);


		//save results
		selectWindow("Results");
		Table.save(out_directory+"POI_Results/"+channel+"-POI_result_"+current_image);


		close("Results");
};
```

Astrocyte Nuclear morphol + C3+4 stain.ijm

```
macro "astro nuc morphol and C3+4 staining" (
	//Ask user for input and output directories.
	/*
	Images should all be stored in one folder!
	Folder may contain images that will not be processed as selection of desrired files will
occur.
	*/

	in_directory = getDirectory("Choose input directory");
	out_directory = getDirectory("Choose output directory");

	//make dirs in out for preprocessed and overlays
	File.makeDirectory(out_directory+"preprocessed");
	File.makeDirectory(out_directory+"Overlays");
	File.makeDirectory(out_directory+"thresholded");
	File.makeDirectory(out_directory+"Nuc_Results");
	File.makeDirectory(out_directory+"POI_Results");
```

```
//get list of files from input directory
in_file_list = getFileList(in_directory);

//Ask user for string identifier of images to be processed from input directory
process_file_identifier = getString(
        "Regular expression indentifying files to be processed. Leave '.*' if all.", ".*"
);



//loop over all files in folder and process images matching desired identifier

Processed_image_counter = 0; //Counter for processed images. Starts at 0, increments by 1 per image. 0 = first image.

for (i = 0; i < in_file_list.length; i++) (

        //Decide whether to proccess current file
        if (in_file_list[i].matches(process_file_identifier)) (
                //Select image to be processed and open
                current_file_path = in_directory + in_file_list[i];
                open(current_file_path);
                rename(replace(getTitle(), " ", "_"));

                current_image = getTitle();

                print("Currently analysing: " + current_image);

                //split and select channel
```

```
                run("Split Channels");

                print("    Currently preforming nuclear morphology analysis...");
                Process_Nuc_morphol();
                print("    Currently preforming POI analysis...");
                Process_POI("C3");
                Process_POI("C4");
                print("Completed analysis of: " + current_image);

                close("*");
            };

        };

        close("*");
        close("ROI Manager");
        close("Results");
        print("All analyses completed!!!");

        function Process_Nuc_morphol () (

            run("Set Measurements...", "area mean standard min shape integrated display
redirect=None decimal=3");

            //select nuc channel
            selectImage("C1-"+current_image);
            run("Blue");
            //run background subtraction
            run("Subtract Background...", "rolling = 50");
```

```
		//run CLAHE (local contrast enhancer
		run("Enhance Local Contrast (CLAHE)", "blocksize=50 histogram=256 maximum=4");
		//save preprocessed
		saveAs("tiff", out_directory+"Preprocessed/"+"C1-Preprocessed_"+current_image);

		//run StarDist on image with described parameters
		run("Command From Macro",
			"command=[de.csbdresden.stardist.StarDist2D], args=['input':"+"C1-Preprocessed_"+current_image+", 'modelChoice':'Versatile (fluorescent nuclei)', 'normalizeInput':'true', 'percentileBottom':'0.19999999999999998', 'percentileTop':'99.8', 'probThresh':'0.6', 'nmsThresh':'0.4', 'outputType':'Both', 'nTiles':'1', 'excludeBoundary':'2', 'roiPosition':'Automatic', 'verbose':'false', 'showCsbdeepProgress':'false', 'showProbAndDist':'false'], process=[false]"
			);
		selectImage("Label Image");
		run("Flatten");
		saveAs("tiff", out_directory+"Overlays/"+"overlay_"+current_image);

		//Measure morphology parameters
		if(roiManager("count") > 1) (
			roiManager("Measure");

			selectWindow("Results");
			Table.save(out_directory+"Nuc_Results/"+"Nuc_result"+current_image);

			close("Results");
			roiManager("delete");

		};
```

```
};


function Process_POI(channel) (
	//select POI channel
	selectImage(channel+"-"+current_image);
	if(channel == "C3")(
		run("Yellow");
	} else (
		run("Red");
	};
	//run background subtraction
	run("Subtract Background...", "rolling = 50");

	//run CLAHE (local contrast enhancer
	run("Enhance Local Contrast (CLAHE)", "blocksize=50 histogram=256
maximum=2");
	//save preprocessed
	saveAs("tiff", out_directory+"Preprocessed/"+channel+"-
Preprocessed_"+current_image);

	run("Set Measurements...", "area mean standard min integrated limit display
redirect=None decimal=3");
	//measure without threshold
	run("Measure");

	//measure with threshold
	setAutoThreshold("RenyiEntropy dark no-reset");
	run("Measure");
	run("Convert to Mask");
```

```
		saveAs("tiff", out_directory+"thresholded/"+channel+"-
thresholded_"+current_image);


		//save results

		selectWindow("Results");

		Table.save(out_directory+"POI_Results/"+channel+"-
POI_result"+current_image+".txt");


		close("Results");

};
```

IPSC neuron nuclei counter + morphol copy.ijm

```
/*

Script to automate the assessment of cell nuclear morphology in

one fluorescent channel via StarDist plugin in images of single channel tiff format.  Variation on original desgned for SH-SY5Y


Currently does not support semi-automatic or nuclei counting.


THis version is optimised for neuronally differentiatied IPSCs and the specific folder / image structure at the time.

Do not use for other cells without adjustment of parameters.


Adjustments may be made in future to accomodate other formats.

*/


macro "Cell Nuclear Morphology" (


	run("Set Measurements...", "area mean shape integrated display redirect=None
decimal=3");
```

```
//Ask user for input and output directories.
/*
Images should all be stored in one folder!
Folder may contain images that will not be processed as selection of desrired files will occur.
*/

in_directory = getDirectory("Choose input directory");
out_directory = getDirectory("Choose output directory");

//get list of files from input directory
in_file_list = getFileList(in_directory);

//Ask user for string identifier of images to be processed from input directory
process_file_identifier = getString(
        "Regular expression indentifying files to be processed. Leave blank if all.", ""
);



//loop over all files in folder and process images matching desired identifier

Processed_image_counter = 0; //Counter for processed images. Starts at 0, increments by 1 per image. 0 = first image.

for (i = 0; i < in_file_list.length; i++) (

        //Decide whether to proccess current file
        if (in_file_list[i].matches(process_file_identifier)) (
```

```
                Process();
            };
        };

        close("*");
        close("ROI Manager");

        //define analysis function
        function Process() (

            //Select image to be processed and open
            current_file_path = in_directory + in_file_list[i];
            open(current_file_path);
            rename(replace(getTitle(), " ", "_"));

            current_image = getTitle();
            print(current_image);
            //run background subtraction
            run("Subtract Background...", "rolling = 50");
            //run StarDist on image with described parameters
            run("Command From Macro",
                "command=[de.csbdresden.stardist.StarDist2D],
args=['input':"+current_image+", 'modelChoice':'Versatile (fluorescent nuclei)',
'normalizeInput':'true', 'percentileBottom':'0.19999999999999998', 'percentileTop':'99.8',
'probThresh':'0.45', 'nmsThresh':'0.4', 'outputType':'ROI Manager', 'nTiles':'1', 'excludeBoundary':'2',
'roiPosition':'Automatic', 'verbose':'false', 'showCsbdeepProgress':'false', 'showProbAndDist':'false'],
process=[false]"
                );

            //Measure morphology parameters
```

```
                if(roiManager("count") > 1) (
                        roiManager("Measure");

                        selectWindow("Results");
                        Table.save(out_directory+(i+1)+"_Results");

                        close("Results");
                        roiManager("delete");

                        Processed_image_counter++;
                };
                close("*");
        };
};
setBatchMode(false);
```